Targeting the microtubules to improve the searching efficiency of cytotoxic T lymphocytes in 3D environments

Dissertation zur Erlangung des

Grades die Doktorin der Naturwissenschaften

der Naturwissenschaftlich-Technischen Fakultät der

Universität des Saarlandes

von

Galia Magela Montalvo Bereau

Saarbrücken
2024

Tag des Kolloquiums: Montag, 3. Februar 2025

Dekan: Univ.-Prof. Dr.-Ing. Dirk Bähre

Berichterstatter: -Prof. Dr. Franziska Lautenschläger
-Priv.-Doz. Dr. Bin Qu
-Prof. Dr. Laura Aradilla Zapata.

Vorsitz: Prof. Dr. Aránzazu del Campo Bécares

Akad. Mitarbeiter: Dr. Alexis Darras

Contents

Abstract

Cell migration is essential for cytotoxic T lymphocytes (CTLs) to effectively search and kill target cells in three-dimensional (3D) environments. Impaired migration of CTLs reduces immune response efficacy and is a challenge for current cell therapies. In fast-moving lymphocytes like CTLs, microtubules (MT) are concentrated and organized behind the nucleus in a microtubule-organizing center (MTOC). The exact role of the MTOC and the MT network during CTLs migration is not fully understood. Disruption of MT stability has been shown to enhance CTLs migration, though the mechanism remains unclear. In this study, we used Pretubulysin, a microtubule depolymerizer, to disrupt the MT network in CTLs. This treatment improved CTLs infiltration and killing efficiency in 3D by enhancing their migratory capabilities. As the mechanism underlaying such enhanced efficiency, we propose localized actomyosin accumulation at the cell's uropod, which alters cell mechanics and morphology, leading to faster and more persistent migration. Additionally, we observed MT dynamics and MTOC positioning during CTLs migration in constricted environments. We found that confinement of the cells forces a polarization status that dictates faster and more persistent migration, linked to less freedom of the MTOC to rotate around the nucleus. Taken together, our findings underscore the role of MTs in regulating CTLs migration and suggest that MT-targeting agents like Pretubulysin could improve CTLs-mediated killing, offering potential for new immunotherapeutic strategies.

Zusammenfassung

Die Zellmigration ist für zytotoxische T-Lymphozyten (CTLs) von entscheidender Bedeutung, damit sie in dreidimensionalen Umgebungen (3D) effektiv nach Zielzellen suchen und diese abtöten können. Eine gestörte Migration von CTLs verringert die Wirksamkeit der Immunantwort und stellt eine Herausforderung für aktuelle Zelltherapien dar. In sich schnell bewegenden Lymphozyten wie CTLs sind die Mikrotubuli (MT) hinter dem Zellkern in einem Mikrotubuli-Organisationszentrum (MTOC) konzentriert und organisiert. Die genaue Rolle des MTOC und des MT-Netzwerks bei der Migration von CTLs ist noch nicht vollständig geklärt. Es hat sich gezeigt, dass eine Störung der MT-Stabilität die Migration von CTLs fördert, obwohl der Mechanismus noch unklar ist. In dieser Studie haben wir Pretubulysin, einen Mikrotubuli-Depolymerisator, verwendet, um das MT-Netzwerk in CTLs zu unterbrechen. Diese Behandlung verbesserte die Infiltrations- und Tötungseffizienz von CTLs in 3D, indem sie ihre Migrationsfähigkeit erhöhte. Als Mechanismus, der dieser verbesserten Effizienz zugrunde liegt, schlagen wir eine lokale Anhäufung von Aktomyosin am Uropod der Zelle vor, die die Zellmechanik und -morphologie verändert und zu einer schnelleren und nachhaltigeren Migration führt. Darüber hinaus haben wir die MT-Dynamik und die MTOC-Positionierung während der Migration von CTLs in eingeschränkten Umgebungen beobachtet. Wir fanden heraus, dass die Enge der Zellen einen Polarisationsstatus erzwingt, der eine schnellere und anhaltendere Migration bedingt, die mit einer geringeren Freiheit des MTOC zur Rotation um den Zellkern verbunden ist. Insgesamt unterstreichen unsere Ergebnisse die Rolle der MTs bei der Regulierung der Migration von CTLs und legen nahe, dass MT-gerichtete Wirkstoffe wie Pretubulysin die CTLs-vermittelte Abtötung verbessern könnten, was Potenzial für neue immuntherapeutische Strategien bietet.

Acknowledgements

Completing this PhD thesis has been a challenging but incredibly rewarding journey, and it would not have been possible without the support, guidance, and encouragement of many individuals. Here, I express my gratitude to them.

First, I would like to thank my current supervisors, Prof. Dr. Franziska Lautenschläger and PD Dr. Bin Qu for their scientific guidance, insightful feedback, and continuous encouragement. Thanks, Franzi and Bin, excellent scientists and dedicated mentors, you have been an inspiration to me leading by example both professionally and personally.

I am profoundly grateful to all my teachers from every level of my education, who have inspired and shaped my academic journey. From my earliest school days to my higher education, each teacher and supervisor has contributed to my growth and learning.

To my current colleagues and lab-mates, your support, feedback, and camaraderie have been indispensable throughout this journey. Thank you for creating a collaborative and stimulating work environment. I would also like to acknowledge my previous coworkers from Center for Molecular Immunology in Cuba and from the Ludwig Institute for Cancer research in Switzerland. Their support and shared knowledge have been instrumental in my development as a researcher. Also, their kindness warmed my heart and enriched my professional experiences.

To my friends, your encouragement and understanding have been a source of strength. Thank you for being there through the highs and lows, and for providing a sense of balance and perspective during this demanding process.

My heartfelt thanks go to my family, whose love and support have been a constant source of motivation.

Finally, I would like to express my gratitude to everyone who has contributed to my personal and academic growth. Your support has been crucial to the completion of this thesis, and I am deeply grateful to each one of you.

Abbreviations

1D, 2D, 3D	One-, two- or three-dimensional
APC	Antigen Presenting Cell
Arp2/3	Actin Related Protein 2/3 complex
CD8/CD3	Cluster of Differentiation 8/3
CFSE	CarboxyFluorescein Succinimidyl Ester
CTLs	Cytotoxic T Lymphocytes
DAPI	4′,6-diamidino-2-phenylindole
DC	Dendritic Cell
DMSO	Dimethyl Sulfoxide
ECM	Extracellular Matrix
f-actin	Filamentous Actin
GEF-H1	Guanine nucleotide Exchange Factor
GTP	Guanosine-5'-triphosphate
mDia	p140 Diaphanous
MFI	Mean Fluorescence Intensity
MHC I	Major Histocompatibility Complex I
MLC	Myosin Light Chain
MSA/MDA	Microtubule stabilization agent / Microtubule destabilization agent
MT/MTs	Microtubule / Microtubules
MTOC	Microtubule Organizing Center
PDMS	Polydimethylsiloxane
pMyo	Phosphorylated Myosin
PT	Pretubulysin
RhoA	Ras homolog family member A
RTDC	Real Time Deformability Cytometry
SEA	Streptococcus Enterotoxin A
TCR	T Cell Receptor
WASP	Wiskott-Aldrich syndrome protein
WAVE	WASP-family verprolin-homologous protein

1. Introduction

1.1. Motivation and aims

Cell migration is an important function of immune cells, facilitating their ability to protect the body from infections (Fowell & Kim, 2021). Among these cells, cytotoxic T lymphocytes (CTLs)—activated T CD8$^+$ cells—play a vital role. They infiltrate tissues, searching for and destroying target cells. However, before they can execute their cytotoxic function, CTLs must traverse complex tissue environments to locate their targets (Barry & Bleackley, 2002) Initially, *naïve* T cells navigate within the lymph nodes. Upon activation, they alter their motile behavior to reach infection sites searching for their specific target expressed on infected cells (Krummel et al., 2016). Thus, a successful immune response relies on the immune cells' search strategy to find pathogens. An optimal search strategy can be modulated by adjusting the speed, the persistence or -as introduced more recently- by tuning the correlation between those two parameters (Shaebani et al., 2020). Adjusting this correlation is especially relevant when the cell's average movement length is much shorter than the size of the area they are searching in, like immune cells in normal tissues trying to find less represented antigens. A "universal coupling between speed and persistence" has been proposed, describing that those cells moving faster exhibit a more persistent movement. This relationship appears to hold true for all migrating cells (Maiuri et al., 2015).

The cell's machinery that defines the patterns and searching efficiency during migration is the cytoskeleton: a dynamic network within cells that serves as the architectural framework guiding many cellular functions (Fletcher & Mullins, 2010). At its core are three major elements: actin, microtubules (MT) and intermediate filaments. Actin provides the structural basis for cell shape and movement, MTs act as highways for intracellular transport and organization, intermediate filaments form a network that provides mechanical support to protect organelles (Hohmann & Dehghani, 2019). All the cytoskeletal elements are dynamically coupled and regulated to coordinate important cellular processes including migration (Moreau et al., 2018).

Many studies tried to comprehend the role that the cytoskeleton plays of CTLs during immune synapse (Douanne & Griffiths, 2021) but much less investigations exist to describe its role in regulating T cell migration within physically complex environments. CTLs migrating in tissues (3D environments) move fast and are confined by the extracellular matrix (Krummel et al., 2016). Such locomotion is mostly integrin-independent and the

actomyosin system is the major force generator machinery (Dupré et al., 2015). The cell propulsion is based on myosin contractions at the uropod allowing detachment and squeezing (Harrison et al., 2019). For example, crossing the endothelial barrier requires myosin-driven contractility and nuclear squeezing through the endothelial cells' junctions. The migration efficiency depends on the amount of generated force (Krummel et al., 2014). In T cell dynamics, while filamentous actin is assumed as fundamental for force generation, the MT also play a role, specially at the interface during activation contacts (Hui & Upadhyaya, 2017). MTs itself do not generate the force but can regulate actin-dependent generated force via guanine nucleotide exchange factor (GEF-H1) (Krendel et al., 2002). GEF-H1 can be found bound to MTs, in which case it is inactive, and becomes activated after MTs depolymerization. This activation can occur due to the inherent physiological instability of MTs or can be induced through the use of MT depolymerizing drugs. Once activated, GEF-H1 stimulates Rho increasing myosin II contractility and actin polymerization (Azoitei et al., 2019; Chang et al., 2008).

By perturbing the MTs, the migratory parameters of the cell can be affected: impaired migration is observed with MTs stabilization (Lautenschlaeger et al., 2009.; Tabdanov et al., 2021), while destabilization of the MT network results in enhancing T cells function (Tabdanov et al., 2021; Zhao et al., 2021). Thus, the MT network of T cells emerges as an attractive target that can be specifically disrupted to maximize the efficacy of immune cells related therapies. For targeting microtubules, several interventions have been reported and pharmacological agents that target MTs can be broadly categorized into two groups: MT-stabilizing agents (MSA) and MT-destabilizing (MDA) agents. Both type of drugs, can interfere with the mitotic spindle dynamic, preventing proper chromosome segregation and cell division. Vinblastine (an example of MDA), for instance, is employed to treat lymphomas, leukemias, and certain solid tumors (Steinmetz & Prota, 2018). Taxol (an example of MSA) is also used to treat various types of cancer: ovarian, esophageal, breast, lung, cervical, and pancreatic.

Natural compounds have been successfully used to target the MTs for a long time, one example is Tubulysins, a highly potent drug family produced by myxobacteria strains. Unfortunately, the production of tubulysins is limited due to challenging fermentation, isolation procedures, and intricate chemical synthesis. To address these challenges, strategies for chemical synthesis are desired, but rarely successful. Pretubulysin (PT), a natural precursor of tubulysins, was successfully synthesized on a large scale. It was shown to be able to kill tumor cell lines, inhibit the migration capacity of cancerous cells and

induce apoptosis *in vitro*, demonstrating that the simplified precursor is as potent as the compound from which it was derived (Herrmann et al., 2012).

While MT-depolymerization agents have garnered significant attention as cytotoxic drugs, there remains a notable scarcity of studies examining their effects on T cells. Existing research predominantly focuses on cancer cells rather than immune cells (Steinmetz & Prota, 2018). Given recent evidence of enhancing CTLs functions by targeting MTs and considering PT is a potent MT-destabilizing agent coupled with the advantage of chemical synthesis, our work aims to bridge an existing gap by evaluating the effect of PT drug on human T cells. To this end, we have outlined the following general aims:

- Assess the efficacy of microtubule-disassembling agent Pretubulysin in enhancing CTLs infiltration and killing in 3D environments.
- Elucidate the underlying mechanism by which microtubule depolymerization affects CTLs migration and searching efficiency.
- Contribute to understanding the function of microtubules and MTOC in CTLs migration and searching.

1.2. State of the art

- Migration and searching for immune cell function.

The immune system grants us defense against pathogens and malignant mutations of our own cells. Motility is fundamental to finding invader pathogens, controlling tissue integrity and eliminating possible tumors even before they are established (Vesperini et al., 2021). Diminished motility of immune cells could lead to serious autoimmune diseases, while enhanced cell migration is related to chronic inflammation and tumor evasion. Understanding immune cells migratory mechanisms is vital to manipulate cellular immunity for maintaining health against infectious diseases and cancer (Simula et al., 2022). The entire immune defense process relies on motility, and since the initial stages precursors of immune cells travel from the primary lymphoid organs, bone marrow and thymus, to other secondary lymphoid organs to maturate (Merino-Casallo et al., 2022). The intricacies of this immune cell's migration have long intrigued researchers. Many factors influence cell migration dynamics, including cell type and mechanical properties, dimensionality, characteristics of the environment, and cell-cell interactions. To capture these rich dynamics, various mathematical models have been proposed. The fact that such diverse approaches exist confirms the complexity and challenges involved in fully describing the cell migration process (Shaebani et al., 2022). In the absence of external cues, cells exhibit random movement patterns, akin to immune cells patrolling an organism in search of pathogens or food sources. External cues, such as chemical gradients, guide cells towards favorable environments while steering them away from potential threats. While the directional movement of microorganisms like *Escherichia coli* is well studied, the mechanisms governing the migration patterns of immune cells in complex environments remain less understood.

A successful immune response relies on efficiently locating specific targets, making it crucial to devise strategies that minimize search time. Understanding how cells achieve this and the strategies they use for optimizing their search efficiency is an important step toward proposing better cell- based therapies. Two parameters that control the search efficiency are speed and persistence, which are coupled for all types of cells, as demonstrated by (Maiuri et al., 2015). This means that when cells move faster, they also tend to maintain their direction for longer periods. Another study, more recently introduced a new concept, demonstrating that the correlation value between speed and persistence is itself a parameter that can be tuned to optimize the search efficiency. They propose that this strategy enhances

search efficiency when the mean persistence length is much shorter than the confinement size or when cells move in environments considerable larger than their standard persistence length (as is the case for dendritic cells in peripheral tissues) (Stankevicins et al., 2020, Shaebani et al., 2020). Overall, those findings shed light on the dynamics of active random searches, with potential applications in designing more effective immunotherapies. Understanding cell migration from a physical perspective is crucial for unraveling its significance.

- Cytotoxic T Lymphocytes: precision immune killers

Cytotoxic T lymphocytes (CTLs) are a subset of $CD8^+$ lymphocytes fundamental in adaptative immunity and host defense against intracellular pathogens. CTLs are defined by the expression of the CD8 molecule on their surface, which interacts with the major histocompatibility complex class I (MHC-I) of the antigen presenting cells (APCs) (Barry & Bleackley, 2002). T cells' life cycle starts in the primary lymphoid organ bone marrow, then the cells continue their maturation in the thymus, and get fully activated once they find a specific target throughout the body. Typically, the lymph nodes are the organs favorable for this encounter, where T cells get activated by dendritic cells or other APCs. The activation of CTLs is a multistep process initiated by the recognition of specific antigenic peptides presented by MHC-I molecules on professional APCs or infected cells. This recognition occurs through the T cell receptor (TCR) on CTLs, in conjunction with co-stimulatory signals provided by other surface molecules such as CD28 and cytokines like Interleukin-2. Upon activation, cells undergo clonal expansion and differentiation into effector CTLs, which possess potent cytotoxic capabilities.

The migratory proprieties of T cells vary depending on the maturation state, and as a result, also the search strategies can be different (Figure 1). This diversity in migration modes allows the initial examination of large areas of the lymph node before activation and/or the persistent migration to find the defined target upon activation (Moreau et al., 2018). Thus, TCR stimulation is considered the physiological trigger for defining and establishing the migration mode. If TCR stimulation is strong enough, T cells fully stop and establish an immunological synapse that rends them active (Moreau et al., 2015). Once activated, T cells switch their migration mode and move from the lymphatic node to the inflammation site to perform their effector function there (Lämmermann & Germain, 2014). Effector

CTLs employ various mechanisms to eliminate target cells. The primary mechanism of killing is the release of cytotoxic granules with molecules such as perforin and granzymes.
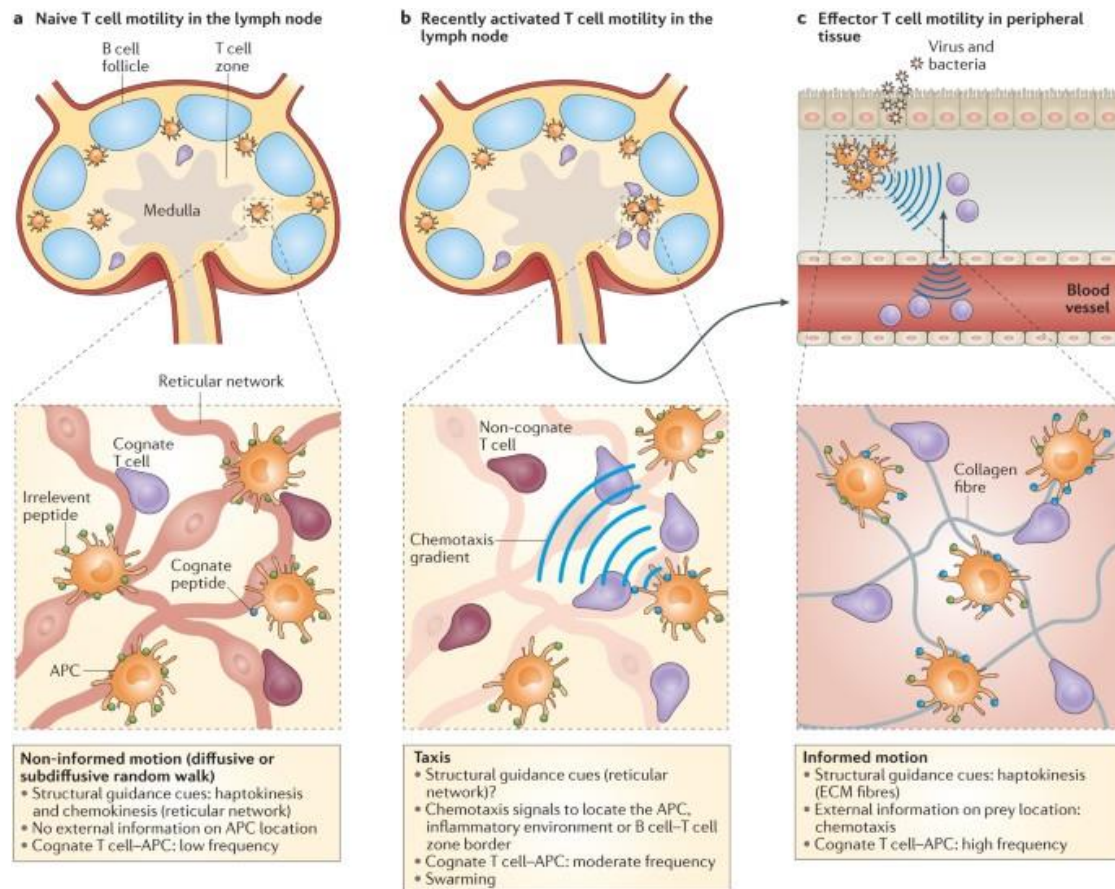

Figure 1. T cell motility in different activation status and microenvironments. A) Naive T cells migration is guided by stromal structures B) Recently activated T cells move directionally towards secondary lymphoid organs. C) Primed T cells become effector T cells and migrate to peripheral sites, their motion is described either as diffusive (Brownian-type) or as superdiffusive (Lévy-type) random walks, depending on the tissue type. Figure was taken from (Krummel et al., 2016)

- Migration of T lymphocytes: mechanisms and challenges

The wide range of microenvironments explored by CTLs implies that they navigate within different scenarios during their physiological migration, including 1D, 2D, and 3D conditions (Figure 2). To enter or leave the lymph nodes, immune cells must cross the lymphatics at the capillaries. Due to the dimeter of such capillaries, this is a classical 1D migration, which proceeds along a linear space. 2D migration, although the best-studied, is the least common form of migration under normal physiological conditions and can be observed when lymphocytes migrate along the interior surface of large blood or lymphatic

vessels. The most common is 3D migration, meaning that cells migrate continuously embedded in the extracellular matrix.

Migration through 3D environments is challenging. In such environments, immune cells need to squeeze through the extracellular matrix, which can be dense and biochemically complex. To do this, T cells activate specific cellular adaptation mechanisms, but remodeling of the extracellular matrix is uncommon (Vesperini et al., 2021). Also, during navigating through diverse environments, cells often interact with other neighboring cells, such interactions provide physical signals to modify their migration (Zhou et al., 2017).
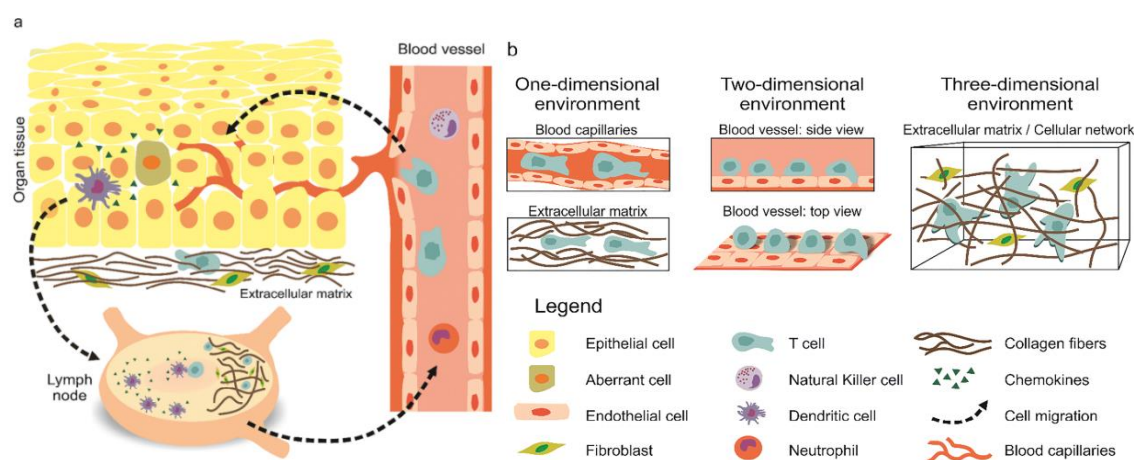

Figure 2. Migration of immune cells in diverse environments. A) General representation of different types of immune cell migrating *in vivo*. B) Schematic of 1D, 2D and 3D physiologically relevant scenarios during migration. Figure taken from (Vesperini et al., 2021)

Interestingly, when the trajectories of CTLs inside 3D collagen matrices were analyzed by Sadjadi et al., 2020, three motility types were found: slow, fast, and mixed. By visualizing CTLs migration, the authors found that initial cell infiltration into the collagen matrix creates pathways by displacing or stretching the collagen fibers. These pathways then enable other T cells to move more quickly, as they can follow the pre-formed channels. Over time, more channels are built by leading migrating T cells, increasing the overall migration speed over time (Sadjadi et al., 2020). These observations show that when CTLs navigate in 3D environments the creation of channels as strategy to move faster, results in a confined migration in 1D.

The mechanisms by which cells move through the body have been intensively studied. In general, there are two migration modes: mesenchymal and amoeboid (Moreau et al., 2018)

(Figure 3). *In vivo*, immune cells commonly use the amoeboid migration mode. Amoeboid migration is described by low adhesion to the surrounding environment, no degradation or minimal modification of the ECM, and rounded cell morphology with prevalence of contractile forces at the back of the cell (Renkawitz et al., 2009). However, the classification of amoeboid migration is still under constant review and none of them is exclusive for a single type of cell. It is rather a mechanism dependent on different parameters, such as activation, physiological surrounding context, and interactions that cells can establish with the extracellular matrix. Moreover, cells can switch between both modes as a cellular mechanism to adapt to their environment (Liu et al., 2015). In general, migration-mode plasticity is an important factor to take into consideration when studying the motility of immune cells.
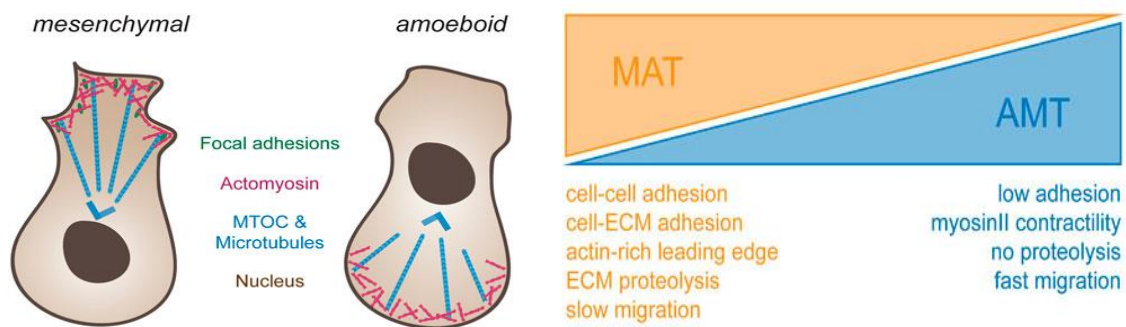

Figure 3. Schematic representation of mesenchymal and amoeboid migration. MAT: mesenchymal-amoeboid transition; AMT: amoeboid-mesenchymal transition. Figure taken from (Pawluchin & Galic, 2022)

- Regulation of cell migration: the cytoskeleton

As previously stated here, amoeboid migration is the typical one observed during immune cell motility in tissues. However, some aspects of the exact mechanisms explaining this migration in 3D environments remain to be elucidated. For example, it is still unclear why T cells do not develop mechanisms to modify the surrounding matrix by enzymatic degradation, and instead prefer to actively change their shape to accommodate to the spaces where they can pass throw (Sadjadi et al., 2020). Another example of a non-explained phenomenon is the proportionality between the efficiency of amoeboid motility and actomyosin contractility in the cell cortex and inverse relationship of such efficiency and the cell interaction/adhesion with the environment (Zhovmer et al., 2024). With the development of new experimental tools, many studies are increasingly reporting technically complex and physiologically relevant models to study immune cell migration.

The cytoskeleton is fundamental in generating the forces for the migration process: Actin is directly involved and responsible for generating two types of forces, the protrusive and the contractile; the MT network provides trails for organelle and protein movement inside the cell and regulates the actin-mediated contractility. Both actin filaments and microtubules are polymers formed by structurally asymmetrical subunits. As a result, both polymers are polarized, with distinguishable starting and ending points. This structural polarity observed for actin and MT, makes them suitable tracks for molecular motors (Fletcher & Mullins, 2010). To build the "contractile structure" at the rear of an amoeboid migrating immune cell not only actin filaments formation is required, but also myosin activity is needed (Jacobelli et al., 2010). For myosin motor function, it has been described that the protein binds to the bundles of filaments of actin aligned, such as in stress fibers. This contractile capacity enables cells to sense their external environment and adapt correspondingly. Signaling pathways (involving proteins like mDia, Rho, Arp2/3 complex, WASP/WAVE family) and other active linker proteins, achieve coordination between cytoskeletal elements (Devreotes & Horwitz, 2015).

The polarized morphology of migrating CTLs underscores the importance of the cytoskeleton in their biological function (Figure 4). CTLs display a leading-edge rich in actin and actin-binding proteins, followed by the rest of the cell body with the nucleus and behind the nucleus, the microtubule-organizing center (MTOC) preceding the uropod. In T cells, the uropod is a contractile structure localized at the back, rich in actomyosin complexes, Rho-A activity, and a meshwork of MTs directed from the MTOC (Huse, 2017).
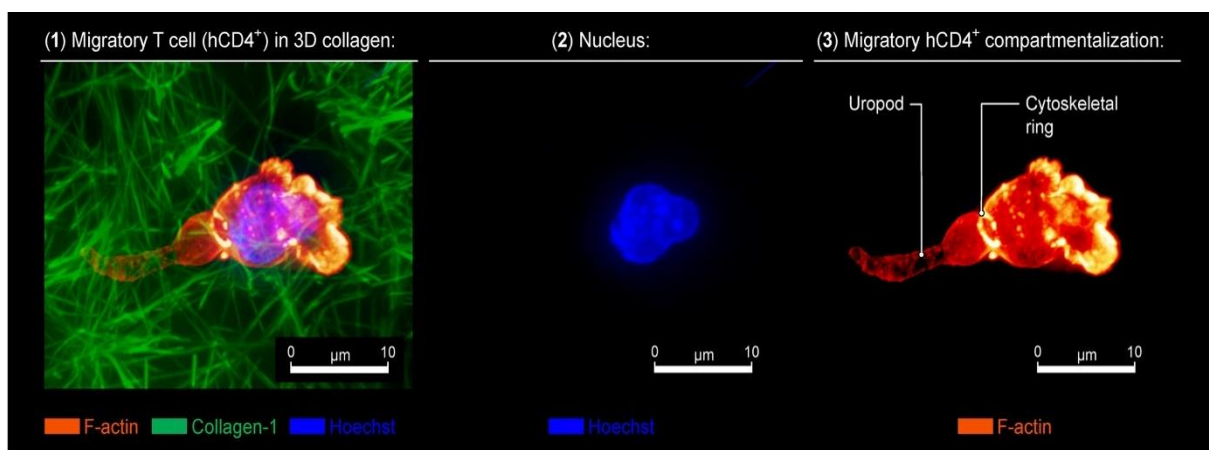

Figure 4. CD4^{+}T cell during amoeboid migration in 3D collagen matrix. The distinctive asymmetrical distribution of actin intensity during migration in 3D can be observed, with low intensity at the uropod and high intensity at the cell front. This figure was cropped from a bigger original one published on (Zhovmer et al., 2024)

Immune cells have been shown to be able to migrate without needing integrins (Lämmermann et al., 2008). In this context, forces are generated coupling their actin retrograde flow to the geometry of an irregular space and transmitted, which has been demonstrated for T cells. Most relevant, this observed phenomenon happens without any known molecular pathway that links the cytoskeleton with the surrounding substrate (Reversat et al., 2020). Additionally, in ameboid migration, actomyosin contractility generates pressure and movement of the cytoplasm, resulting in the formation of membrane deformations called blebs. Blebs have been described as an important mechanism in amoeboid migration.

To date, significant works have helped on the understanding of the role of the actin cytoskeleton for amoeboid migration, but much less is known about microtubules' impact on regulating T cell migration in 3D complex environments.

- Microtubules in amoeboid migration

The connection between cell movement and microtubules (MT) remains a subject of fascination among biologists. Despite advancements in understanding the biophysics of the MT for immune synapse, little is known about their role in T-cell migration through complex microenvironments (Kopf et al., 2020).

MTs play a crucial role in symmetry breaking during cell migration, with post-translational modifications driving this process. They also facilitate directional trafficking and organized signaling to control actin machinery during the formation of membrane protrusions. Dynamic microtubules transiently dock at membrane complexes called cortical microtubule stabilizing complexes and connecting microtubules to adhesion sites (Legátová et al., 2023). In immune surveillance, microtubules coordinate dendritic cell movement by serving as shape sensors. This spatial coordination is crucial for coherent migration and can be disrupted by nocodazole-induced microtubule destabilization. Recent research suggests that MTs, particularly those associated with the microtubule organizing center (MTOC), may serve as an internal shape sensor for cell navigation. This was demonstrated in leukocytes migrating through complex environments, where the MTOC position, relative to the nucleus was a critical (Kopf et al., 2020).

T lymphocytes activation also prompts rapid MT polarization, facilitating the secretion of specific cytokines in the right orientation and direction. At the interface between T cells and the presenting cell, the interaction between the TCR and CD3 molecule induces traction

stress that helps the activation of the lymphocyte and induces functional changes. During this process, dynamic MTs play a crucial role in modulating force generation by downregulating actin -associated contractility (via Rho), highlighting the interplay between microtubules and actin in T-cell activation (Hui & Upadhyaya, 2017).

The interplay between microtubules and contractility, has recently been termed the 'microtubule-contractility axis' (Schmidt & Stehbens, 2024) and regulates cell shape and mechanical properties during migration, mediated by a guanine nucleotide exchange factor: GEF-H1. The mechanism starts with the depolymerization of the MT and subsequently, GEF-H1 is released in active form. Active GEF-H1 (phosphorylated) induces the activation of RhoA and triggers the contractile response (Joo & Olson, 2021) (Figure 5). Experimental results have reported activation of GEF-H1 after naturally or pharmacologically induced MT depolymerization, always accompanied by increased actin filaments formation and myosin-dependent contraction (Krendel et al., 2002).

A very important confirmation of the link between GEF-H1 function and the contractile phenotype, was reported by depleting endogenous GEF-H1 in cells. In that experiment, contractile response to nocodazole-induced microtubule disassembly was abolished (Chang et al., 2008). In the same study, GEF-H1-depleted cells showed impaired RhoA activation and subsequent phosphorylation of myosin. The authors thus proved that GEF-H1 is the key mediator between microtubule disassembly and contractile force generation (Chang et al., 2008).

Local microtubule acetylation may modulate GEF-H1 release, affecting synaptic actin reorganization. This interplay between mechanical cues and microtubule properties regulates GEF-H1 activity spatially and temporally (Seetharaman et al., 2022). As shown recently, manipulating this axis enhances T cell movement in complex 3D environments (Tabdanov et al., 2021; Zhao et al., 2021).
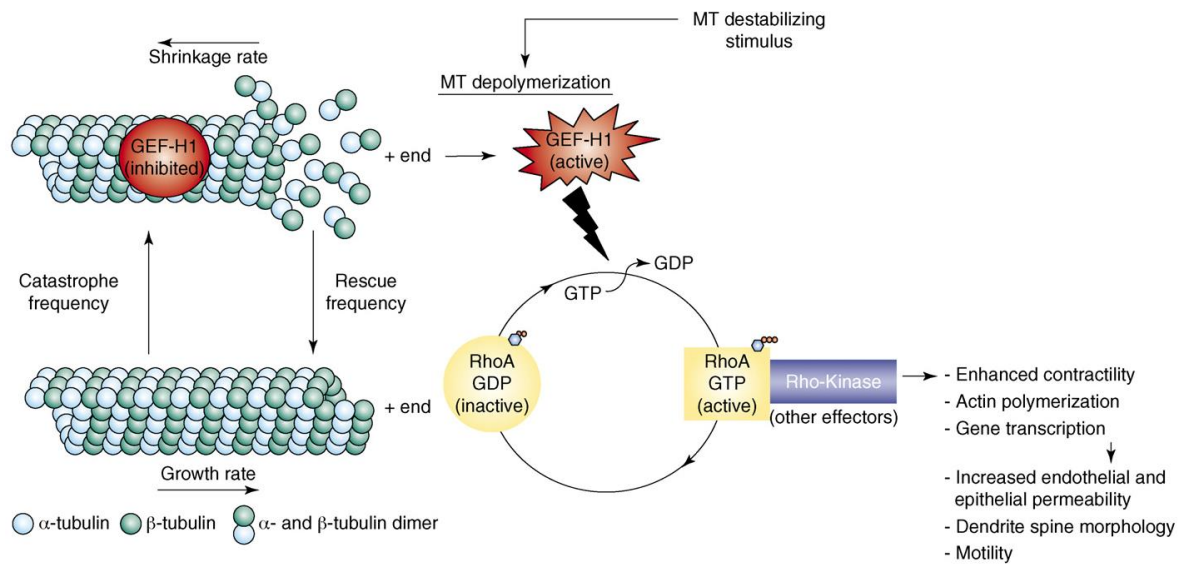
Figure 5. Microtubule-depolymerization dependent mechanism of GEF-H1 activation. GEF-H1 activation after MT depolymerization induces actin polymerization, contractility, and motility. This figure was taken from (Birkenfeld et al., 2008)

- Targeting microtubules: impact on immune cells migration

As the microtubule cytoskeleton is crucial for various cellular functions, it has been a target for cytotoxic agents used in cancer treatment (Steinmetz & Prota, 2018). Microtubules are cytoskeletal filaments, consisting of α-tubulin and β-tubulin heterodimers. Their hollow, cylindrical structure provides mechanical rigidity, enabling the formation of large intracellular assemblies. The capacity of microtubules to alternate between growing and shrinking, constantly and naturally, makes them be considered highly dynamic cellular structures (Janke & Magiera, 2020). Microtubule-targeting agents are pharmacological compounds that specifically interfere with the dynamics and structure of MTs. These agents can either stabilize or destabilize MTs, disrupting critical cellular processes such as mitosis/meiosis, intracellular molecular transport, and cell shape maintenance and coordination. Nowadays, the use of complex structural biology tools has made it possible to identify and characterize six binding sites for specific ligands, on tubulin. Two of those described sites are targeted by MSA; four sites are targeted by MDA. Notably, most MT binding sites are located on β-tubulin, possibly due to its role in the GTP hydrolysis cycle essential for MT dynamics. Surprisingly, no ligands targeting the nucleotide site on β-tubulin have been identified yet, which could directly disrupt MT dynamics (Steinmetz & Prota, 2018). Exploring additional binding sites, particularly on α-tubulin, presents intriguing possibilities for future research.

Despite promising success, the therapeutic utility of many MDA is impeded by issues such as toxicity and resistance, prompting active exploration of novel compounds. Tubulin-binding agents like taxol and vincristine are vital in treating metastatic cancer, but their complex structures pose synthesis-related challenges. Similar limitations are faced with Tubulysins, a group of anticancer drugs that are very potent but only available in limited amounts (Braig et al., 2014). Pretubulysin (PT), a simpler precursor of tubulysin, shows potent anti-cancer effects comparable to tubulysin (Eirich et al., 2012; Herrmann et al., 2012). It inhibits cell proliferation, induces cell death, and exhibits *in vivo* efficacy in various cancer models. Its synthesis is feasible, making it a promising candidate for further development as an anticancer agent. PT inhibits cancer cells growth and acts similarly to tubulysin, suggesting its potential as an antimitotic agent for the treatment of tumors (Kubisch et al., 2014).

In summary, although microtubule-depolymerization agents have received considerable attention as cytotoxic drugs, there is a noticeable lack of research exploring their impact on T cells, with most studies concentrating on cancer cells rather than immune cells. Given the above reviewed findings demonstrating the potential to enhance cytotoxic T lymphocytes functions through microtubule targeting and the availability of PT as a potent microtubule-destabilizing agent with the advantage of chemical synthesis, our study aims to fill this void by examining the effects of PT on activated human CD8^{+} T cells. This research endeavor holds promise for the development of more effective therapeutic strategies.

The significant findings of this thesis are included in the following original manuscript in preparation:

Montalvo G., Shaebani R., Nandakumar S., Cowley N., Zhao R., Hawkins R., Lauterbach M. A., Aradilla L., Qu B. and Lautenschläger F *Targeting the microtubules to improve the searching efficiency of T cells.* Manuscript in preparation for PNAS.

My contributions to the manuscript are:

Designed and performed experiments, prepared figures and wrote the manuscript.

The experiments and analysis I performed are as follows:

- CTLs preparation and cell culture: 80 %
- Microfabrication of 1D channels: 100%
- 1D migration experiment: 100%
- Preparation of Collagen Matrix: 100%
- 3D killing experiment and analysis: 80 %
- 3D infiltration experiment and analysis: 100%
- Real-time deformability cytometry (RT-DC): 100%
- Immunostaining: 100%
- Quantification of fluorescence intensity: 100%

All the authors have declared with their signature their agreement with this contribution description.

2. Materials and Methods

2.1. Materials and methods for Results 1)

Copied from the original manuscript in preparation:

Montalvo G., Shaebani R., Nandakumar S., Cowley N., Zhao R., Hawkins R., Lauterbach M. A., Aradilla L., Qu B. and Lautenschläger F *Targeting the microtubules to improve the searching efficiency of T cells.* Manuscript in preparation for PNAS.

Antibodies and Reagents. The following antibodies were used: α-Tubulin (Invitrogen REF 32- 2500), pMyosin light chain (Cell Signaling REF: 08/2019), Alexa Fluor 647 conjugated goat antirabbit (Invitrogen A21244), and Alexa 488 conjugated donkey anti mouse (Invitrogen A21202). The following reagents were used: Phalloidin-iFluor 594 (abcam REF: 176757) Hoechst 33342 (ThermoFisher Scientific), Fluoromount-G with DAPI (Invitrogen REF00-4959-52), Carboxyfluorescein succinimidyl ester (CFSE), FibriCol® type I collagen Solution (Bovine, Advanced Biomatrix), cell-Tak (Corning), poly-dimethylsiloxane (PDMS) (RTV-615; Momentive Performance Materials), (PEG-PLL) (Susos, Dübendorf, Switzerland). The following drugs were used: Pretubulysin (synthesized as described in (20), Nocodazole (Sigma-Aldrich). The compounds were dissolved in DMSO at 10 mM and stored at −20°C. For experiments, the compounds were diluted to 10 μM or 1 μM in cell culture medium.

CTLs preparation and cell culture. Human peripheral blood mononuclear cells (PBMCs) of healthy donors were isolated from the Leukocyte Reduction System Chamber using a gradient centrifugation (450g, 30min) with Lymphocyte Separation Medium 1077 (PromoCell). Remaining red blood cells were removed by the lysis buffer (155 mM NH4Cl, 10 mM KHCO3, 0.1 mM EDTA, pH=7.3). For migration and killing experiments, PBMCs were stimulated with Streptococcal Enterotoxin A (SEA) at 0.5 μg/ml for 30 minutes and then diluted 50X in AIMV medium (ThermoFisher Scientific) containing 10% FCS and Interleukin-2 (50 U/ml). After 5 days in culture, CTLs were isolated using Human CD8$^+$ T Cell Isolation Kit (Miltenyi Biotec). All CD8$^+$ T cells were cultured in AIMV medium (ThermoFisher Scientific) containing 10% FCS and recombinant human Interleukin-2 (ThermoFisher Scientific). NALM-6 pCasper cells were generated by Knörck et al. (41) and were cultured in RPMI-1640 (ThermoFisher Scientific) containing 10% FCS and 1% Penicillin-Streptomycin in the presence of puromycin (0.2 μg/ml).

CTLs treatment with drugs. Cells were treated with Pretubulysin at 1 μM or 10, with Nocodazole at 1 μM or 10 μM or with DMSO at 0.1 % for 30 minutes prior the experiments. For 1D migration experiments, cells were loaded in medium with the corresponding drug. For 3D migration, infiltration, and killing experiments, cells were washed after drug treatment, before being placed on top of collagen layer. For immunofluorescence microscopy, cells were fixed immediately after drug treatment (30 minutes). For RTDC experiment, treated cells were resuspended in cell carrier buffer with drugs at the corresponding concentration.

Microfabrication of 1D channels. Using nanoscribe-generated stamps, microchannels were fabricated by pouring polydimethylsiloxane (PDMS) precursor mixture (Sylgard 184, base: curing agent = 10 : 1) and curing at 70°C for 2 h. Then, circular-shaped reservoirs (2mm) were drilled, and shape was adjusted using a razor blade. After the PDMS chips were brough into the correct size, they were cleaned by sonication for 30 sec in 70 % of

ethanol. Chips were dried afterwards with air and activated for 30 sec at 300 mTorr by plasma treatment (air or oxygen). The binding was enhanced afterwards by placing the chips for 1 hr in the oven at 65 °C. For coating the microchannels, right before adding the coating solution (0.5 mg/mL PLL-PEG), chips were activated by air plasma at 300 mTorr for 1 min and after 30 min of incubation with the coating solution, chambers were washed with PBS.

1D migration experiment. The chambers prepared with PLL-PEG-coated channels were equilibrated for 1 h at 37°C with cell culture medium either with Pretubulysin 1 μM or 10 μM, Nocodazole 1 μM or 10 μM, or DMSO 0.1%, before loading the cells. Cells were stained with Hoechst 33342 (200 ng/ml) for 30 minutes at 37°C and 5% CO_2. Treated CTLs were loaded in the chambers in 10 μl at 20 Mio cells/ml and the chip was covered with medium. We used a life cell epi-fluorescence microscope (Nikon) with a 10X objective lens (Plan-Neofluor, NA = 0.5) with temperature and CO_2 control (Live Cell Instrument, Korea). Cells migrated spontaneously for 15 hours and images were acquired every 3 minutes.

1D migration tracking and analysis. Custom-written routines in Matlab (Mathworks, Natick, USA) were used for tracking analysis. First, images were rotated (bilinear interpolation) so that the channels are perfectly horizontal in the movies. To obtain a flatfield for correction of inhomogeneous background over the field of view (FOV), a large (30x30 pixels) median filter was applied to each fluorescence image. This removes all cells, leaving a flatfield, which was subsequently subtracted from each frame. Positions of microfluidic channels were automatically identified. Positions of the microfluidic channels were identified as follows: First a maximum intensity projection over time was calculated, then all pixels were summed horizontally, leading to a peak for each channel that contained at least once a fluorescent cell. These peaks were detected with MATLAB's findpeaks command]. Nonchannel regions were replaced by the average intensity of the image. The resulting images were smoothed with a Gaussian filter of 5 pixels full width at half maximum. Cells were identified as local intensity maxima (Matlabs command imregionalmax) exceeding a threshold in the resulting images. Cells were subsequently tracked (i.e. re-identified in consecutive frames) by minimizing the squared distance between all particles in consecutive frames as described in (42). Each microfluidic channel was treated separately during tracking. Cell speeds were calculated as displacement between frames divided by the time interval between frames.

Preparation of Collagen Matrix. As described in (14) bovine collagen type I stock solution was neutralized (pH 7.0-7.4) with 0.1 N NaOH and PBS 10X on ice. PBS was used to further dilute the collagen solution to the final experimental concentrations and distributed in the 96-well plates maintaining cool conditions. The collagen solution was finally incubated for 1 hour at 37°C with 5% CO2 for fibrillation.

3D killing experiment. For killing assays, NALM-6-pCaspe (NALM-6 cells expressing the apoptosis reporter pCasper-pMax) were used as target cells. NALM-6-pCasper were treated with staphylococcal enterotoxin A (0.1 μg/ml) for 40 min at 37°C with 5% CO_2, then resuspended in chilled collagen solution. Afterwards, we transferred them in 96-well plates, and centrifuged them at 4°C (200 g, 7.5 min) to sediment them on the bottom of the well. Afterwards, the mix target cells collagen (50 μL/well) was solidified in the incubator for 1 hr at 37°C with 5% CO_2 for collagen fibrillation. Afterwards, we added the CTLs on top of the solid collagen matrix in medium without drug or DMSO. Images were taken by

ImageXpress (Molecular Devices) with Spectra X LED illumination (Lumencor) every 20 min for 36 hours. Culture conditions were maintained at 37°C with 5% CO2.

3D infiltration experiment. CTLs were stained with CFSE (5 μM in PBS + 4.5% FCS) at room temperature and protected from light for 15 min, washed once with PBS, then resuspended in culture medium AIMV +10% FCS, and kept at 37°C with 5% CO_2 for recovery during 1 hr. Then, CTLs were treated with Pretubulysin 1 μM or 10 μM, Nocodazole 1 μM or 10 μM or DMSO and loaded on top of solidified collagen matrix. Images were taken by ImageXpress (Molecular Devices) with Spectra X LED illumination (Lumencor) every 20 min for 24 hours. Culture conditions were maintained at 37°C with 5% CO2.

Immunostaining. CTLs were immobilized on coverslips using the Cell-Tak adhesive (Corning) following the manufacturer instructions. Next, cells were added to the cell-Tak treated coverslip, immediately after Pretubulysin or DMSO treatment and incubated for 2 minutes. cell-Tak treated coverslip were carefully washed with PBS. Right after, pre-warmed paraformaldehyde (PFA, 4%) was added and incubated for 10 minutes at room temperature. Next, coverslips with immobilized cells were carefully washed twice with PBS, permeabilized with Triton -100 (0.05%) for 10 minutes and blocked with 2% BSA in PBS for 1 hour. Staining with the indicated antibody or Phalloidin was performed in PBS+BSA 2% for time and dilution indicated in the antibodies and reagents section. DAPI was added to the slides for nuclei staining and coverslips were placed on mounting slides for imaging. Fixed/stained cells were imaged using the 63x immersion oil objective (Zeiss, PlanApochromat 63x/1.40 oil DIC M27) of a Zeiss LSM 900 confocal microscope with the Axiocam 705 Mono camera (Zeiss).

Real-time deformability cytometry (RT-DC). CTLs were treated with Pretubulysin or DMSO for 30 minutes, pelleted by centrifugation and resuspended in 100 μl of Cell Carrier B solution (phosphate-buffered saline + long-chain methylcellulose polymers of 0.6 % w/v) with Pretubulysin or DMSO. A 20 μm microfluidic PDMS chip was assembled on the stage of an inverted microscope (Zeiss). CTLs homogenously resuspended were loaded on the chip using a syringe pump. Using a CMOS camera, CTLs were live imaged while flowed through the channel were. At least 3000 events were acquired for each condition (Pretubulysin or DMSO treated) and experiment, flowrate (0.04 to 0.12 μls-1) was used, according to the range suggested by the manufacturer for the channel size and carrier buffer. The stiffness of the cells was analyzed using ShapeOut (Zell Mechanik, Dresden). We used linear mixed models provided by the manufacturer to calculate statistical significances.

Quantification of fluorescence intensity. Microscope data was analyzed using ImageJ/Fiji. For protein intensity quantification, Sum Intensity projections were generated for each cell and background was subtracted. Based on actin staining, the cell border was established. Considering the nuclei, two compartments were analyzed (at the back and at the front of the nuclei). The mean intensity fluorescence in the region (for F-actin and for pMyosin) and the area were automatically obtained with the software, the total F-actin and total pMyosin were calculated by multiplying MFI*Area.

***In vitro* reconstitution assays.** <u>Tubulin purification and labeling:</u> We purified tubulin from fresh bovine brains. For this, we used three cycles of assembly and disassembly, leveraging the temperature sensitivity of microtubules to separate tubulin from other proteins. The cycles were carried out in Brinkley Buffer 80 (BRB80 buffer; 80mM PIPES, pH 6.8, 1mM EGTA, 1mM MgCl2 and 1mM GTP). We then labeled the tubulin with biotin or fluorescent

markers with ATTO488 (ATTO-TEC, AD488) and ATTO565 (ATTO-TEC, AD565) dyes as described in (43). Preparation of Silane-PEG -Biotin passivated cover glasses: Cover glasses were cleaned using subsequent washes with acetone, 96% ethanol, Hellmanex III solution (2% in water, Hellmanex) followed by treatment using an UV cleaner before incubation in a 9:1 or 7:3 mix of tri-ethoxy-silane-PEG and tri-ethoxy-silane-PEG-biotin (30kDa, PSB-2014, Creative PEG works) as described in (43). Microfluidic Circuit Fabrication: We used PDMS (Sylgard 184, Dow Corning) to build the microfluidic devices by standard soft lithography. TFE Teflon tubing (Supelco, inner diameter: 0.8mm, outer diameter: 1.58mm, Merck) was inserted into the port serving as an outlet. Tubing with 0.03mm inner and 1.58mm outer diameter was used to connect the inlet with sample reservoir, via a manual shut-off valve to a pressure controlled microfluidic pump (LineUP Flow EZ 345 mbar, Fluigent). *In vitro* reconstitution experiments using microfluidics: For the *in vitro* assays, 10mM stock solutions of Pretubulysin and Nocodazole (dissolved in DMSO) were further diluted in 11 1xBRB80 buffer. The PDMS chip was placed on a passivated cover glass and fixed on to the microscope stage. The chip was first perfused with a solution of 1xBRB80. The surface was then perfused with 300μl of Neutravidin (50 μg μl−1 in BRB80; Pierce), followed by 300μl of PLL-g-PEG (PII 20K-G35-PEG2K, Jenkam Technology) at 0.1mg/ml in 10mM Na-HEPES buffer (pH =7.4) before another wash with 1xBRB80 to remove the excess, unbound compounds. ATTO-565 labeled Biotin microtubule seeds prepared according to (43) were flowed into the chamber. We then washed out the seeds which had not bound immediately using BRB80 supplemented with 1% BSA. The seeds were then elongated by addition of the elongation mix containing 10 μM of tubulin (20 % ATTO-488 labeled) in BRB80 supplemented with 1 mM GTP, an oxygen scavenger cocktail (20 mM dithiothreitol, 1.2 mg ml−1 glucose, 8 μg ml−1 catalase and 40 μg ml−1 glucose oxidase), 0.1% BSA and 0.025 % methyl cellulose (1500 cp, Sigma). After 10 mins of elongation, the elongation mix containing 10μM of tubulin (to prevent microtubule disassembly due to dilution) along with various concentrations of the drugs (Pretubulysin/Nocodazole) was perfused into the chamber. For control experiments, just the elongation mix containing 10 μM of tubulin with equivalent concentrations of DMSO was flushed in. Microtubules were imaged before, during and after addition of each drug. Imaging: Microtubules were visualized using a 63x oil immersion objective (Zeiss, Plan-Apochromat 63x/1.40 oil DIC M27) on a Zeiss LSM 900 confocal microscope with the Axiocam 705 Mono camera (Zeiss). Experiments were carried out at 37° C using a stage controller (Insert-P, PeCon). Time-lapse recording (with a frame interval of 0.99s) was performed using the line scan mode in the Zen blue software (version 3.2, Zeiss). We used the subtract background and smooth functions of ImageJ (version 1.53t) to increase the signal/noise ratio in our videos. From our videos, we generated the kymographs for each time-lapse sequences using the built-in reslice function in ImageJ and the depolymerization velocity was estimated using a customized ImageJ macro. Microtubule mass before and after drug addition was calculated by measuring the total length of microtubules in a single field of view over a period of 8 mins.

Persistent random search simulations. In our Monte Carlo simulations, we chose a 3D box of lateral sizes L×L and height h to simulate our discrete time random walk processes. We used default values L = 5.6 mm and h = 1.5 mm, unless mentioned otherwise. The simulation box, shown in Figure 2A, was laterally confined with reflecting boundaries. In the vertical direction, the system was confined between an upper entry plate and an

absorbing boundary at the bottom to mimic the experimental conditions. Starting from a random position on the top surface with a random incident angle towards the bulk, each random walker continued the motion until hitting and eliminating one of the targets located on the bottom plate. The area of each target was 200 μm^2 and a total number of 25000 targets were distributed randomly on the bottom plate. Each target was eliminated upon first contact with a searcher. The killing kinetics was monitored in a target zone of area 0.7 mm^2 at the center of the bottom plate; see Figure 2A. The time step of the simulations was chosen to be $\Delta t = 30$ s. The random walkers performed a persistent random walk with the given mean speed and persistence. At each step of the simulation, the directional change θ of the walker with respect to the previous direction of motion was obtained from $\theta = \arccos(p)$ (44,45). An azimuthal angle perpendicular to the direction of motion was also chosen randomly from the range $[0, 2\pi]$. Next, the position was updated according to an instantaneous speed randomly extracted from an exponential distribution with the given mean value. The extension of this algorithm to multistate processes (46,47) was employed in (23) to distinguish between different categories of CTLs speeds in collagen matrices at relatively short time scales. However, the single-state persistent random walk mode has been employed for the present study since the time scales are beyond the transient dynamic's regime.

Active droplet simulations. The active droplet is modelled as a viscous fluid with an active boundary, implemented using the immersed boundary method. Full details of the numerical implementation of the hydrodynamics and immersed boundary can be found in (48). The active boundary of the droplet has an associated concentration representing active particles which spontaneously polarizes, leading to gradients in boundary tension driving droplet motion. To set the concentration profile to values similar to those seen in experiment we set a concentration maximum by introducing a tangential forcing term on the boundary above a threshold 12 concentration. We set the concentration threshold to $[1.5c_0, 2.5c_0]$ for the low and high case respectively, where c_0 is the average concentration, corresponding to the initial uniform concentration on the boundary.

Statistical Analysis. For RT-DC, linear mixed model included in the ShapeOut software. GraphPad Prism 9.5.1 Software (GraphPad) was used for statistical analysis of the rest of experiments. In Graph Pad, first normality is tested (D'Agostino and Pearson). We then followed the test chosen by Graph Pad (if 2 groups which are normal distributed: paired t-test. If there is no normal distribution, then Mann–Whitney–U-test is used. If more than 2 groups are compared, we used a one-way ANOVA test for statistical significance and Dunn's test to compare each group with each other.

Ethical Considerations. Our work for this study with healthy donor material (leukocyte reduction system chambers from human blood donors) was authorized by the local ethic committee [declaration from 16.4.2015 (Ha 84/15; Prof. Dr. Rettig-Stürmer) and amendment from 23.03.2021 (Ha 84/15; Prof. Dr. Markus Hoth)].

2.2. Materials and Methods for Results 2)

Microtubule staining *in vivo:* To label the microtubule network in live CTLs we used SiR-tubulin Kit (SpiroChrome002) and followed the fabricator instructions: Sir-tubulin was diluted in the culture medium at 1 μM and incubated for 1h before imaging.

Microfabrication of 1D channels. Using nanoscribe-generated stamps, microchannels were fabricated by pouring polydimethylsiloxane (PDMS) precursor mixture (Sylgard 184, base: curing agent = 10 : 1) and curing at 70°C for 2 h. Then, circular-shaped reservoirs (2mm) were drilled, and shape was adjusted using a razor blade. After the PDMS chips were brough into the correct size, they were cleaned by sonification for 30 sec in 70 % of ethanol. Chips were dried afterwards with air and activated for 30 sec at 300 mTorr by plasma treatment (air or oxygen). The binding was enhanced afterwards by placing the chips for 1 hr in the oven at 65 °C. For coating the microchannels, right before adding the coating solution (0.5 mg/mL PLL-PEG), chips were activated by air plasma at 300 mTorr for 1 min and after 30 minutes of incubation with the coating solution, chambers were washed with PBS.

1D migration experiment. The chambers prepared with PLL-PEG-coated channels were equilibrated for 1 h at 37°C with cell culture medium before loading the cells. Cells were stained with Hoechst 33342 (200 ng/ml) for 30 minutes at 37°C and 5% CO_2 and/or with Sir-tubulin (SpiroChrome). Treated CTLs were loaded in the chambers in 10 µl at 20 Mio cells/ml and the chip was covered with medium. A fluorescence microscope (Nikon) with Andor camera was used for imaging. For live cell imaging, the chamber was mounted on the microscope stage maintaining 37°C and 5% CO_2 with an incubator system (Live Cell Instrument, Korea). Cells migrated spontaneously for 15 hours and images were acquired every 3 minutes for migration experiment and every 30 seconds for MTOC imaging. .

Migration tracking and image analysis: The plug in TrackMate from ImageJ was used to track the cells migrating in 1D, the speed and persistence are automatically calculated after tracking. The cell size, MTOC-Nuclei distance and MTOC-Nuclei angle were manually determined using ImageJ software.

3. Results

3.1. Results 1)

Targeting microtubules to improve the searching efficiency of T cells

The significant findings of this thesis are included in the following original manuscript in preparation:

<u>Montalvo G.</u>, Shaebani R., Nandakumar S., Cowley N., Zhao R., Hawkins R., Lauterbach M. A., Aradilla L., Qu B. and Lautenschläger F *Targeting the microtubules to improve the searching efficiency of T cells.* Manuscript in preparation for PNAS.

My contributions to the manuscript are:

Designed and performed experiments, prepared figures and wrote the manuscript.

The experiments and analysis I performed are as follows:

- CTLs preparation and cell culture: 80 %
- Microfabrication of 1D channels: 100%
- 1D migration experiment: 100%
- Preparation of Collagen Matrix: 100%
- 3D killing experiment and analysis: 80 %
- 3D infiltration experiment and analysis: 100%
- Real-time deformability cytometry (RT-DC): 100%
- Immunostaining: 100%
- Quantification of fluorescence intensity: 100%

All the authors have declared with their signature their agreement with this contribution description.

Targeting microtubules to improve the searching efficiency of T cells

Abstract

Cell migration is a crucial process for cytotoxic T lymphocytes (CTLs), that allows effective navigation through three-dimensional (3D) environments to locate target cells and execute cytotoxic functions. Impaired CTLs infiltration into solid tumors remains a significant challenge, often limiting the efficacy of immunotherapies. To address this challenge, recent evidence suggests microtubules (MT) as a promising target, since perturbing MT stability improves T-cell migration and killing efficiency in dense matrices, but the underlying mechanisms remain poorly understood. Here we use Pretubulysin, a known MT depolymerizer to unmask mechanism how MT stability influences T-cell migration. We found that complete disassembly of the microtubule network significantly increased CTLs infiltration and migration in a 3D environment. Asking how migration actually improves killing efficiency, we focused on the cell search efficiency, since finding a target is a crucial prerequisite to kill it. Using a persistent random walk model, we prove the ability of Pretubulysin to enhance T-cell search efficiency. We are proposing an underlying mechanism explaining this enhanced searching efficiency of T cells after Pretubulysin treatment: Depolymerizing microtubules in activated T cells leads to localized actomyosin accumulation at the uropod, altering cell mechanics and favoring stronger contraction forces at the rear of the cell. This results in faster and more persistent migration. Overall, our findings shed light on the role of MTs in search mechanisms of immune cells, regulating CTLs migration in 3D environments. We highlight the potential of MT-disassembling agents like Pretubulysin to optimize immune therapies against solid tumors.

Significance Statement: We show how microtubule (MT) disruption with Pretubulysin can be used to enhance cell search behavior and therewith the function of CTLs. By inducing rapid and potent depolymerization of MTs, Pretubulysin treatment induces profound changes in CTLs behavior and mechanics. Pretubulysin treated CTLs exhibit increased migration speed and persistence, leading to improved infiltration, 2 search and therefore killing in complex 3D. These enhancements are explained by alterations in cell stiffness, morphology, and relocalization of cytoskeletal elements, including enrichment of actomyosin activity at the uropod. We provide necessary insights into the intricate interplay between cytoskeletal dynamics and CTLs function. This knowledge will inform the development of novel immunotherapeutic strategies targeting the cytoskeleton to boost T cell-mediated cytotoxicity in the treatment of various diseases.

Introduction

Cell migration is a key feature of immune function, and immune cells are particularly specialized to migrate in nearly all tissues within the human body (1). This motility and the capability to infiltrate into tissues is especially essential for cytotoxic CD8+ T cells, also known as cytotoxic T lymphocytes (CTLs) to efficiently locate tumorigenic or pathogen-infected cells for their efficient removal (2). This remarkable capacity is the result of migration patterns and related searching strategies optimized for finding cognate target cells. Cells can control their searching efficiency by tuning migratory proprieties such as speed and persistence (3–6). We described previously a universal coupling between speed and persistence in which faster cells move more persistently (7) which in turns optimizes

the time cells need to find an object (4,5). The coupling between speed and persistence depends on both actin polymerization and cell polarization that inherently coexist in actomyosin driven motion (7). T cells use amoeboid locomotion, in which cell shape changes dynamically. Cellular polarization with rapid generation of protrusions at the leading edge and a uropod at the posterior region, together with high actomyosin contractility, serves as major force generator machinery (8). Two major components of the cellular cytoskeleton, actin and microtubules (MT) are dynamically coupled and regulated to coordinate migration (9). During T cell migration, the formation of protrusions at the leading edge is driven by polymerization of branched F-actin, which pushes the plasma membrane providing the primary driving force for forward movement. Meanwhile, the microtubule-organizing center (MTOC) is located at the uropod, behind the nucleus (10). In contrast, for mesenchymal motility the MTOC is positioned between the nucleus and the leading edge (11). MTOC positioning plays a decisive role in defining T cell polarity to govern migration direction (10). For migrating T cells, actomyosin contractions at the uropod allow detachment from the substrate for further migration and provide rearward squeezing forces to facilitate movement of the nucleus through confined spaces (8). The seemingly distinctively located networks, actin and MT, can interact and influence each other's dynamics, including at the interface between T cells and target cells where actomyosin dynamics influence microtubule disassembly (12). In vivo, CTLs must navigate through complex 3D environments to locate target cells. The extracellular matrix (ECM), composed of fibrous proteins such as collagen, plays a crucial role in maintaining tissue architecture. However, in the context of solid tumors, the ECM often becomes condensed, creating a physical barrier that hinders CTLs infiltration resulting in evasion of immune surveillance (13). This limitation contributes significantly to the low efficacy of adoptive immunotherapy against solid tumors, as confined spaces within the dense ECM impair CTLs migration and reduce killing efficiency (14). Recent research has highlighted the potential of targeting MTs to enhance CTLs function, particularly in condensed 3D matrices. Disrupting the MT network using agents like Nocodazole, or the chemotherapeutic drug Vinblastine significantly improves CTLs migration and killing efficiency in 3D environments, especially within dense collagen matrices (14,15). In T cells, MT network disruption enhances surface tension (15) and activates 3 Rho A (16), a key regulator of cell contractility. Additionally, at the interface between T cells and target cells, MT dynamics play an essential role in regulating cell contractility (17). Similarly, in migrating dendritic cells, MT dynamics influence the protrusion retraction and overall migration, which also involves Rho A (18) Despite these insights, the precise mechanisms by which MT disruption improves T cell motility in 3D environments is not yet fully understood. In this work, we used Pretubulysin, a MT destabilizer, to inhibit MT polymerization, and found that complete MT disassembly substantially boosts CTLs infiltration into 3D collagen. Further, this treatment also enables CTLs to navigate through narrow channels rapidly and persistently. Simulations using persistent random search models revealed that CTLs with disrupted MTs can penetrate deeper into tissues and exhibit a higher killing efficiency, a performance unattainable by control CTLs, even when applied in greater numbers. Furthermore, we observed that a repositioning of the actomyosin network towards the uropod contributes to enhanced migration speed as confirmed by

viscous droplet simulation. In conclusion, our findings demonstrate that MT disassembly induces a reorientation of the actomyosin network from the leading edge to the uropod. This reorientation is crucial for accelerating T cell movement and improving their killing efficiency in 3D environments.

Results

Pretubulysin treatment increases search and cytotoxic efficiency of CTLs in 3D environments. To manipulate MT dynamics, we used Pretubulysin, an innovative drug with potent microtubule depolymerization capacity that is used to treat cancer cells (19–22). To examine infiltration, CTLs were fluorescently labeled with CFSE and placed on top of a collagen matrix (Figure 1A).
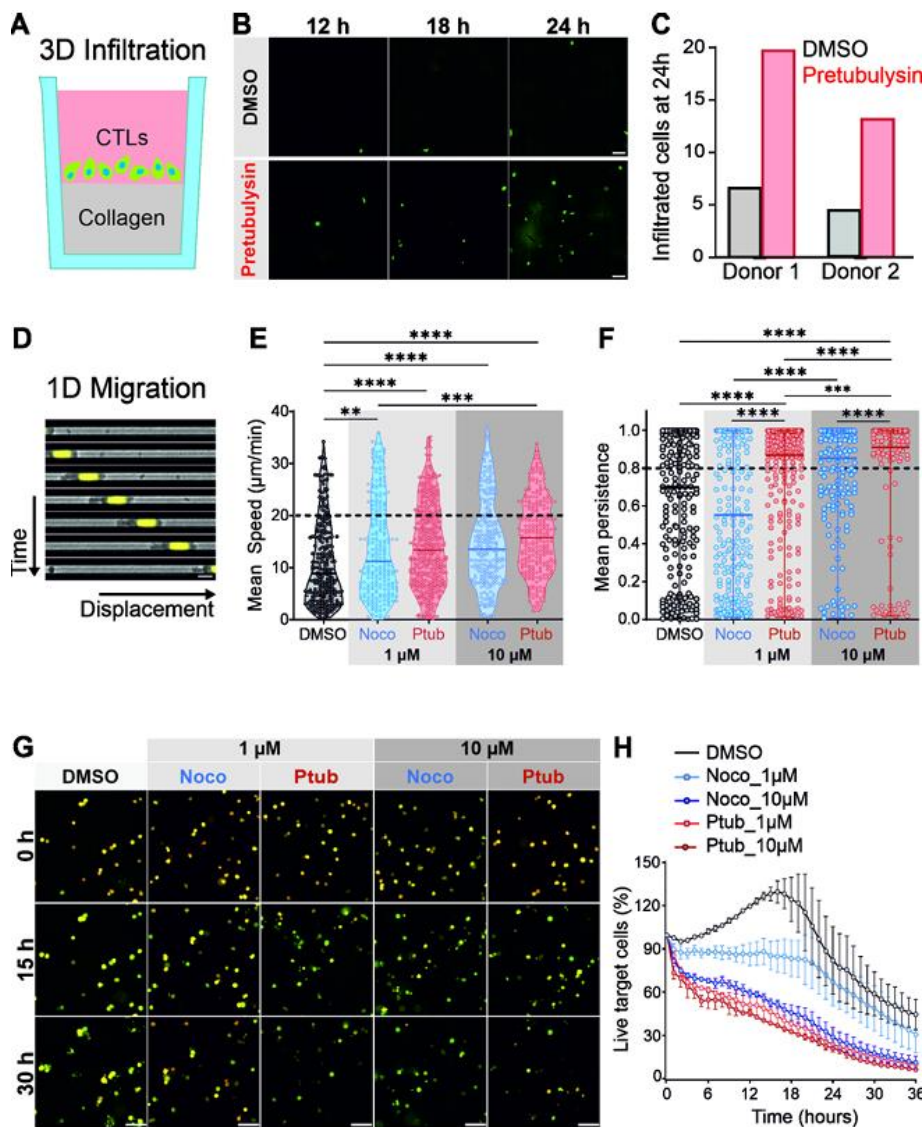

Figure 1. Pretubulysin enhances CTLs function in 3D by improving migration parameters.
(A) Scheme of CTLs infiltration into 3D collagen matrix. CTLs were stained with carboxyfluorescein succinimidyl ester (CFSE), treated with DMSO or Pretubulysin (10 μM) for 30 min and added on top of solidified collagen matrix (collagen represented in grey, CTLs culture medium without any drug is represented in pink). Cells were visualized as they reached the bottom of the well. (B) Images taken at different timepoints during the 3D infiltration assay from one representative donor treated with DMSO or Pretubulysin (10 μM). CFSE-CTLs were visualized at

the bottom of the plate (in green). Scale bar is 50 μm. (C) Quantification of particles after 24 hours. Data from donors (D1 and D2) treated with DMSO or Pretubulysin (10 μM). (D) Images taken at different timepoints during the 1D migration assay from one representative donor. Hoechst-stained CTLs (yellow nuclei) were treated with DMSO or drugs and loaded on PEG-coated channels (length: 400 μm; width: 5 μm; height: 5 μm). Cells migrated spontaneously for 15 hours and images were acquired every 2 minutes. Scale bar is 10 μm. (E-F) Time lapse videos were analyzed for automatic tracking of CTLs from 2 different donors treated with DMSO, Nocodazole at 1 μM or 10 μM, or Pretubulysin at 1 μM or 10 μM. In the graphs, one dot represents the mean speed (E) or mean persistence (F) of the track. For statistical analysis, one-way ANOVA and the Kruskal-Walli test for multiple comparisons were used. (H) Images taken at different timepoints during the 3D killing assay of cells from one representative donor treated with DMSO, Nocodazole at 1 μM or 10 μM, or Pretubulysin at 1 μM or 10 μM. Live target cells are orange–yellow, apoptotic target cells are green, and dead cells lose fluorescence. Scale bar is 50 μm. (I) Quantification of target cell death during the 3D killing assay. Dots represent the mean value of two donors, error bars represents the standard deviation (SD).

The focal plane was at the bottom of the matrix, allowing visualization of infiltrated cells. We observed that Pretubulysin-treated CTLs appeared at the focal plane at much earlier time points (Figure 1B) and with greater numbers compared to controls (Figure 1C). This result indicates that the MT network plays a pivotal role in governing CTLs infiltration into 3D matrices. Previously we reported that during CTLs migration in a 3D context, CTLs preferably enter preexisting confined tunnels in collagen matrices (23). To gain further insight into this aspect and with full control over parameters, we used microfabricated channels to mimic the tunnels found in collagen and tracked Hoechst-labeled T cells (Figure 1D). Pretubulysin-treated CTLs were substantially faster (Figure 1E) and more persistent (Figure 1F) compared to the DMSO-treated control groups, suggesting that MT disassembly promotes CTLs motility under confinement in a 3D environment. Notably, the effect of Pretubulysin on enhancing CTLs migration was more potent than Nocodazole, a well-known and widely used microtubule-disrupting drug (14,15), at both the low (1 μM) and high (10 μM) concentrations (Figure1E-F). Concerning the fraction of highly persistent CTLs (persistence > 0.8), at the low concentration this fraction was doubled for the Pretubulysin-treated group (81%) relative to the Nocodazole-treated counterparts (39%). At the high concentration, the difference between Pretubulysin- and Nocodazole-treated CTLs was reduced, but still present (91% vs 73%). To examine the impact of Pretubulysin on CTLs killing function, we applied a 3D killing assay in which tumor cells stably expressing pCasper, an apoptosis reporter, were embedded in collagen matrices and after solidification CTLs were added from above (24). We compared Pretubulysin with Nocodazole- treated CTLs. Time lapse (Figure 1H) and quantification results of the 3D killing assay (Figure 1I) show that both Pretubulysin and Nocodazole enhanced CTLs killing efficiency in 3D matrices compared to treatment with DMSO. Remarkably, at the low concentration Pretubulysin 4 much more potently enhanced CTL killing efficiency in the 3D matrix relative to Nocodazole (Figure 1H, I). Importantly, the effect of Pretubulysin at 1 μM is comparable to that of Nocodazole at 10 μM (Figure 1H, I). Furthermore, lytic granule release was not affected by complete MT disassembly induced by Pretubulysin or Nocodazole (Supplementary Figure 1). These findings demonstrate that disruption of the MT network promotes CTLs motility and persistence. Thus, this approach offers a reliable

and powerful way to enhance CTLs killing efficiency in a matrix. Furthermore, Pretubulysin was found to be about 10 times more potent than Nocodazole.

Increase in speed and persistence is responsible for enhanced migration and killing efficiency of CTLs, as we confirmed by random walk simulations in 3D. To obtain a detailed understanding of the influence of migration speed and persistence on the infiltration efficiency of CTLs, we performed persistent random search simulations in 3D, mimicking the experimental conditions. The CTLs were modeled as persistent random walkers which enter the 3D space from the top surface (Figure 2A, starting plane), migrate until they reach the target cells at the bottom plane (Figure 2A, Target area). Each CTLs/target contact was assumed to result in target destruction. In our previous experiments of CTLs migration in 3D collagen matrices (23) we analyzed mean CTLs migration speed and persistence at different collagen densities. Those experimental data were used as input for our simulations as the control group. The speed and persistence of Pretubulysin-treated CTLs in 3D collagen matrices were estimated based on fold change obtained from our microfluidic channel experiments (presented in Figure 1). For our experiments, we assumed that the migration through narrow paths created by CTLs in 3D collagen matrices is similar to the motion in our 1D microfluidic channels. This assumption was validated by the satisfactory match between the killing kinetics obtained from simulations and experiments (Supplementary Figure 2).

CTLs are responsible for killing targets in various regions of the body, requiring them to patrol environments of different sizes. In our experiments the thickness of the collagen matrix (i.e. the initial distance between the starting plane and target area) was approximately 1.5 mm. We next asked how the observed improvement of infiltration efficiency by Pretubulysin treatment depends on the choice of matrix thickness (height, h). Thus, thickness was varied in the simulations and the migration efficiency of control and Pretubulysin-treated CTLs compared. The number of migrating cells which reached the target area at the bottom plate decreased with increasing layer thickness, but with different rates for control and Pretubulysin-treated CTLs (Figure 2B). Moreover, as shown in the inset of Figure 2B, the difference between control and treated cells increases with h. Specifically, with a twofold increase in h (from 1.5 to 3.0 mm) the ratio of treated cells to control cells reaching the target area grew from approximately 6 to 108, indicating a nearly 17-fold increase. We further analyzed the relationship between CTLs killing efficiency and matrix thickness (h) by quantifying the killing halftime (t_{50}), which is the time required to eliminate 50% of targets. The difference in t_{50} between control and Pretubulysin-treated CTLs increases with h (Figure 2C). These results suggest that the advantage of Pretubulysin treatment becomes even more pronounced with increasing h, i.e. in larger environments.

Another key factor which can considerably influence the killing efficiency of CTLs is the ratio of CTLs to target cells. In our experiments, the ratio ($N_{CTLs}/N_{targets}$) was 5. To understand the impact of this ratio on CTLs killing efficiency, we varied the initial number of CTLs over a wide range in the simulations. Figure 2D shows an example of the numerical results for both control and Pretubulysin-treated cells at collagen matrix density 2 mg/ml. For both the control and Pretubulysin-treated groups, increasing the relative number of CTLs 5 decreased the t_{50}, thereby enhancing the killing efficiency. This improvement continued until the ratio of $N_{CTLs}/N_{targets}$ reached between 10 and 20 (Figure 2D). Notably,

with the same ratio of $N_{CTLs}/N_{targets}$, the killing efficiency of the Pretubulysin-treated group was higher compared to that of the control group (Figure 2D). These findings suggest that CTLs migration in 3D plays a critical role in regulating the killing efficiency of these cells.
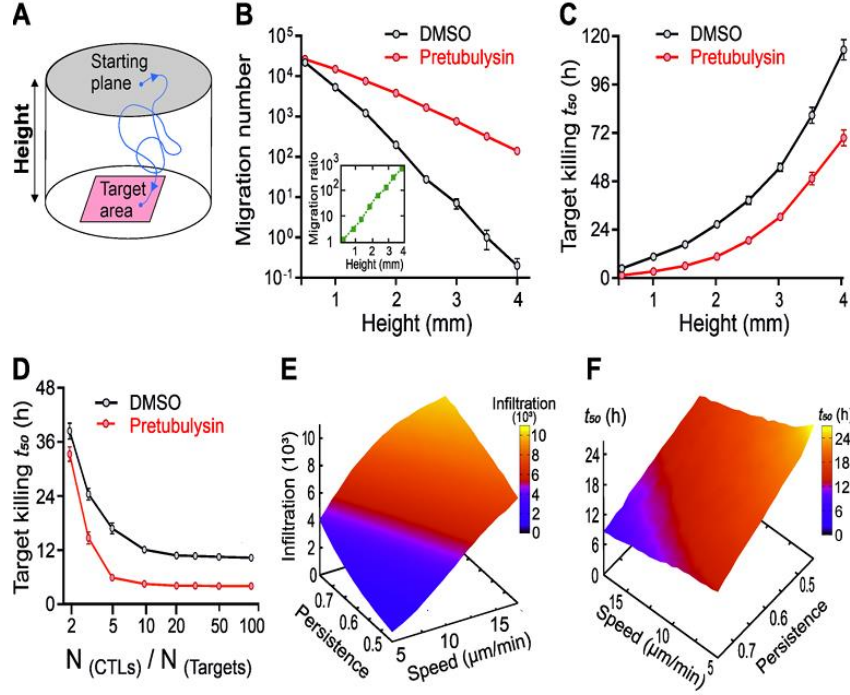

Figure 2. Quantification of migration and killing efficiency of control and Pretubulysin-treated CTLs in 3D obtained from persistent random search simulations. A) Schematic of the simulation. CTLs were modeled as persistent random walkers entering the medium from the top surface, indicated as "starting plane", and migrating until they reach the target cells at the bottom plate, indicated as "target area". (B) Improvement of migration efficiency by Pretubulysin treatment depending on the thickness of collagen matrix (height). During the simulations, the collagen thickness was varied, and the migration efficiency of control and Pretubulysin-treated CTLs was compared. The inset shows the ratio between the number of treated and control cells which reached the target area in terms of height: the higher the distance, the higher the difference between control and treated cells. (C) Relative killing capacity of treated and control CTLs depending on the thickness of collagen matrix (height, h). The graph represents the calculated killing halftime t_{50} (which is the time spent to eliminate 50% of the targets) versus the height. (D) Relative killing capacity depending on the ratio between the number of CTLs and target cells ($N_{CTLs}/N_{targets}$). To clarify how changing this ratio influences the killing efficiency, the initial number of CTLs was varied over a wide range in simulations, and the killing halftime (t_{50}) was calculated. (E) Number of migrating cells which reached the target area in terms of mean speed and persistence. (F) Killing halftime (t_{50}) versus mean speed and persistence.

We note that the lower bound on t_{50} (i.e. the saturation value) is imposed by the minimum travel time required for CTLs to cross the collagen layer and reach the target area with a given mean speed and persistence. We also examined the integrative impact of speed and persistence on CTLs migration and killing efficiency using persistent random search simulations. By varying the migration speed and persistence of the searchers, we measured the number of CTLs which reached the target area and t_{50} with parameters used in experiments (h = 1.5 mm and $N_{CTLs}/N_{targets}$ = 5). The surface plots show that the number of

cells which arrive at the target area drastically decreases (Figure 2E) while t_{50} increases (Figure 2F) with decreasing migration speed and/or persistence.

Pretubulysin induces instantaneous MT depolymerization *in vitro* and increases cell stiffness on CTLs. We performed microfluidics-based in vitro reconstitution assays using purified tubulin to characterize the depolymerizing potential of Pretubulysin at the single, dynamic microtubule level in a controlled environment.
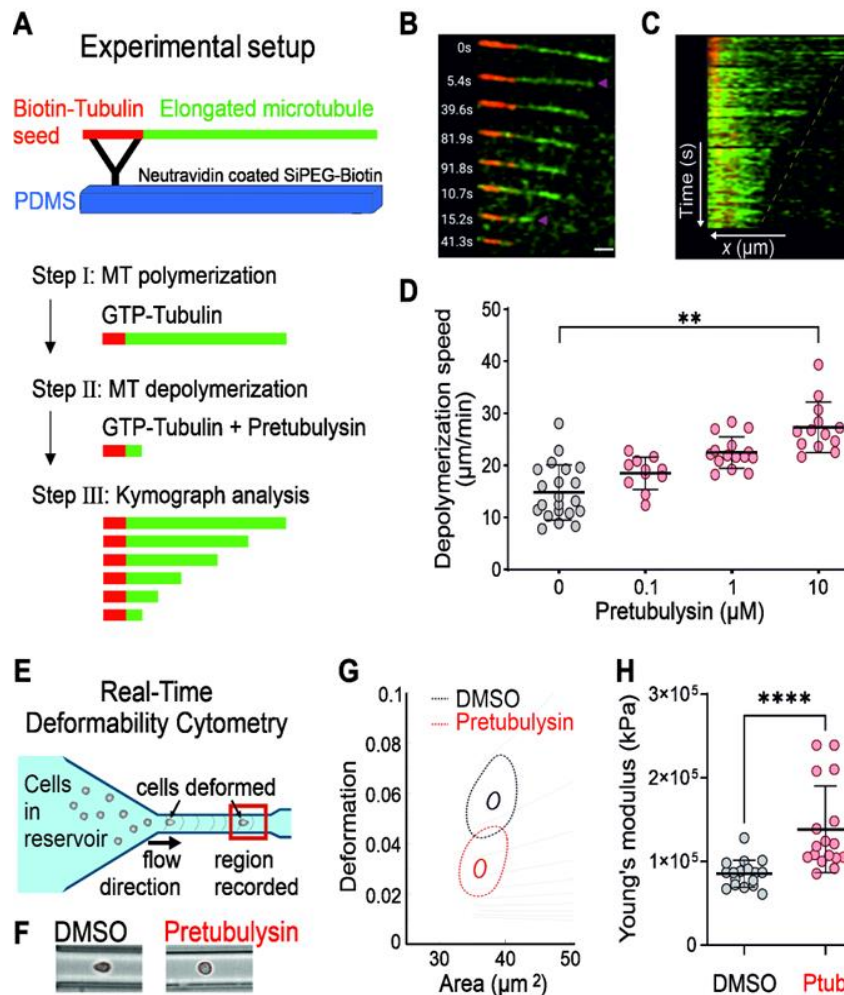

Figure 3. Pretubulysin is a potent microtubule depolymerization agent and stiffens CTLs. (A) Scheme of the microfluidics-based *in vitro* reconstitution assays using purified tubulin. Short biotin-containing microtubule fragments (red) were attached using neutravidin (yellow) onto a passivated surface and used as 'seeds' to induce MT growth. Microtubules (green) were elongated from these seeds by continuous flushing of labeled tubulin. In a second step, drug and labeled tubulin were flushed in. (B-C) Representative Kymographs depicting microtubule length distribution. (D) Quantification of Pretubulysin disassemble capacity on microtubules. Dots represent individual experiments. Results are presented as Mean ± SD. The Mann-Whitney test was used for statistical significance (*** $p<0,0001$, **$p<0,0017$). (E) Scheme of real-time deformability cytometer setup. A 20 µm microfluidic PDMS chip was assembled on the stage of an inverted microscope. The cell suspension was loaded on the reservoir and deformed by shear stresses and pressure gradient caused by the flow profile. (F) Representative images of cells during real-time deformability cytometry showing the typical bullet shape for control cells (DMSO) versus round shape observed for Pretubulysin-treated CTLs. (G) Representative kernel density estimate plot depicting cell area versus deformation showing Pretubulysin treatment makes CTLs less deformable than DMSO-

treated control cells. (H) Apparent Young´s modulus was calculated and analyzed using linear mixed models available with the ShapeOut2.0 software. The results obtained from three different donors are represented on the graph, where one dot represents one experiment and error bars represent standard deviation of the mean. At least 3,000 events were acquired for each condition in every experiment. For statistical analysis, one-way ANOVA and Kruskal-Walli test for multiple comparisons were used ($p < 0.0001$).

In this assay, short biotin-containing MT fragments (Figure 3A, in red), serving as 'seeds' to induce MT growth, were attached onto a passivated SiPEG-Biotin coverslip using Neutravidin. Microtubules (in green, Figure 3A) were elongated from these seeds using 10 µM fluorescently labelled purified tubulin. Subsequently, the drug mix containing 0.1, 1 and 10 µM of Pretubulysin along with 1 mM GTP and 10 µM tubulin (to prevent microtubule disassembly from dilution) was flushed in. The use of a microfluidic circuit helped to suitably control the addition of the drug mix without moving the microtubules in the field-of-view under observation. We observed rapid MT depolymerization immediately after flushing in 10 µM Pretubulysin with a MT depolymerization speed of 27.29 ± 4.85 (mean $\pm$ SD) µm/min, which is about twice as fast as the depolymerization speed of dynamic control microtubules (14.82 ± 5.2 µm/min). This was accompanied by a loss of 89.92 ± 1.57 % of microtubule mass (See Fig 3 B-D).

As we did in our migration data, we compared the in vitro results with Nocodazole. Interestingly, we found that most MTs entered a state of 'pause' immediately after flushing in 10 µM Nocodazole (Supplementary Figure 3, Supplementary Table 1) with no significant MT shrinkage concurring with the observations of Vasquez et al., 1997 (25). From our in vitro experiments, we conclude that Pretubulysin acts as a potent MT depolymerizing agent, inducing rapid shrinkage of MTs.

As MTs are the most rigid cytoskeletal filaments (26), we postulated that MT disassembly induced by Pretubulysin softens CTLs, facilitating their infiltration and migration. To test this, we determined CTLs stiffness with Real-Time Deformability-Cytometry (RT-DC, Figure 3E). For this, cells were flowed through a microfluidic channel (20 µm) and the shear stress-induced cell deformation was used to calculate the apparent Young´s modulus (27). Pretubulysin treatment induced reduced deformation without changing cell size (Figure 3F, G). Concomitantly, the Young's moduli of CTLs was enhanced after Pretubulysin treatment compared to that of DMSO-treated counterparts (Figure 3H). These results indicate that MT disassembly does not lead to softening, but rather stiffening of CTLs. To understand the underlying mechanism, actin filaments and myosin motors were next investigated.

Disassembly of MT network results in enrichment of F-actin and myosin at the uropod. The MT network and dynamics play a critical role in actin cytoskeletal dynamics as well as actomyosin contractility, which are essential for cell motility (28). To further understand how MT disassembly enhances CTLs infiltration and migration in 3D, we examined the distribution of filamentous actin (F-actin) and phosphorylated myosin (pMyosin) using immunostaining. In the DMSO-treated control CTLs, F-actin was

primarily located at the leading edge and around the nucleus, with pMyosin surrounding the nucleus and present in both the protrusions and the uropod (Figure 4A, DMSO).
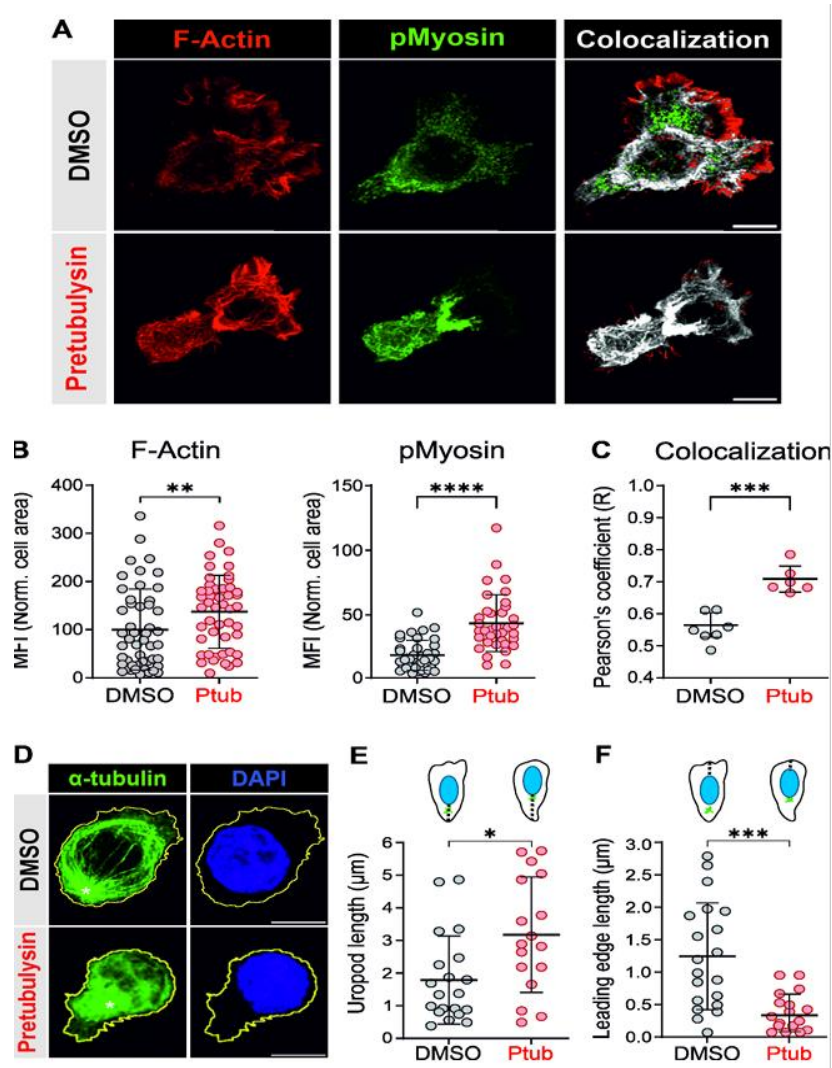

Figure 4. Pretubulysin alters cytoskeleton and morphology of CTLs. (A) z-stack of representative CTLs treated with DMSO or Pretubulysin (10 μM), immobilized on cell-tack coated coverslips, fixed/permeabilized, and immune-stained for F-actin (red), pMyosin (green) and the colocalized region of F-actin and pMyosin (grey). Colocalization analysis was carried out using ImageJ coloc2 plugin. Scale bar is 10 μm. (B) Quantification of F-Actin and pMyosin fluorescent signal on CTLs treated with DMSO or Pretubulysin (10 μM). Treated CTLs were immobilized on cell-tack coated coverslips and fixed/permeabilized for immune-staining. Cell border based on actin staining was defined as ROI. F-Actin and pMyosin in the region were quantified using Sum Intensity Projections with ImageJ and normalized with the cell area. Dots represent individual cells from at least two different donors. Error bars represent the standard deviation of the mean (mean ± SD). The Mann-Whitney test was used for statistical significance (**p=0.0089). Scale bar is 10 μM. (C) Pearsons's correlation coefficient was calculated using ImageJ coloc2 plugin. Dots represent individual cells. Error bars represent the standard deviation of the mean (mean ± SD). The Mann-Whitney test was used for statistical significance (*** p=0.0004). Scale bar is 10 μM. (D) Maximal Intensity projection of one representative cell for each condition (DMSO and Pretubulysin 10 μM), immobilized on cell-tack coated coverslips showing that Pretubulysin induced MT network disassembly on CTLs. Cell border based on actin staining is shown in yellow, α-tubulin in green, and nucleus in blue. The arrows indicate the MTOC. Scale bar is 10 μm. (E-F) Length of the uropod and of the leading edge were calculated manually using ImageJ from fluorescent confocal images.

Schematics at the top represent CTLs under two conditions: DMSO or Pretubulysin (10 μM) treated. Nuclei are blue, the MTOC is green, and the dotted line represents the distance measured. For uropod, distance was from the cell edge to the nuclei. For leading edge, distance was from the nuclei to the cell edge. On the graphs, dots represent individual cells from two donors. Error bars represent the standard deviation of the mean (mean ± SD). For statistical significance, the Mann-Whitney test was used for analyzing the back and front distance ($p < 0,0165$ and $p < 0,0001$ respectively).

Colocalization of F-actin and pMyosin was observed mainly in the perinuclear region as well as along the contour of the leading edge and the uropod (Figure 4A, DMSO). In comparison, in Pretubulysin-treated CTLs, F-actin was primarily located in the uropod and around the nucleus, with pMyosin also enriched in the uropod (Figure 4A, Pretubulysin). Colocalization of F-actin and pMyosin was found predominantly in the uropod and the perinuclear region (Figure 4A, Pretubulysin). Quantification of our results shows that the levels of both F-actin and pMyosin are increased in Pretubulysin-treated CTLs relative to their control counterparts (Figure 4B). Notably, colocalization between F-actin and pMyosin was also enhanced after Pretubulysin treatment (Figure 4C). These findings indicate that disassembly of the MT network repolarizes the F-actin network and the associated actomyosin contractility to the rear part of CTLs.

While analyzing the images, we noticed that the morphology of Pretubulysin-treated CTLs were also altered. To confirm this, we stained α-tubulin and nuclei in CTLs. In control cells, the MT network was clearly visible with a bright spot indicating the MTOC (Figure 4D, DMSO). In Pretubulysin-treated CTLs, α-tubulin did not form filaments, was relatively evenly distributed in the cytosol, and a relatively bright spot, likely the MTOC, could still be identified (Figure 4D, Pretubulysin). The orientation of CTLs was determined by MTOC positioning, which is always located at the uropod during migration. Interestingly, in MT-disassembled CTLs, the nucleus was relocated from its usual position at the front side edge (Figure 4D, Pretubulysin). Quantification of these results show that when the MT network was disassembled by Pretubulysin, the uropod was bigger (Figure 4E) and the leading edge smaller (Figure 4F). The enlarged uropod might be a result of enrichment of actin and pMyosin, leading to enhanced contractile forces in this region.

Pretubulysin induced actomyosin enrichment in the uropod increases migration speed. Since actomyosin contractility plays an indispensable role in cell migration, we investigated whether the relocation of actomyosin to the uropod has any functional impact on migration. To address this question, we first quantified the relative cellular distribution of F-actin and pMyosin.

Fluorescence intensity was evaluated in two specific compartments: the back and the front of the cell. Three representative images are shown in Figure 5A for each DMSO and Pretubulysin-treated CTLs. Quantification of the results again confirmed that F-actin and pMyosin are significantly accumulated at the back of Pretubulysin-treated CTLs compared to the DMSO control, with an enhancement of around 10-fold for F-actin and around 100-fold for pMyosin (Figure 5B).
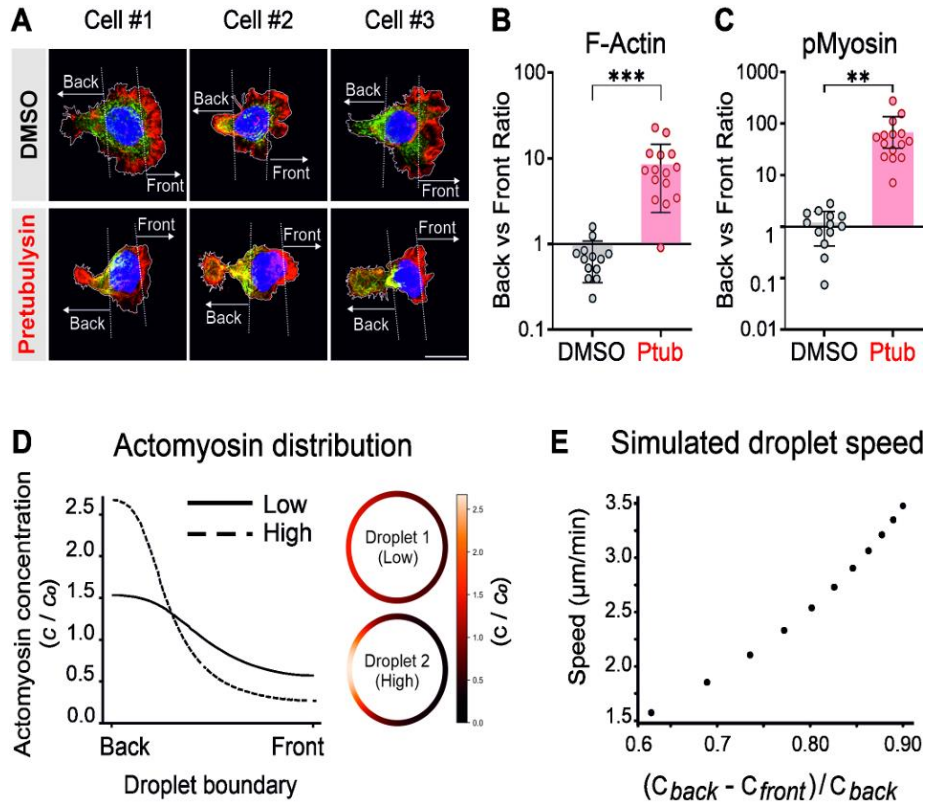
Figure 5. Microtubule disruption-induced actomyosin accumulation at the uropod favors migration. (A) Maximal intensity projection of three cells for each condition: DMSO and Pretubulysin (10 M), immobilized on cell-tack coated coverslips. F-actin is shown in red, pMyosin in green and the nucleus in blue. The cell border (white) was established based on actin staining. "Back" and "front" regions were defined by the positioning of the nuclei and are represented with dotted lines (white) defined by the position of the nuclei. Scale bar is 10 μm. (B-C) Sum Intensity Projections were generated using ImageJ. Total F-Actin (B) and pMyosin (C) were calculated for "back" and "front" regions (MFI * region area). The graph represents the ratio between Front and Back. Dots represent individual cells and the mean ± SD is shown. The unpaired Student's t-test with Welch's correction was used for statistical significance (*** p=0.0002 for F-Actin and **p=0.0023). (D-E) Using computational methods amoeboid cell migration was modeled as a viscous droplet with an active boundary analogous to the cell's cortex. (D) A concentration of actomyosin, c, was placed on the boundary correlating to experimental values. Droplet 1 represents an example of a small difference between back and front (low ratio), comparable with the experimental data obtained for control (DMSO) CTLs. Droplet 2 represents an extreme example of high difference between back and front (high ratio) comparable with the experimental data obtained for Pretubulysin (10 μM) treated CTLs. The concentration profile is shown by the color scale, where c is normalized by c_0, the average droplet concentration. Both droplets have equal total and average concentration. (E) Droplet speed against concentration where the difference was normalized against the concentration at the back of the droplet. The calculations indicate that greater difference in actomyosin from front to back leads to faster migration.

To gain further insight into the relationship between actomyosin distribution and cell migration behavior, we modeled amoeboid cell migration as a viscous droplet with an active boundary, which is analogous to the cell's cortex. Relative cellular distribution of F-actin and pMyosin (back/front) is referred to as concentration ratio in this model. As shown in Figure 5D, actomyosin concentration was placed along the droplet boundary considering two situations: Droplet 1 with low concentration ratio, representing DMSO-treated cells;

and Droplet 2 with high concentration ratio, resembling Pretubulysin-treated CTLs. The concentration profile is shown by the color scale (Figure 5D), where c is normalized by c0, the average droplet concentration. Both droplets had equal total and average concentration. The simulations show that for a motile active droplet, the translational velocity was dependent on the boundary concentration of actomyosin: higher droplet speeds were obtained for 7 droplets with greater concentration at the back of the cell, relative to the front of the cell (Figure 5E). These results show that enrichment of actomyosin leads to enhanced migration speed.

Discussion

In summary, our work establishes Pretubulysin as a potent MT disrupting agent that induces complete MT disassembly. Compared to Nocodazole, Pretubulysin treatment can further enhance CTLs migration, search and therefore killing efficiency in 3D collagen, particularly in dense collagen. Notably, MT-disassembled CTLs exhibit increased speed and persistence in microfabricated narrow channels, which mimic the confining tunnels in collagen matrices. This characteristic leads to overall enhanced motility and faster searching efficiency in 3D environments as suggested by our random persistent searcher simulations. Furthermore, we observed that MT disassembly results in elongation of the uropod and repolarization of F-actin and phosphorylated myosin from the protrusions at the leading edge towards the elongated uropod. This redistribution of the actomyosin network provides additional pushing forces for cell motility, favoring accelerated migration, as predicted by viscous droplet models. Our findings offer crucial insight into the intricate interplay between cytoskeletal dynamics and T cell function, offering potential avenues for enhancing immunotherapeutic strategies targeting T cell-mediated cytotoxicity. The MT network of T cells has emerged as an attractive target that can be specifically disrupted to maximize the efficacy of immune cell-related therapies. While MT depolymerizing agents have received considerable attention as cytotoxic drugs, there is a notable scarcity of studies examining their effects on T cells. Moreover, the existing studies predominantly focus on cancer cells rather than immune cells (29–31). Also, despite promising success, the therapeutic utility of many MT depolymerization agents is impeded by issues such as toxicity and resistance, prompting active exploration of novel compounds. Pretubulysin serves as a good example and is a synthetic precursor of Tubulysin with accessible chemical synthesis while maintaining powerful antitumoral activity (21,22,32). CTLs can navigate through 3D tissues very fast (10–15 μm/min) and are confined by existing tunnels and cellular networks embedded in the extracellular matrix (33). In dendritic cells, MT dynamics is important for navigating the cells through pillar forests, by modulating retraction of protrusions via Rho A and its exchange factor Lfc (18). For adherent cells, disruption of MTs inhibits trail retraction and therefore impairs cell migration on 2D surfaces and transmigration through membranes with pores (34). Interestingly, by perturbing the MT, the migratory parameters of the cell can be affected: impaired migration is observed with MT stabilization (15,35). Our results show that in CTLs, migration persistence and speed are coordinated by the MT network. Our random persistence searcher simulations even suggest that persistence and speed can collectively tailor search and killing efficiency of CTLs in 3D environments. Besides their mechanical

properties, MTs serve as a repository for guanine nucleotide exchange factors, which activate small GTPases that regulate actin assembly and actomyosin contractility. (31,36). Therefore, disruption of MTs can alter cell mechanics not only by changing the microtubule network mechanics, but also by inducing changes within the actin cytoskeleton (37). Previous studies reported that pharmacological dissociation of MTs leads to increased contractility (15,17,31). Furthermore, the interplay between microtubules and cellular contractility has been demonstrated to modulate the morphology and mechanical properties of migrating cells. The enhanced cell stiffness in MT-disassembled CTLs could be attributed to enhanced actomyosin contractility. Although MTs do not directly contribute to the generation of forces that drive cell migration they are involved in the regulation of actin-dependent motility via guanine nucleotide exchange factor GEF-H1, in what has been recently described as the 8 microtubule-contractility axis (15). When GEF-H1 is bound to MTs, it is inactive. It becomes activated when MT depolymerize, which happens either due to the inherent instability of MTs or due to the treatment with MT-depolymerizing compounds. Activated GEF-H1 activates Rho, which in turn induces the upregulation of myosin II contractility and actin polymerization (36–39). It is also reported that GEF-H1 plays an essential role in crosslinking the MT network and contractility in CTLs (15) Actomyosin contractility provides primary driving forces for cells, including T cells, to move. To cross the barrier formed by the endothelium, T cells use actomyosin and the resulting contractility to squeeze in between endothelial cells. The efficiency of migration is adjusted by the amount of force generated and the level of traction applied. (40). While actin polymerization is essential for force generation by T cells, dynamic MTs at the interface also play a fundamental role (17). Actomyosin contractility at the uropod has been described as fundamental in generating the forces that drive migration in amoeboid cells (8). In this work, we observed that in Pretubulysin-treated CTLs, F-actin and p-Myosin were redistributed from the protrusions to the uropod. The results from viscous droplet models suggest that enrichment of actomyosin at the uropod can increase migration speed. This symmetry-break in the distribution of the cytoskeletal elements results in morphological changes, mechanical perturbations, and migration enhancement of CTLs, which can then kill their targets more efficiently.

Supplementary Information

Supplementary Figure 1. CTLs degranulation is not affected by Pretubulysin or Nocodazole.
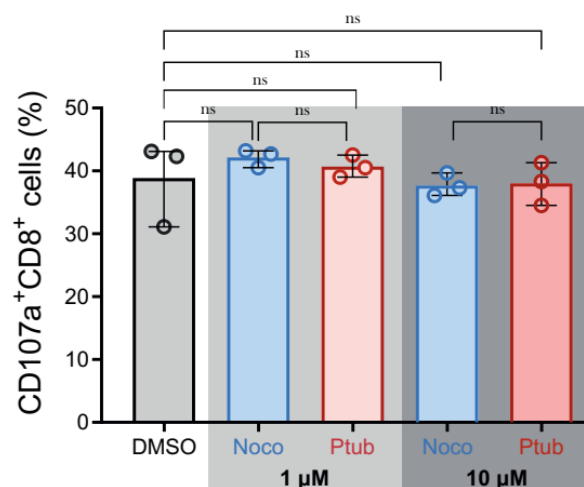

Supplementary Figure 2. Comparison of killing kinetics between simulations and experimental data.
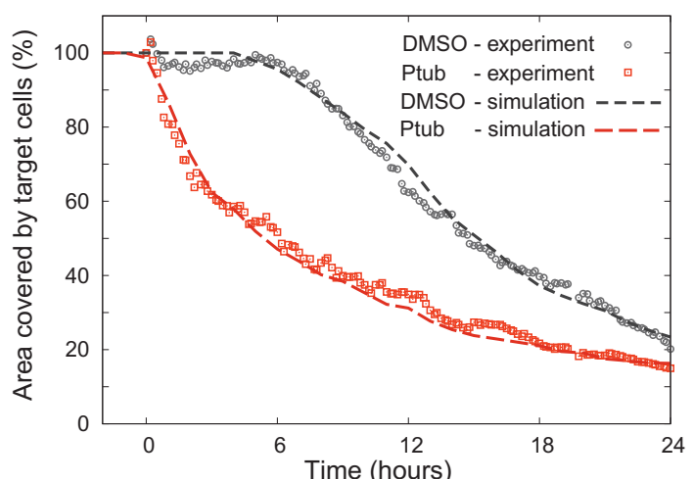
Supplementary Figure 3. Characterizing microtubule depolymerization potential of Nocodazole using In vitro reconstitution assays. (A) Timelapse sequence showing microtubule pause (with no subsequent change in microtubule length) following treatment with 10μM Nocodazole (Scale bar 2 m). Images are representative of three independent experiments. (B) Kymograph from A, depicting no change in microtubule length vs time after treatment with 10μM Nocodazole. (C) Timelapse sequence showing microtubule pause and then elongate following treatment with 10μM Nocodazole (Scale bar-2 m). Images are representative of three independent experiments. (D) Kymograph from C, depicting pause and increase in microtubule length vs time after treatment with 10μM Nocodazole. (E)Comparison of depolymerization velocity of microtubules following treatment with Nocodazole (10, 50, 100 and 250μM), Pretubulysin (0.1, 1 and 10 μM) with Control (DMSO). Data represent Mean ± SD from three independent experiments.

Mann-Whitney test was used for statistical significance. (MTs that entered pause state after nocodazole treatment were excluded from analysis).
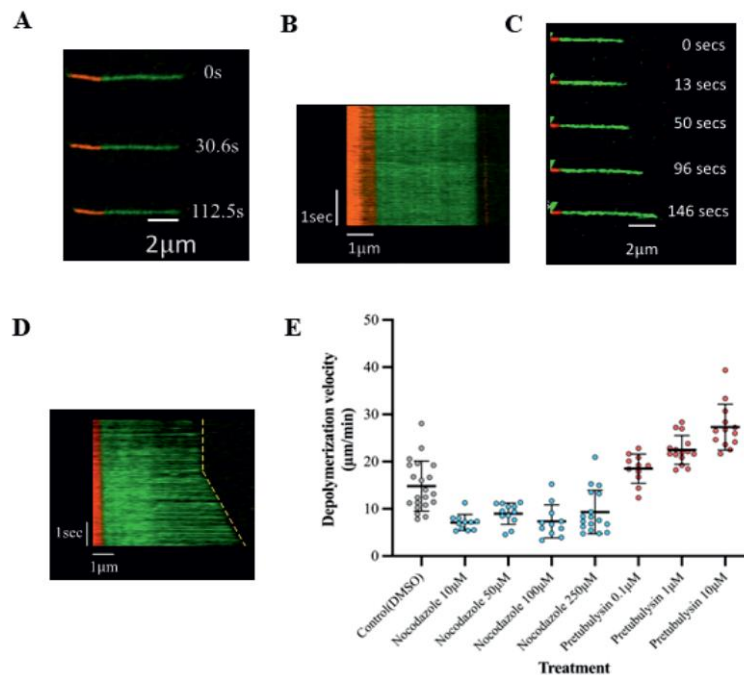
Supplementary Table 1. P-values of comparison between tested concentrations of Nocodazole and Pretubulysin with Control (DMSO) (Statistical analysis: Mann-Whitney test).

	Control (DMSO)	Pretubulysin 0.1 μM	Pretubulysin 1 μM	Pretubulysin 10 μM
Control (DMSO)	–	0.0339	<0.0001	<0.0001
Nocodazole (10 μM)	<0.0001	<0.0001	<0.0001	<0.0001
Nocodazole (50 μM)	0.0003	<0.0001	<0.0001	<0.0001
Nocodazole (100 μM)	<0.0001	<0.0001	<0.0001	<0.0001
Nocodazole (250 μM)	0.0012	<0.0001	<0.0001	<0.0001

References
1.   Fowell DJ, Kim M. The spatio-temporal control of effector T cell migration. Nat Rev Immunol. 2021;21(9):582-596. doi:10.1038/s41577-021-00507-0
2.   Fridman WH, Zitvogel L, Sautès-Fridman C, Kroemer G. The immune contexture in cancer prognosis and treatment. Nat Rev Clin Oncol. 2017;14(12):717-734. doi:10.1038/nrclinonc.2017.101
3.   Wortel IMN, Textor J. Interpreting T-cell search "strategies" in the light of evolution under constraints. PLoS Comput Biol. 2023;19(2):e1010918. Published 2023 Feb 27. doi: 10.1371/journal.pcbi.1010918
4.   Shaebani MR, Jose R, Santen L, Stankevicins L, Lautenschläger F. Persistence-Speed Coupling Enhances the Search Efficiency of Migrating Immune Cells. Phys Rev Lett. 2020;125(26):268102. doi:10.1103/PhysRevLett.125.268102

5.   Shaebani MR, Piel M, Lautenschläger F. Distinct speed and direction memories of migrating dendritic cells diversify their search strategies. Biophys J. 2022;121(21):4099-4108. doi: 10.1016/j.bpj.2022.09.033

6.   Shaebani MR, Stankevicins L, Vesperini D, et al. Effects of vimentin on the migration, search efficiency, and mechanical resilience of dendritic cells. Biophys J. 2022;121(20):3950-3961. doi: 10.1016/j.bpj.2022.08.033

7.   Maiuri P, Rupprecht JF, Wieser S, et al. Actin flows mediate a universal coupling between cell speed and cell persistence. Cell. 2015;161(2):374-386. doi: 10.1016/j.cell.2015.01.056

8.   Dupré L, Houmadi R, Tang C, Rey-Barroso J. T Lymphocyte Migration: An Action Movie Starring the Actin and Associated Actors. Front Immunol. 2015;6:586. Published 2015 Nov 18. doi:10.3389/fimmu.2015.00586

9.   Moreau HD, Piel M, Voituriez R, Lennon-Duménil AM. Integrating Physical and Molecular Insights on Immune Cell Migration. Trends Immunol. 2018;39(8):632-643. doi:10.1016/j.it.2018.04.007

10.   Kopf A, Kiermaier E. Dynamic Microtubule Arrays in Leukocytes and Their Role in Cell Migration and Immune Synapse Formation. Front Cell Dev Biol. 2021;9:635511. Published 2021 Feb 9. doi:10.3389/fcell.2021.635511

11.   Théry M, Racine V, Piel M, et al. Anisotropy of cell adhesive microenvironment governs cell internal organization and orientation of polarity. Proc Natl Acad Sci U S A. 2006;103(52):19771-19776. doi:10.1073/pnas.0609267103

12.   Rey-Suarez I, Rogers N, Kerr S, Shroff H, Upadhyaya A. Actomyosin dynamics modulate microtubule deformation and growth during T-cell activation. Mol Biol Cell. 2021;32(18):1641-1653. doi:10.1091/mbc.E20-10-0685

13.   Giraldo NA, Sanchez-Salas R, Peske JD, et al. The clinical role of the TME in solid cancer. Br J Cancer. 2019;120(1):45-53. doi:10.1038/s41416-018-0327-z

14.   Zhao R, Zhou X, Khan ES, et al. Targeting the Microtubule-Network Rescues CTL Killing Efficiency in Dense 3D Matrices. Front Immunol. 2021;12:729820. Published 2021 Aug 17. doi:10.3389/fimmu.2021.729820

15.   Tabdanov ED, Rodríguez-Merced NJ, Cartagena-Rivera AX, et al. Engineering T cells to enhance 3D migration through structurally and mechanically complex tumor microenvironments. Nat Commun. 2021;12(1):2815. Published 2021 May 14. doi:10.1038/s41467-021-22985-5

16.   Takesono A, Heasman SJ, Wojciak-Stothard B, Garg R, Ridley AJ. Microtubules regulate migratory polarity through Rho/ROCK signaling in T cells. PLoS One. 2010;5(1):e8774. Published 2010 Jan 19. doi: 10.1371/journal.pone.0008774

17.   Hui KL, Upadhyaya A. Dynamic microtubules regulate cellular contractility during T-cell activation. Proc Natl Acad Sci U S A. 2017;114(21):E4175-E4183. doi:10.1073/pnas.1614291114

18.   Kopf A, Renkawitz J, Hauschild R, et al. Microtubules control cellular shape and coherence in amoeboid migrating cells. J Cell Biol. 2020;219(6):e201907154. doi:10.1083/jcb.201907154

19.   Braig S, Wiedmann RM, Liebl J, et al. Pretubulysin: a new option for the treatment of metastatic cancer. Cell Death Dis. 2014;5(1):e1001. Published 2014 Jan 16. doi:10.1038/cddis.2013.510

20.   Herrmann J, Elnakady YA, Wiedmann RM, et al. Pretubulysin: from hypothetical biosynthetic intermediate to potential lead in tumor therapy. PLoS One. 2012;7(5):e37416. doi: 10.1371/journal.pone.0037416

21.   Kubisch R, von Gamm M, Braig S, et al. Simplified pretubulysin derivatives and their biological effects on cancer cells. J Nat Prod. 2014;77(3):536-542. doi:10.1021/np4008014

22.   Kern S, Truebenbach I, Höhn M, et al. Combined antitumoral effects of pretubulysin and methotrexate. Pharmacol Res Perspect. 2019;7(1):e00460. Published 2019 Jan 22. doi:10.1002/prp2.460

23.   Z, Zhao R, Hoth M, Qu B, Rieger H. Migration of Cytotoxic T Lymphocytes in 3D Collagen Matrices. Biophys J. 2020;119(11):2141-2152. doi: 10.1016/j.bpj.2020.10.020

24.   Zhao R, Yanamandra AK, Qu B. A high-throughput 3D kinetic killing assay. Eur J Immunol. 2023;53(11):e2350505. doi:10.1002/eji.202350505

25.   Vasquez RJ, Howell B, Yvon AM, Wadsworth P, Cassimeris L. Nanomolar concentrations of nocodazole alter microtubule dynamic instability in vivo and in vitro. Mol Biol Cell. 1997;8(6):973-985. doi:10.1091/mbc.8.6.973

26.   Pegoraro AF, Janmey P, Weitz DA. Mechanical Properties of the Cytoskeleton and Cells. Cold Spring Harb Perspect Biol. 2017;9(11):a022038. Published 2017 Nov 1. doi:10.1101/cshperspect.a022038

27.   Mietke A, Otto O, Girardo S, et al. Extracting Cell Stiffness from Real-Time Deformability Cytometry: Theory and Experiment. Biophys J. 2015;109(10):2023-2036. doi:10.1016/j.bpj.2015.09.006

28.   Schmidt CJ, Stehbens SJ. Microtubule control of migration: Coordination in confinement. Curr Opin Cell Biol. 2024;86:102289. doi: 10.1016/j.ceb.2023.102289

29.   Steinmetz MO, Prota AE. Microtubule-Targeting Agents: Strategies To Hijack the Cytoskeleton. Trends Cell Biol. 2018;28(10):776-792. doi: 10.1016/j.tcb.2018.05.001

30.   Xiangrong X, Yao L, Yao A. The Recent Developments of ADCs with the Tubulysins as the Payloads. Mini Rev Med Chem. 2023;23(18):1797-1805. doi:10.2174/1389557523666230220121648

31.   Chang YC, Nalbant P, Birkenfeld J, Chang ZF, Bokoch GM. GEF-H1 couples nocodazole-induced microtubule disassembly to cell contractility via RhoA. Mol Biol Cell. 2008;19(5):2147-2153. doi:10.1091/mbc.e07-12-1269

32.   Ullrich A, Chai Y, Pistorius D, et al. Pretubulysin, a potent and chemically accessible tubulysin precursor from Angiococcus disciformis. Angew Chem Int Ed Engl. 2009;48(24):4422-4425. doi:10.1002/anie.200900406

33.   Krummel MF, Bartumeus F, Gérard A. T cell migration, search strategies and mechanisms. Nat Rev Immunol. 2016;16(3):193-201. doi:10.1038/nri.2015.16

34.   Ganguly A, Yang H, Zhang H, Cabral F, Patel KD. Microtubule dynamics control tail retraction in migrating vascular endothelial cells. Mol Cancer Ther. 2013;12(12):2837-2846. doi: 10.1158/1535-7163.MCT-13-0401

35.   Lautenschläger F, Paschke S, Schinkinger S, Bruel A, Beil M, Guck J. The regulatory role of cell mechanics for migration of differentiating myeloid cells. Proc Natl Acad Sci U S A. 2009;106(37):15696-15701. doi:10.1073/pnas.0811261106

36.   Krendel M, Zenke FT, Bokoch GM. Nucleotide exchange factor GEF-H1 mediates cross-talk between microtubules and the actin cytoskeleton. Nat Cell Biol. 2002;4(4):294-301. doi:10.1038/ncb773

37.   Joo E, Olson MF. Regulation and functions of the RhoA regulatory guanine nucleotide exchange factor GEF-H1. Small GTPases. 2021;12(5-6):358-371. doi:10.1080/21541248.2020.1840889

38.   Pineau J, Pinon L, Mesdjian O, Fattaccioli J, Lennon Duménil AM, Pierobon P. Microtubules restrict F-actin polymerization to the immune synapse via GEF-H1 to maintain polarity in lymphocytes. Elife. 2022;11:e78330. Published 2022 Sep 16. doi:10.7554/eLife.78330

39.   Azoitei ML, Noh J, Marston DJ, et al. Spatiotemporal dynamics of GEF-H1 activation controlled by microtubule- and Src-mediated pathways. J Cell Biol. 2019;218(9):3077-3097. doi:10.1083/jcb.201812073

40.   Krummel MF, Friedman RS, Jacobelli J. Modes and mechanisms of T cell motility: roles for confinement and Myosin-IIA. Curr Opin Cell Biol. 2014;30:9-16. doi: 10.1016/j.ceb.2014.05.003

41.   Knörck A, Schäfer G, Alansary D, et al. Cytotoxic Efficiency of Human CD8+ T Cell Memory Subtypes. Front Immunol. 2022;13:838484. Published 2022 Apr 13. doi:10.3389/fimmu.2022.838484

42.   Westphal V, Rizzoli SO, Lauterbach MA, Kamin D, Jahn R, Hell SW. Video-rate far-field optical nanoscopy dissects synaptic vesicle movement. Science. 2008;320(5873):246-249. doi:10.1126/science.1154228

43.   Castoldi M, Popov AV. Purification of brain tubulin through two cycles of polymerization-depolymerization in a high-molarity buffer. Protein Expr Purif. 2003;32(1):83-88. doi:10.1016/S1046-5928(03)00218-3

44.   Sadjadi Z, Shaebani MR. Orientational memory of active particles in multistate non-Markovian processes. Phys Rev E. 2021;104(5-1):054613. doi: 10.1103/PhysRevE.104.054613

45.   Tierno P, Shaebani MR. Enhanced diffusion and anomalous transport of magnetic colloids driven above a two-state flashing potential. Soft Matter. 2016;12(14):3398-3405. doi:10.1039/c6sm00237d

46.   Shaebani, M. R., and H. Rieger, Transient anomalous diffusion in run-and-tumble dynamics. Front. Phys., 2019, 7:120. doi: 10.3389/fphy.2019.00120

47.   Shaebani MR, Rieger H, Sadjadi Z. Kinematics of persistent random walkers with two distinct modes of motion. Phys Rev E. 2022;106(3-1):034105. doi:10.1103/PhysRevE.106.034105.

48.   Whitfield CA, Hawkins RJ. Immersed Boundary Simulations of Active Fluid Droplets. PLoS One. 2016;11(9):e0162474. Published 2016 Sep 8. doi: 10.1371/journal.pone.0162474

3.2. Results 2)

Microtubules and CTLs migration in channels

Cytotoxic T lymphocytes (CTLs) are crucial components of the adaptive immune system, and their effective function relies on their ability to migrate through three-dimensional (3D) environments. For CTLs to perform their immune functions, proper mobility is essential. Unlike mesenchymal migrating cells that alter the extracellular matrix, amoeboid migrating cells like CTLs adapt their shape and morphology to their surroundings. Previous studies from our group have shown that CTLs navigate through narrow 1D channels within 3D matrices (Sadjadi et al., 2020), a behavior that enhances the speed of cell migration.

In this study we aim to investigate why CTLs exhibit increased speed and persistence under confinement and what is the role of the microtubule-organizing center (MTOC) in this process.

- Speed and persistence of CTLs in confinement

To examine CTLs migration under confinement, we designed straight micro-channels with three different dimensions (height x width): 1) 2x5 µm, 2) 5x5 µm, and 3) 10x10 µm; the channels length was 400 µm (Figure 1 A). Hoechst-labeled CTLs were loaded into these chambers, and their migration was monitored at 37°C every 3 minutes for 15 hours.
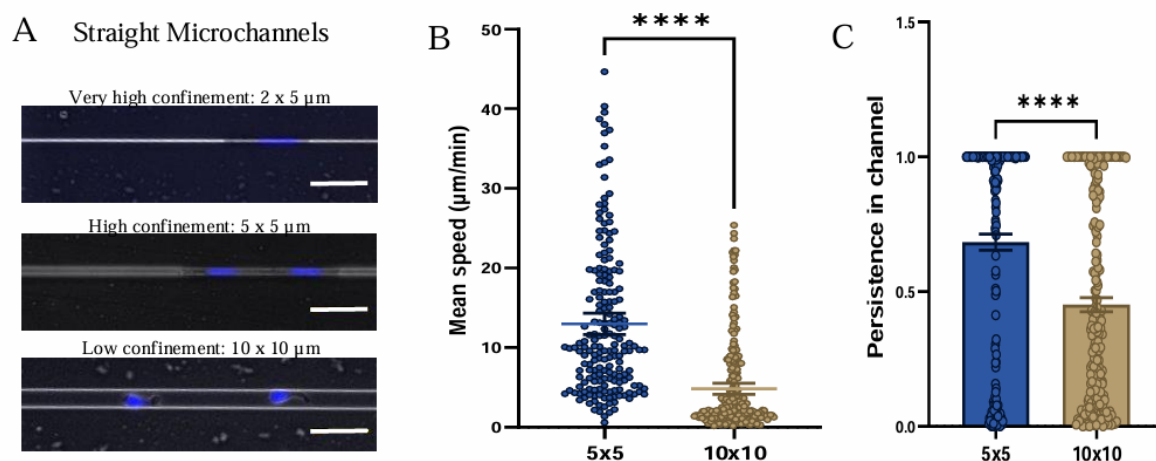

Figure 1. Characterization of CTLs migration in 1D. A) Microfabricated straight microchannels designed with different size (width x height): 2 x 5 µM, 5 x 5 µM, 10 x 10 µM. Hoechst stained CTLss (nucleus in blue) were loaded on the chips, previously coated with PEG. Cells migrated spontaneously for 15 hours. Scale bar 25 µm. B) Using track Mate plugin from ImageJ, cells migrating in channels were automatically tracked. For each track, mean speed (B) and mean persistence (C) were calculated.

Our first set of results demonstrated that 2x5 μm is a very confined space, and the numbers of CTLs migrating inside the channels was too low to perform any analysis. In our experimental conditions CTLs do not enter the 2 x5 μm, thus, we continued our study on CTLs migrating through the 5x5 and 10x10 μm channels.

We analyzed over 100 cells from two different donors for both channel size (5x5μm and 10x10μm) using the TrackMate plugin in ImageJ. Our quantification reveals that CTLs migrate faster and more persistently in 5 x 5 μm channels compared to 10 x 10 μm channels (Figure 1C-D).

- MTOC position during CTLs migration in 1D

The MTOC, located at the rear of CTLs, is a key feature of polarization and amoeboid migration mode. To track the MTOC during migration under confinement, we stained CTLs with SiR-tubulin for real-time tubulin polymerization and Hoechst for the nucleus. Time-lapse images were analyzed to determine MTOC positioning. We determined cell size inside the channel, by manually measuring the length and the height. Cells in high confinement adopted a more elongated shape, with a length double than the height. Distinctively, cells migrating in low confinement adopted a rounded shape, with an average equal length and height (Figure 2A upper panel). The SiR-tubulin dye allowed us to see a specially brighter spot, that we consider the MTOC, as can be seen in Figure 2 A. Representative images for each confinement condition are shown in Figure 2A. The nuclei is represented in blue, and the microtubules are represented in green, the brighter point was considered the MTOC for the analysis. Next, we manually calculated the distance between the MTOC and the nucleus, and the MTOC's position relative to the nucleus center. The data is summarized in Figure 2B-C.

As shown in Figure 2, CTLs migrating in high confinement showed an elliptical shape, while cells migrating in low confinement adopted a rounded shape. We observed the same effect on the nuclear shape. To calculate the distance between the MTOC and nucleus, the center of the nuclei was considered, therefore the values obtained were normalized by the nucleus size. Our results suggest that the larger distance between the MTOC and the nucleus that we observe is not only because the nucleus is larger, but because the MTOC positions further in the cytoplasm, really at the rear part of the cell during migration. When analyzing the angle between the MTOC and the nucleus (considering the direction of migration), cells in high confinement showed homogeneous distribution of values around 0, meaning that

the MTOC and the nuclei are on the same line. CTLs migrating under low confinement showed a broad range of values, between 0 a 180, meaning that there was no preferred position of the MTOC when the cell is inside the channel.
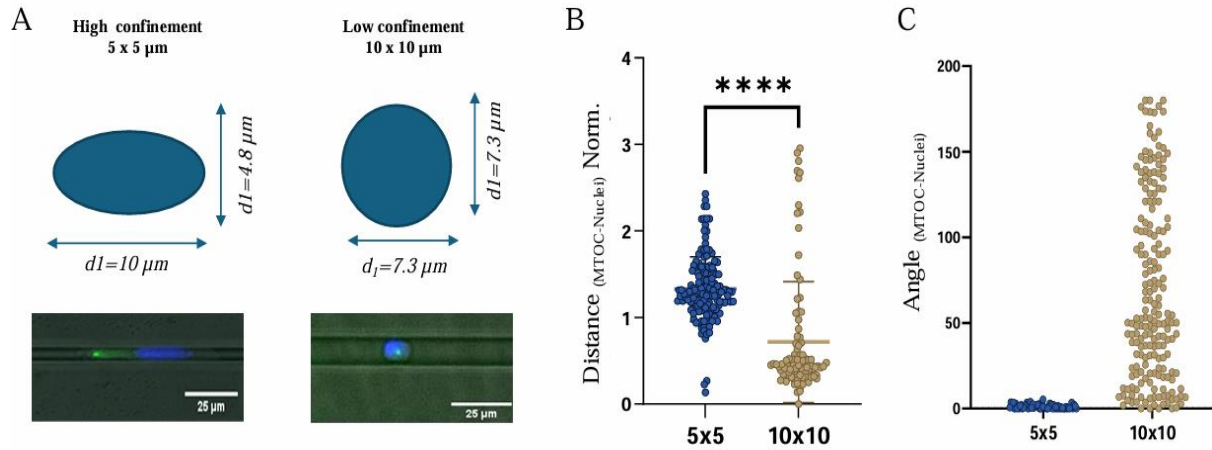

Figure 2. MTOC during cell migration in confinement. A) Representative images on time point during cell migration in channels (left 5 x 5 µM, right 10 x 10µM). Images were acquired with Nikon Fluorescence Microscope, 20X magnification. Nuclei is represented in blue, MTOC is represented in green. B) Schematic representation of cell shape and size, the average value for both axes measured, are written. CTLs migrating in 5 x 5 are elongated, while CTLs migrating in 10 x 10 are rounded. C) Nuclear size was calculated, and the major and minor axe length are represented. D) The distance between the MTOC and the center of the nuclei normalized by the cell size and E) the angle between the MTOC and the nuclei were manually calculated.

Taken together, our preliminary results suggest that high confinement (e.g., 5x5 µm channels) forces a polarized state in CTLs (because of physical confinement). This results in more persistent migration, possibly due to the restricted rotation of the MTOC around the nucleus. Conversely, less confined spaces allow MTOC relocation and repolarization, resulting in less persistent migration.

4. Discussion

While cytotoxic T lymphocytes (CTLs) can navigate complex environments in tissues to target infected or tumorigenic cells, optimizing CTLs migration and search strategies is needed to improve cell mediated therapies. This migration is driven by the cytoskeleton, primarily the actomyosin system, which coordinates cell motility through actin polymerization and myosin contractions. Although microtubules (MTs) do not directly generate force, they modulate actin dynamics and thus influence cell migration. Targeting MTs with pharmacological agents offers potential therapeutic benefits, with MT-destabilizing agents enhancing T cell functions in 3D environments, but the exact mechanisms behind this enhancement remain elusive to date. Pretubulysin (PT), a potent MT-destabilizing agent, emerges as a promising candidate for improving CTLs efficacy. In this study, we explore the role of MTs in the migration of activated human T cells: by utilizing PT to disrupt the MT network, we examine the mechanisms that enhance immune functions; by employing live cell imaging we investigate the function of the microtubule organizing center (MTOC) during T cell migration under confinement.

Our findings reveal that disrupting the MT network in CTLs with PT results in enhanced speed and persistence of cell movement. These results are consistent with published data, where similar effects were observed using another MT depolymerizing agent: Nocodazole (Zhao et al., 2021). Our comparative results with Nocodazole reveals that Pretubulysin is more potent at same molecular concentrations, highlighting the potential of Pretubulysin. Zhao et al. also evaluated the killing efficiency and migration parameters using primary human CTLs in experimental settings similar to ours. They examined the morphology of the nucleus of CTLs with impaired motility in dense 3D matrices and found that increased nuclear flexibility following MT depolymerization correlated with the observed migration enhancements (Zhao et al., 2021). Although we did not analyze nuclear deformation in PT-treated CTLs in 3D, we hypothesize that the absence of a MT network, as shown in Figure 4D, and the increased actomyosin accumulation behind the nucleus, as shown in Figure 5A-C, imply stronger forces pushing the nucleus through extracellular matrix networks in 3D. This likely results in greater nuclear deformation when necessary. Since the MT network provides a mechanically stable structure around the nucleus to protect chromatin integrity, along with laminin A/C and other proteins of the nuclear envelope, it is important

to investigate in the future, the susceptibility of PT-treated CTLs to apoptosis during or after migration through dense collagen matrices.

The effect of MT depolymerization on migration has been reported for other immune cell types. Specifically, Nocodazole was used to investigate the mechanistic involvement of MTs in dendritic cell migration (Kopf et al., 2020). The authors showed that local MT depolymerization causes retraction of the cell body, while total depletion of MTs resulted in cell halt because of inappropriate retraction of lateral protrusions. Notably, in that same experimental setup, when DCs migrated in a straight channel towards a junction with four possible paths, MT depolymerization did not impact cell coherence but did reduce locomotion speed and caused frequent direction changes, unlike untreated cells that moved persistently through the channels (Kopf et al., 2020).

Despite showing a contrary effect on migration parameters than what we are showing here, the authors also reported that MT depolymerization in peripheral regions locally triggers the activation of actomyosin-mediated contraction (Kopf et al., 2020). Two important differences with our approach are (1) the experimental system and (2) the concentration of the MT-depolymerizing agent (Kopf et al. 2020 used lower concentration). In any case, this diversity in outcomes highlights the lack of a full understanding of how different cell types maintain their dynamic shape and coherence. This problem is especially critical in large migrating cells, such as dendritic cells, which can adopt ramified shapes. Additionally, while Nocodazole has been widely used in literature and its effect in different cell types can be found, the exact mechanism of action is yet unknown. Opposite effects depending on the dose used have been reported for the same cell type and its effect is reversible relatively fast, all of this should be considered when interpreted published results (Liao et al., 1995; Vasquez et al., 1997). Pharmacological interventions are not the only reported approach to targeting microtubules. Through genome engineering, Tabdanov et al., 2021 manipulated the microtubule-contractility axis, resulting in engineered T cells that more effectively moved through 3D matrices and tumor volumes (Tabdanov et al., 2021). Therefore, designing cells to more efficiently traverse 3D microenvironments, through genetic engineering, could be a successful approach to improving the effectiveness of immune therapies.

In addition to the experimental approaches, computational modeling has been used in this work. The random walk model described in this work predicts that the significant

improvements observed with PT treatment will have far-reaching positive implications, according to the simulation results. This is a promising approach, considering that computational simulations can overcome possible technical limitations of laboratory experiments. For a better interpretation of the data, some aspects should be discussed. The model considers CTLs as a homogeneous population of cells, which is not the case experimentally. We know that heterogeneity in T cell phenotypes affects immune function as well as migratory properties (Krummel et al., 2016). Future work should address how cell phenotype correlates with migratory properties to better describe the population under our study, which is relevant for therapeutic approaches. Additionally, the model assumes that all effector cells (CTLs) are equally able to kill target cells upon first encounter. Experimental data suggest that killing efficiency is not solely dependent on searching efficiency. Unpublished results from our lab indicate that only around 10 % of *in vitro*-generated CTLs can kill the contacted target cell. This value could also vary with PT treatment, complicating the decision of which percentage to use in the model. Proper experimental confirmation is needed, for example, by defining the percentage of cells that contact (find) the target compared to the percentage of cells that actually induce target cell killing.

As discussed, data showing the enhancement of migratory properties of T cells after targeting MT is available. However, how the immune synapse and the killing machinery are affected by microtubule depolymerizing strategies, and how cells can kill without a proper MT network, need to be investigated. Fundamental immunological questions, such as how cytotoxic granules are transported and located at the interface contacting target cells, should be thoroughly addressed for MT-depolymerized CTLs. Despite several studies highlighting the need of the MT network for immune synapse formation and target release after apoptosis (Kopf & Kiermaier, 2021), other studies have shown that MTs might be dispensable for the formation of a functional immune synapse, with experimental differences depending on the type of MT-targeting drug used (Huby et al., 1998; Hui & Upadhyaya, 2017; Ueda et al., 2015). Recent studies highlight actomyosin-mediated contraction and not MT dynamics, as a fundamental mechanism to terminate the immune synapse, showing that only contraction is enough to induce the dissolution of the immune synapse (Sanchez et al., 2023).

In another direction, recent studies show that taxanes can directly induce on T cells the capacity of killing of carcer cells, in an unusual way independent of the TCR. T cells treated

with taxanes are able to produce and release cytotoxic extracellular vesicles, causing apoptosis only in tumor cells, sparing healthy epithelial cells (Vennin et al., 2023). The authors proposed that this approach of *ex vivo* treatment of T cells with taxanes can be used prior to adoptive transfer therapies. With this strategy, the expected systemic toxicity of the drug could be overcome. Taken together, these studies confirm that much more understanding is needed of the implications of targeting the MT network of immune cells.

From a mechanical perspective, our studies demonstrate that disrupting the stiffest polymer in the cytoskeleton renders cells even stiffer likely due to the enhancement of actomyosin function. This result aligns with findings reported by Tabdanov et al., 2021, who used atomic force microscopy instead of RTDC. Despite the differences in techniques and the MT depolymerization agent used, both results are consistent: disrupting the MT network in cells renders CTLs stiffer. In our work, we explain the stiffness increase based on the observed enhancement in actomyosin expression and colocalization after treatment. Although this provides direct evidence, it is not a direct measurement of the contraction force generated. Indeed, we attempted to measure this parameter using traction force microscopy (Denisin et al., 2024) but technical problems occurred: the lack of adhesion of T cells to the hydrogels made it impossible to obtain parameters using this technique. T cells, while migrating, exert very weak forces on the hydrogel and did not generate beads displacement, not even in the control group. Also, PT-treated CTLs migrated much faster, escaping the field of view very rapidly. In the literature, direct measurement of T cell contraction has been reported with traction force microscopy using a lymphocyte-derived cell line, specifically the Jurkat cell line (Hui & Upadhyaya, 2017). The authors measured cell contraction and reported that nocodazole-treated cells showed increased contraction due to enhanced actomyosin activity. One important difference in their approach is that they measured the effect of MT dynamics on contractility during T cell activation, using hydrogels coated with activating antibodies, specifically anti-CD3. Their results, although technically different, are in line with our observations and findings.

From a mechanistic standpoint, much remains to be explained regarding the direct effects of PT on microtubules. What signaling pathways are involved in enhancing actomyosin function upon MT destabilization? How does PT specifically alter the dynamics of actin polymerization and myosin contractility at a molecular level? These questions are beyond the scope of this work but are fundamentally important. Preliminary bioinformatics approaches indicate that PT binds to the interface between alpha and beta tubulin, inducing

a conformational change that disrupts the heterodimer structure and impairs MT assembly. However, the reversibility of this interaction is still unknown, although preliminary theoretical results predict a very stable union. Experimental results are needed to determine how long it takes to recover the MT network after Pretubulysin treatment in CTLs, if recovery is possible.

Overall, our findings, along with other published data, suggest that a complete microtubule (MT) network is not only unnecessary but actually undesirable for faster and more persistent T cell movement. This raises the question of whether MTs act as a brake on CTLs migration. While MTs are essential for cell division and activation, they might become dispensable after T cells are fully activated and committed to their cytotoxic function.

Our preliminary results indicate that in high confinement, CTLs move faster and more persistently, possibly due to restricted MTOC rotation. This suggests that limiting the paths available for exploration could enhance the efficiency of their search, by enhancing persistent migration. Such confinement could result from physical barriers (like a in our experimental approach with 5x5 μm channels) or from the absence of MTs to guide new directions. Therefore, we anticipate that without a MT network, such as after Pretubulysin treatment, CTLs would also move faster and more persistently on 2D surfaces without confinement. Further investigation is needed into how MTOC positioning and MT depolymerization affect migration in 1D. Although we aimed to explore this, experimental challenges, such as tracking the MTOC after MT disassembly, remain unresolved. A potential solution is using MTOC-specific proteins instead of tubulin for visual tracking. Published works like Weier et al. (2022) could guide future studies to address these challenges.

In summary, our results indicate that targeting the MT network of activated T cells with PT can be an effective strategy to enhance CTLs migration, thus, the therapeutic efficacy of adoptive cell transfer therapies. The unbalanced distribution of f-actin and pMyosin, concentrated at the uropod after PT treatment, creates a potent motor capable of driving faster amoeboid cell migration. This cytoskeletal arrangement transforms CTLs into more efficient searchers, poised to improve target identification and immune function. It is crucial to determine how well these *in vitro* findings and simulation results translate to *in vivo* models of cancer and infection. From a therapeutic perspective, we propose that PT can be combined with other immunotherapies or chemotherapies to synergistically enhance

anti-tumor responses. Additionally, we hypothesize that this effect could improve the migration of other amoeboid cells, such as neutrophils.

5. Conclusions

Considering our initial aims and results in exploring the role of the microtubule network during CTLs migration in 3D environments, we summarize our key findings as follows:

- Microtubule depolymerization induced by Pretubulysin enhances cytotoxic T lymphocyte (CTLs) migration, searching and killing. This underscores the role of microtubules in regulating CTLs motility and highlights the potential of microtubule-disassembling agents to improve immune responses.

- The observed increase in cell stiffness following microtubule depolymerization implies a significant mechanical alteration in CTLs, contributing to their enhanced migration efficiency. Understanding these cytoskeletal changes offers insights into the complex relation between cell mechanics and cell migration.

- The accumulation of actomyosin at the uropod of CTLs following microtubule depolymerization highlights the link between microtubule dynamics and actomyosin contractility leading to faster migration. These findings consolidate the coordination of cytoskeletal elements as fundamental in driving CTLs motility and provide a basis for developing therapeutic strategies targeting microtubules.

- CTLs migration is faster and more persistent in highly confined spaces. The physical polarization of the cells within narrow channels, combined with the restricted capacity for the MTOC to change position, likely compels the cells to maintain movement direction, thereby enhancing their speed and persistence.

6. References

Azoitei, M. L., Noh, J., Marston, D. J., Roudot, P., Marshall, C. B., Daugird, T. A., Lisanza, S. L., Sandí, M. J., Ikura, M., Sondek, J., Rottapel, R., Hahn, K. M., & Danuser, G. (2019). Spatiotemporal dynamics of GEF-H1 activation controlled by microtubule- And Src-mediated pathways. *Journal of Cell Biology*, *218*(9), 3077–3097. https://doi.org/10.1083/JCB.201812073

Barry, M., & Bleackley, R. C. (2002). Cytotoxic T lymphocytes: All roads lead to death. In *Nature Reviews Immunology* (Vol. 2, Issue 6, pp. 401–409). European Association for Cardio-Thoracic Surgery. https://doi.org/10.1038/nri819

Birkenfeld, J., Nalbant, P., Yoon, S. H., & Bokoch, G. M. (2008). Cellular functions of GEF-H1, a microtubule-regulated Rho-GEF: is altered GEF-H1 activity a crucial determinant of disease pathogenesis? *Trends in Cell Biology*, *18*(5), 210–219. https://doi.org/10.1016/J.TCB.2008.02.006

Braig, S., Wiedmann, R. M., Liebl, J., Singer, M., Kubisch, R., Schreiner, L., Abhari, B. A., Wagner, E., Kazmaier, U., Fulda, S., & Vollmar, A. M. (2014). Pretubulysin: a new option for the treatment of metastatic cancer. *Cell Death & Disease*, *5*. https://doi.org/10.1038/cddis.2013.510

Chang, Y. C., Nalbant, P., Birkenfeld, J., Chang, Z. F., & Bokoch, G. M. (2008). 3GEF-H1 couples nocodazole-induced microtubule disassembly to cell contractility via RhoA. *Molecular Biology of the Cell*, *19*(5), 2147–2153. https://doi.org/10.1091/mbc.E07-12-1269

Denisin, A. K., Kim, H., Riedel-Kruse, I. H., & Pruitt, B. L. (2024). Field Guide to Traction Force Microscopy. *Cellular and Molecular Bioengineering*, *17*(2). https://doi.org/10.1007/S12195-024-00801-6

Devreotes, P., & Horwitz, A. R. (2015). Signaling networks that regulate cell migration. *Cold Spring Harbor Perspectives in Biology*, *7*(8). https://doi.org/10.1101/CSHPERSPECT.A005959

Douanne, T., & Griffiths, G. M. (2021). Cytoskeletal control of the secretory immune synapse. *Current Opinion in Cell Biology*, *71*, 87–94. https://doi.org/10.1016/J.CEB.2021.02.008

Dupré, L., Houmadi, R., Tang, C., & Rey-Barroso, J. (2015). T lymphocyte migration: An action movie starring the actin and associated actors. In *Frontiers in Immunology* (Vol. 6, Issue NOV). Frontiers Research Foundation. https://doi.org/10.3389/fimmu.2015.00586

Eirich, J., Burkhart, J. L., Ullrich, A., Rudolf, G. C., Vollmar, A., Zahler, S., Kazmaier, U., & Sieber, S. A. (2012). Pretubulysin derived probes as novel tools for monitoring the microtubule network via activity-based protein profiling and fluorescence microscopy. *Molecular BioSystems*, *8*(8), 2067–2075. https://doi.org/10.1039/c2mb25144b

Fletcher, D. A., & Mullins, R. D. (2010). Cell mechanics and the cytoskeleton. In *Nature* (Vol. 463, Issue 7280, pp. 485–492). https://doi.org/10.1038/nature08908

Fowell, D. J., & Kim, M. (2021). The spatio-temporal control of effector T cell migration. In *Nature Reviews Immunology* (Vol. 21, Issue 9, pp. 582–596). Nature Research. https://doi.org/10.1038/s41577-021-00507-0

Harrison, D. L., Fang, Y., & Huang, J. (2019). T-cell mechanobiology: Force sensation, potentiation, and translation. In *Frontiers in Physics* (Vol. 7, Issue APR). Frontiers Media SA. https://doi.org/10.3389/fphy.2019.00045

Herrmann, J., Elnakady, Y. A., Wiedmann, R. M., Ullrich, A., Rohde, M., Kazmaier, U., Vollmar, A. M., & Müller, R. (2012). Pretubulysin: From hypothetical biosynthetic intermediate to potential lead in tumor therapy. *PLoS ONE*, *7*(5). https://doi.org/10.1371/journal.pone.0037416

Hohmann, T., & Dehghani, F. (2019). The cytoskeleton—a complex interacting meshwork. *Cells*, *8*(4). https://doi.org/10.3390/cells8040362

Huby, R. D. J., Weiss, A., & Ley, S. C. (1998). Nocodazole inhibits signal transduction by the T cell antigen receptor. *The Journal of Biological Chemistry*, *273*(20), 12024–12031. https://doi.org/10.1074/JBC.273.20.12024

Hui, K. L., & Upadhyaya, A. (2017). Dynamic microtubules regulate cellular contractility during T-cell activation. *Proceedings of the National Academy of Sciences of the United States of America*, *114*(21), E4175–E4183. https://doi.org/10.1073/pnas.1614291114

Huse, M. (2017). Mechanical forces in the immune system. In *Nature Reviews Immunology* (Vol. 17, Issue 11, pp. 679–690). Nature Publishing Group. https://doi.org/10.1038/nri.2017.74

Jacobelli, J., Friedman, R. S., Conti, M. A., Lennon-Dumenil, A. M., Piel, M., Sorensen, C. M., Adelstein, R. S., & Krummel, M. F. (2010). Confinement-optimized three-dimensional T cell amoeboid motility is modulated via myosin IIA-regulated adhesions. *Nature Immunology*, *11*(10), 953–961. https://doi.org/10.1038/ni.1936

Janke, C., & Magiera, M. M. (2020). The tubulin code and its role in controlling microtubule properties and functions. In *Nature Reviews Molecular Cell Biology* (Vol. 21, Issue 6, pp. 307–326). Nature Research. https://doi.org/10.1038/s41580-020-0214-3

Joo, E., & Olson, M. F. (2021). Regulation and functions of the RhoA regulatory guanine nucleotide exchange factor GEF-H1. In *Small GTPases* (Vol. 12, Issues 5–6, pp. 358–371). Taylor and Francis Ltd. https://doi.org/10.1080/21541248.2020.1840889

Kopf, A., & Kiermaier, E. (2021). Dynamic Microtubule Arrays in Leukocytes and Their Role in Cell Migration and Immune Synapse Formation. In *Frontiers in Cell and Developmental Biology* (Vol. 9). Frontiers Media S.A. https://doi.org/10.3389/fcell.2021.635511

Kopf, A., Renkawitz, J., Hauschild, R., Girkontaite, I., Tedford, K., Merrin, J., Thorn-Seshold, O., Trauner, D., Häcker, H., Fischer, K. D., Kiermaier, E., & Sixt, M. (2020). Microtubules control cellular shape and coherence in amoeboid migrating cells. *Journal of Cell Biology*, *219*(6). https://doi.org/10.1083/JCB.201907154

Krendel, M., Zenke, F. T., & Bokoch, G. M. (2002). Nucleotide exchange factor GEF-H1 mediates cross-talk between microtubules and the actin cytoskeleton. *Nature Cell Biology*, *4*(4), 294–301. https://doi.org/10.1038/ncb773

Krummel, M. F., Bartumeus, F., & Gérard, A. (2016). T cell migration, search strategies and mechanisms. In *Nature Reviews Immunology* (Vol. 16, Issue 3, pp. 193–201). Nature Publishing Group. https://doi.org/10.1038/nri.2015.16

Krummel, M. F., Friedman, R. S., & Jacobelli, J. (2014). Modes and mechanisms of T cell motility: Roles for confinement and Myosin-IIA. In *Current Opinion in Cell Biology* (Vol. 30, Issue 1, pp. 9–16). Elsevier Ltd. https://doi.org/10.1016/j.ceb.2014.05.003

Kubisch, R., Von Gamm, M., Braig, S., Ullrich, A., Burkhart, J. L., Colling, L., Hermann, J., Scherer, O., Müller, R., Werz, O., Kazmaier, U., & Vollmar, A. M. (2014). Simplified pretubulysin derivatives and their biological effects on cancer cells. *Journal of Natural Products*, *77*(3), 536–542. https://doi.org/10.1021/np4008014

Lämmermann, T., Bader, B. L., Monkley, S. J., Worbs, T., Wedlich-Söldner, R., Hirsch, K., Keller, M., Förster, R., Critchley, D. R., Fässler, R., & Sixt, M. (2008). Rapid leukocyte migration by integrin-independent flowing and squeezing. *Nature*, *453*(7191), 51–55. https://doi.org/10.1038/nature06887

Lämmermann, T., & Germain, R. N. (2014). The multiple faces of leukocyte interstitial migration. In *Seminars in Immunopathology* (Vol. 36, Issue 2, pp. 227–251). Springer Verlag. https://doi.org/10.1007/s00281-014-0418-8

Lautenschlä Ger, F., Paschke, S., Schinkinger, S., Bruel, A., Beil, M., & Guck, J. (n.d.). *The regulatory role of cell mechanics for migration of differentiating myeloid cells*. Retrieved July 23, 2024, from www.pnas.org/cgi/content/full/

Legátová, A., Pelantová, M., Rösel, D., Brábek, J., & Škarková, A. (2023). The emerging role of microtubules in invasion plasticity. In *Frontiers in Oncology* (Vol. 13). Frontiers Media S.A. https://doi.org/10.3389/fonc.2023.1118171

Liao, G., Nagasaki, T., & Gundersen, G. G. (1995). Low concentrations of nocodazole interfere with fibroblast locomotion without significantly affecting microtubule level: implications for the role of dynamic microtubules in cell locomotion. *Journal of Cell Science*, *108 (Pt 11)*(11), 3473–3483. https://doi.org/10.1242/JCS.108.11.3473

Liu, Y. J., Le Berre, M., Lautenschlaeger, F., Maiuri, P., Callan-Jones, A., Heuzé, M., Takaki, T., Voituriez, R., & Piel, M. (2015). Confinement and low adhesion induce fast amoeboid migration of slow mesenchymal cells. *Cell*, *160*(4), 659–672. https://doi.org/10.1016/j.cell.2015.01.007

Maiuri, P., Rupprecht, J. F., Wieser, S., Ruprecht, V., Bénichou, O., Carpi, N., Coppey, M., De Beco, S., Gov, N., Heisenberg, C. P., Lage Crespo, C., Lautenschlaeger, F., Le Berre, M., Lennon-

Dumenil, A. M., Raab, M., Thiam, H. R., Piel, M., Sixt, M., & Voituriez, R. (2015). Actin flows mediate a universal coupling between cell speed and cell persistence. *Cell*, *161*(2), 374–386. https://doi.org/10.1016/j.cell.2015.01.056

Merino-Casallo, F., Gomez-Benito, M. J., Hervas-Raluy, S., & Garcia-Aznar, J. M. (2022). Unravelling cell migration: defining movement from the cell surface. In *Cell Adhesion and Migration* (Vol. 16, Issue 1, pp. 25–64). Taylor and Francis Ltd. https://doi.org/10.1080/19336918.2022.2055520

Moreau, H. D., Lemaître, F., Garrod, K. R., Garcia, Z., Lennon-Duménil, A. M., Bousso, P., & Cahalan, M. D. (2015). Signal strength regulates antigen-mediated T-cell deceleration by distinct mechanisms to promote local exploration or arrest. *Proceedings of the National Academy of Sciences of the United States of America*, *112*(39), 12151–12156. https://doi.org/10.1073/pnas.1506654112

Moreau, H. D., Piel, M., Voituriez, R., & Lennon-Duménil, A. M. (2018). Integrating Physical and Molecular Insights on Immune Cell Migration. In *Trends in Immunology* (Vol. 39, Issue 8, pp. 632–643). Elsevier Ltd. https://doi.org/10.1016/j.it.2018.04.007

Pawluchin, A., & Galic, M. (2022). Moving through a changing world: Single cell migration in 2D vs. 3D. In *Frontiers in Cell and Developmental Biology* (Vol. 10). Frontiers Media S.A. https://doi.org/10.3389/fcell.2022.1080995

Renkawitz, J., Schumann, K., Weber, M., Lämmermann, T., Pflicke, H., Piel, M., Polleux, J., Spatz, J. P., & Sixt, M. (2009). Adaptive force transmission in amoeboid cell migration. *Nature Cell Biology*, *11*(12), 1438–1443. https://doi.org/10.1038/ncb1992

Reversat, A., Gaertner, F., Merrin, J., Stopp, J., Tasciyan, S., Aguilera, J., de Vries, I., Hauschild, R., Hons, M., Piel, M., Callan-Jones, A., Voituriez, R., & Sixt, M. (2020). Cellular locomotion using environmental topography. *Nature*, *582*(7813), 582–585. https://doi.org/10.1038/s41586-020-2283-z

Sadjadi, Z., Zhao, R., Hoth, M., Qu, B., & Rieger, H. (2020). Migration of Cytotoxic T Lymphocytes in 3D Collagen Matrices. *Biophysical Journal*, *119*(11), 2141–2152. https://doi.org/10.1016/j.bpj.2020.10.020

Sanchez, E. E., Tello-Lafoz, M., Guo, A. J., de Jesus, M., Elbanna, Y. A., Winer, B. Y., Budhu, S., Chan, E., Rosiek, E., Kondo, T., DuSold, J., Taylor, N., Altan-Bonnet, G., Olson, M. F., & Huse, M. (2023). Apoptotic contraction drives target cell release by cytotoxic T cells. *Nature Immunology*, *24*(9), 1434–1442. https://doi.org/10.1038/s41590-023-01572-4

Schmidt, C. J., & Stehbens, S. J. (2024). Microtubule control of migration: Coordination in confinement. In *Current Opinion in Cell Biology* (Vol. 86). Elsevier Ltd. https://doi.org/10.1016/j.ceb.2023.102289

Seetharaman, S., Vianay, B., Roca, V., De Pascalis, C., Boëda, B., Dingli, F., Loew, D., Vassilopoulos, S., Théry, M., & Etienne-Manneville, S. (n.d.). *Microtubules tune mechanosensitive cell responses*. https://doi.org/10.1101/2020.07.22.205203

Shaebani, M. R., Jose, R., Santen, L., Stankevicins, L., & Lautenschläger, F. (2020). Persistence-Speed Coupling Enhances the Search Efficiency of Migrating Immune Cells. *Physical Review Letters*, *125*(26). https://doi.org/10.1103/PhysRevLett.125.268102

Shaebani, M. R., Piel, M., & Lautenschläger, F. (2022). Distinct speed and direction memories of migrating dendritic cells diversify their search strategies. *Biophysical Journal*, *121*(21), 4099–4108. https://doi.org/10.1016/j.bpj.2022.09.033

Simula, L., Ollivier, E., Icard, P., & Donnadieu, E. (2022). Immune Checkpoint Proteins, Metabolism and Adhesion Molecules: Overlooked Determinants of CAR T-Cell Migration? In *Cells* (Vol. 11, Issue 11). MDPI. https://doi.org/10.3390/cells11111854

Stankevicins, L., Ecker, N., Terriac, E., Maiuri, P., Schoppmeyer, R., Vargas, P., Lennon-Duménil, A.-M., Piel, M., Qu, B., Hoth, M., Kruse, K., & Lautenschläger, F. (n.d.). *Deterministic actin waves as generators of cell polarization cues*. https://doi.org/10.1073/pnas.1907845117/-/DCSupplemental

Steinmetz, M. O., & Prota, A. E. (2018a). Microtubule-Targeting Agents: Strategies To Hijack the Cytoskeleton. In *Trends in Cell Biology* (Vol. 28, Issue 10, pp. 776–792). Elsevier Ltd. https://doi.org/10.1016/j.tcb.2018.05.001

Steinmetz, M. O., & Prota, A. E. (2018b). *Microtubule-Targeting Agents: Strategies To Hijack the Cytoskeleton*. https://doi.org/10.1016/j.tcb.2018.05.001

Tabdanov, E. D., Rodríguez-Merced, N. J., Cartagena-Rivera, A. X., Puram, V. V., Callaway, M. K., Ensminger, E. A., Pomeroy, E. J., Yamamoto, K., Lahr, W. S., Webber, B. R., Moriarity, B. S., Zhovmer, A. S., & Provenzano, P. P. (2021a). Engineering T cells to enhance 3D migration through structurally and mechanically complex tumor microenvironments. *Nature Communications*, *12*(1). https://doi.org/10.1038/s41467-021-22985-5

Ueda, H., Zhou, J., Xie, J., & Davis, M. M. (2015). Distinct Roles of Cytoskeletal Components in Immunological Synapse Formation and Directed Secretion. *Journal of Immunology (Baltimore, Md. : 1950)*, *195*(9), 4117–4125. https://doi.org/10.4049/JIMMUNOL.1402175

Vasquez, R. J., Howell, B., Yvon, A.-M. C., Wadsworth, P., & Cassimeris, L. (1997). Nanornolar Concentrations of Nocodazole Alter Microtubule Dynamic Instability In Vivo and In Vitro. In *Molecular Biology of the Cell* (Vol. 8).

Vennin, C., Cattaneo, C. M., Bosch, L., Vegna, S., Ma, X., Damstra, H. G. J., Martinovic, M., Tsouri, E., Ilic, M., Azarang, L., van Weering, J. R. T., Pulver, E., Zeeman, A. L., Schelfhorst, T., Lohuis, J. O., Rios, A. C., Dekkers, J. F., Akkari, L., Menezes, R., … van Rheenen, J. (2023). Taxanes trigger cancer cell killing in vivo by inducing non-canonical T cell cytotoxicity. *Cancer Cell*, *41*(6), 1170-1185.e12. https://doi.org/10.1016/j.ccell.2023.05.009

Vesperini, D., Montalvo, G., Qu, B., & Lautenschläger, F. (2021). Characterization of immune cell migration using microfabrication. In *Biophysical Reviews* (Vol. 13, Issue 2, pp. 185–202). Springer Science and Business Media Deutschland GmbH. https://doi.org/10.1007/s12551-021-00787-9

Weier, A. K., Homrich, M., Ebbinghaus, S., Juda, P., Miková, E., Hauschild, R., Zhang, L., Quast, T., Mass, E., Schlitzer, A., Kolanus, W., Burgdorf, S., Gruß, O. J., Hons, M., Wieser, S., & Kiermaier, E. (2022). Multiple centrosomes enhance migration and immune cell effector functions of mature dendritic cells. *The Journal of Cell Biology*, *221*(12). https://doi.org/10.1083/JCB.202107134

Zhao, R., Zhou, X., Khan, E., Yang, W., Schwarz, E. C., Del Campo Bécares, A., Hoth, M., & Qu, B. (n.d.). *Disruption of microtubule network rescues impaired killing of CD8 + T cells in high density extracellular matrix*.

Zhou, X., Zhao, R., Schwarz, K., Mangeat, M., Schwarz, E. C., Hamed, M., Bogeski, I., Helms, V., Rieger, H., & Qu, B. (2017). Bystander cells enhance NK cytotoxic efficiency by reducing search time. *Scientific Reports*, *7*. https://doi.org/10.1038/srep44357

Zhovmer, A. S., Manning, A., Smith, C., Nguyen, A., Prince, O., Sáez, P. J., Ma, X., Tsygankov, D., Cartagena-Rivera, A. X., Singh, N. A., Singh, R. K., & Tabdanov, E. D. (2024). I M M U N O L O G Y Septins provide microenvironment sensing and cortical actomyosin partitioning in motile amoeboid T lymphocytes. In *Sci. Adv* (Vol. 10). https://www.science.org

7. Supplemental Information

In addition to the results shown in this thesis, during my PhD time I contributed to the following scientific works:

1. C. Richter; L. Latta; D. Harig; P. Carius; J. D. Stucki; N. Hobi; A. Hugi; P. Schumacher; T. Krebs; A. Gamrekeli; F. Stöckle; K. Urbschat; **G. Montalvo**; F. Lautenschläger; B. Loretz; A. Hidalgo; N. Schneider-Daum and C. M. Lehr. *A stretchable human lung-on-chip model of alveolar inflammation for evaluating anti-inflammatory drug response.* Manuscript under revision in Bioengineering & Translational Medicine.

I performed microscopy experiments to evaluate the mobility of macrophages in co-culture with an alveolar epithelial cell line (Arlo). I used an epi-fluorescent microscope to image fluorescently labeled macrophages and analyze their trajectories when treated with different compounds. Specifically, I contributed to the results shown in Supplementary Figure 5.

2. D. A. D. Flormann, L. Kainka, **G. Montalvo**, C. Anton, J. Rheinlaender, D. Thalla, D. Vesperini, M. O. Pohland, K. H. Kaub, M. Schu, F. Pezzano, V. Ruprecht, E. Terriac, R. J. Hawkinsg, and F. Lautenschläger. *The structure and mechanics of the cell cortex depend on the location and adhesion state.* PNAS, 2024.

I performed research, contributed new reagents/analytic tools, and analyzed data. Particularly, I contributed to the results shown in Supplementary Figure 1: by using confocal microscopy I quantified filamentous actin on RPE-1 cells adhered and in suspension. I prepared the samples, performed the microscopy experiment, analyzed the data and created the figure. I also contributed to the results shown in Supplementary Figure 10: by using confocal microscopy I analyzed the distribution of Myosin II in different compartments of RPE-1 cells. I prepared the samples, performed the microscopy experiment, analyzed the data and contributed to the figure.

3. A. K. Yanamandra, J. Zhang, **G. Montalvo**, X. Zhou, D. Biedenweg, R. Zhao, S. Sharma, M. Hoth, F. Lautenschläger, O. Otto, A. Del Campo and B. Qu. *PIEZO1-mediated mechanosensing governs NK-cell killing efficiency and infiltration in three-dimensional matrices.* European Journal of Immunology, 2024

I measured the stiffness of K562-pCasper cell line under different treatments, using real time deformability cytometry (RT-CD). Particularly, I contributed to the results shown in Figure 2A and 2C, where I performed the measurements with the RT-DC machine. I also contributed to the results shown in Supplementary Figure 2 and Supplementary Figure 4A, were I prepared the samples, preformed the RTDC measurements and analyzed the data.

4. D. Vesperini, **G. Montalvo**, B. Qu and and F. Lautenschläger. *Characterization of immune cell migration using microfabrication.* Biophysical Reviews, 2021.

I equally contributed with D. Vesperini to writing this Review paper. I designed and created Figures 1 and 2.

A stretchable human lung-on-chip model of alveolar inflammation for evaluating anti-inflammatory drug response

Clémentine Richter[ab], Lorenz Latta[a], Daria Harig[ab], Patrick Carius[ab], Janick D. Stucki[cd], Nina Hobi[cd], Andreas Hugi[c], Tobias Krebs[e], Alexander Gamrekeli[f], Felix Stöckle[f], Ralf Seipelt[g], Klaus Urbschat[g], Galia Montalvo[hij], Franziska Lautenschläger[hj], Brigitta Loretz[a], Alberto Hidalgo[a], Nicole Schneider-Daum[a], Claus-Michael Lehr[ab]

a) Helmholtz Institute for Pharmaceutical Research Saarland, 66123 Saarbrücken, Germany

b) Department of Pharmacy, Saarland University, 66123 Saarbrücken, Germany

c) AlveoliX AG, Swiss Organs-on-Chip Innovation, 3010 Bern, Switzerland

d) ARTORG Center for Biomedical Engineering Research, Organs-on-Chip Technologies, University of Bern, Bern, Switzerland

e) Vitrocell® Systems GmbH, 79183 Waldkirch, Germany

f) Center for Thorax Medicine, Clinic Saarbrücken, 66119 Saarbrücken, Germany

g) Section of Thoracic Surgery of the Saar Lung Center, SHG Clinics, 66333 Völklingen, Germany

h) Department of Experimental Physics, Saarland University, 66123 Saarbrücken, Germany

i) Center for Biophysics, Saarland University, 66123 Saarbrücken, Germany

j) Biophysics, Center for Integrative Physiology and Molecular Medicine (CIPMM), School of Medicine, Saarland University, 66421 Homburg, Germany

Co-author details:

Contact information: Provide the full address information for the corresponding author (NSD).

Author Guidelines

https://aiche.onlinelibrary.wiley.com/hub/journal/23806761/homepage/forauthors.html

Figures

Graphical Abstract. The journal's table of abstracts will be presented in graphical form. The image supplied should fit within the dimensions of 50mm x 60mm and be fully legible at this size.

Abstract

preferred length for abstracts is 150 words or fewer and no more than 250 words

This study describes a complex human *in vitro* model for evaluating anti-inflammatory drug response in the alveoli that may contribute to the reduction of animal testing in the pre-clinical stage of drug development of potential new anti-inflammatory compounds.

The model is based on the human alveolar epithelial cell line Arlo co-cultured with macrophages differentiated from the THP-1 cell line, creating a physiological microenvironment. To mimic the three-dimensional architecture and dynamic expansion and relaxation of the air-blood-barrier, they are grown on a stretchable micro-physiological lung-on-chip.

Three different protocols have been developed that display the balance between distinct disease marker elevation after inflammation and reduction of these markers after treatment with the anti-inflammatory model glucocorticoid BUD (budesonide): (1) an inflammation caused by bacterial LPS (lipopolysaccharides) to simulate an LPS-induced acute lung injury, which can be measured best with cytokine IL-6 release; (2) an inflammation caused by LPS at ALI (air-liquid interface) to investigate aerosolized anti-inflammatory treatment, which can be measured with chemokine IL-8 release; and (3) an inflammation with a combination of human inflammatory cytokines TNFα and IFNγ to simulate a critical cytokine storm, where the eventual weakening or protection of the epithelial barrier can be measured.

In all cases, the presence of macrophages, which are the main immune system component in the deep lung, appeared to be crucial to mediating inflammatory changes of the alveolar epithelium. The dynamic stretching to emulate breathing-like mechanics significantly modulated the response to the TNFα/INFγ-induced inflammation, whereas inflammatory response upon LPS was unaffected by the stretch.

Translational Impact Statement

Provide a short (85-word maximum) descriptive sentence of your work that summarizes the translational and clinical significance of the work, aimed at a more general readership.

Organ-on-chips form a predictive link between late pre-clinical research on animal models and clinical investigations on humans. The human *in vitro* model of pulmonary inflammation presented

in this study is intended to predict the anti-inflammatory effects of new potential drug candidates. To demonstrate this, human alveolar epithelial and immune cells were co-cultivated in a dynamic lung-on-chip, inflamed, and treated with the known glucocorticoid Budesonide as proof of concept.

Keywords

Provide up to 7 words or short phrases that best describe your work.

lung-on-chip, immuno-competent, microfluidic, aerosolization, 3R, acute lung injury, cytokine storm

Graphical Abstract

Provide a graphical abstract that summarizes your work. Your graphical abstract image should fit within the dimensions of 50mm x 60mm and be fully legible at this size.

Introduction

Inhaled anti-inflammatory drugs have one of the highest attrition rates in clinical testing compared to other diseases. Most respiratory drugs fail in late clinical stages due to efficacy issues, highlighting the need for reliable proof of concept models for drug response to identify these failing candidates earlier and reduce future costs [1, 2]. By using lung-on-chips, which simulate the pulmonary microenvironment more accurately than traditional static and 2-dimensional *in vitro* models, the predictability of human drug response is expected to be more accurate [3, 4]. To date, various complex microfluidic models have been used to investigate treatment options and efficacy against airway infection [5, 6], lung cancer [7], lung edema [8], and lung thrombosis [9], some including different cell types, medium flow, lateral stretch, or an ALI. In perspective, such complex *in vitro* models may provide reliable alternatives to animal models and facilitate the translation from pre-clinical to clinical investigation [10–15].

This study aims to develop an *in vitro* model of alveolar inflammation by incorporating multiple cell types and the option to include breathing-like mechanical stretch. Additionally, compared to other microfluidic setups, the one used here is the only one with the possibility to apply aerosols to the ALI. Contrary to models mimicking the healthy state as used in toxicology/ safety studies, models to evaluate drug response must mimic a certain state of disease and be able to demonstrate restoration of the healthy state.

The model presented here is intended for the evaluation of anti-inflammatory drug response for the treatment of alveolar inflammation. The structural and dynamic micro-environment of the alveoli was recreated by the microfluidic chip AX12: Cells are grown on a flexible, porous membrane, which mimics the 3-dimensional structure of the air-blood-barrier with the unique possibility of combining lateral stretch with the deposition of aerosols directly on the apical air-interface of the cells [3, 16, 17]. The flexibility of the membrane allows for the inclusion of dynamic lateral stretch which emulates the expansion and relaxation of the breathing alveolus [8, 18] and may alter the inflammatory or barrier response [19]. It has been reported that mechanical stretch can positively influence epithelial cell proliferation [2], differentiation [20], and migration [21] and that it can increase the resistance against viral infections *in vitro* [22]. To model the pulmonary air-blood barrier, we used the human alveolar epithelial cell line Arlo [23], either alone or in co-culture with monocyte-derived macrophages as surrogates for alveolar macrophages [24, 25]. Similar to primary hAEpC (human alveolar epithelial cell), the Arlo cell line displays a very low paracellular permeability, mediated by tight intercellular junctions [26, 27]. This particularly qualifies this cell line to investigate mechanisms of barrier disruption and restoration. THP-1 cells were used as

surrogates for alveolar macrophages, since have long been used as a model for M1 macrophages [28, 29], especially in the context of acute alveolar inflammation [25, 30]. It was hypothesized that the implementation of mechanical stretch, aerosol exposure, and immune cells into the model leads to a more realistic representation of alveolar (patho)physiology [31].

LPS (bacterial lipopolysaccharides) was chosen as an inflammatory stimulus because it is widely used in mice [32–35] and *in vitro* [25, 36, 37] to model acute lung injury. Alternatively, a combination of high doses of the human inflammatory cytokines TNFα and IFNγ was used to simulate a critical cytokine storm leading to epithelial barrier disruption [38], like what would be expected e.g. in severe progress of COVID-19 infection [39–41].

Measuring inflammatory cytokines is an established read-out in inflammatory models, whereas changes in the alveolar air-blood-barrier function may be monitored by measuring TEER (transepithelial electrical resistance). As a proof of concept to demonstrate the restoration of the "healthy" state from such inflammatory changes, the anti-inflammatory glucocorticoid BUD (budesonide) was used [42].

As LPS-induced and TNFα/IFNγ-induced inflammations rely on different mechanisms, different protocols were needed to demonstrate the associated pathophysiological changes and their restoration by BUD. The LPS-induced cytokine release during the modeled acute lung injury was only significant in the presence of macrophages. Changes in epithelial barrier function and the restoration by BUD, however, could only be detected after TNFα/INFγ-induced cytokine storm-mediated inflammation and were most pronounced in the presence of macrophages in combination with breathing-like mechanical stretch.

Materials and Methods

Cell culture methods

Arlo cell line

The cell line "Arlo" was cultured according to a recent publication [23]. For experiments on AX12, Arlo was seeded with a density of 4×10^5 cells/cm².

THP-1 cell line

The THP-1 cell line [28] (No. ACC-16, DMSZ) was cultivated and differentiated according to a previously published protocol with minor changes [30]. 3×10^6 THP-1 cells were differentiated to macrophages (dTHP-1) with 7.5 ng/mL of PMA (Phorbol 12-myristate 13-acetate, Sigma-Aldrich PA585) in 10 mL RPMI medium supplemented with 10% FCS for two to three days. dTHP-1 cells

were washed twice with PBS (Sigma-Aldrich D8537), incubated with 3 mL Accutase (Sigma-Aldrich A6964) for 30 min at 37 °C, and gently detached with a cell scraper (Greiner bio-one 541070).

Co-cultures of Arlo and THP-1 cell lines

Co-cultures of alveolar epithelial cells and alveolar macrophage surrogates were set up according to a previous publication [30]. Upon reaching a tight epithelial barrier with Arlo cells, dTHP-1 cells were seeded on top of the epithelial barrier in a density of 2.4×10^5 cells/cm² [43]. After macrophage cell seeding, co-cultures were left to settle and accustomed to their new surrounding for 24h before the start of inflammation experiments (Fig. 1C).

Human alveolar epithelial cells (hAEpC)

Primary hAEpC were isolated according to a previously published protocol [26]. The human tissue was provided by the Clinic Saarbrücken and the SHG Clinics Völklingen. They were seeded and cultivated on chip with 3.5×10^5 cells/cm².

^{AX}Lung-On-Chip System

AX12

The ^{AX}Lung-On-Chip system (AlveoliX AG) has been previously described in detail (Fig. 1B) [44, 45]. In brief, the ^{AX}Lung-On-Chip System consists of the AX12 containing a porous ultrathin membrane. The AX12 is connected to the electro-pneumatic control units (^{AX}Exchanger and ^{AX}Breather) through the ^{AX}Dock. The ^{AX}Exchanger is used for medium exchange, sampling of basolateral samples, and TEER measurements. The ^{AX}Breather is applying cyclic 3-dimensional stretch.

ALI (air-liquid interface) and nebulizing

Arlo cultures were switched to ALI after the formation of a tight barrier approx. on day 12 after seeding. Nebulizing of LPS and BUD was performed using the Cloud α AX12 [18, 46] with an Aeroneb® Lab Nebulizer [47] (standard VMAD, 4.0–6.0 µm droplet diameter) connected to an Aerogen® USB controller according to supplier instructions.

Inflammation and treatment protocols

Inflammation with LPS

LPS from E. coli O26:B6 (Sigma-Aldrich L2762-5MG) stock solution was prepared with 1 µg/mL in PBS, aliquoted, and frozen at -20°C. Mono- and co-cultured were inflamed with assay concentrations of 0.05 to 5.0 µg/mL LPS. In the case of ALI cultures on chip, LPS was nebulized using the Cloud α AX12.

Inflammation with TNFα/IFNγ

TNFα (Sigma-Aldrich H8916) stock solution was prepared with 1.0 μg/mL in PBS, aliquoted, and frozen at -20 °C. IFNγ (Miltenyi Biotec 130-096-48) stock solution was prepared with 100 μg/mL in PBS, aliquoted, and frozen at -20 °C. Inflammation with a combination of TNFα/ IFNγ [38] was performed with assay concentrations of 0.1 μg/mL each.

Treatment with BUD

BUD (Sigma-Aldrich, Pharmaceutical Secondary Standard PHR1178) stock was suspended in 100% EtOH (ethanol) with 3 mg/mL. Cultures were treated with an assay concentration of 1 μM BUD apically. In the case of ALI cultures on chip, BUD was nebulized with the Cloud α AX12.

Read-outs

Cytokine quantification

Released cytokines were measured via bead-based FACS assay using the Human Soluble Protein Flex Sets for IL-6 (558276), TNFα (560112), and IL-8 (558277) with the Human Soluble Protein Master Buffer Kit (558264, all BD Biosciences). All samples were taken 24h after LPS inflammation. 60 μL apical medium was centrifuged for 4 min at 300xg and 55 μL supernatant was immediately frozen at -80°C. In the case of ALI cultures, LCC (liquid-covered conditions) were re-established 30 min before the end of the 24h and sampled the same way as LCC cultures. All samples were thawed only once directly before performing the assay.

Beads were sorted and analyzed with a BD LSRFortessaTM FACS (BD Biosciences). Data was analyzed with FCAP Array Version 3.0.1 for Windows (BD Biosciences).

Barrier measurement methods

TEER on AX12 was measured with EVOM2 with adapted range (World Precision Instruments 300523) and electrodes for 96-well plates (World Precision Instruments STX100M). Raw resistance data was corrected for cell growth area with the following formula:

$$TEER\left[\Omega cm^2\right] = (raw\left[\Omega\right] - blank\left[\Omega\right]) \times surface\ area\left[cm^2\right]$$

The value for the blank is 450 Ω, the porous surface area of the AX12 is 0.071 cm^2

The p$_{app}$ (apparent permeability) of the small molecule Fluorescein sodium salt (FluNa, Sigma-Aldrich F6377) was evaluated according to a previous protocol with minor changes [48]: The medium was exchanged for HBSS (Gibco Thermo Fisher Scientific Inc. 14025-050) containing 10 μg/mL FluNa apically, and if needed, 8 mM EDTA (ethylenediamine tetraacetic acid disodium salt dihydrate, Carl ROTH® 8043.1). Basal HBSS was sampled every hour, and the missing volume was replaced with fresh HBSS for 7h. Samples were analyzed with Tecan Infinite 200Pro

Photometer (ex = 485 nm; em = 530 nm), and p_{app} was calculated according to the following equation:

$$p_{app} = \frac{\frac{dQ}{dt}\left[\frac{\mu g}{s}\right]}{surface\ area\ [cm^2]} \times c_{start}\left[\frac{\mu g}{mL}\right]$$

Cell stress and cell death measurement

Cell stress and death on chip after the start of the application of stretch were measured with the RealTime-Glo™ Annexin V Apoptosis and Necrosis Assay (Promega JA1011) with adapted smaller volumes to match the AX12. 3 µL of each component of the assay kit was mixed with 900 µL medium. 30 µL of this mixture was added to the apical compartment, for a total apical volume of 100 µL. Dead control cells were challenged with 10% DMSO (dimethyl sulfoxide).

Luminescence (1000 ms) and fluorescence (ex = 485 nm, em = 525 nm) were measured with a Tecan Spark Cyto 600 cell imager and plate reader. Blanks were measured and subtracted from all values.

Confocal microscopy

Macrophages were stained before seeding with Far Red Cell Tracer (Invitrogen C34564) according to manufacturer specifications. Co-cultures with stained macrophages were not used for any other experiments than confocal microscopy.

Fixation and staining of all cultures were performed according to a previous publication with modifications to adapt it to macrophage-epithelial co-cultures [49]: cultures were washed very gently three times with PBS, fixated with 4% PFA (paraformaldehyde, Sigma-Aldrich 30525-89-4) for 15 min at RT (room temperature), washed again very gently three times with PBS and kept under PBS at 4 °C until staining.

Before staining, cultures were permeabilized and blocked with permeabilization buffer (0,05% Saponin (Sigma-Aldrich 43036) and 1% BSA (Sigma-Aldrich A9647) in PBS) for 1h. Occludin was detected with primary antibody (Invitrogen 33-1500, dil. 1:400) overnight at 4 °C and secondary antibody (Invitrogen A21050, dil. 1:2000) for 1h at RT. Actin was stained with Phalloidin with Alexa 488 (Invitrogen A12379, dil. 1:1000) for 30 min at RT. Cell nuclei were stained with DAPI (4', 6-Diamidino-2-phenylindole dihydrochloride, Sigma-Aldrich 32670, dil. 1:1000) for 30 min at RT. Cells were washed three times for 10 min with PBS while gently shaking between each staining. After staining, AX12 were disassembled according to manufacturer specification and mounted with DAKO Fluorescence Mounting Medium (Agilent 85 S302380-2) on coverslips.

Confocal images were taken with a Spectral Confocal Microscope (Leica Dmi8 Confocal Laser Scanning Microscope) with a 25x water immersion objective. Images were analyzed with Imaris Version 9.7.2 for Windows (Oxford Instruments).

RNA Sequencing and Analysis

RNA was harvested by incubation in RLT Buffer (Qiagen 79216) from the basal and apical side for 5 min. Two wells were pooled for one sample, and a total of 6 samples out of three independent passages resp. tissues were collected. Isolation of RNA was performed with the RNeasy Micro Kit (Qiagen 74004) and the RNase-Free DNase Set (Qiagen 79254) according to the manufacturer's instructions. Samples showing guanidin salt contaminations were additionally cleaned with the Monarch® RNA Cleanup Kit (New England Biolabs T2030L) to achieve the minimum requirements for sequencing (500 ng total RNA, RQN > 8).

Sequencing was performed by strand-specific mRNA analysis. mRNA library was prepared with the NEB Next Ultra II Directional RNA Library Prep Kit (New England Biolabs E7765,). Sequencing was performed on NovaSeq 6000, PE50 (2x 50bp) with 30 mio NGS reads per sample and 800 mio cluster flow cell output.

Fastq data was analyzed with a preset pipeline using RNAdetector [50] running in a docker container. Star alignment with feature counts for read summarizing was chosen as the alignment algorithm [51]. The gene counts table was normalized for inherent systematic or experimental biases using the Bioconductor package edgeR. A complete analysis summary with a run log can be found in the supplementary data (Suppl. Fig. 8)

Statistics

Numerical data are shown as mean ± standard deviation. Graphs were created with GraphPad Prism Version 9.5.0 for Windows. To compare the statistical significance of the results, one-way ANOVA with subsequent Tukey's multiple comparisons was used. The statistical thresholds for p values were set as follows: 0.12 (ns), 0.033 (*), 0.002 (**), <0.001 (***), according to NEJM (The New England Journal of Medicine) policies [52].

All experiments were performed at least three independent times, with the exact number of replicates specified in the corresponding figure legends.

Results

LPS-induced acute lung injury on chip

Setup of inflammation and treatment parameters

The concentration of LPS and treatment time point of BUD were first investigated in macrophage mono-cultures to set up the inflammation and treatment protocols and to investigate the *in vitro* relevance of the immune cell component of the deep lung to LPS [53].

The optimum concentration of LPS was determined by inflaming dTHP-1 mono-cultures in 96-well plates with doses of LPS ranging from 0.05 µg/mL to 5.0 µg/mL (Fig. 2A). The release of cytokines IL-6 and TNFα was measured in the supernatant 24h after inflammation with LPS and was dose-dependent. For all following experiments, a concentration of 0.5 µg/mL LPS was used.

The optimal treatment time point *in vitro* was investigated by pre-treating the inflamed dTHP-1 mono-cultures 2h before inflammation with 1 µM BUD, or post-treat them 2 or 6h after inflammation (Fig. 2B). While prophylactic pre-treatment yields the best results in cytokine release prevention, a therapeutic post-treatment was considered more relevant and realistic. All following experiments were performed with 1 µM BUD 2h after inflammation.

Inflammation with LPS and treatment with BUD in liquid-covered conditions (LCC)

The inflammation with LPS and treatment with BUD were transferred to chip and epithelial mono-cultures compared to macrophage-epithelial co-cultures by keeping the previously established parameters (0.5 µg/mL LPS and 1 µM BUD 2h after LPS). IL-6 and TNFα release into the apical supernatant was measured 24h after inflammation with LPS. For comparability, all doses, number of macrophages, and volumes were kept the same as in the macrophage mono-cultures.

In epithelial mono-cultures on chip, cytokine IL-6 and TNFα release were in most cases below the lower limit of quantification (LLOQ) of the assay and consequently, no effect of BUD could be observed either (Fig. 2C). The presence of macrophages in macrophage-epithelial co-cultures increased the cytokine release to measurable levels, pointing to the crucial role of macrophages to model LPS-induced acute lung injury on chip. In both static and stretch conditions, an increase in cytokine release after LPS inflammation and decreased release after treatment with BUD could be measured (Fig. 2C).

Inflammation with LPS and treatment with BUD at the air-liquid interface (ALI)

To increase the physiological relevance of the LPS-induced acute lung injury protocol, the macrophage-epithelial co-cultures were adapted to ALI conditions, allowing exposure to LPS and BUD as aerosols using the Cloud α AX12. The nebulizer is placed on top of the nebulization

chamber. Aerosol deposition can be monitored in real-time using the QCM (quartz crystal microbalance) (Fig. 3A). The final deposition is read after opening the chamber and equilibration of the QCM value to ambient humidity (Fig. 3B). Separate experiments with FluNa to check the deposition efficiency and reliability of the QCM showed a good correlation between the QCM reading, the manually recovered FluNa from the plate, and the manually recovered FluNa from QCM itself (Fig. 3C). This allows for the calculation and use of comparable doses of LPS and BUD as in the previous experiments in LCC by estimating that 30% of the nebulized dose is deposited on the cells [15].

Both LPS and BUD can be aerosolized in this protocol and apical chemokine IL-8 release can be measured after 24h. Comparable to the results in LCC, co-cultures of Arlo and dTHP-1 at ALI can be inflamed with nebulized LPS (increased chemokine release) and subsequently treated with BUD (decreased chemokine release), with no difference between static and stretch conditions (Fig. 3D).

Characterization of epithelial cells on chip

Effect of stretch on epithelial barrier formation

Cyclic stretch was applied as soon as the epithelial cells grew confluent on day 2 for the whole duration of the experiment, leading to generally lower TEER values in stretching conditions (Fig. 4A). While weaker after stretching, the barrier was still tight (> 500 Ω/cm²) and stable over two weeks of culture in both conditions. The lower TEER values of Arlo in stretch conditions after 6-7 days correspond to the TEER values shown by hAEpC in both static and stretch conditions (Fig. 4B).

High TEER values of Arlo could be correlated to low permeability of small molecule FluNa, while the p_{app} of FluNa was increased with lower TEER (Fig. 4C). Adding EDTA as chelator of divalent cations led to lower TEER and higher p_{app}, confirming the presence of functional tight junctions (Fig. 4D). Less organized and more delocalized cytoskeleton and tight junction proteins explain the lower TEER values in stretching conditions (Fig. 4E).

Short-term stretch effect

To investigate potential short-term negative effects caused by the onset of stretching dynamics, cell stress, and cell death were measured and compared to cells additionally challenged by the addition of 10% DMSO (Fig. 5A and 5B). Without the addition of DMSO, no cell stress could be measured in either static or stretch conditions (Fig. 5A). Like cell stress, no increased cell death upon stretching could be observed (Fig. 5B).

Long-term stretch effect

RNA of Arlo and hAEpC was collected after 6-7 days of culture (corresponding to 4-5 days of ongoing cyclic stretch) and sequenced. Direct comparison of Arlo in static and stretch conditions

showed no significant differences in the transcriptome (Fig. 5C), as shown by false discovery rate (FDR) > 1.0 (Suppl Fig. 8). The same was found also for hAEpC under static and stretch conditions (Fig. 5D).

When comparing Arlo and hAEpC in static conditions (Fig. 5E) or in stretch conditions (Fig. 5F), the individual expression profiles of the respective cell types were well preserved in either condition.

TNFα/IFNγ-induced cytokine storm on chip

In epithelial mono-cultures (Fig. 6A), a weak disruption of the barrier could only be measured after 48h inflammation in stretch conditions. Similarly, the co-culture with macrophages in static conditions only showed a weak TNFα/IFNγ effect after 48h (Fig. 6B). However, the combined presence of macrophages and stretch conditions led to a further weakened barrier after 24 and 48h of inflammation, causing a significant drop in TEER. Treatment with BUD 2h after inflammation restored the barrier after 48h in the co-culture when stretch was applied (Fig. 6B).

Discussion

LPS-induced acute lung injury on chip

Setup of inflammation and treatment parameters

Setting up a new *in vitro* model requires the characterization of a complex network of parameters, all influencing each other. In this first step, the inflammatory stimulus (LPS), the anti-inflammatory treatment (BUD), the cell type (dTHP-1), and the read-outs (IL-6 and TNFα) were investigated and defined. The optimum concentration of LPS and treatment timepoint of BUD was found to be 0.5 µg/mL LPS (Fig. 2A) and 1 µM BUD 2h after inflammation (Fig. 2B) for this protocol. Based on the seeding density of macrophages, 0.5 µg/mL LPS corresponds to 1.75 pg/macrophage, which is comparable to LPS doses in human LPS-induced inflammation setups *in vivo*, which are also in the single-digit pg-range per alveolar macrophage [54–59].

For this study, the THP-1 cell line was differentiated to a macrophage-like state using 7.5 ng/mL PMA (25 fg/cell) for 2-3 days and left to recover after detaching and seeding [60, 61]. This protocol ensures that the positive control would be differentiated to macrophages (as shown by morphologic changes and attachment to the plastic surface, suppl. Fig. 1), but show no cytokine release in the absence of additional inflammatory stimuli (Fig. 2) [53, 62, 63], and are fully adapted to the new environment with epithelial cells and mixed medium (Fig. 1C) [64].

The release of cytokines IL-6 and TNFα was measured in the supernatant 24h after inflammation with LPS, similar to time points *in vivo* in mouse and human LPS-induced lung injury [34, 59]. The cytokine release in dTHP-1 is dose-dependent, and for all following experiments, a concentration

of 0.5 µg/mL LPS (1,75 pg/cell) was used to inflame the cultures (Fig. 2A). Using a higher concentration of LPS did not seem to further enhance cytokine release and increased the variability of the results (Fig. 2A).

BUD is applied with maximum doses in humans of 800 µg twice daily [65, 66]. Although the lung fraction is highly dependent on the patient's inhalation technique, approx. 20% of inhaled BUD should reach the lung without the use of a spacer [67]. That would correspond to approx. 50 fg/macrophage or 0.3 ng/cm² *in vivo*. The BUD dose per cm² *in vitro* on chip has been chosen to be approx. 1000 times higher (350 ng/cm²) than the maximum daily *in vivo* dose to ensure that a strong drug effect should be measurable *in vitro*. This corresponds to an assay concentration of 1 µM. For future investigations, it would be interesting to see the dose-response curves of different doses of anti-inflammatory drugs on these presented models here.

Inflammation with LPS and treatment with BUD in liquid-covered conditions (LCC)

The presence of macrophages as the main immune cell component in the deep lung was crucial for measuring inflammatory signals by cytokine release after LPS inflammation in the *in vitro* alveolus model on chip (Fig. 2C). It is reported that the human lung epithelium does not express toll-like receptor 4 (TLR4) and its associated proteins CD14 and MD-2 for LPS recognition [68, 69]. This is reflected by the poor response to LPS in epithelial mono-cultures in this study, in most cases with cytokine releases below the LLOQ (Fig. 2C).

There is a difference in released cytokines from macrophages in mono- or co-cultures (Fig. 2B vs. 2C). According to the literature, this may be due to macrophage-epithelial cross-talk to maintain homeostasis [70], or the presence of a mixed cell culture medium in the co-cultures, which may bind LPS differently [71]. The most critical factor however appeared to be the presence or absence of hydrocortisone in the co-culture medium (see Suppl. Fig. 2), which is chemically identical to the human steroid hormone cortisol. Hydrocortisone has long been identified as essential for the development of a tight epithelial barrier [38, 72, 73] and was therefore included in the mixed medium for epithelial cells and co-cultures in physiological concentration (0.5 µg/mL measured via UV spectrometry in the SAGM Single Quots, data not shown).

The application of stretching to replicate the lateral stretch caused by breathing motion within the alveoli was achieved by using the ᴬˣLung-On-Chip System (Fig. 1B) [45]. In this protocol of LPS-induced acute lung injury, stretching does not seem to impact the severity of the inflammation or the effect of the BUD treatment in the macrophage-epithelial co-cultures (Fig. 2C). This leads to the conclusion that the LPS-induced inflammation is mainly macrophage-driven and that the stretching does not affect the macrophages or macrophage-epithelial cellular cross-talk.

Inflammation with LPS and treatment with BUD at the air-liquid interface (ALI)

The Cloud α AX12 (Fig. 3A) is specifically adapted to the AX12 and was used to nebulize both the pro-inflammatory mediator LPS and the anti-inflammatory treatment BUD directly on top of the cells. An initial check of deposition efficiency allowed for the calculation of comparable doses of LPS and BUD to the previous experiments in LCC (Fig. 3C) [15].

Under ALI conditions, *in vitro* models can show very different cytokine and chemokine releases compared to their LCC counterparts [74]. The same could be observed here, where the apical release of IL-6 and TNFα was too low to be measured (data not shown). However, the positive drug effect of nebulized BUD could be clearly shown by measuring the release of the chemokine IL-8 (Fig. 3D). While there are various reasons discussed for the differences between LCC and ALI, the most important are the differences in cell differentiation, substance depositions rates, and dissolution rates [74]. In the future, it might be interesting to add surfactant including surfactant proteins [75, 76] in the ALI setup to investigate the effect on inflammatory processes [77], as it has already been shown for infection dynamics [5]. To our knowledge, this study represents the first microfluidic model investigating human drug response after aerosolized drug application.

Characterization of epithelial cells on chip

Effect of stretch on epithelial barrier formation

It is in accordance with previous findings that the TEER values of Arlo are lower in stretch compared to static conditions on chip (Fig. 4A) [84]. However, the TEER of primary cells was not affected by stretch, while the reduced TEER of Arlo was comparable to hAEpC (Fig. 4B). This implies that the chip system and the biocompatible silicone membrane are well tolerated by the cells and lower TEER in Arlo is not caused by increased stress or cell death. Especially when using a cell line forming a very tight barrier such as Arlo, an overestimation of barrier strength under static conditions may be possible.

The observed delocalization of ZO-1 and actin in the epithelial cells subjected to stretch (Fig. 4E) confirm earlier observations that mechanical forces on epithelia induce changes in the actin cytoskeleton and remodeling of tight junctions, leading to increased paracellular permeability and peri-junctional actin levels [78, 79]. Stretch also decreases ZO-1 and occludin levels at tight junction sites, causing cytoskeletal rearrangements that disrupt the uniform localization of tight junction proteins along cell-cell junctions, ultimately disrupting barrier function [80]. It has been shown in the intestinal CaCo2 cell line that such effects on the tight junctions can be caused by a mechanism dependent on JNK2 (a MAP kinase associated with cell stress), c-Src (a tyrosine kinase

phosphorylating junction proteins amongst others), and MLCK (a kinase regulating the structure of actin filaments) [81].

Short-term stretch effect

Measuring cell stress and cell death directly after initiating the stretching showed a good adaptation of Arlo to the mechanical stimulus. Neither increased cell stress nor death was measured by outer leaflet phosphatidylserine and free DNA (Fig. 5A and 5B). While changes in barrier function (TEER), cytoskeleton, and tight junction organization could be observed with Arlo grown on chip in stretching conditions (Fig. 4), the lack of cell stress or lack of increased cell death in the first hours after stretch start highlighted the good short-term adaptation of Arlo to chip culture and cyclic stretch. This concurs with observations in the context of VILI, where it has been shown that short-term and high mechanical stress (37% stretch) caused by high-tidal-volume mechanical ventilation leads to increased barrier permeability and lung edema, whereas lower stress (12% or 25% stretch) does not lead to any changes on the physiological level [82–87]. The mechanisms for VILI include both macroscopic structural damage [88] and strong inflammation at the cellular level, caused amongst others by increased oxidative stress [89].

Long-term stretch effect

The stretch was applied as soon as the epithelial cells grew confluent for the whole duration of the experiment (Fig. 4A). RNA sequencing was performed after barrier formation to screen for any long-term changes after stretch in control conditions, such as cell stress, cell differentiation, and junction formation. In healthy conditions, the long-term effects of mechanical stretching seem to exclude changes in the transcriptome (Fig. 5C and 5D) and prolonged mechanical stretching does not appear to exert any significant measurable influence on the transcriptome. The differences between static and stretch conditions do affect functional parameters (TEER, p_{app}, and cellular morphology, Fig. 4), but are not reflected in the transcriptomic data. Therefore, the functional changes seem to be mainly regulated at translational and post-translational protein levels. Both primary cells and Arlo demonstrate the same high degree of adaptability to prolonged mechanical stretching, as no stress response-related pathways were upregulated.

TNFα/IFNγ-induced cytokine storm on chip

A cytokine storm was imitated by inflaming the cells with high doses of TNFα and IFNγ and treated with BUD 2h after inflammation (Fig. 6). The presence of macrophages to multiply inflammatory signaling [90–94] in combination with stretching (Fig. 6D) provided the best conditions for disease modeling and drug effect investigation, shown by strong epithelial inflammation with barrier disruption, as well as barrier protection after BUD treatment.

Conclusion

This study describes different protocols to study inflammatory lung diseases and the effects of anti-inflammatory drugs *in vitro*, based on the human alveolar epithelial cell line Arlo and differentiated THP-1 macrophages cultivated on a microfluidic chip which imitates lateral stretch during breathing motion.

Under appropriate conditions, co-cultures of Arlo with macrophages provide characteristic inflammatory read-outs but also respond to treatment with BUD. The protocols were: (1) LPS-induced acute lung injury in LCC with cytokine measurement, (2) LPS-induced acute lung injury at ALI after aerosolization of LPS and BUD with chemokine measurement, and (3) TNFα/IFNγ-induced cytokine storm with TEER measurement.

The LPS-induced acute lung injury on chip was not feasible with epithelial mono-cultures, which thus demonstrates the importance of the presence of macrophages. Increased cytokine/chemokine release after inflammation could be prevented by BUD, also at ALI when delivered as an aerosol.

The TNFα/IFNγ-induced cytokine storm on chip provided the most prominent inflammatory read-outs and response to BUD when both macrophages and stretch were present, emphasizing the advantage of such a dynamic microenvironment for emulating the human air-blood-barrier.

These approaches could be used in the future to develop predictive *in vitro* models which may be validated to serve as predictive tools for developing new pulmonary anti-inflammatory therapies.

Acknowledgments

Conflict of Interest Declaration

The authors of this study are employed by the companies and institutions disclosed on the title page of this manuscript. AH, JS, and NH are employed by AlveoliX AG. JS and NH are minor shareholders of AlveoliX AG. TK is an employee and shareholder of Vitrocell® Systems GmbH. All other authors declare that they have no conflicts of interest.

Data availability statement

The data that support the findings of this study are available on request from xxx. The RNA-Sequencing dataset is also available at the research data archive RADAR (number xxx). These data are not publicly available due to privacy or ethical restrictions.

Funding statement

Ethics approval statement

The procedure and use of patient material were permitted by the local ethics committee of the state of Saarland, Germany (21st May 2019 under sign 113/19 and 10th May 2021 under sign 97/21). All patient materials were delivered with anonymized labels, ensuring patient privacy.

Patient consent statement

The local ethics committee of the state of Saarland, Germany has reviewed the patient consent forms as well.

References

1   Barnes, P.J., Bonini, S., Seeger, W., Belvisi, M.G., Ward, B., Holmes, A. (2015) Barriers to new drug development in respiratory disease. *The European respiratory journal*, **45** (5), 1197–1207.

2   Franzen, N., van Harten, W.H., Retèl, V.P., Loskill, P., van den Eijnden-van Raaij, J., IJzerman, M. (2019) Impact of organ-on-a-chip technology on pharmaceutical R&D costs. *Drug discovery today*, **24** (9), 1720–1724.

3   Barros, A.S., Costa, A., Sarmento, B. (2021) Building three-dimensional lung models for studying pharmacokinetics of inhaled drugs. *Advanced drug delivery reviews*, **170**, 386–395.

4   Konar, D., Devarasetty, M., Yildiz, D.V., Atala, A., Murphy, S.V. (2016) Lung-On-A-Chip Technologies for Disease Modeling and Drug Development. *Biomedical engineering and computational biology*, **7** (Suppl 1), 17–27.

5   Thacker, V.V., Dhar, N., Sharma, K., Barrile, R., Karalis, K., McKinney, J.D. (2020) A lung-on-chip model of early Mycobacterium tuberculosis infection reveals an essential role for alveolar epithelial cells in controlling bacterial growth. *eLife*, **9**.

6   Si, L., Bai, H., Rodas, M., Cao, W., Oh, C.Y., Jiang, A., Moller, R., Hoagland, D., Oishi, K., Horiuchi, S., Uhl, S., Blanco-Melo, D., Albrecht, R.A., Liu, W.-C., Jordan, T., Nilsson-Payant, B.E., Golynker, I., Frere, J., Logue, J., Haupt, R., McGrath, M., Weston, S., Zhang, T., Plebani, R., Soong, M., Nurani, A., Kim, S.M., Zhu, D.Y., Benam, K.H., Goyal, G., Gilpin, S.E., Prantil-Baun, R., Gygi, S.P., Powers, R.K., Carlson, K.E., Frieman, M., tenOever, B.R., Ingber, D.E. (2021) A human-airway-on-a-chip for the rapid identification of candidate antiviral therapeutics and prophylactics. *Nature biomedical engineering*, **5** (8), 815–829.

7   Xu, Z., Gao, Y., Hao, Y., Li, E., Wang, Y., Zhang, J., Wang, W., Gao, Z., Wang, Q. (2013) Application of a microfluidic chip-based 3D co-culture to test drug sensitivity for individualized treatment of lung cancer. *Biomaterials*, **34** (16), 4109–4117.

8   Huh, D., Leslie, D.C., Matthews, B.D., Fraser, J.P., Jurek, S., Hamilton, G.A., Thorneloe, K.S., McAlexander, M.A., Ingber, D.E. (2012) A human disease model of drug toxicity-induced pulmonary edema in a lung-on-a-chip microdevice. *Science translational medicine*, **4** (159), 159ra147.

9   Jain, A., Barrile, R., van der Meer, A.D., Mammoto, A., Mammoto, T., Ceunynck, K. de, Aisiku, O., Otieno, M.A., Louden, C.S., Hamilton, G.A., Flaumenhaft, R., Ingber, D.E. (2018) Primary Human Lung Alveolus-on-a-chip Model of Intravascular Thrombosis for Assessment of Therapeutics. *Clinical pharmacology and therapeutics*, **103** (2), 332–340.

10 Ingber, D.E. (2018) Developmentally inspired human 'organs on chips'. *Development (Cambridge, England)*, **145** (16).

11 Nawroth, J.C., Barrile, R., Conegliano, D., van Riet, S., Hiemstra, P.S., Villenave, R. (2019) Stem cell-based Lung-on-Chips: The best of both worlds? *Advanced drug delivery reviews*, **140**, 12–32.

12 Kolanjiyil, A.V., Kleinstreuer, C., Kleinstreuer, N.C., Pham, W., Sadikot, R.T. (2019) Mice-to-men comparison of inhaled drug-aerosol deposition and clearance. *Respiratory physiology & neurobiology*, **260**, 82–94.

13 Ehrmann, S., Schmid, O., Darquenne, C., Rothen-Rutishauser, B., Sznitman, J., Yang, L., Barosova, H., Vecellio, L., Mitchell, J., Heuze-Vourc'h, N. (2020) Innovative preclinical models for pulmonary drug delivery research. *Expert opinion on drug delivery*, **17** (4), 463–478.

14 Hiemstra, P.S., Grootaers, G., van der Does, A.M., Krul, C.A.M., Kooter, I.M. (2018) Human lung epithelial cell cultures for analysis of inhaled toxicants: Lessons learned and future directions. *Toxicology in vitro : an international journal published in association with BIBRA*, **47**, 137–146.

15 Bannuscher, A., Schmid, O., Drasler, B., Rohrbasser, A., Braakhuis, H.M., Meldrum, K., Zwart, E.P., Gremmer, E.R., Birk, B., Rissel, M., Landsiedel, R., Moschini, E., Evans, S.J., Kumar, P., Orak, S., Doryab, A., Erdem, J.S., Serchi, T., Vandebriel, R.J., Cassee, F.R., Doak, S.H., Petri-Fink, A., Zienolddiny, S., Clift, M.J.D., Rothen-Rutishauser, B. (2022) An inter-laboratory effort to harmonize the cell-delivered in vitro dose of aerosolized materials. *NanoImpact*, **28**, 100439.

16 Brandenberger, C., Rothen-Rutishauser, B., Mühlfeld, C., Schmid, O., Ferron, G.A., Maier, K.L., Gehr, P., Lenz, A.-G. (2010) Effects and uptake of gold nanoparticles deposited at the air-liquid interface of a human epithelial airway model. *Toxicology and applied pharmacology*, **242** (1), 56–65.

17 Rothen-Rutishauser, B., Gibb, M., He, R., Petri-Fink, A., Sayes, C.M. (2023) Human lung cell models to study aerosol delivery - considerations for model design and development. *European journal of pharmaceutical sciences : official journal of the European Federation for Pharmaceutical Sciences*, **180**, 106337.

18 Sengupta, A., Dorn, A., Jamshidi, M., Schwob, M., Hassan, W., Maddalena, L.L. de, Hugi, A., Stucki, A.O., Dorn, P., Marti, T.M., Wisser, O., Stucki, J.D., Krebs, T., Hobi, N., Guenat, O.T. (2023) A multiplex inhalation platform to model in situ like aerosol delivery in a breathing lung-on-chip. *Frontiers in pharmacology*, **14**, 1114739.

19 Cagino, L.M., Hensley, M.K., Fortier, S.M., Dickson, R.P. (2020) Mechanical Stretch: An Important and Understudied Feature of Acute and Chronic Lung Injury. *American journal of respiratory and critical care medicine*, **201** (8), 992–994.

20 Niu, M., Zhu, Y., Ding, X., Zu, Y., Zhao, Y., Wang, Y. (2023) Biomimetic Alveoli System with Vivid Mechanical Response and Cell-Cell Interface. *Advanced healthcare materials*, e2300850.

21 López-Martínez, C., Huidobro, C., Albaiceta, G.M., López-Alonso, I. (2018) Mechanical stretch modulates cell migration in the lungs. *Annals of translational medicine*, **6** (2), 28.

22 Bai, H., Si, L., Jiang, A., Belgur, C., Zhai, Y., Plebani, R., Oh, C.Y., Rodas, M., Patil, A., Nurani, A., Gilpin, S.E., Powers, R.K., Goyal, G., Prantil-Baun, R., Ingber, D.E. (2022) Mechanical control of innate immune responses against viral infection revealed in a human lung alveolus chip. *Nature communications*, **13** (1), 1928.

23 Carius, P., Jungmann, A., Bechtel, M., Grißmer, A., Boese, A., Gasparoni, G., Salhab, A., Seipelt, R., Urbschat, K., Richter, C., Meier, C., Bojkova, D., Cinatl, J., Walter, J., Schneider-Daum, N., Lehr, C.-M. (2023) A Monoclonal Human Alveolar Epithelial Cell Line ("Arlo") with

Pronounced Barrier Function for Studying Drug Permeability and Viral Infections. *Advanced science (Weinheim, Baden-Wurttemberg, Germany)*, e2207301.

24 Rothen-Rutishauser, B.M., Kiama, S.G., Gehr, P. (2005) A three-dimensional cellular model of the human respiratory tract to study the interaction with particles. *American journal of respiratory cell and molecular biology*, **32** (4), 281–289.

25 Drasler, B., Karakocak, B.B., Tankus, E.B., Barosova, H., Abe, J., Sousa de Almeida, M., Petri-Fink, A., Rothen-Rutishauser, B. (2020) An Inflamed Human Alveolar Model for Testing the Efficiency of Anti-inflammatory Drugs in vitro. *Frontiers in bioengineering and biotechnology*, **8**, 987.

26 Daum, N., Kuehn, A., Hein, S., Schaefer, U.F., Huwer, H., Lehr, C.-M. (2012) Isolation, cultivation, and application of human alveolar epithelial cells. *Methods in molecular biology (Clifton, N.J.)*, **806**, 31–42.

27 Sarmento, B. (ed) (2016) *Concepts and models for drug permeability studies: Cell and tissue based In vitro culture models*, Elsevier Ltd, Amsterdam.

28 Chanput, W., Peters, V., Wichers, H. (2015) The Impact of Food Bioactives on Health: in vitro and ex vivo models: THP-1 and U937 Cells.

29 Auwerx, J. (1991) The human leukemia cell line, THP-1: a multifacetted model for the study of monocyte-macrophage differentiation. *Experientia*, **47** (1), 22–31.

30 Kletting, S., Barthold, S., Repnik, U., Griffiths, G., Loretz, B., Schneider-Daum, N., Souza Carvalho-Wodarz, C. de, Lehr, C.-M. (2018) Co-culture of human alveolar epithelial (hAELVi) and macrophage (THP-1) cell lines. *ALTEX*, **35** (2), 211–222.

31 Ferreira, J.M.C., Huhle, R., Müller, S., Schnabel, C., Mehner, M., Koch, T., Gama de Abreu, M. (2022) Static Stretch Increases the Pro-Inflammatory Response of Rat Type 2 Alveolar Epithelial Cells to Dynamic Stretch. *Frontiers in physiology*, **13**, 838834.

32 Yang, J.-X., Li, M., Chen, X.-O., Lian, Q.-Q., Wang, Q., Gao, F., Jin, S.-W., Zheng, S.-X. (2019) Lipoxin A4 ameliorates lipopolysaccharide-induced lung injury through stimulating epithelial proliferation, reducing epithelial cell apoptosis and inhibits epithelial-mesenchymal transition. *Respiratory research*, **20** (1), 192.

33 Tsikis, S.T., Fligor, S.C., Hirsch, T.I., Pan, A., Yu, L.J., Kishikawa, H., Joiner, M.M., Mitchell, P.D., Puder, M. (2022) Lipopolysaccharide-induced murine lung injury results in long-term pulmonary changes and downregulation of angiogenic pathways. *Scientific reports*, **12** (1), 10245.

34 Matute-Bello, G., Frevert, C.W., Martin, T.R. (2008) Animal models of acute lung injury. *American journal of physiology. Lung cellular and molecular physiology*, **295** (3), L379-99.

35 Domscheit, H., Hegeman, M.A., Carvalho, N., Spieth, P.M. (2020) Molecular Dynamics of Lipopolysaccharide-Induced Lung Injury in Rodents. *Frontiers in physiology*, **11**, 36.

36 Movia, D., Bruni-Favier, S., Prina-Mello, A. (2020) In vitro Alternatives to Acute Inhalation Toxicity Studies in Animal Models-A Perspective. *Frontiers in bioengineering and biotechnology*, **8**, 549.

37 Hittinger, M., Mell, N.A., Huwer, H., Loretz, B., Schneider-Daum, N., Lehr, C.-M. (2016) Autologous co-culture of primary human alveolar macrophages and epithelial cells for investigating aerosol medicines. Part II: evaluation of IL-10-loaded microparticles for the treatment of lung inflammation. *Alternatives to laboratory animals : ATLA*, **44** (4), 349–360.

38 Metz, J.K., Wiegand, B., Schnur, S., Knoth, K., Schneider-Daum, N., Groß, H., Croston, G., Reinheimer, T.M., Lehr, C.-M., Hittinger, M. (2020) Modulating the Barrier Function of Human Alveolar Epithelial (hAELVi) Cell Monolayers as a Model of Inflammation. *Alternatives to laboratory animals : ATLA*, **48** (5-6), 252–267.

39 Chen, R., Lan, Z., Ye, J., Pang, L., Liu, Y., Wu, W., Qin, X., Guo, Y., Zhang, P. (2021) Cytokine Storm: The Primary Determinant for the Pathophysiological Evolution of COVID-19 Deterioration. *Frontiers in immunology*, **12**, 589095.

40 Cappanera, S., Palumbo, M., Kwan, S.H., Priante, G., Martella, L.A., Saraca, L.M., Sicari, F., Vernelli, C., Di Giuli, C., Andreani, P., Mariottini, A., Francucci, M., Sensi, E., Costantini, M., Bruzzone, P., D'Andrea, V., Gioia, S., Cirocchi, R., Tiri, B. (2021) When Does the Cytokine Storm Begin in COVID-19 Patients? A Quick Score to Recognize It. *Journal of clinical medicine*, **10** (2).

41 Alam, M., Choudhury, R., Lamers, R.-J. (2022) An adaptable in vitro cytokine release assay (CRA): Susceptibility to cytokine storm in COVID-19 as a model. *Current research in immunology*, **3**, 239–243.

42 Shrestha, J., Ghadiri, M., Shanmugavel, M., Razavi Bazaz, S., Vasilescu, S., Ding, L., Ebrahimi Warkiani, M. (2019) A rapidly prototyped lung-on-a-chip model using 3D-printed molds. *Organs-on-a-Chip*, **1**, 100001.

43 Stone, K.C., Mercer, R.R., Gehr, P., Stockstill, B., Crapo, J.D. (1992) Allometric relationships of cell numbers and size in the mammalian lung. *American journal of respiratory cell and molecular biology*, **6** (2), 235–243.

44 Stucki, J.D., Hobi, N., Galimov, A., Stucki, A.O., Schneider-Daum, N., Lehr, C.-M., Huwer, H., Frick, M., Funke-Chambour, M., Geiser, T., Guenat, O.T. (2018) Medium throughput breathing human primary cell alveolus-on-chip model. *Scientific reports*, **8** (1), 14359.

45 Sengupta, A., Roldan, N., Kiener, M., Froment, L., Raggi, G., Imler, T., Maddalena, L. de, Rapet, A., May, T., Carius, P., Schneider-Daum, N., Lehr, C.-M., Kruithof-de Julio, M., Geiser, T., Marti, T.M., Stucki, J.D., Hobi, N., Guenat, O.T. (2022) A New Immortalized Human Alveolar Epithelial Cell Model to Study Lung Injury and Toxicity on a Breathing Lung-On-Chip System. *Frontiers in toxicology*, **4**, 840606.

46 Lenz, A.G., Karg, E., Lentner, B., Dittrich, V., Brandenberger, C., Rothen-Rutishauser, B., Schulz, H., Ferron, G.A., Schmid, O. (2009) A dose-controlled system for air-liquid interface cell exposure and application to zinc oxide nanoparticles. *Particle and fibre toxicology*, **6**, 32.

47 Byron, P.R. (2004) Drug delivery devices: issues in drug development. *Proceedings of the American Thoracic Society*, **1** (4), 321–328.

48 Kuehn, A., Kletting, S., Souza Carvalho-Wodarz, C. de, Repnik, U., Griffiths, G., Fischer, U., Meese, E., Huwer, H., Wirth, D., May, T., Schneider-Daum, N., Lehr, C.-M. (2016) Human alveolar epithelial cells expressing tight junctions to model the air-blood barrier. *ALTEX*, **33** (3), 251–260.

49 Montefusco-Pereira, C.V., Horstmann, J.C., Ebensen, T., Beisswenger, C., Bals, R., Guzmán, C.A., Schneider-Daum, N., Carvalho-Wodarz, C.d.S., Lehr, C.-M. (2020) P. aeruginosa Infected 3D Co-Culture of Bronchial Epithelial Cells and Macrophages at Air-Liquid Interface for Preclinical Evaluation of Anti-Infectives. *Journal of visualized experiments : JoVE* (160).

50 La Ferlita, A., Alaimo, S., Di Bella, S., Martorana, E., Laliotis, G.I., Bertoni, F., Cascione, L., Tsichlis, P.N., Ferro, A., Bosotti, R., Pulvirenti, A. (2021) RNAdetector: a free user-friendly stand-alone and cloud-based system for RNA-Seq data analysis. *BMC bioinformatics*, **22** (1), 298.

51 Dobin, A., Davis, C.A., Schlesinger, F., Drenkow, J., Zaleski, C., Jha, S., Batut, P., Chaisson, M., Gingeras, T.R. (2013) STAR: ultrafast universal RNA-seq aligner. *Bioinformatics (Oxford, England)*, **29** (1), 15–21.

52 The New England Journal of Medicine New Manuscripts: Statistical Reporting Guidelines. https://www.nejm.org/author-center/new-manuscripts (2 August 2023).

53 Bisig, C., Voss, C., Petri-Fink, A., Rothen-Rutishauser, B. (2019) The crux of positive controls - Pro-inflammatory responses in lung cell models. *Toxicology in vitro : an international journal published in association with BIBRA*, **54**, 189–193.

54 Sandström, T., Bjermer, L., Rylander, R. (1992) Lipopolysaccharide (LPS) inhalation in healthy subjects increases neutrophils, lymphocytes and fibronectin levels in bronchoalveolar lavage fluid. *The European respiratory journal*, **5** (8), 992–996.

55   Michel, O., Nagy, A.M., Schroeven, M., Duchateau, J., Nève, J., Fondu, P., Sergysels, R. (1997) Dose-response relationship to inhaled endotoxin in normal subjects. *American journal of respiratory and critical care medicine*, **156** (4 Pt 1), 1157–1164.

56   Thorn, J. and Rylander, R. (1998) Inflammatory response after inhalation of bacterial endotoxin assessed by the induced sputum technique. *Thorax*, **53** (12), 1047–1052.

57   O'Grady, N.P., Preas, H.L., Pugin, J., Fiuza, C., Tropea, M., Reda, D., Banks, S.M., Suffredini, A.F. (2001) Local inflammatory responses following bronchial endotoxin instillation in humans. *American journal of respiratory and critical care medicine*, **163** (7), 1591–1598.

58   Zielen, S., Trischler, J., Schubert, R. (2015) Lipopolysaccharide challenge: immunological effects and safety in humans. *Expert review of clinical immunology*, **11** (3), 409–418.

59   Brooks, D., Barr, L.C., Wiscombe, S., McAuley, D.F., Simpson, A.J., Rostron, A.J. (2020) Human lipopolysaccharide models provide mechanistic and therapeutic insights into systemic and pulmonary inflammation. *The European respiratory journal*, **56** (1).

60   Chanput, W., Mes, J.J., Wichers, H.J. (2014) THP-1 cell line: an in vitro cell model for immune modulation approach. *International immunopharmacology*, **23** (1), 37–45.

61   Giambelluca, S., Ochs, M., Lopez-Rodriguez, E. (2022) Resting time after phorbol 12-myristate 13-acetate in THP-1 derived macrophages provides a non-biased model for the study of NLRP3 inflammasome. *Frontiers in immunology*, **13**, 958098.

62   Park, E.K., Jung, H.S., Yang, H.I., Yoo, M.C., Kim, C., Kim, K.S. (2007) Optimized THP-1 differentiation is required for the detection of responses to weak stimuli. *Inflammation research : official journal of the European Histamine Research Society … [et al.]*, **56** (1), 45–50.

63   Takashiba, S., van Dyke, T.E., Amar, S., Murayama, Y., Soskolne, A.W., Shapira, L. (1999) Differentiation of monocytes to macrophages primes cells for lipopolysaccharide stimulation via accumulation of cytoplasmic nuclear factor kappaB. *Infection and immunity*, **67** (11), 5573–5578.

64   Yao, Y., Miethe, S., Kattler, K., Colakoglu, B., Walter, J., Schneider-Daum, N., Herr, C., Garn, H., Ritzmann, F., Bals, R., Beisswenger, C. (2023) Mutual Regulation of Transcriptomes Between Murine Pneumocytes and Fibroblasts Mediates Alveolar Regeneration in Air-Liquid Interface Cultures. *American journal of respiratory cell and molecular biology*.

65   Brogden, R.N. and McTavish, D. (1992) Budesonide. An updated review of its pharmacological properties, and therapeutic efficacy in asthma and rhinitis. *Drugs*, **44** (3), 375–407.

66 Davis, K.C. and Small, R.E. (1998) Budesonide inhalation powder: a review of its pharmacologic properties and role in the treatment of asthma. *Pharmacotherapy*, **18** (4), 720–728.

67 Hirst, P.H., Bacon, R.E., Pitcairn, G.R., SILVASTI, M., Newman (2001) A comparison of the lung deposition of budesonide from Easyhaler®, Turbuhaler®and pMDI plus spacer in asthmatic patients // A comparison of the lung deposition of budesonide from Easyhaler, Turbuhaler and pMDI plus spacer in asthmatic patients. *Respiratory Medicine*, **95** (9), 720–727.

68 Sikkema, L., Ramírez-Suástegui, C., Strobl, D.C., Gillett, T.E., Zappia, L., Madissoon, E., Markov, N.S., Zaragosi, L.-E., Ji, Y., Ansari, M., Arguel, M.-J., Apperloo, L., Banchero, M., Bécavin, C., Berg, M., Chichelnitskiy, E., Chung, M.-I., Collin, A., Gay, A.C.A., Gote-Schniering, J., Hooshiar Kashani, B., Inecik, K., Jain, M., Kapellos, T.S., Kole, T.M., Leroy, S., Mayr, C.H., Oliver, A.J., Papen, M. von, Peter, L., Taylor, C.J., Walzthoeni, T., Xu, C., Bui, L.T., Donno, C. de, Dony, L., Faiz, A., Guo, M., Gutierrez, A.J., Heumos, L., Huang, N., Ibarra, I.L., Jackson, N.D., Kadur Lakshminarasimha Murthy, P., Lotfollahi, M., Tabib, T., Talavera-López, C., Travaglini, K.J., Wilbrey-Clark, A., Worlock, K.B., Yoshida, M., van den Berge, M., Bossé, Y., Desai, T.J., Eickelberg, O., Kaminski, N., Krasnow, M.A., Lafyatis, R., Nikolic, M.Z., Powell, J.E., Rajagopal, J., Rojas, M., Rozenblatt-Rosen, O., Seibold, M.A., Sheppard, D., Shepherd, D.P., Sin, D.D., Timens, W., Tsankov, A.M., Whitsett, J., Xu, Y., Banovich, N.E., Barbry, P., Duong, T.E., Falk, C.S., Meyer, K.B., Kropski, J.A., Pe'er, D., Schiller, H.B., Tata, P.R., Schultze, J.L., Teichmann, S.A., Misharin, A.V., Nawijn, M.C., Luecken, M.D., Theis, F.J. (2023) An integrated cell atlas of the lung in health and disease. *Nature medicine*, **29** (6), 1563–1577.

69 Mills-Goodlet, R., Schenck, M., Chary, A., Geppert, M., Serchi, T., Hofer, S., Hofstätter, N., Feinle, A., Hüsing, N., Gutleb, A.C., Himly, M., Duschl, A. (2020) Biological effects of allergen–nanoparticle conjugates: uptake and immune effects determined on hAELVi cells under submerged vs. air–liquid interface conditions. *Environ. Sci.: Nano*, **7** (7), 2073–2086.

70 Bissonnette, E.Y., Lauzon-Joset, J.-F., Debley, J.S., Ziegler, S.F. (2020) Cross-Talk Between Alveolar Macrophages and Lung Epithelial Cells is Essential to Maintain Lung Homeostasis. *Frontiers in immunology*, **11**, 583042.

71 Stromberg, L.R., Mendez, H.M., Kubicek-Sutherland, J.Z., Graves, S.W., Hengartner, N.W., Mukundan, H. (2018) Presentation matters: Impact of association of amphiphilic LPS with serum carrier proteins on innate immune signaling. *PloS one*, **13** (6), e0198531.

72 Kürti, L., Veszelka, S., Bocsik, A., Ozsvári, B., Puskás, L.G., Kittel, A., Szabó-Révész, P., Deli, M.A. (2013) Retinoic acid and hydrocortisone strengthen the barrier function of human RPMI 2650 cells, a model for nasal epithelial permeability. *Cytotechnology*, **65** (3), 395–406.

73 Zhaeentan, S., Amjadi, F.S., Zandie, Z., Joghataei, M.T., Bakhtiyari, M., Aflatoonian, R. (2018) The effects of hydrocortisone on tight junction genes in an in vitro model of the human fallopian epithelial cells. *European journal of obstetrics, gynecology, and reproductive biology*, **229**, 127–131.

74 Lenz, A.-G., Karg, E., Brendel, E., Hinze-Heyn, H., Maier, K.L., Eickelberg, O., Stoeger, T., Schmid, O. (2013) Inflammatory and oxidative stress responses of an alveolar epithelial cell line to airborne zinc oxide nanoparticles at the air-liquid interface: a comparison with conventional, submerged cell-culture conditions. *BioMed research international*, **2013**, 652632.

75 Hobi, N., Siber, G., Bouzas, V., Ravasio, A., Pérez-Gil, J., Haller, T. (2014) Physiological variables affecting surface film formation by native lamellar body-like pulmonary surfactant particles. *Biochimica et biophysica acta*, **1838** (7), 1842–1850.

76 Hobi, N., Giolai, M., Olmeda, B., Miklavc, P., Felder, E., Walther, P., Dietl, P., Frick, M., Pérez-Gil, J., Haller, T. (2016) A small key unlocks a heavy door: The essential function of the small hydrophobic proteins SP-B and SP-C to trigger adsorption of pulmonary surfactant lamellar bodies. *Biochimica et biophysica acta*, **1863** (8), 2124–2134.

77 Cañadas, O., Olmeda, B., Alonso, A., Pérez-Gil, J. (2020) Lipid-Protein and Protein-Protein Interactions in the Pulmonary Surfactant System and Their Role in Lung Homeostasis. *International journal of molecular sciences*, **21** (10).

78 Uray, I.P. and Uray, K. (2021) Mechanotransduction at the Plasma Membrane-Cytoskeleton Interface. *International journal of molecular sciences*, **22** (21).

79 Xia, M., Wu, M., Li, Y., Liu, Y., Jia, G., Lou, Y., Ma, J., Gao, Q., Xie, M., Chen, Y., He, Y., Li, H., Li, W. (2023) Varying mechanical forces drive sensory epithelium formation. *Science advances*, **9** (44), eadf2664.

80 Varadarajan, S., Stephenson, R.E., Miller, A.L. (2019) Multiscale dynamics of tight junction remodeling. *Journal of cell science*, **132** (22).

81 Samak, G., Gangwar, R., Crosby, L.M., Desai, L.P., Wilhelm, K., Waters, C.M., Rao, R. (2014) Cyclic stretch disrupts apical junctional complexes in Caco-2 cell monolayers by a JNK-2-, c-Src-, and MLCK-dependent mechanism. *American journal of physiology. Gastrointestinal and liver physiology*, **306** (11), G947-58.

82 Cavanaugh, K.J., Oswari, J., Margulies, S.S. (2001) Role of stretch on tight junction structure in alveolar epithelial cells. *American journal of respiratory cell and molecular biology*, **25** (5), 584–591.

83 Cavanaugh, K.J. and Margulies, S.S. (2002) Measurement of stretch-induced loss of alveolar epithelial barrier integrity with a novel in vitro method. *American journal of physiology. Cell physiology*, **283** (6), C1801-8.

84 Cohen, T.S., Cavanaugh, K.J., Margulies, S.S. (2008) Frequency and peak stretch magnitude affect alveolar epithelial permeability. *The European respiratory journal*, **32** (4), 854–861.

85 Cavanaugh, K.J., Cohen, T.S., Margulies, S.S. (2006) Stretch increases alveolar epithelial permeability to uncharged micromolecules. *American journal of physiology. Cell physiology*, **290** (4), C1179-88.

86 Song, M.J., Davidovich, N., Lawrence, G.G., Margulies, S.S. (2016) Superoxide mediates tight junction complex dissociation in cyclically stretched lung slices. *Journal of biomechanics*, **49** (8), 1330–1335.

87 Mitsui, Y., Koutsogiannaki, S., Fujiogi, M., Yuki, K. (2020) In Vitro Model of Stretch-Induced Lung Injury to Study Different Lung Ventilation Regimens and the Role of Sedatives. *Translational perioperative and pain medicine*, **7** (3), 258–264.

88 Silva, P.L., Scharffenberg, M., Rocco, P.R.M. (2023) Understanding the mechanisms of ventilator-induced lung injury using animal models. *Intensive care medicine experimental*, **11** (1), 82.

89 Joelsson, J.P., Asbjarnarson, A., Sigurdsson, S., Kricker, J., Valdimarsdottir, B., Thorarinsdottir, H., Starradottir, E., Gudjonsson, T., Ingthorsson, S., Karason, S. (2022) Ventilator-induced lung injury results in oxidative stress response and mitochondrial swelling in a mouse model. *Lab Anim Res*, **38** (1).

90 Holt, D.J., Chamberlain, L.M., Grainger, D.W. (2010) Cell-cell signaling in co-cultures of macrophages and fibroblasts. *Biomaterials*, **31** (36), 9382–9394.

91 Holt, P.G. and Strickland, D.H. (2008) The CD200-CD200R axis in local control of lung inflammation. *Nature immunology*, **9** (9), 1011–1013.

92 Holt, P.G., Strickland, D.H., Wikström, M.E., Jahnsen, F.L. (2008) Regulation of immunological homeostasis in the respiratory tract. *Nature reviews. Immunology*, **8** (2), 142–152.

93 Tao, H., Xu, Y., Zhang, S. (2023) The Role of Macrophages and Alveolar Epithelial Cells in the Development of ARDS. *Inflammation*, **46** (1), 47–55.

94 Ishii, H., Hayashi, S., Hogg, J.C., Fujii, T., Goto, Y., Sakamoto, N., Mukae, H., Vincent, R., van Eeden, S.F. (2005) Alveolar macrophage-epithelial cell interaction following exposure to atmospheric particles induces the release of mediators involved in monocyte mobilization and recruitment. *Respiratory research*, **6** (1), 87.
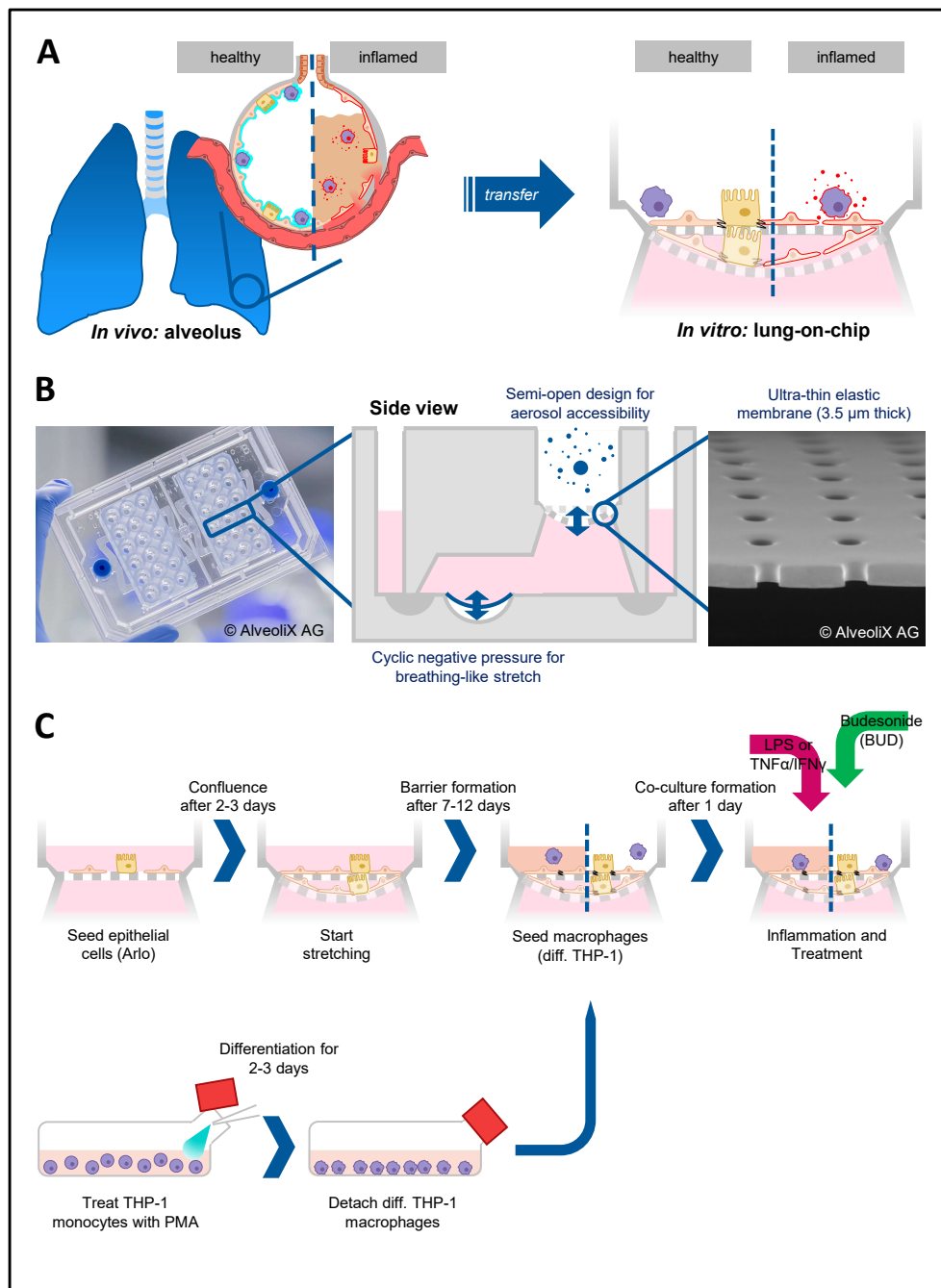
Figure 1: Chip and experimental design

A Experimental idea of transferring the inflamed alveolar state to an *in vitro* model on chip, creating a disease model that is sensible to anti-inflammatory drugs.

B Lung-on-chip design of the AX12. The AX12 is based on a 96-well plate format, with two chips in each plate. Each chip contains six individual lung-on-chip units, with a central well separated horizontally by a flexible porous membrane on which the cells can be grown. The two wells on each side of the central well are the inlet and outlet to reach the basal compartment. A cyclic negative pressure applied at the bottom of the basal chamber deflects the diaphragm and this deflection is transferred to the porous membrane with the cells.

C Setup and experimental protocol for a stretchable microphysiological model of the human air-blood barrier: First, epithelial cells (Arlo) are seeded on the porous membrane of the lung-on-chip. After the cells have attached and grown to confluence, the cells are subjected to stretch for the remaining time of the experiment. In parallel, THP-1 monocytes are differentiated with 7.5 ng/mL PMA for 2-3 days. After barrier formation (checked by regular TEER measurement), co-cultures with macrophage surrogates (differentiated THP-1 cells) are set up and left to acclimate for 24 hours before inflaming the co-cultures with either LPS or a combination of TNFα/IFNγ. Co-cultures are treated with the anti-inflammatory drug Budesonide two hours after inflammation.
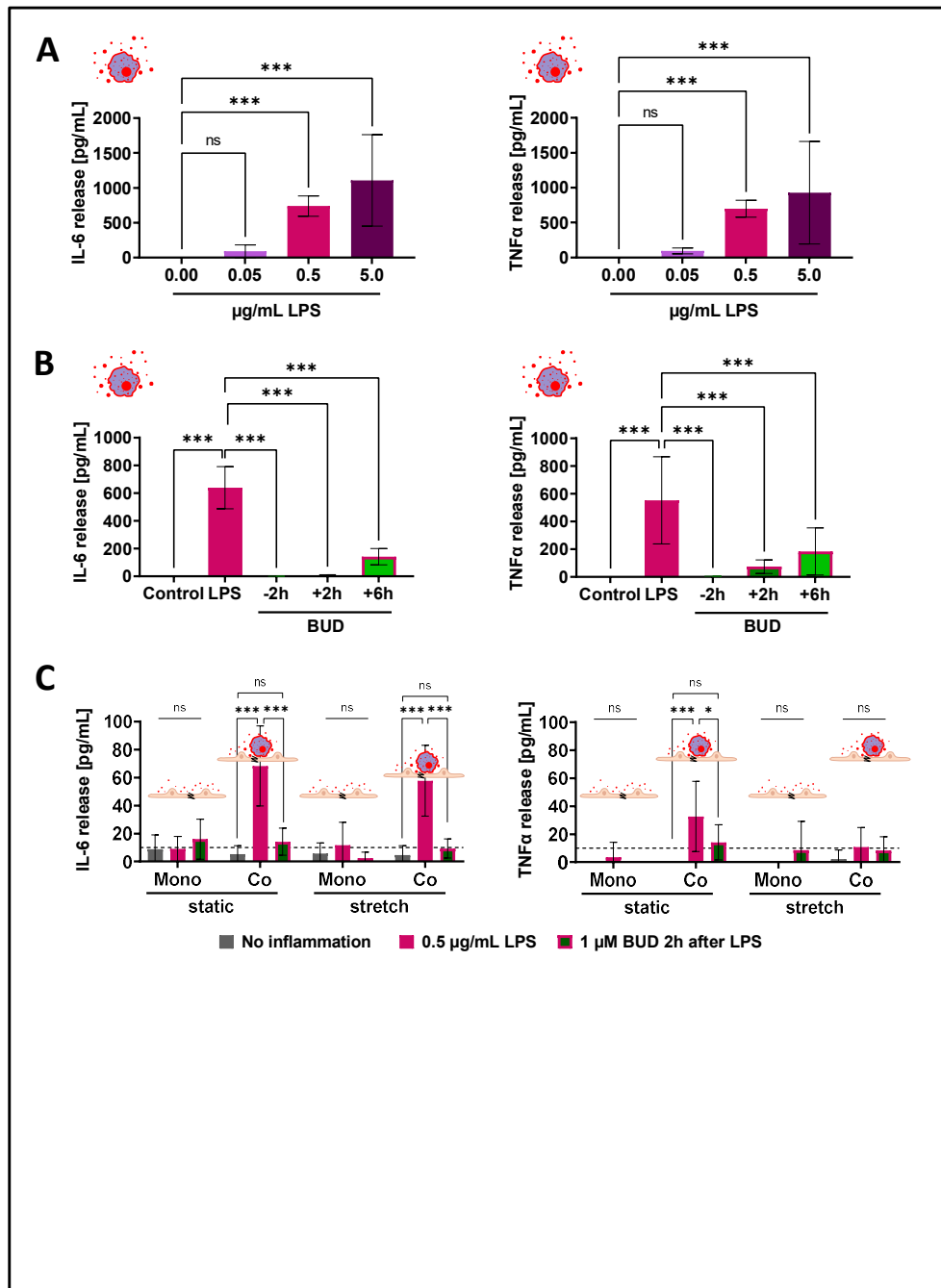
Figure 2: LPS-induced actue lung injury model setup and treatment results on chip in liquid-covered condition

A LPS dose finding in macrophage mono-culture via cytokine IL-6 and TNFα release in macrophage mono-cultures. LPS assay concentrations of 0.05 µg/mL, 0.5 µg/mL and 5.0 µg/mL are compared to medium controls. Both cytokines show a dose-dependent cytokine release. For following experiment, LPS concentration of 0.5 µg/mL is used (n = 11-15 out of 5 independent experiments; One-way ANOVA with subsequent Tukey's multiple comparison)

B Budesonide treatment timepoint finding in macrophage mono-culture via cytokine IL-6 and TNFα release in differentiated THP-1 mono-cultures. 1 µM Budesonide is added two hours prior to inflammation, or two hours after inflammation, or six hours after inflammation with 0.5 µg/mL LPS. Prophylactic pre-treatment completely prevents cytokine release, both therapeutic post-treatments significantly reduce cytokine release for IL-6 and TNFα. For following experiments, therapeutic post-treatment two hours after inflammation is used (n = 14-15 out of 6 independent experiments; One-way ANOVA with subsequent Tukey's multiple comparison)

C Inflammation on chip in epithelial mono-culture and macrophage-epithelial co-culture showing cytokine release after inflammation and treatment comparing static and dynamic conditions. The dashed line represents the lower limit of quantification (LLOQ) of the assay. In general, released amounts of TNFα are lower compared to IL-6. For almost all epithelial mono-cultures, cytokine IL-6 and TNFα release is below the LLOQ. IL-6 shows strong increase of release after inflammation with 0.5 µg/mL LPS and significant reduction of release after Budesonide treatment two hours after inflammation (n = 9-12 out of 3-4 independent experiment)
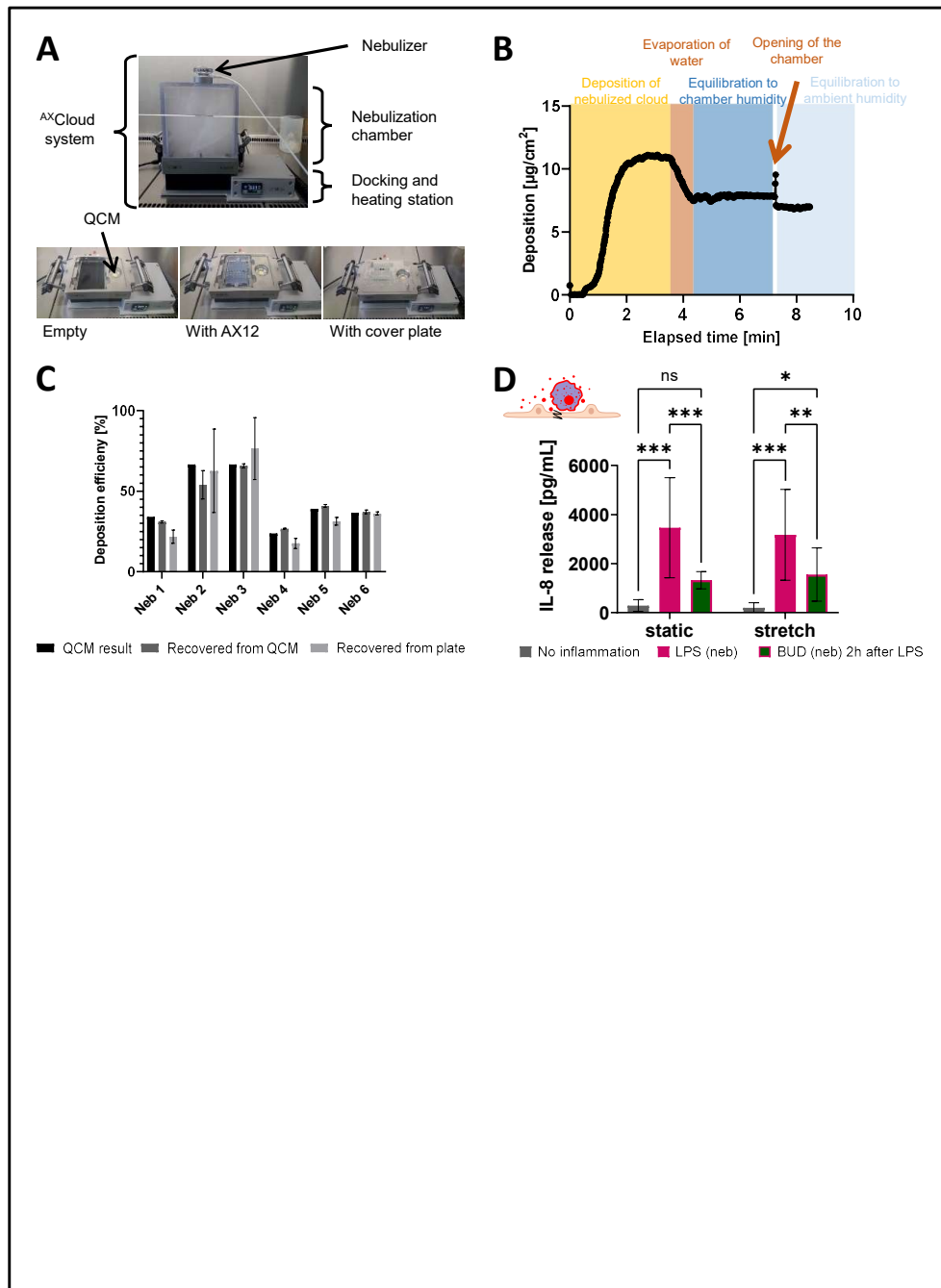
Figure 3: LPS-induced actue lung injury model at air-liquid interface with nebulization of LPS and Budesonide

A Pictures of the Cloud α AX12 deposition device. The Cloud α AX12 consists of a heated docking station for the AX12 and the nebulizer on top of the nebulization chamber.

B Time course of aerosol deposition as monitored by the quartz crystal microbalance (QCM). The initial increase is due to the deposition of aqueous aerosol, the decrease after approx. 3 min is due to evaporation of residual water. Once the value has stabilized, the nebulization chamber is removed (spike in the value) and the final deposition measured after approx. one minute of equilibration. Weight of PBS salts must be subtracted to calculate the amount of deposited drug (here fluorescein-Na).

C Validation of QCM Cloud α AX12 deposition efficiency using aerosolised fluorescein-Na. Values from the QCM are compared to fluorescence signal after recovery of fluorescein from plate and QCM respectively, indicating acceptable efficacy and reproducibility for six independent nebulization maneuvers

D Inflammation on chip at air-liquid interface in macrophage-epithelial co-culture showing chemokine IL-8 release comparing static and dynamic conditions. IL-8 shows strong increase of release after inflammation with 0.5 µg/mL LPS and significant reduction after Budesonide treatment two hours after inflammation (n = 10-13 out of 4 independent experiments; One-way ANOVA with subsequent Tukey's multiple comparison)
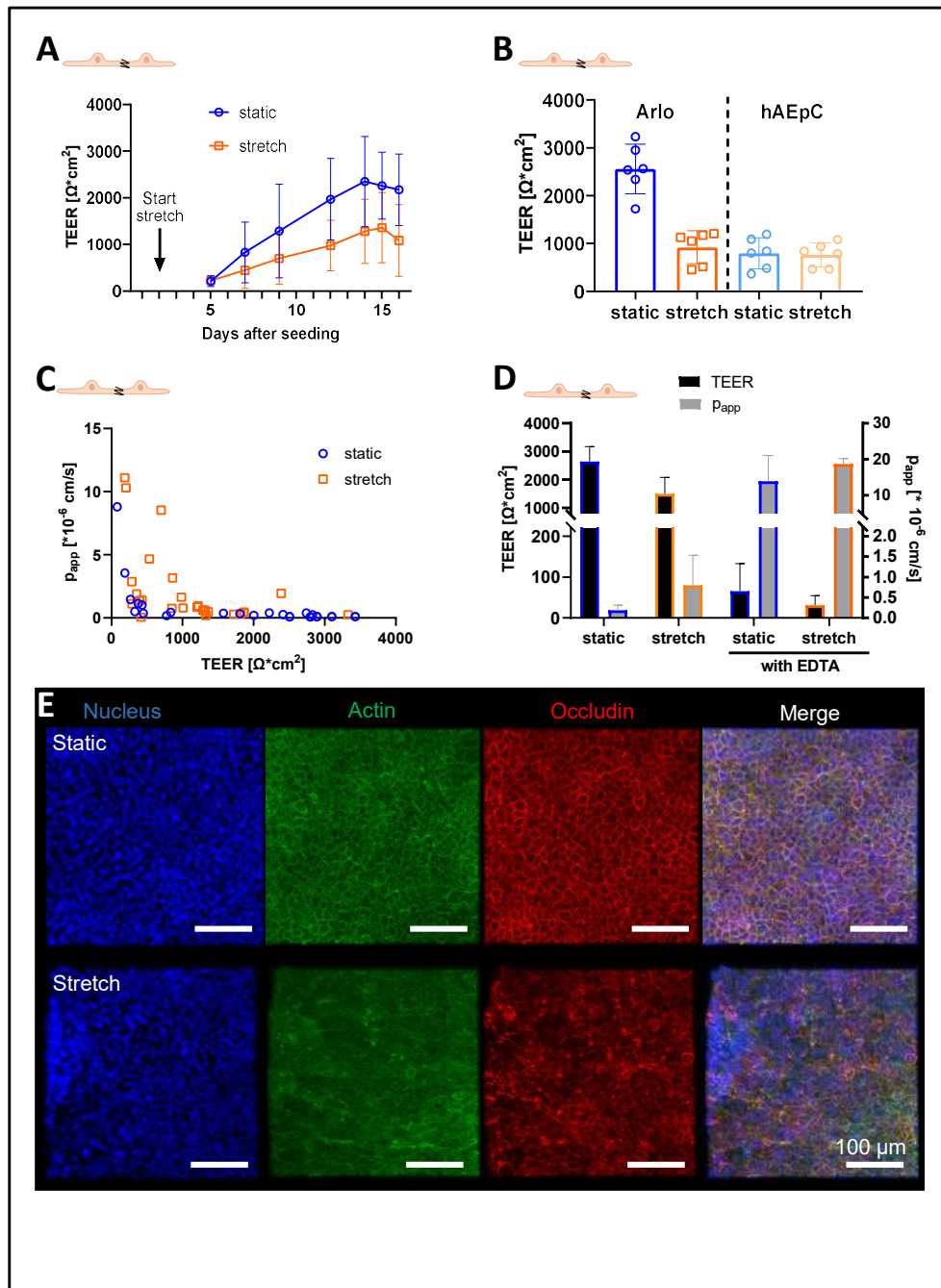
Figure 4: Characterisation of microphysiological alveolar epithelial barrier in static and stretching conditions

A TEER development of Arlo on chip over time in static and dynamic conditions. Breathing dynamics are applied starting on day 2 (n = 60-64 out of 6 independent experiments)

B TEER values after 6-7 days in culture comparing the plateau values in static and stretch conditions for Arlo and hAEpCs. Stretching lowers TEER values of Arlo to the more physiological level of hAEpC (n = 6 out of 3 independent experiments)

C Correlation of TEER values (electrical resistance) to apparent permeability of small molecule fluorescein (papp) in Arlo. High TEER correlates with low permeability in both static and dynamic conditions. Experiments are carried out at different time points to include data points with low barrier stability (26-29 single values, out of 5 independent experiments)

D TEER and p_{app} (Fluorescein) data with and without EDTA treatment in Arlo. EDTA complexes Ca^{2+} ions, thereby reversibly opening the tight junction in the epithelial layer. After EDTA treatment, a lower TEER correlates with an increased permeability in both static and dynamic conditions (n = 16-19 out of 4 independent experiments)

E Confocal images of fixated Arlo cells on chip in static and dynamic conditions. Cell nuclei are stained in blue with DAPI, actin filaments in green with Phalloidin and tight junctions in red with an Occludin-specific antibody. While still present in stretching conditions, actin filaments and tight junctions are clearly more organized in static conditions. Scale bar represents 100 µM. Representative images from several repeated experiments.
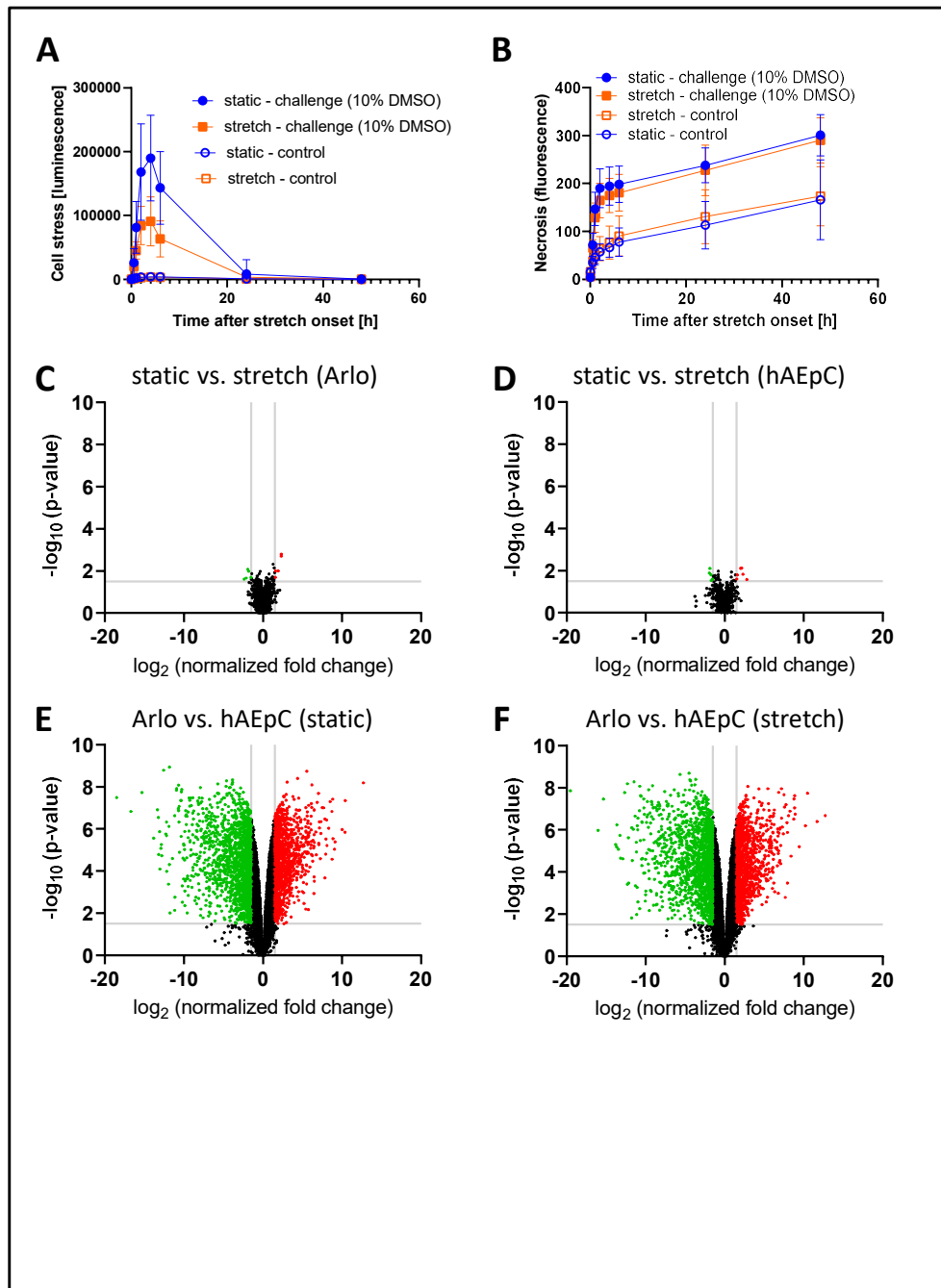
Figure 5: Investigation of stretch effect

A Cell stress measurement directly after applying stretch on day 2 of culture. In healthy conditions, no cell stress and no difference between static and stretching conditions can be observed. Upon adding 10% DMSO as challenge, cells in stretching conditions seem more resistant to the treatment. (n = 15-23 out of 3-4 independent experiments)

B Cell death measurement directly after applying stretch on day 2 of culture. Stretch does not negatively affect cell death compared to static conditions. (n = 15-23 out of 3-4 independent experiments)

C RNA-seq volcano plot of Arlo on chip depicting the differences between static and stretch conditions (n = 6 out of 3 independent experiments)

D RNA-seq volcano plot of hAEpCs on chip depicting the differences between static and stretch conditions (n = 6 out of 3 independent experiments)

E RNA-seq volcano plot of static conditions depicting the differences between Arlo and hAEpC (n = 6 out of 3 independent experiments)

F RNA-seq volcano plot of stretch conditions depicting the differences between Arlo and hAEpC (n = 6 out of 3 independent experiments)

5
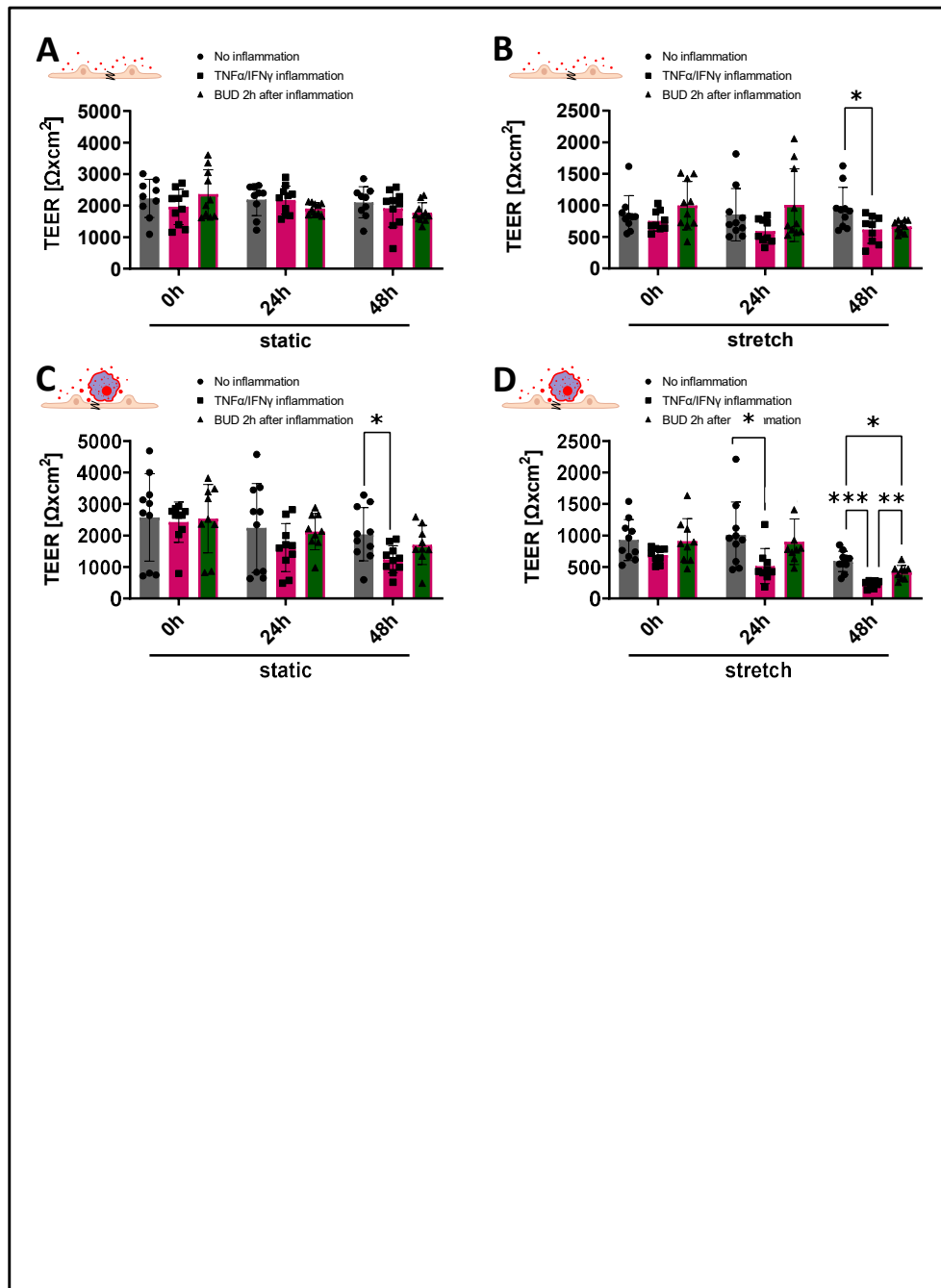
Figure 6: Inflammation of epithelial barrier on chip with a combination of TNFα/IFNγ and treatment with Budesonide

A TEER changes of Arlo mono-culture on chip in static and stretching conditions. Only in stretching conditions after 48h can a slight decrease of barrier stability be measured. No effect of the Budesonide can be measured in the epithelial mono-culture. (n = 9-11 out of 3-4 independent experiments, mean ± SD, One-way ANOVA with subsequent Tukey's multiple comparison)

B TEER changes of co-culture of Arlo with diff. THP-1 on chip in static and stretching conditions. In static conditions, a slight decrease in barrier stability can be measured after 48h. In stretching condition, barrier weakening occurs already after 24h and the protective effect of Budesonide can be measured after 48h. (n = 9-10 out of 3-5 independent experiments, mean ± SD, One-way ANOVA with subsequent Tukey's multiple comparison)

Suppl. Fig. 1: Light microscope images of THP-1 cell line and differentiated THP-1 cells
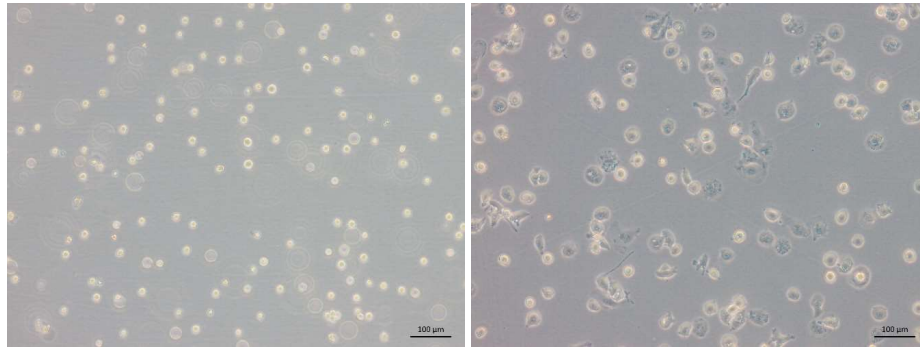
Suppl. Fig. 1: THP-1 and differentiated THP-1 cells showing distinct morphological differences
Images were taken with an Axio Vert.A1 light microscope (Zeiss) equiped with an AxioCam Erc 5s camera (Zeiss), and analyzed with
ZEN Imaging Software (Version ZEN 3.0, blue edition, Zeiss).

Suppl. Fig. 2: Effect of Hydrocortisone (HC) on inflammatory markers
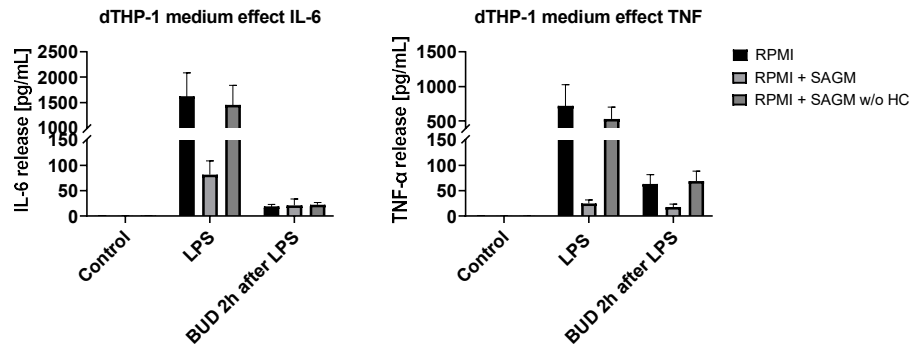
Suppl. Fig. 2: IL-6 and TNFα release in dTHP-1 mono-cultures cultured with different cell culture media to uncover the effect of HC in the standard co-culture medium on macrophages
RPMI = standard medium for dTHP-1 (contains no HC)
SAGM = standard medium für Arlo (contains HC)
RPMI + SAGM = standard medium for co-cultures (1:1 v/v)
(n = 9 out of 3 independent experiments)

Suppl. Fig. 3: TEER values of LPS-inflamed co-cultures on chip in LCC
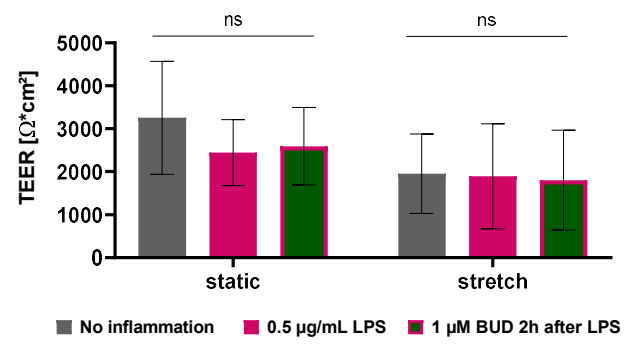
n = 14-17 out of 7 independent experiments

Suppl. Fig. 4: Confocal images of co-culture characterisation

Nucleus   Actin   Mph   Merge

100 μm
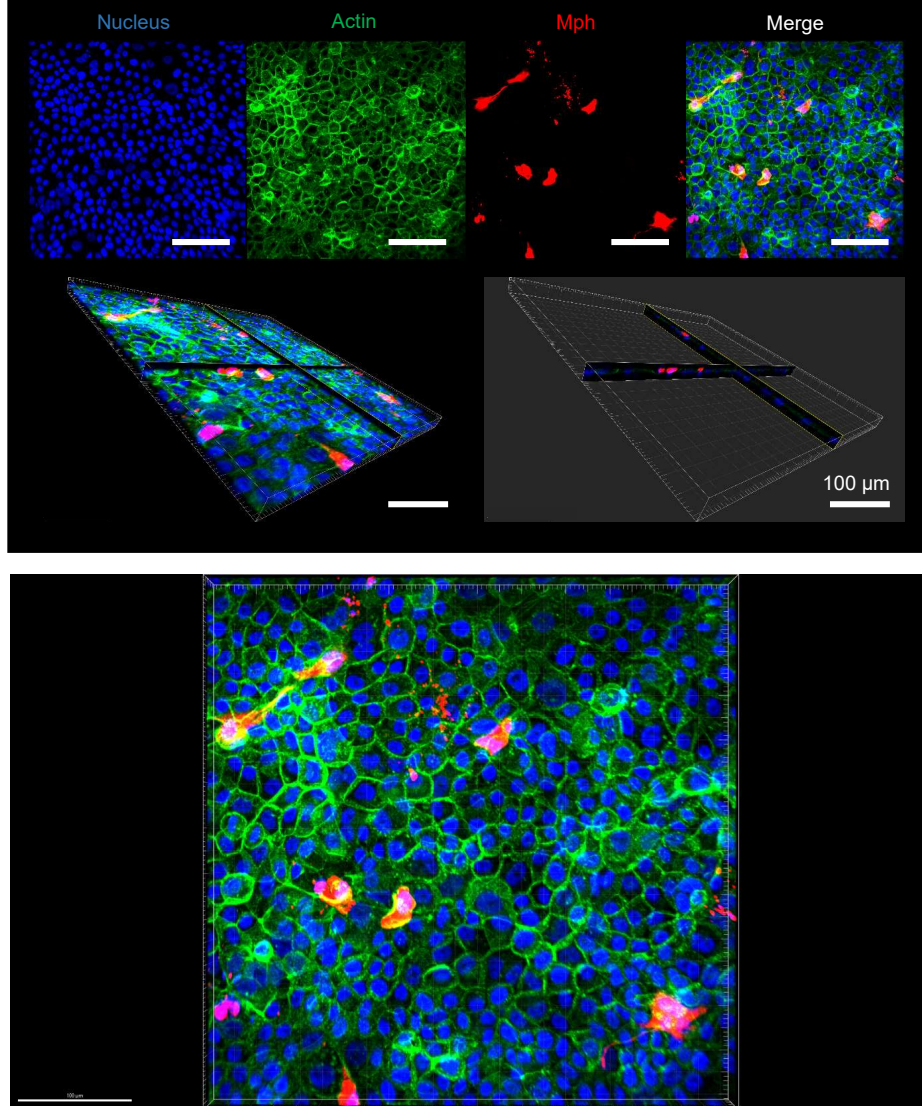
Suppl. Fig. 5: Aggregation and mobility of dTHP-1 macrophages in co-culture with Arlo
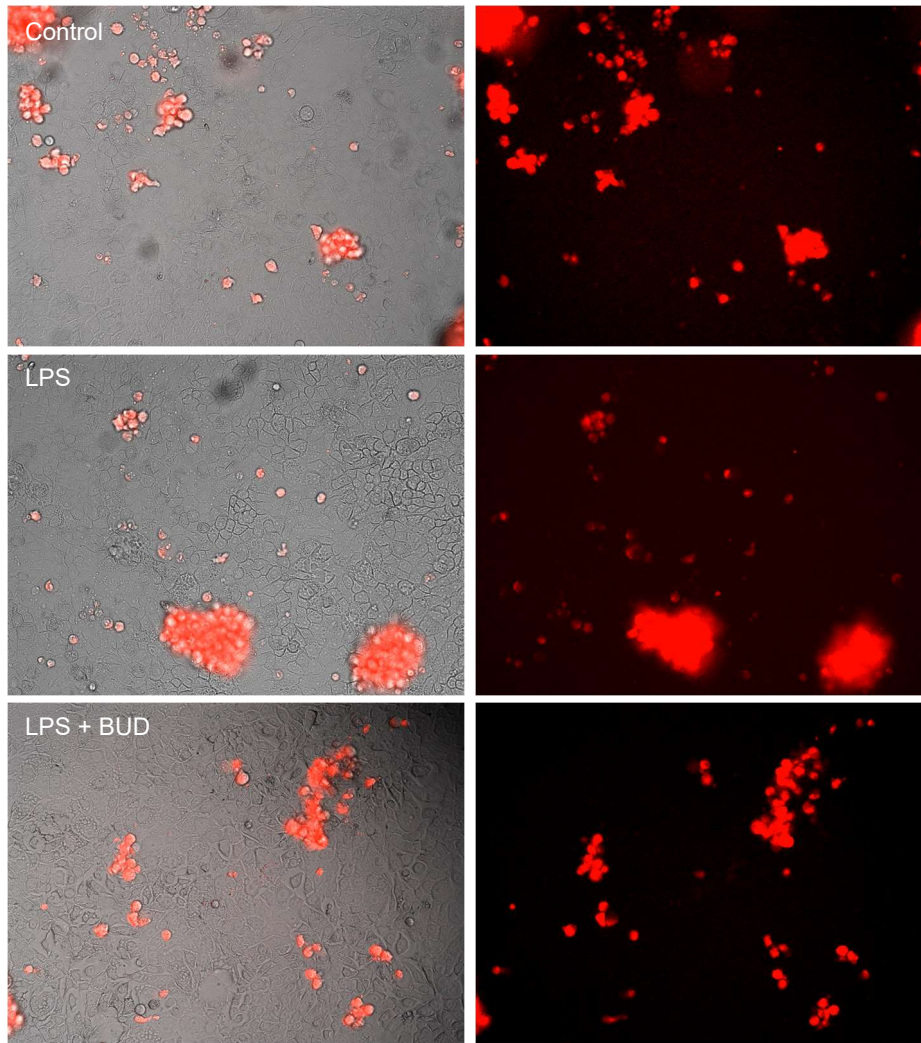
Suppl. Fig. 5: Aggregation and mobility of dTHP-1 macrophages in co-culture with Arlo
Arlo was grown to confluence on Fluorodishes (FD35-100, World Precision Instruments). THP-1 were differentiated and stained with CellTrace Far Red (C34564, Invitrogen) according to supplier protocol. After 24h of acclimatisation, co-cultures were inflamed and treated and analyzed with xxx.
Brigthfield and fluorescent images were taken every 2 min for a total runtime of 20h (1 s video corresponds to 20 min in real time). Cells were kept at 37 °C and 5% CO2 for the whole time of the experiment.
Representative videos out of 6 replicates.

Suppl. Fig. 6: AXCloud video
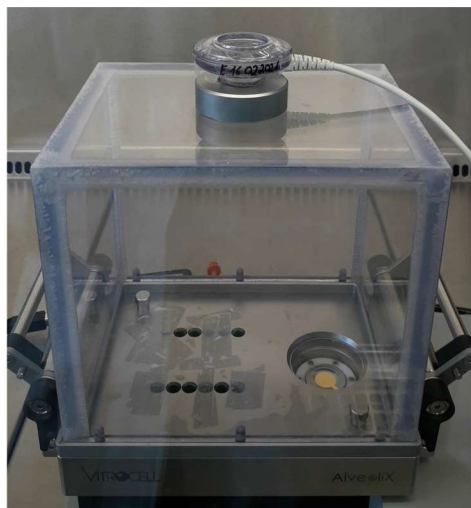
Suppl. Fig. 7: TEER developement after challenge with 10% DMSO
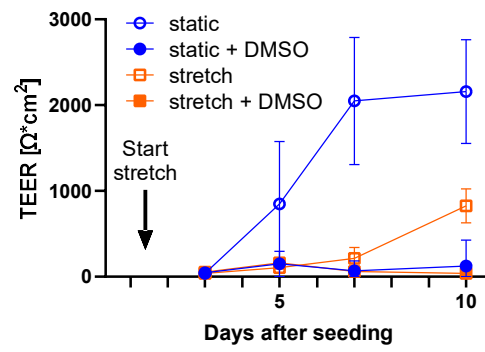
n = 4-24 out of 3-4 independent experiments

Suppl. Fig. 8: Run log of RNA Seq Analysis

Index.html

The structure and mechanics of the cell cortex depend on the location and adhesion state

D. A. D. Flormann[a], L. Kainka[a], G. Montalvo Bereau[a] (ID), C. Anton[a], J. Rheinlaender[b], D. Thalla[a], D. Vesperini[a] (ID), M. O. Pohland[a], K. H. Kaub[a,c], M. Schu[a], F. Pezzano[d] (ID), V. Ruprecht[d,e,f] (ID), E. Terriac[a], R. J. Hawkins[g] (ID), and F. Lautenschläger[a,h,1] (ID)

Affiliations are included on p. 8.

Cells exist in different phenotypes and can transition between them. A phenotype may be characterized by many different aspects. Here, we focus on the example of whether the cell is adhered or suspended and choose particular parameters related to the structure and mechanics of the actin cortex. The cortex is essential to cell mechanics, morphology, and function, such as for adhesion, migration, and division of animal cells. To predict and control cellular functions and prevent malfunctioning, it is necessary to understand the actin cortex. The structure of the cortex governs cell mechanics; however, the relationship between the architecture and mechanics of the cortex is not yet well enough understood to be able to predict one from the other. Therefore, we quantitatively measured structural and mechanical cortex parameters, including cortical thickness, cortex mesh size, actin bundling, and cortex stiffness. These measurements required developing a combination of measurement techniques in scanning electron, expansion, confocal, and atomic force microscopy. We found that the structure and mechanics of the cortex of cells in interphase are different depending on whether the cell is suspended or adhered. We deduced general correlations between structural and mechanical properties and show how these findings can be explained within the framework of semiflexible polymer network theory. We tested the model predictions by perturbing the properties of the actin within the cortex using compounds. Our work provides an important step toward predictions of cell mechanics from cortical structures and suggests how cortex remodeling between different phenotypes impacts the mechanical properties of cells.

actin | cortex | cytoskeleton | cells | suspended

Actin is the most abundant protein in eukaryotic cells (1). Its filamentous form, in combination with microtubules and intermediate filaments, defines the cytoskeleton (2). The main structure responsible for the mechanical properties of cells is the actin cortex, which is a filamentous network of actin assembled directly under the plasma membrane (3). Interacting with the actin filaments are many actin-binding proteins such as nucleators, cross-linkers, bundling proteins, and molecular motors (4–8). As the actin cortex is such a pivotal cellular element, it has stimulated a lot of studies, especially for its roles in cell mitosis, migration, and differentiation (1, 3, 9–11). Key to the function of these cell processes are the structure and mechanics of the cortex (12, 13). However, the mechanisms of how the structure is related to the mechanics of the cell cortex are not yet well understood.

Simpler actin networks studied in vitro have led to some helpful insights into the relationship between structure and mechanics which might be relevant in living cells. Gardel et al. (14) investigated in vitro the effect of the concentration of actin and cross-linkers on network stiffness using a parallel plate bulk rheometer. In their work, a constant cross-linker concentration with an increasing actin concentration resulted in a decrease of actin mesh size and a subsequent increase of stiffness, showing a negative correlation between the actin mesh size and its stiffness. This is consistent with earlier theoretical work by MacKintosh et al. (15). However, when Gardel et al. (14) kept the actin concentration constant and increased the cross-linker concentration, the mesh size also increased but resulted in an increase of stiffness due to thicker actin bundles. So, in this case, the actin mesh size and the stiffness were positively correlated. This positive correlation is also consistent with the theory in ref. 15 assuming cross-linking increases bundling.

Due to its importance in biology (16, 17), we wondered how the actin mesh size correlates with stiffness in living cells. Because of the large number of actin-binding proteins present in living cells (4, 18), the regulation of the actin cortex is considerably more complex than that of minimalistic in vitro reconstituted networks. Regulation of the actin

Significance

The actomyosin cortex plays a dominant role in determining cell mechanics and therefore a plethora of cellular functions such as migration, division, and differentiation. Understanding the relationship between the structure and mechanics of the cortex in different situations is necessary to explain cell properties crucial to health and disease, for example, cancer. Therefore, we quantitatively characterized the cortex in suspended and adhered cells and found significant differences. We show a clear correlation between the structure and stiffness of the cortex. Aspects of our data in cells fit with earlier theoretical predictions based on in vitro experiments. We provide an important step toward predicting and controlling the mechanical behavior and therefore function of cells from the underlying structure of their cortex.

cortex can lead to changes in its properties when cells are in different situations (19). For example, consider a white blood cell suspended in the blood flow. To respond to immune system signaling it adheres to the blood vessel walls prior to transmigration (20). Since the behavior of adhered and suspended cells differs (21), we questioned whether the properties of their cortices differ. Therefore, we investigated the amount and structure of actin and myosin as well as the cortex stiffness in adhered and suspended cells (Fig. 1A) by fluorescence microscopy. To test our understanding of the relationships between structure and mechanics, we used commercial compounds to alter the concentrations of actin and myosin in the system.

We used a combination of fluorescence and scanning electron microscopy (SEM) (22) to measure the structure of the cortex of hTERT-RPE1 cells. In particular, we measured the cortical mesh size, thickness of the actin cortex and amount of actin and myosin in both adhered and suspended cells. To investigate the mechanical properties we used atomic force microscopy (AFM) (23) (Fig. 1B). In the case of adhered cells, we considered two distinct regions: the nuclear and the perinuclear region (Fig. 1C). The full description of the methods and analysis can be found in *SI Appendix, Materials and Methods*.

Results and Discussion

We expect changes in mesh size and stiffness with changes in actin concentrations. Initial measurements of the amount of actin in the cortex of adhered and suspended cells using fluorescent
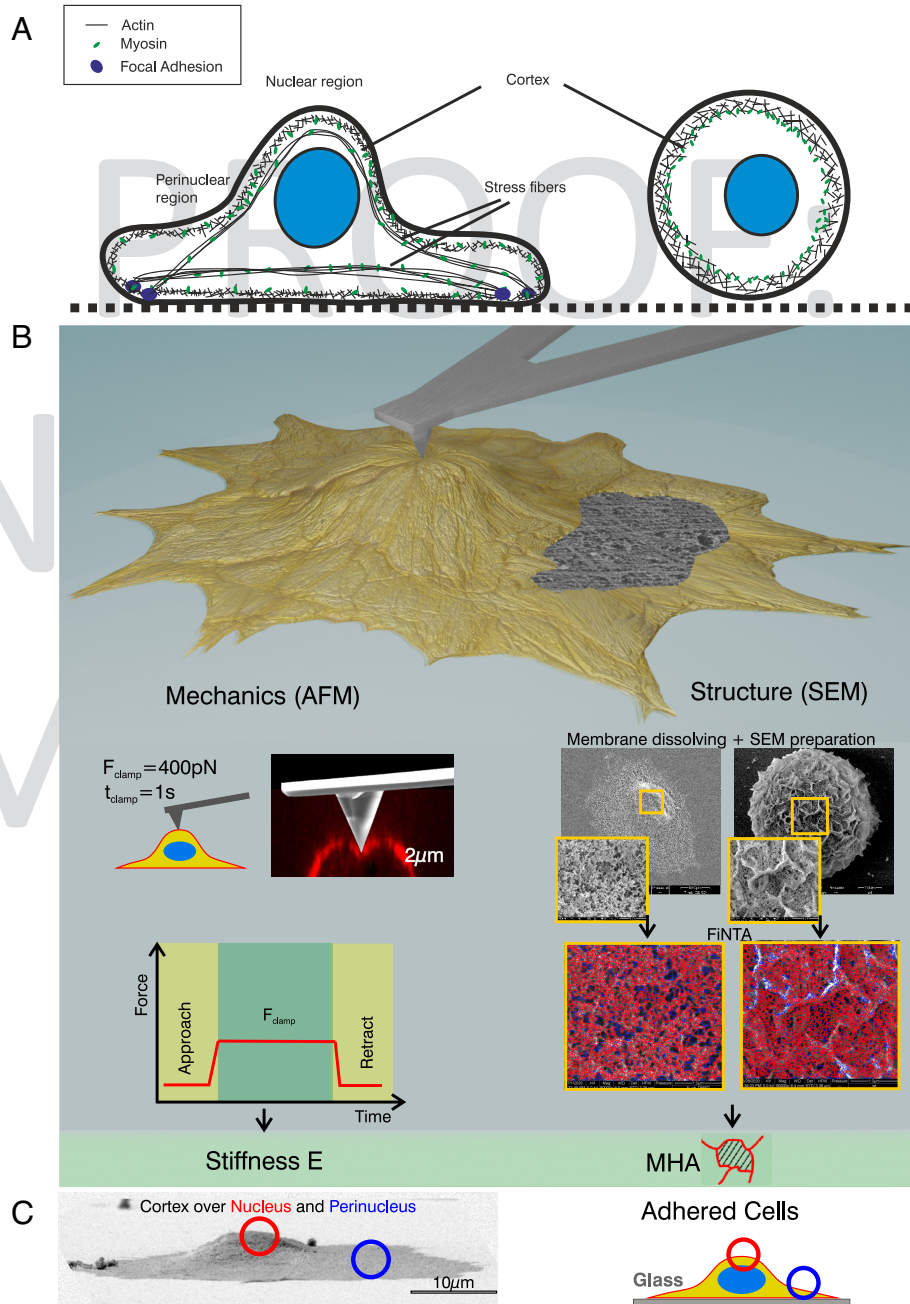

Fig. 1. Overview of adhesion states and investigation methods. (*A*) Scheme of the actin–myosin cortex of an adhered versus a suspended cell. (*B*) Representation of the main methods used: Mechanics was measured by atomic force microscopy (AFM), the cortex structure by scanning electron microscopy (SEM) followed by a mesh analysis using a filament network-tracing algorithm (FiNTA). (*C*) The cortex of adhered cells was analyzed at two different locations: one location directly above the nucleus (nucleus) and one in the periphery of the nucleus (perinucleus).

microscopy showed different amounts of F-actin per unit area (*SI Appendix*, Fig. SI1). This convinced us that cells in different adhesive states provide a test bed for our investigation of the mesh size and stiffness of the cortex.

The Structure of the Actin Network Depends on the Cell Location and Adhesion State. Cell mechanics is dependent on the structure of the actin network. We characterized the structure of the actin cortex by measuring three key parameters namely the cortex thickness, filament bundling, and the mesh size.

Actin cortex thickness differs depending on the cell location and adhesion state. To deepen our investigation of the amount of actin in different cell locations, we measured the thickness of the actin cortex. To our knowledge, this has only been done before in suspended cells where the measurement can be made in the horizontal plane (24, 25). For adhered cells, the thickness measurement is difficult due to the limited resolution in z (26). To avoid this problem and increase the resolution to a maximum, we did measurements on the apical side of the cell using expansion microscopy (27) on a cross-section of adhered cells to obtain the thickness in the highest resolution available in the xy plane (Fig. 2 *A* and *B* and *SI Appendix*, Fig. SI2), thus allowing us to measure the thickness of the cortex in adhered cells (Fig. 2 *C* and *D*).

We found that in adhered cells, the nuclear and perinuclear regions of the cortex have a similar cortex thickness (Fig. 2*E*). However, in suspended cells, the cortex is thicker (Fig. 2*E*) than in adhered cells. The values we find are similar to those found by Clark et al. (28).

Actin bundling differs depending on the cell location and adhesion state. Gardel et al. showed that actin bundling has an important effect on network mechanics in vitro (14, 29). To test whether bundling is important in the actin cortex of living cells, we investigated differences in bundles of actin in our different regions of interest.

We analyzed our SEM images by tracing the network connections of particular thicknesses using our own and commercial software [e.g., filament network-tracing algorithm (FiNTA) (30) (*SI Appendix*, Fig. SI4), Filament Sensor 2.0 (31), and Fiji (32)]. However, none of these tools were able to quantify the bundling in the actin cortex, e.g., FiNTA double counts some thick filament bundles as two single filaments and is generally ill-suited to capturing bundling (*SI Appendix, Actin Bundles Analysis Using FiNTA* and Fig. SI4). We therefore estimated the number of bundles by hand (Fig. 2 *F* and *G* and *SI Appendix*, Fig. SI5) classifying each image into one of three categories; no, few (1-5), or many (>5) bundles. From this, we conclude that suspended cells contain very few bundles, most bundles are in the perinuclear region of adhered cells and some in the nuclear region.

Many different actin-binding proteins may be responsible for bundling (6). If such a protein were differently expressed in adhered and suspended cells, it could explain the differences in bundling we observe. One such candidate is myosin (33). We found that the distribution of myosin as quantified from fluorescent images is different in suspended and adhered cells. However, myosin cannot be responsible for the bundling we see since there is more myosin in suspended cells where we see less bundling (*SI Appendix, Myosin II*).

There are also physical explanations for bundle formation based on depletion forces, electrostatic interactions (34–36), and mechanical strain. When cells are placed under strain, they may form focal adhesions that are connected by stress fibers (37). It is also known that strain can induce the alignment of filaments in polymer networks such as actin (38, 39). Such alignment may cause what we see as bundles in our SEM images and cause strain stiffening (40, 41) in a similar way as the bundles formed by cross-linkers in Gardel et al.'s work (14). We note that a strain alignment mechanism for bundling could fit with our observation of more bundles in the perinuclear region compared to the nuclear region. This might indicate that the perinuclear region experiences more mechanical strain compared to the nuclear region.

Mesh Size and Stiffness of the Actin Cortex Positively Correlate. The third key characteristic of the actin cortex is the network mesh size. We recently developed a robust method to visualize (22) and quantitatively analyze (30) the cortical mesh size from SEM images (Fig. 3*A*). Interestingly, the mean mesh hole area (MHA) of the cortex differed significantly between suspended cells and the nuclear and perinuclear regions of adhered cells (Fig. 3*A*).

We expect the mesh size to affect the stiffness of the cortex. To determine the stiffness, we used AFM to deform the surface and measured the force-distance curves (23). We found significant differences in stiffness between the cortex of suspended cells and the nuclear, perinuclear regions of adhered cells (Fig. 3*B*). We further confirmed these trends with AFM measurements in HeLa cells (*SI Appendix*, Fig. SI8*C*).

Next, we investigated the correlation between the MHA and stiffness. We find a clear positive correlation between stiffness and mesh size (Fig. 3*C*). We found that fluidity is inversely correlated with mesh size (42), which is consistent with the general observation that stiffness and fluidity are inversely correlated in living cells (43, 44). Fluidity measurement data are shown in *SI Appendix*, Fig. SI6*A*. To ensure that our AFM method using a sharp pyramidal tip does not lead to distortions, we took some measurements with a colloidal tip for comparison and found that the trends are similar, i.e., the perinuclear region is stiffer than the nuclear region (*SI Appendix*, Fig. SI6*B*). We used the sharp pyramidal tip in all future measurements since it is easier to obtain localized data on the perinuclear region than with a colloidal tip. Additionally, we used AFM to image a stiffness map of whole cells (*SI Appendix*, Fig. SI7). These maps do not show any obvious stress fibers. We therefore conclude that the indentation we are using is small enough (400 nm on average, *SI Appendix*, Fig. SI8) that we are measuring the actin cortex but not any underlying actin stress fibers.

We next describe the differences we observed between nuclear and perinuclear regions of adhered cells and between these and suspended cells. We explain these differences using densely cross-linked semiflexible biopolymer theory.

Mesh size and stiffness increase in the perinuclear compared to nuclear region of adhered cells. We find that both the mesh size and stiffness are larger in the perinuclear region compared to the nuclear region (Fig. 3 *A* and *B*), i.e., there is a positive correlation between mesh size and stiffness. It is striking to note that this positive correlation agrees with the densely cross-linked semiflexible biopolymer theory (15), in which the elastic modulus (stiffness) is given by

$$G \sim \frac{K_B{}^2}{k_B T \xi^{5'}}, \qquad [1]$$

where the thermal energy is $k_B T$, and the bending rigidity of an actin bundle is $K_B \sim D_B{}^4$ where D_B is the bundle thickness. Gardel et al. (14) and Shin et al. (29) found in their in vitro experiments that the bundle thickness depends on the cross-linker to actin ratio as $D_B \sim ([crosslink]/[actin])^{0.3}$. The mesh size, ξ, is related to the bundle thickness and the concentration of actin, $\xi \sim D_B/[actin]^{1/2}$ and therefore
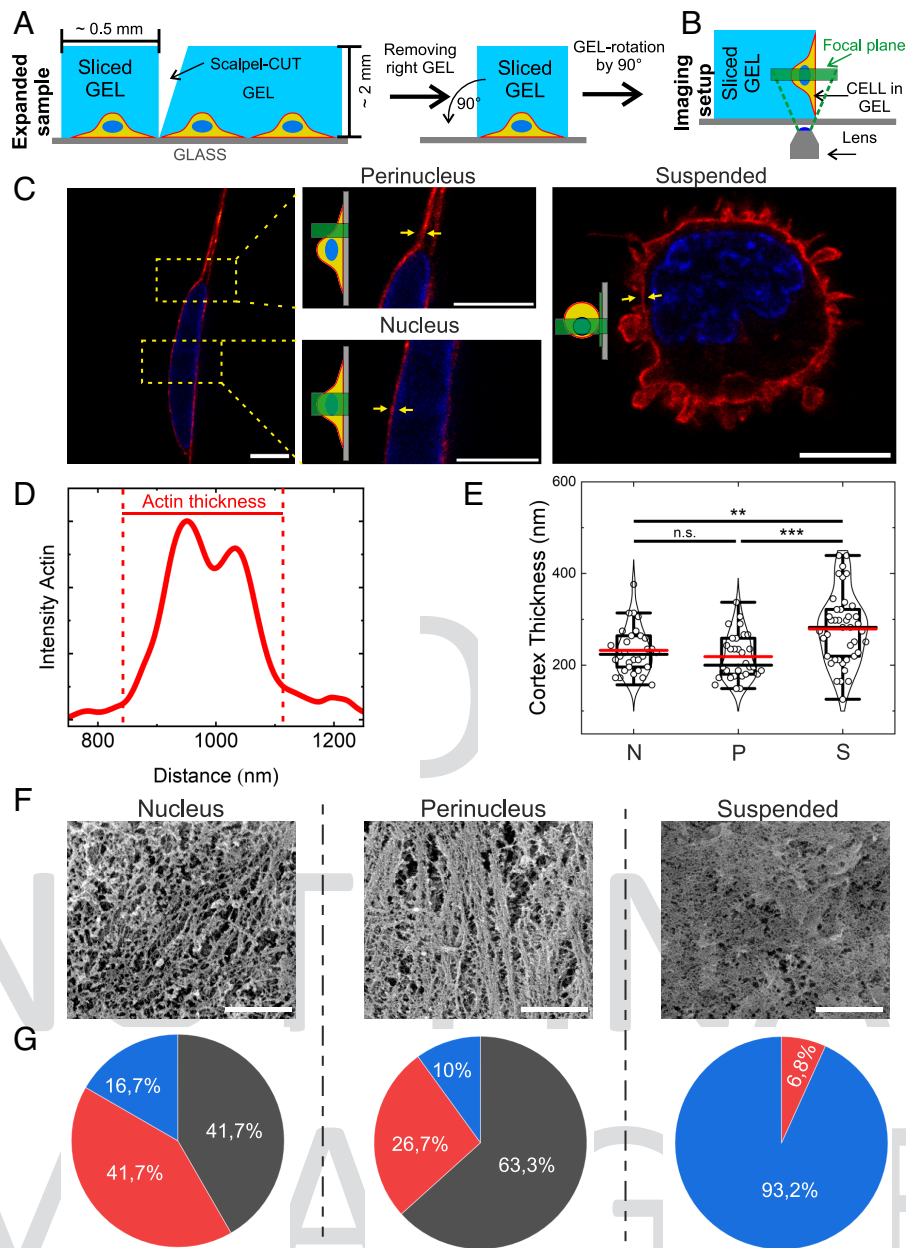
Fig. 2. In suspended cells, the actin cortex is thicker than in adhered cells but contains fewer bundles. (*A*) Scheme of the preparation procedure for side-view imaging of adhered cells using expanded samples. (*B*) Final imaging setup after gel (and hence cells) were rotated by 90° to enable side-view imaging. This is further illustrated in *SI Appendix*, Fig. SI2. (*C*) Side view of expanded nuclear and perinuclear regions as well as suspended hTERT-RPE1-cells imaged with expansion microscopy in combination with confocal imaging (Airyscan 2). Yellow arrows indicate representative measurement areas. The protocol for choosing the regions for measurements is provided in *SI Appendix*, Fig. SI3. All scale bars: 10 μm. (*D* and *E*) Analysis of intensity profiles leads to actin cortex thickness. The red horizontal lines represent the means of the distributions, and the black horizontal lines represent the medians of the distributions. In the graph (*E*), each dot represents a region. (*F*) Representative example SEM images of the cortex in the nuclear and perinuclear regions of adhered cells and the cortex of suspended cells (*Left* to *Right*) (Scale bar: 1 μm.) (*G*) Pie charts of the percentage of images showing many (black, over 5 bundles per ROI), few (red, between 1 and 5 bundles per ROI), or no (blue, no bundles per ROI) bundles in images like the example ones in *F* (~30 images per region). The star method is representing statistical Welch-corrected *t* tests: n.s.: not significant, *$P < 0.05$, **$P < 0.01$, ***$P < 0.001$. Cell counts: n = 10. Numbers of total measurements: ventral: nucleus = 30 (3 per cell), perinucleus = 30 (3 per cell), suspended cells = 41 (at least three per cell).

$$G \sim \frac{[actin]^{5/2} D_B{}^3}{k_B T}.$$ [2]

The concentration of actin, [*actin*], in the cortex depends not only on the thickness but also on the mesh size, which we analyzed (Fig. 3). The total length of filamentous actin in the cortex is proportional to the thickness, *h*, divided by the MHA ξ^2. From our measurements, we calculate hξ^{-2} to be 0.07 nm^{-1} in the nuclear region, 0.06 nm^{-1} in the perinuclear region, and 0.10 nm^{-1} in suspended cells. From this, we conclude that the amount of

F-actin in the nuclear and perinuclear cortex regions of adhered cells is similar but that the amount of actin in the cortex of suspended cells is larger.

For constant actin concentration in adhered cells therefore

$$G \sim D_B{}^3 \sim \xi^3,$$ [3]

i.e., a positive correlation between stiffness and mesh size is expected. This theory assumes that a larger mesh size with no change in the amount of actin is due to increased cross-linking causing thicker actin bundles between larger holes. Since thicker bundles are stiffer,
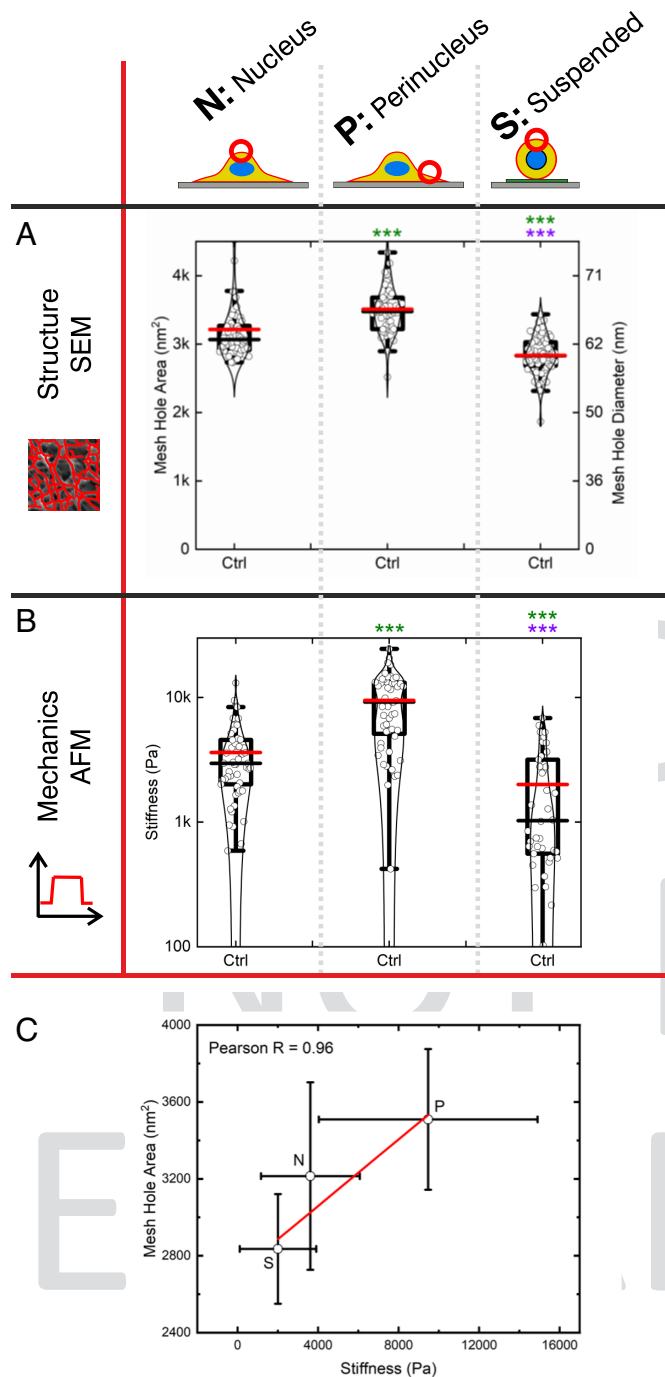
$$\xi \sim \frac{[crosslink]^{0.3}}{[actin]^{0.8}}. \qquad [4]$$

In Eq. **4**, the larger mesh size is due to a larger amount of cross-linking and therefore bundling.

In section actin cortex thickness, we observe that the amount of actin in adhered cells is similar in the nuclear and perinuclear regions, and we would therefore expect Eq. **3** to hold. Our results agree with Eq. **3** in that we see a positive correlation between stiffness and mesh size in the different regions of adhered cells (Fig. 3). In our SEM images, we also see more bundling in the perinuclear region compared to the nuclear region (Fig. 2*G*) indicating that the increased mesh size and increased stiffness are indeed due to actin bundles, as in Eq. **3**. Therefore, we expect that there may be an increase in cross-linking in the perinuclear region compared to the nuclear region as in Eqs. **3** and **4**.

Mesh size and stiffness decrease in suspended compared to adhered cells. Suspended cells also show a positive correlation between mesh size and stiffness but both are lower than in adhered cells (Fig. 3). This is consistent with our understanding that an increase in F-actin concentration leads to a smaller mesh size (14). In suspended cells, we see almost no bundling (Fig. 2) but we see a denser actin network with a smaller mesh size (Fig. 3). The decrease in stiffness we measure is consistent with a decrease in bundling, despite the increase in the amount of actin.

Effects of Chemical Treatment on Mesh Size and Stiffness. We found differences between the mesh size and stiffness in suspended cells compared to adhered cells (Fig. 3). These differences are consistent with the changes in actin concentration and bundling that we observe, as discussed in the previous sections. To further test our understanding of the system we used blebbistatin, an inhibitor of myosin II activity (45), and latrunculin A, an inhibitor of actin polymerization (46) to manipulate actin and myosin II in the cells (Fig. 4). We used drug concentrations small enough to not destroy the actin cortex (*SI Appendix*, Fig. SI9). Specifically, we measured the mesh size (Fig. 4*A*), stiffness (Fig. 4*B*), and bundling (Fig. 4*C*). In Fig. 4, we compare control cells (the same data as presented in Fig. 3) to blebbistatin- and latrunculin A–treated cells.

Blebbistatin does not alter the bundling of actin. The distribution of myosin II (*SI Appendix,* Fig. SI10) as well as a detailed discussion of the effects of myosin II on the mesh size (Fig. 4*A*) and stiffness (Fig. 4*B*) of cells can be found in *SI Appendix*. Inhibiting myosin II activity using blebbistatin did not, as we had expected, alter the bundling of actin (Fig. 4*C* and *SI Appendix, Myosin II Is Not Bundling Actin*) and was therefore not included in our theoretical description (*Discussion and Conclusion*).

Stiffness decreases and mesh size increases with latrunculin a treatment. Latrunculin A inhibits polymerization of actin (46). As demonstrated by Laplaud et al. (25) and Cartagena-Rivera et al. (47), actin treated with latrunculin A continues its depolymerization process without subsequent repolymerization, leading to a decrease in the overall concentration of polymerized actin filaments, which leads to a thinner actin cortex (25).

In adhered cells, we observed that the mesh size increases after latrunculin A treatment (Fig. 4*A*). This is what we expect due to the decreased concentration of actin, as shown in Eq. **4**. Physically, we expect latrunculin A to decrease the amount of actin sufficiently to break thin bundles/filaments thus reducing the network connectivity, resulting in a larger mesh size.

In suspended cells, however, we find the mesh size is not significantly affected by latrunculin A. We suspect that since suspended cells originally have a thicker cortex with more actin than adhered cell,

N: Nucleus   **P:** Perinucleus   **S:** Suspended

A Structure SEM

B Mechanics AFM

C

Pearson R = 0.96

Fig. 3. Structure and mechanics of the cellular cortex of adhered (nucleus and perinucleus) and suspended hTERT-RPE1 cells. (*A*) The MHA of the actin cortex was quantitatively analyzed using SEM images and the analysis software FiNTA. (*B*) The stiffness was quantitatively analyzed employing creep compliance measurements using AFM. (*C*) Correlation plots between MHA and stiffness (Pearson R = 0.96). Stars represent statistical difference as quantified with Welch-corrected *t* tests. Green stars compare controls to nucleus controls, and purple stars compare suspended controls to perinucleus controls. n.s.: not significant, *$P < 0.05$, **$P < 0.01$, ***$P < 0.001$. Cell numbers n are in the order Structure (SEM): nucleus: n = 63; perinucleus: n = 57; suspended cells: n = 66; Mechanics (AFM): nucleus: n = 53; perinucleus: n = 52; suspended cells: n = 42. The dots in Fig. 3*A* represent individual region (field of view) captured for analysis, and the dots in Fig. 3*B* represent individual cell. The control measurements in Figs. 3 and 4 are the same. For the AFM measurements on suspended cells, we excluded cells that were rolling during the measurements.

this explains the higher stiffness. For their in vitro system, Gardel et al. (14) and Shin et al. (29) analyzed EM images and show that $D_B \sim ([crosslink]/[actin])^{0.3}$ and therefore

605
606
607
608
609
610
611
612
613
614
615
616
617
618
619
620
621
622
623
624
625
626
627
628
629
630
631
632
633
634
635
636
637
638
639
640
641
642
643 Q:19
644
645
646

666
667
668
669
670
671
672
673
674
675
676
677
678
679
680
681
682
683
684
685
686
687
688
689
690
691
692
693
694
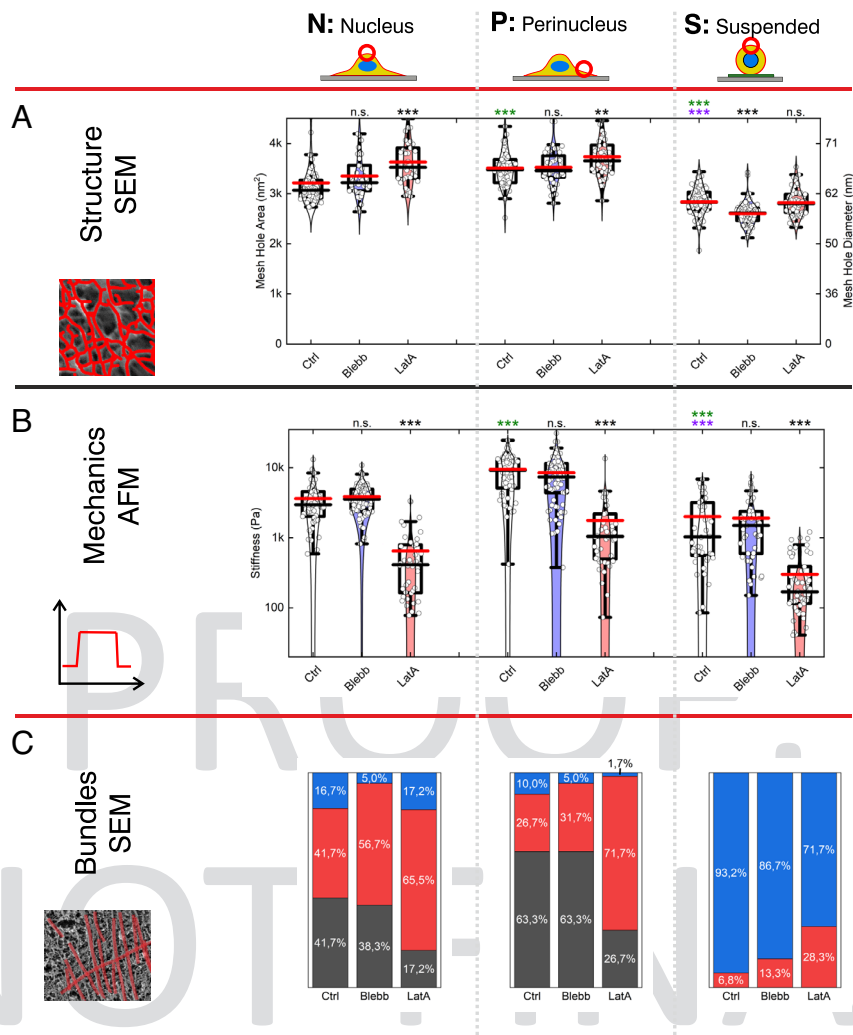695
696
697
698
699
700
701
702
703
704
705
706
707

Fig. 4. Effect of blebbistatin and latrunculin A on structure and mechanics of the cellular cortex of adhered (nucleus and perinucleus) and suspended hTERT-RPE1 cells. (A)The mesh size of the actin cortex was quantitatively analyzed using SEM images using software FiNTA. (B) The stiffness was quantitatively analyzed employing creep compliance measurements using AFM. Stars represent statistical Welch-corrected t tests. Black stars compare treated cells with the controls for each panel, green stars compare controls to nucleus controls, and purple stars compare suspended controls to perinucleus controls. n.s.: not significant, *$P < 0.05$, **$P < 0.01$, ***$P < 0.001$. Cell numbers n are in the order controls, blebbistatin, latrunculin: Structure (SEM): nucleus: n = 63, 39, 37; perinucleus: n = 57, 40, 44; suspended cells: n = 66, 75, 61; Mechanics (AFM): nucleus: n = 53, 88, 40; perinucleus: n = 52, 73, 43; suspended cells: n = 42, 47, 54. (C) Bar charts of percentages of images with many (black), few (red), or no (blue) bundles in SEM images (~30 images per region).

even with latrunculin A treatment the cortex remains thick enough to prevent the loss of network connectivity thus keeping the small mesh size of the untreated cells but reducing the cortex thickness. It is worth noting that assuming actin filaments generally have their barbed (plus) ends pointing outward (48), depolymerization will occur generally from the inside, thus thinning the cortex before affecting the outer surface. Our SEM images confirm that at the latrunculin A concentration we use (0.1 mM), the outer surface of the cortex remains intact (*SI Appendix*, Fig. SI9A). However, larger concentrations of latrunculin A can break up the cortex as seen in (*SI Appendix*, Fig. SI9B).

Stiffness decreases with latrunculin A treatment in all cells (Fig. 4B). This is expected due to the decrease in actin concentration (46, 49) and the strong dependence of biopolymer network stiffness on actin concentration shown in Eq. **2** (15) and was previously observed by others (50). Physically, the increased mesh size in adhered cells results in a softer network. In suspended cells, the thinner cortex is softer since it can bend more easily.

It is noteworthy that in adhered cells treated with latrunculin A, we see a negative correlation between mesh size and stiffness.

This is contrary to what we saw when comparing untreated adhered cells with untreated suspended cells in which the correlation was positive. These two opposite correlation behaviors are seen depending on whether actin concentration is held constant with bundling changing as seen in Figs. 2G and 3 (positive correlation) or bundling held constant while actin concentration changes as seen in Fig. 4 B and D (negative correlation).

Discussion and Conclusion

We have shown and quantitatively described how the structure and mechanics of the actin cortex differ when cells are suspended compared to when they are adhered. We find that changes in the mesh size and stiffness between different cortex regions are positively correlated. We established a protocol to measure the thickness of the actin cortex in adhered cells using expansion microscopy. Using this technique, we find there is a similar amount of actin in the nuclear and perinuclear regions of adhered cells. In contrast, we see more actin in the cortex of suspended cells compared to adhered cells but less actin bundling.

708
709
710
711
712
713
714
715
716
717
718
719
720
721 Q:20
722
723
724
725
726

Microscopic Model of Actin Cortex Structure Predicts Mechanical Stiffness in Living Cells. The scheme (Fig. 5) shows our understanding of the relationship between mesh size and stiffness in the cell cortex. If the amount of actin increases without increased cross-linking (Fig. 5A) the mesh size decreases and the network becomes stiffer, i.e., a negative correlation between mesh size and stiffness. This is the same as seen in the in vitro work of ref. 14 on changing the actin concentration keeping cross-linking constant. We see this effect at work in our data with latrunculin A treatment on adhered cells, which results in a larger mesh size and softer network. If the amount of actin remains the same but there is an increase in proteins that cause bundling, the mesh size increases (Fig. 5B). In this case, the mesh becomes stiffer due to the bundles being stiffer than single filaments. This results in a positive correlation between increased mesh size and increased stiffness, as seen in ref. 14. We see this effect in our adhered cells since we see evidence of increased bundling in the stiffer perinuclear region compared to the softer nuclear region. We suggest this bundling is not caused by myosin II but by another actin bundling protein or by strain alignment of actin filaments, because inhibition of myosin II activity did not significantly change mesh size and stiffness in adhered cells. However, myosin has multiple effects (Fig. 5 C–F) as discussed later.

We summarize our findings by mapping them onto a theoretical map (Fig. 5G). This is a contour plot of the mesh size and stiffness on a graph with bundling on the vertical axis against actin concentration on the horizontal axis. The stiffness is given by Eq. **2** which comes from MacKintosh's polymer theory (15). The mesh size is given by Eq. **4** which comes from ref. 14.

The left-hand side of the theoretical map (Fig. 5G), corresponding to low actin concentrations, shows a large mesh size and low stiffness. The top right (high actin concentration and high bundling) is stiff for a variety of mesh sizes from medium to small for the highest actin concentration. We can map the cell adhesion states we have studied onto this diagram. Adhered cells are positioned in the middle of the diagram. Suspended cells have more actin in the cortex and less bundling than adhered cells and are in the region with small mesh size and relatively soft network.

We can also visualize the effects of latrunculin A treatment on this theoretical diagram by moving horizontally left to lower actin concentrations. We see that for adhered cells, the mesh size increases. This is also the case for suspended cells but more gradually and therefore moving a small distance may not show a significant effect. Moving horizontally left to lower actin concentrations also moves away from the stiff region to softer, as seen in our experiments.

Therefore, we show that the bundled biopolymer theory by MacKintosh al. (15) holds in living cells despite the cortex being more complex than the bundled actin system assumed in the theory and measured in vitro.
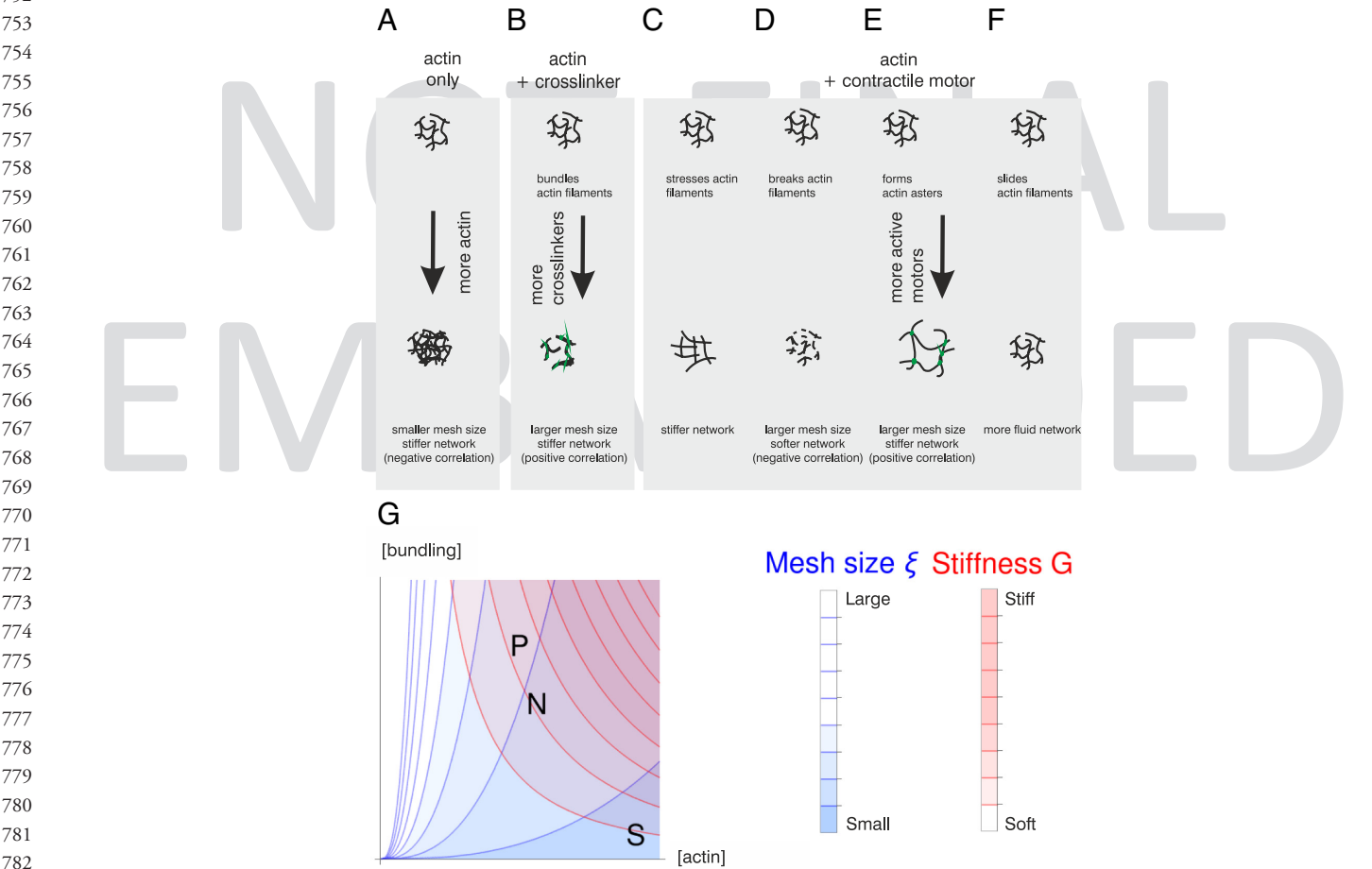

Fig. 5. Conceptual overview. (A–F) Scheme of effects of actin concentration, actin cross-linker, and actin cross-linker plus contractile motors on the actin mesh. (G) Theoretical map. Contour plot of mesh size given by Eq. **4**, $\xi = [bundling]^{0.3}/[actin]^{0.8}$ with the color scale blue–white corresponding to small–large mesh size. Contour plot of stiffness given by $G = [actin]^{2.5}\left([bundling]^{0.3}/[actin]^{0.3}\right)^3$ with the color scale white-red corresponding to soft-stiff. White regions are soft with large mesh size, and purple regions are stiff with small mesh size. The cases measured here are plotted in: P stands for adhered cell, perinuclear region, N stands for adhered cell, nuclear region, S stands for suspended cell.

The Multifaceted Role of Myosin on Structure and Mechanics in Living Cells Remains an Open Question for the Field. As detailed in section *SI Appendix, Myosin* while we do not think myosin is responsible for the actin bundling, we see, we do observe myosin affecting the actin network in suspended cells (*SI Appendix, Cortex Thickness and Mesh Size*). Actomyosin is a more complex system than that assumed by MacKintosh et al. in the polymer theory and in the in vitro experiments with actin and the nonmotor cross-linker scruin performed by Gardel et al. and Shin et al. (14, 29). Gardel et al. (51) show that the effects of myosin activity depend on the architecture of actin bundles.

In our cells, we expect myosin to have multiple effects. In the following, we summarize different effects myosin may have. Actomyosin contractility can stiffen the network by exerting pre-stress on the network (Fig. 5C) (10, 52). In extreme cases, myosin activity can result in the breakage of actin filaments and network disassembly (53, 54), which in turn would lead to a larger mesh size and softer network similar to what is seen with decreasing actin concentration (Fig. 5D).

Clusters of myosin can also change the structure of the actin by forming asters of actin (Fig. 5E). This is seen in vitro by Vogel et al. (55, 56) and in cells by Verkhovsky et al. (57). This mechanism also increases the mesh size but without increasing bundling. We expect this clustering to also increase the stiffness since actin asters are likely to be stiffer than single actin filaments as seen by Murrell and Gardel (58). In this case, the mesh size and stiffness are positively correlated. We see such myosin clusters in suspended cells (*SI Appendix*, Fig. SI10) which have more actin, a smaller mesh size, less bundling, and are softer. The suspended cells have more myosin clusters in the cortex than adhered cells. We might expect such myosin clusters and actin asters to increase the mesh size and stiffen the network, however, in our suspended cells we see a smaller mesh size and softer network corresponding with more actin and less bundling. Similarly, it was previously shown that when Vero cells detach from the substrate, a notable decrease in Young's modulus was observed, however it appeared to correlate with the disassembly of stress fibers (59).

If our expectation that active myosin does increase the mesh size is correct, we would see a decrease in mesh size on inactivating myosin. We tested this using blebbistatin treatment in suspended cells and indeed observe a decrease in mesh size (Fig. 4A).

There is a final way in which myosin can act, namely its motor activity sliding filaments along each other and thus decreasing the stiffness (60) (Fig. 5F). This mechanism is likely to occur in suspended cells due to less anchoring of the actin cortex to the surrounding, partly explaining why their cortex is softer despite the increased amount of myosin compared to adhered cells. We expect the reduction in myosin activity caused by blebbistatin to increase the stiffness compared to the softened active network. However, the effect described in Fig. 5E would decrease the stiffness due to the reduction in myosin cluster forming asters. In fact, we see no significant difference in the stiffness with blebbistatin treatment

in suspended cells (Fig. 4B), indicating that these opposing effects are compensatory.

Mesh Size and Stiffness of the Cortex Depend on the Cell State. In conclusion, we showed how the mesh size and stiffness of the cortex differ depending on whether a cell is adhered or suspended. In particular, we measured the cortex thickness in adhered as well as in suspended cells. We used FiNTA to measure the cortical mesh size in SEM images. Characterizing the structure and mechanics of the cortex in different situations is essential in explaining various cell properties from morphology to migration behavior. In turn, the effects of these in living organisms are crucial to the progression of health and disease. In this work, we characterized the differences in properties of the cortex between two states of cells, namely adhered and suspended. We can view these as particular points in a state space and consider transitions between them. In the future, it will be possible to characterize other points within state space, for example cells with/without confinement. Due to the complex nature of cellular materials, corresponding state spaces are multidimensional. Here, we consider the key parameters of the structure and mechanics of the cortex (mesh size, stiffness, and bundling). We show that both mesh size and bundling play an equally important role in this phase space, however, with means of today the mesh size is still easier to obtain. Future will provide better tools to quantitatively assess the bundling of actin in the cortex. In addition, there are other parameters that might be important to characterize state transitions within multidimensional phase spaces. For example, it was shown that the process of cell spreading requires a temporary reduction in cortical tension, facilitating the formation of membrane protrusions. These protrusions, in turn, enable the cell to expand and spread (61). More work is required to establish which parameters define which transitions. In this work, we provide a starting point by mapping the important properties of the actin cortex and how it differs between two cell states that are key to function.

Author affiliations: ᵃDepartment of Physics, Saarland University, Saarbrücken, Germany; Q:5 ᵇInstitute of Applied Physics, University of Tübingen, Tübingen 72076, Germany; Q:6 ᶜDepartment of Biophysical Chemistry, Georg-August-University, Göttingen, Germany; ᵈCenter for Genomic Regulation, The Barcelona Institute of Science and Technology, Q:7 Barcelona, Spain; ᵉUniversitat Pompeu Fabra, Barcelona, Spain; ᶠICREA, Barcelona 08010, Q:8 Spain; ᵍDepartment of Physics and Astronomy, University of Sheffield, Sheffield, United Kingdom; and ʰCenter for Biophysics, Saarland University, Saarbrücken, Germany

1. P. Chugh, E. K. Paluch, The actin cortex at a glance. *J. Cell Sci.* **131**, jcs186254 (2018).
2. D. A. Fletcher, R. D. Mullins, Cell mechanics and the cytoskeleton. *Nature* **463**, 485–492 (2010).
3. G. Salbreux, G. Charras, E. Paluch, Actin cortex mechanics and cellular morphogenesis. *Trends Cell Biol.* **22**, 536–545 (2012).
4. T. D. Pollard, Actin and actin-binding proteins. *Cold Spring Harb. Perspect. Biol.* **8**, a018226 (2016).
5. T. D. Pollard, L. Blanchoin, R. D. Mullins, Molecular mechanisms controlling actin filament dynamics in nonmuscle cells. *Annu. Rev. Biophys.* **29**, 545–576 (2000).
6. N. Castaneda, J. Park, E. H. Kang, Regulation of actin bundle mechanics and structure by intracellular environmental factors. *Front. Phys.* **9**, 675885 (2021).
7. P. Matsudalra, Modular organization of actin crosslinking proteins. *Trends Biochem. Sci.* **16**, 87–92 (1991).
8. M. Schliwa, G. Woehlke, Molecular motors. *Nature* **422**, 759–765 (2003).
9. F. Lautenschläger et al., The regulatory role of cell mechanics for migration of differentiating myeloid cells. *Proc. Natl. Acad. Sci. U.S.A.* **106**, 15696–15701 (2009).

10. A. Cordes et al., Prestress and area compressibility of actin cortices determine the viscoelastic response of living cells. *Phys. Rev. Lett.* **125**, 068101 (2020).
11. C. J. Chan et al., Myosin II activity softens cells in suspension. *Biophys. J.* **108**, 1856–1869 (2015).
12. D. Bray, J. G. White, Cortical flow in animal cells. *Science* **239**, 883–888 (1988).
13. S. Mukhina, Y. Wang, M. Murata-Hori, α-actinin is required for tightly regulated remodeling of the actin cortical network during cytokinesis. *Dev. Cell* **13**, 554–565 (2007).
14. M. L. Gardel et al., Elastic behavior of cross-linked and bundled actin networks. *Science* **304**, 1301–1305 (2004).
15. F. C. MacKintosh, J. Käs, P. A. Janmey, Elasticity of semiflexible biopolymer networks. *Phys. Rev. Lett.* **75**, 4425–4428 (1995).
16. A. Colin, P. Singaravelu, M. Théry, L. Blanchoin, Actin-network architecture regulates microtubule dynamics. *Curr. Biol.* **28**, 2647–2656 (2018).
17. J. Azoury et al., Spindle positioning in mouse oocytes relies on a dynamic meshwork of actin filaments. *Curr. Biol.* **18**, 1514–1519 (2008).

18. S. J. Winder, K. R. Ayscough, Actin-binding proteins. *J. Cell Sci.* **118**, 651–654 (2005).
19. M. Schnoor, Endothelial actin-binding proteins and actin dynamics in leukocyte transendothelial migration. *J. Immnuol.* **194**, 3535–3541 (2015).
20. T. A. Springer, Traffic signals on endothelium for lymphocyte recirculation and leukocyte emigration. *Ann. Rev. Physiol.* **57**, 827–872 (1995).
21. R. A. Whipple, A. M. Cheung, S. S. Martin, Detyrosinated microtubule protrusions in suspended mammary epithelial cells promote reattachment. *Exp. Cell Res.* **313**, 1326–1336 (2007).
22. M. Schu *et al.*, Scanning electron microscopy preparation of the cellular actin cortex: A quantitative comparison between critical point drying and hexamethyldisilazane drying. *PLoS One* **16**, e0254165 (2021).
23. D. A. D. Flormann *et al.*, Oscillatory microrheology, creep compliance and stress relaxation of biological cells reveal strong correlations as probed by atomic force microscopy. *Front. Phys.* **9**, 71186 (2021).
24. P. Chugh *et al.*, Actin cortex architecture regulates cell surface tension. *Nat. Cell Biol.* **19**, 689–697 (2017).
25. V. Laplaud *et al.*, Pinching the cortex of live cells reveals thickness instabilities caused by myosin II motors. *Sci. Adv.* **7**, eabe3640 (2021).
26. C. A. Combs, H. Shroff, Fluorescence microscopy: A concise guide to current imaging methods. *Curr. Protoc. Neurosci.* **79**, 2.1.1–2.1.25 (2017).
27. F. Chen, P. W. Tillberg, E. S. Boyden, Optical imaging. Expansion microscopy. *Science* **347**, 543–548 (2015).
28. A. G. Clark, K. Dierkes, E. K. Paluch, Monitoring actin cortex thickness in live cells. *Biophys. J.* **105**, 570–580 (2013).
29. J. H. Shin, M. L. Gardel, L. Mahadevan, P. Matsudaira, D. A. Weitz, Relating microstructure to rheology of a bundled and cross-linked F-actin network in vitro. *Proc. Natl. Acad. Sci. U.S.A.* **101**, 9636–9641 (2004).
30. D. A. D. Flormann *et al.*, A novel universal algorithm for filament network tracing and cytoskeleton analysis. *FASEB J.* **35**, e21582 (2021).
31. L. Hauke *et al.*, FilamentSensor 2.0: An open-source modular toolbox for 2D/3D cytoskeletal filament tracking. *PLoS One* **18**, e0279336 (2023).
32. J. Schindelin *et al.*, Fiji: An open-source platform for biological-image analysis. *Nat. Methods* **9**, 676–682 (2012).
33. J. Kolega, Cytoplasmic dynamics of myosin IIA and IIB: Spatial sorting of isoforms in locomoting cells. *J. Cell Sci.* **111**, 2085–2095 (1998).
34. J. X. Tang, T. Ito, T. Tao, P. Traub, P. A. Janmey, Opposite effects of elecrostatics and steric exclusion on bundle formation by F-Actin and other filamentous polyelectrolytes. *Biochemistry* **36**, 12395–12652 (1997).
35. J. Schnauß, T. Händler, J. A. Käs, Semiflexible biopolymers in bundled arrangements. *Polymers (Basel)* **8**, 274 (2016).
36. M. Hosek, J. X. Tang, Polymer-induced bundling of F actin and the depletion force. *Phys. Rev. E Stat. Nonlin. Soft Matter Phys.* **69**, 051907 (2004).
37. A. M. Greiner, H. Chen, J. P. Spatz, R. Kemkemer, Cyclic tensile strain controls cell shape and directs actin stress fiber formation and focal adhesion alignment in spreading cells. *PLoS One* **8**, e77328 (2013).
38. D. R. Scheff *et al.*, Actin filament alignment causes mechanical hysteresis in cross-linked networks. *Soft Matter* **17**, 5499–5507 (2021).
39. K. M. Schmoller, P. Fernández, R. C. Arevalo, D. L. Blair, A. R. Bausch, Cyclic hardening in bundled actin networks. *Nat. Commun.* **1**, 134 (2010).
40. G. Žagar, Patrick R. Onck, E. van der Giessen, Two fundamental mechanisms govern the stiffening of cross-linked networks. *Biophys. J.* **108**, 1470–1479 (2015).
41. C. Storm, J. J. Pastore, F. C. MacKintosh, T. C. Lubensky, P. A. Janmey, Nonlinear elasticity in biological gels. *Nature* **435**, 191–194 (2005).
42. D. A. D. Flormann *et al.*, The role of actin and myosin II in the cell cortex of adhered and suspended cells. bioRxiv [Preprint] (2021). https://doi.org/10.1101/2021.08.03.454901. Q:27
43. B. Fabry *et al.*, Scaling the microrheology of living cells. *Phys. Rev. Lett.* **87**, 148102 (2001).
44. F. M. Hecht *et al.*, Imaging viscoelastic properties of live cells by AFM: Power-law rheology on the nanoscale. *Soft Matter* **11**, 4584–4591 (2015).
45. M. Kovács, J. Tóth, C. Hetényi, A. Málnási-Csizmadia, J. R. Sellers, Mechanism of blebbistatin inhibition of myosin II. *J. Biol. Chem.* **279**, 35557–35563 (2004).
46. M. Coué, S. L. Brenner, I. Spector, E. D. Korn, Inhibition of actin polymerization by latrunculin A. *FEBS Lett.* **213**, 316–318 (1987).
47. A. X. Cartagena-Rivera, J. S. Logue, C. M. Waterman, R. S. Chadwick, Actomyosin cortical mechanical properties in nonadherent cells determined by atomic force microscopy. *Biophys. J.* **110**, 2528–2539 (2016).
48. T. Svitkina, The actin cytoskeleton and actin-based motility. *Cold Spring Harb. Perspect. Biol.* **10**, a018267 (2018).
49. W. M. Morton, K. R. Ayscough, P. J. McLaughlin, Latrunculin alters the actin-monomer subunit interface to prevent polymerization. *Nat. Cell Biol.* **2**, 376–378 (2000).
50. T. Wakatsuki, B. Schwab, N. C. Thompson, E. L. Elson, Effects of cytochalasin D and latrunculin B on mechanical properties of cells. *J. Cell Sci.* **114**, 1025–1036 (2001).
51. K. L. Weirich, S. Stam, E. Munro, M. L. Gardel, Actin bundle architecture and mechanics regulate myosin II force generation. *Biophys. J.* **120**, 1957–1970 (2021).
52. D. Mizuno, C. Tardin, C. F. Schmidt, F. C. MacKintosh, Nonequilibrium mechanics of active cytoskeletal networks. *Science* **315**, 370–373 (2007).
53. C. A. Wilson *et al.*, Myosin II contributes to cell-scale actin network treadmilling through network disassembly. *Nature* **465**, 373–377 (2010).
54. M. P. Murrell, M. L. Gardel, F-actin buckling coordinates contractility and severing in a biomimetic actomyosin cortex. *Proc. Natl. Acad. Sci. U.S.A.* **109**, 20820–20825 (2012).
55. S. K. Vogel, Z. Petrasek, F. Heinemann, P. Schwille, Myosin motors fragment and compact membrane-bound actin filaments. *Elife* **2**, e00116 (2013).
56. S. Stam *et al.*, Filament rigidity and connectivity tune the deformation modes of active biopolymer networks. *Proc. Natl. Acad. Sci. U.S.A.* **114**, E10037–E10045 (2017).
57. A. B. Verkhovsky, T. M. Svitkina, G. G. Borisy, Polarity sorting of actin filaments in cytochalasin-treated fibroblasts. *J. Cell Sci.* **110**, 1693–1704 (1997).
58. M. Murrell, M. L. Gardel, Actomyosin sliding is attenuated in contractile biomimetic cortices. *Mol. Biol. Cell* **25**, 1845–1853 (2014).
59. Y. M. Efremov *et al.*, Distinct impact of targeted actin cytoskeleton reorganization on mechanical properties of normal and malignant cells. *Biochim. Biophys. Acta* 1853, 3117–3125 (2015).
60. D. Humphrey, C. Duggan, D. Saha, D. Smith, J. Käs, Active fluidization of polymer network through molecular motors. *Nature* **416**, 413–416 (2002).
61. A. Pietuch, A. Janshoff, Mechanics of spreading cells probed by atomic force microscopy. *Open Biol.* **3**, 130084 (2013).

Author Query Form

Query reference	Query
Q1	Your article will appear in the following sections of the journal: Biological Sciences (Biophysics and Computational Biology) and Physical Sciences (Biophysics and Computational Biology). Please confirm that this is correct.
Q2	Please confirm the edits made to the article title.
Q3	Please review 1) the author affiliation and footnote symbols, 2) the order of the author names, and 3) the spelling of all author names, initials, and affiliations and confirm that they are correct as set.
Q4	Please note that the spelling of the following author names in the manuscript differs from the spelling provided in the article metadata: D.A.D. Flormann, L. Kainka, G. Montalvo Bereau, C. Anton, J. Rheinlaender, D. Thalla, D. Vesperini, M.O. Pohland, K.H. Kaub, M. Schu, F. Pezzano, V. Ruprecht, E. Terriac, R.J. Hawkins, and F. Lautenschläger. The spelling provided in the manuscript has been retained; please confirm.
Q5	Per PNAS style post codes are required in all affiliations. Please provide the same in affiliations a, c–e, g, and h.
Q6	Please include the division or department with which the author is associated in affiliations b, e, and h.
Q7	There is no provided division/section/unit for affiliations d and f. Please provide if this is available.
Q8	Per PNAS style abbreviations are not allowed in the affiliation. Please provide the expansion for 'ICREA'.
Q9	Please review the author contribution footnote carefully. Ensure that the information is correct and that the correct author initials are listed. Note that the order of author initials matches the order of the author line per journal style. You may add contributions to the list in the footnote; however, funding may not be an author's only contribution to the work.
Q10	You have chosen to publish your PNAS article with the delayed open access option under a CC BY-NC-ND license. Your article will be freely accessible 6 months after publication, without a subscription; for additional details, please refer to the PNAS site: https://www.pnas.org/authors/fees-and-licenses. Please confirm this is correct.
Q11	Certain compound terms are hyphenated when used as adjectives and unhyphenated when used as nouns. This style has been applied consistently throughout where (and if) applicable.
Q12	Please confirm whether the edited sentence "Therefore, we investigated. . ." conveys the intended meaning.
Q13	Would you consider rephrasing the sentence "Representation of the main. . ." for better clarity?
Q14	PNAS articles should be accessible to a broad scientific audience; as such, please spell out the abbreviations hTERT-RPE1 and ROI.
Q15	Please check the citation whether it should be retained as such or changed to "SI Appendix, Fig. S1 to S10".
Q16	Claims of priority or primacy are not allowed, per PNAS policy (https://www.pnas.org/authors/submitting-your-manuscript); please consider rewording/eliminating the sentence "To our knowledge, this has only been done. . ." or explain why it should not be considered a priority claim and should be retained.
Q17	Please check the phrase "gel (and hence cells) were".
Q18	Please confirm whether the edited sentence "Cell numbers n are in the. . ." conveys the intended meaning.
Q19	Please confirm whether the edited sentence "Cell numbers n are in the. . ." conveys the intended meaning.
Q20	Claims of priority or primacy are not allowed, per PNAS policy (https://www.pnas.org/authors/submitting-your-manuscript); therefore, the term "new" has been deleted. If you have concerns with this course of action, please reword the sentence or explain why the deleted term should not be considered a priority claim and should be reinstated.
Q21	Would you consider changing "Microscopic model" to "The microscopic model" or "A microscopic model"?
Q22	Would you consider changing "observe" to "observed"?

Q23	Note that all data deposited in a publicly accessible database (and therefore not directly available in the paper or SI) must be cited in the text with an entry in the reference list. References must include the following information: 1) author names, 2) data/page title, 3) database name, 4) a direct URL to the data, 5) the date on which the data were accessed or deposited (not the release date). For an example reference entry, visit https://www.pnas.org/author-center/submitting-your-manuscript#manuscript-formatting-guidelines. Please also indicate where the new reference citation should be added in the main text and/or data availability statement. Please add a reference for the following data: 10.6084/m9.figshare.26139370.v1.
Q24	Please check the sentence "SFB 1027 and INM for funding. . ." for completeness.
Q25	In acknowledgments, PNAS articles should be accessible to a broad scientific audience; as such, please spell out the abbreviation EIC-ESMEA.
Q26	If you have any changes to your Supporting Information (SI) file(s), please provide revised, ready-to-publish replacement files without annotations.
Q27	Please provide the accessed date (DD/MM/YYYY) in ref. 42.

Innate immunity

Basic

Research Article

PIEZO1-mediated mechanosensing governs NK-cell killing efficiency and infiltration in three-dimensional matrices

Archana K. Yanamandra[1,2], Jingnan Zhang[2], Galia Montalvo[1,3,4], Xiangda Zhou[1], Doreen Biedenweg[5], Renping Zhao[1] (ID), Shulagna Sharma[1], Markus Hoth[1] (ID), Franziska Lautenschläger[3,4], Oliver Otto[5], Aránzazu del Campo[2,6] and Bin Qu[1] (ID)

[1] Biophysics, Center for Integrative Physiology and Molecular Medicine (CIPMM), School of Medicine, Saarland University, Homburg, Germany
[2] INM – Leibniz Institute for New Materials, Saarbrücken, Germany
[3] Department of Experimental Physics, Saarland University, Saarbrücken, Germany
[4] Center for Biophysics, Saarland University, Saarbrücken, Germany
[5] Institute of Physics, University of Greifswald, Greifswald, Germany
[6] Chemistry Department, Saarland University, Saarbrücken, Germany

Natural killer (NK) cells play a vital role in eliminating tumorigenic cells. Efficient locating and killing of target cells in complex three-dimensional (3D) environments are critical for their functions under physiological conditions. However, the role of mechanosensing in regulating NK-cell killing efficiency in physiologically relevant scenarios is poorly understood. Here, we report that the responsiveness of NK cells is regulated by tumor cell stiffness. NK-cell killing efficiency in 3D is impaired against softened tumor cells, whereas it is enhanced against stiffened tumor cells. Notably, the durations required for NK-cell killing and detachment are significantly shortened for stiffened tumor cells. Furthermore, we have identified PIEZO1 as the predominantly expressed mechanosensitive ion channel among the examined candidates in NK cells. Perturbation of PIEZO1 abolishes stiffness-dependent NK-cell responsiveness, significantly impairs the killing efficiency of NK cells in 3D, and substantially reduces NK-cell infiltration into 3D collagen matrices. Conversely, PIEZO1 activation enhances NK killing efficiency as well as infiltration. In conclusion, our findings demonstrate that PIEZO1-mediated mechanosensing is crucial for NK killing functions, highlighting the role of mechanosensing in NK-cell killing efficiency under 3D physiological conditions and the influence of environmental physical cues on NK-cell functions.

Keywords: 3D matrices · Killing efficiency · Mechanosensing · NK cells · PIEZO1

📱 Additional supporting information may be found online in the Supporting Information section at the end of the article.

Correspondence: Dr. Bin Qu
e-mail: bin.qu@uks.eu

Introduction

Natural killer (NK) cells belong to the innate immune system and are responsible for eliminating aberrant cells such as tumorigenic cells and pathogen-infected cells. In both physiological and

pathological conditions, NK cells must navigate through three-dimensional (3D) environments to locate their target cells. NK cells identify the cognate target cells through the engagement of their activating receptors with ligands on the target cell surface and/or detection of the absence of self-molecules using their inhibitory receptors [1]. Upon target cell recognition, NK cells form an intimate contact termed immunological synapse (IS) and reorient the killing machineries toward target cells [2]. The primary killing mechanism employed by NK cells is lytic granules containing cytotoxic proteins such as pore-forming protein perforin and serine protease granzymes. Lytic granules are enriched and released at the IS to induce apoptosis or direct lysis of target cells [3]. The release of lytic granules, also known as degranulation, is a hallmark of NK activation triggered by target cell recognition.

Stiffness is a physical characteristic that can differ significantly between healthy and diseased tissues, and stiffness at the tissue level and cell level can differ significantly. For instance, solid tumors are often stiffer than the neighboring healthy tissues primarily due to a highly compacted ECM [4]. Conversely, malignant cells with a high potential for metastasis are typically softer than their counterparts [5, 6]. Despite the extensive research on the functional role of chemical cues, the impact of stiffness on functions of immune killer cells, especially in killing-related processes, has only recently gained attention. For NK cells, stiffer substrates potentiate polarization of MTOC, enrichment and release of lytic granules, cytokine production, and the stability of the IS [7]. In addition, the actin retrograde flow at the IS, which regulates the NK-cell response, is influenced by substrate stiffness [8]. The stiffness of cancer cells typically ranges from a few hundred to a few thousand Pa [9–13]. The levels of substrate stiffness used to investigate the stiffness-regulated NK-cell function are often two to three orders of magnitude higher than the actual stiffness of cancer cells. Therefore, the precise effect of the physiological range of tumor cell stiffness on the effector functions and the corresponding killing efficiency of NK cells remains unclear.

To detect environmental stiffness, cells rely on mechanosensing through surface mechanosensors, mainly mechanically activated ion channels [14]. In this regard, the PIEZO family members are the most extensively studied mechanosensors. In T cells, PIEZO1-mediated mechanosensing of fluid shear stress has been found to potentiate T-cell activation [15]. Additionally, PIEZO1 activation at the IS is essential for optimal T-cell receptor signal transduction, potentially through PIEZO1-mediated Ca^{2+} influx [16]. In mice, the genetic deletion of PIEZO1 in T cells selectively expands Treg population and attenuates the severity of EAE, an animal model for MS [17]. In myeloid cells, PIEZO1-mediated mechanosensing of cyclical pressure, as experienced in lungs, plays a key role in the initiation of proinflammatory response elicited by macrophages and monocytes [18]. However, the functional roles of PIEZOs in NK cells have not been characterized.

In this study, we show that the efficiency of NK-cell-mediated target cell elimination is regulated by the stiffness of target cells.

Specifically, the cytotoxicity of NK cells is decreased against softer target cells and elevated against stiffer target cells. In human NK cells, mechanosensing is primarily mediated by PIEZO1, and the perturbation of PIEZO1 abolishes stiffness-dependent responsiveness of NK cells. Furthermore, PIEZO1-mediated mechanosensing governs the infiltration of NK cells into 3D collagen matrices, significantly impacting NK-cell killing efficiency in 3D scenarios. In summary, our results highlight the critical regulatory roles of mechanosensing in NK-cell-mediated target cell elimination in physiologically relevant 3D scenarios.

Results

NK-cell activation is regulated by surface stiffness

To investigate how the stiffness of target cells affects NK-cell responsiveness, we used functionalized hydrogels of various stiffness as a model system to mimic target cells as reported previously [19]. Specifically, we employed poly (acrylamide-*co*-acrylic acid) (PAAm-*co*-AA) hydrogels with Young's modulus of 2, 12, and 50 kPa functionalized with an activating antibody targeting NKp46 (Fig. 1A), which belongs to the natural cytotoxicity receptor family. The coating efficiency for the hydrogels with these three stiffness levels has been demonstrated the same in our previous work [19]. We used NK cells that were isolated from healthy donors and stimulated with IL-2 for 3 days. To evaluate NK activation, we settled NK cells on the functionalized hydrogels at 37°C for 4 h and assessed the degranulation of lytic granules based on the levels of CD107a on the surface of the NK cells. CD107a is exclusively expressed on the vesicular membrane of lytic granules and can only be integrated into the plasma membrane of NK cells after lytic granule release [20]. Based on activation-triggered degranulation, we found that NK cells fell into four categories: only activated on 50 kPa (5 out of 12 donors, Fig. 1B), only activated on 12 kPa (3 out of 12 donors, Fig. 1C), activated on all three stiffness levels (2 out of 12 donors, Fig. 1D), or no response (2 out of 12 donors, Fig. 1E). Importantly, degranulation was only triggered by the activation of NKp46, as isotype IgG-coated hydrogels did not induce degranulation (Fig. 1B–D, isotype). Notably, NK cells from most donors (10 out of 12) did not respond to very soft hydrogels (2 kPa) (Fig. 1F and G). These findings show that NK cells cannot be fully activated on soft substrates, which is consistent with the reports from the others [7, 8]. Based on these results, we hypothesized that softening target cells would impair NK killing capacity.

Target cell stiffness modulates NK-cell cytotoxicity

To test this hypothesis, we softened the target cells (K562 cells) by DMSO treatment as determined by real-time deformability cytometry (RT-DC) (Fig. 2A). The K562 cells used in our study stably express a FRET-based apoptosis reporter pCasper (K562-pCasper), consisting of a GFP and RFP pair linked by a caspase
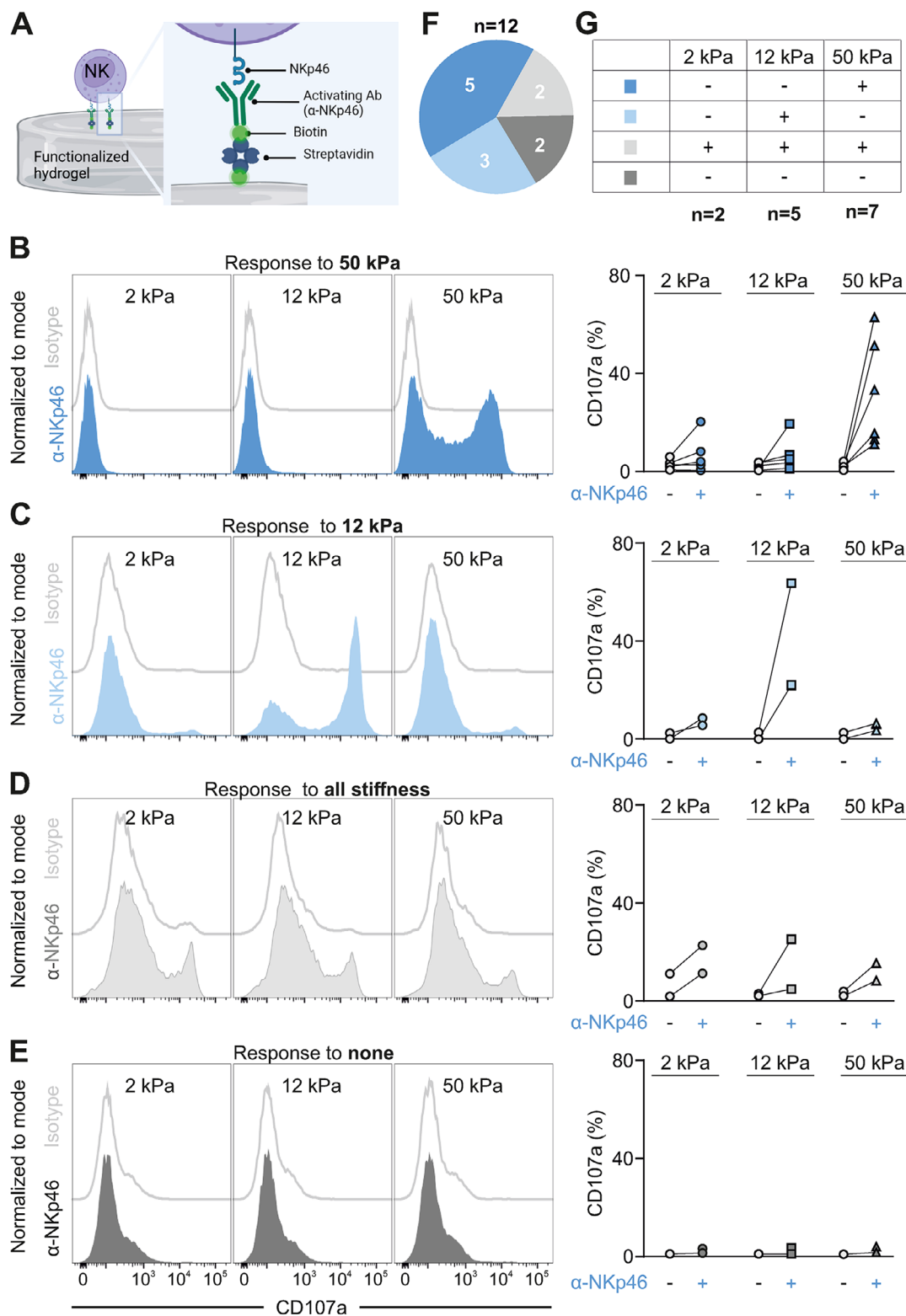
Figure 1. Natural killer (NK)-cell responsiveness to varying levels of substrate stiffness. Primary human NK cells from healthy donors were stimulated with IL-2 for 3 days prior to the experiments. (A) Sketch of functionalization of hydrogels. PAAm-*co*-AA hydrogels were first treated with streptavidin and then incubated with biotinylated anti-NKp46 antibodies. (B–E) NK-cell responsiveness is substrate stiffness-dependent. The activation of NK cells was evaluated using the CD107a degranulation assay. The NK cells were settled on functionalized hydrogels at 37°C with 5% CO_2 for 4 h in the presence of anti-CD107a antibody and Golgi Stop. The samples were then analyzed using flow cytometry. The NK cells responded to 50 kPa (B, *n* = 5), 12 kPa (C, *n* = 3), all stiffness levels (D, *n* = 2), or did not respond to any stiffness (E, *n* = 2). One representative donor is shown in the left panel, and the quantification of all donors is shown in the right panel. (F and G) Summary of the NK-cell responsiveness from different donors.
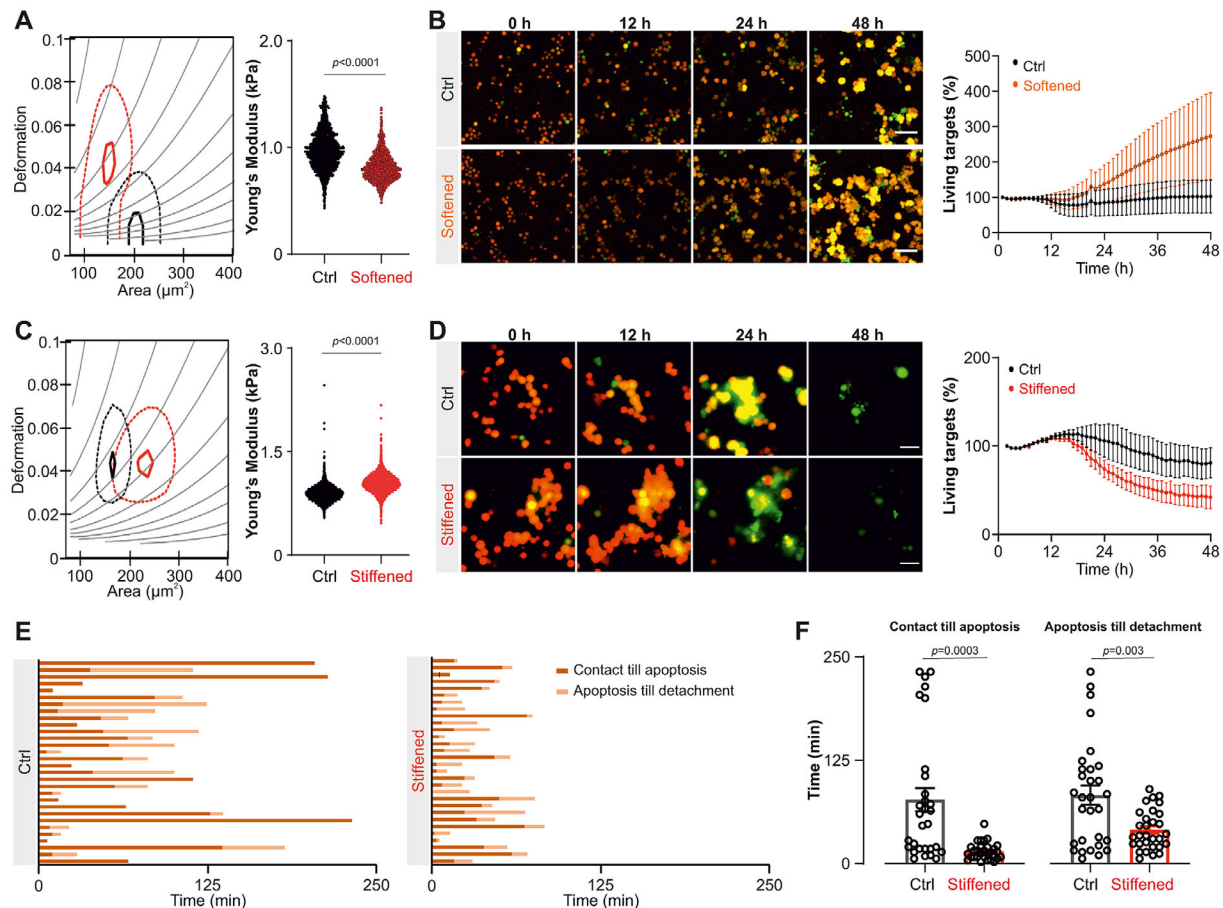
Figure 2. The killing efficiency of natural killer (NK) cells in three-dimensional (3D) scenarios is regulated by tumor cell stiffness. Primary human NK cells from healthy donors were stimulated with IL-2 for 3 days prior to the experiments. K562-pCasper target cells were embedded in collagen matrices (2 mg/mL), and the NK cells were added from the top. Live target cells are in orange–yellow and apoptotic target cells in green. (A and B) Softening tumor cells impairs NK-cell killing efficiency in 3D. K562-pCasper cells were pretreated with DMSO (1:2000, softened) for 12 h. Their stiffness was determined using real-time deformability cytometry (RT-DC) (A). Time lapse of killing events was obtained in 10× magnification, and the quantification is shown in (B). (C and D) NK cells eliminate stiffened tumor cells more efficiently. K562-pCasper cells were pretreated with blebbistatin (50 μM, stiffened) for 12 h. Their stiffness was determined using RT-DC (C). Statistical analysis for RT-DC was done using linear mixed models. Time lapse of killing events was obtained in 20× magnification, and the quantification is shown in (D). (E and F) The duration required for NK-cell killing and detachment from the stiffened tumor cells is shortened. K562-pCasper target cells were treated with DMSO (Ctrl) or blebbistatin (stiffened). The NK cells were coincubated with target cells for 4 h. The NK cells were tracked manually. The duration required for each killing event (the time from the initiation of NK/target contact to target cell apoptosis) and the duration required for NK-cell detachment (the time from the initiation of NK/target contact to disengagement of NK cells from the targets) for all NK cells analyzed are shown in the left and right panels of (E), respectively. The quantification of these durations is shown in (F). For statistical analysis, the Mann–Whitney–*U*-test was used. The results were from at least three independent experiments. The data are presented as mean ± SEM. Scale bars are 40 μm.

recognition site (DEVD) [21]. Upon the initiation of apoptosis, the orange target cells lose their FRET signal and turn green. In the case of necrosis, fluorescent proteins would leak out of the destroyed plasma membrane, resulting in the complete loss of fluorescence. To evaluate NK-cell killing efficiency in a 3D environment, we embedded K562-pCasper target cells in bovine type I collagen and added IL-2-stimulated primary human NK cells from the top after solidification. This setup allows NK cells to infiltrate the collagen matrix and search for their target cells in a physiologically relevant scenario. We monitored killing events at 37°C every 20 min for 48 h using a high-content imaging system. Our results show that the killing efficiency of NK cells against softened target cells was reduced compared to that against the control

group (Fig. 2B, Supporting Information Movie 1). These findings suggest that the softening of tumor cells weakens NK-cell killing capacity.

Next, we examined whether increasing the stiffness of tumor cells could have the opposite effect. To do this, we used blebbistatin, a myosin IIA inhibitor known to enhance the stiffness of cells in suspension by perturbing actomyosin contractility [22]. Our analysis of RT-DC revealed that blebbistatin treatment reduced the deformability of target cells, indicating an increase in their stiffness relative to vehicle-treated control cells (Fig. 2C). Consistent with the postulation, we observed an elevated killing efficiency of NK cells against the stiffened blebbistatin-treated tumor cells (Fig. 2D, Supporting Information Movie 2). Notably,
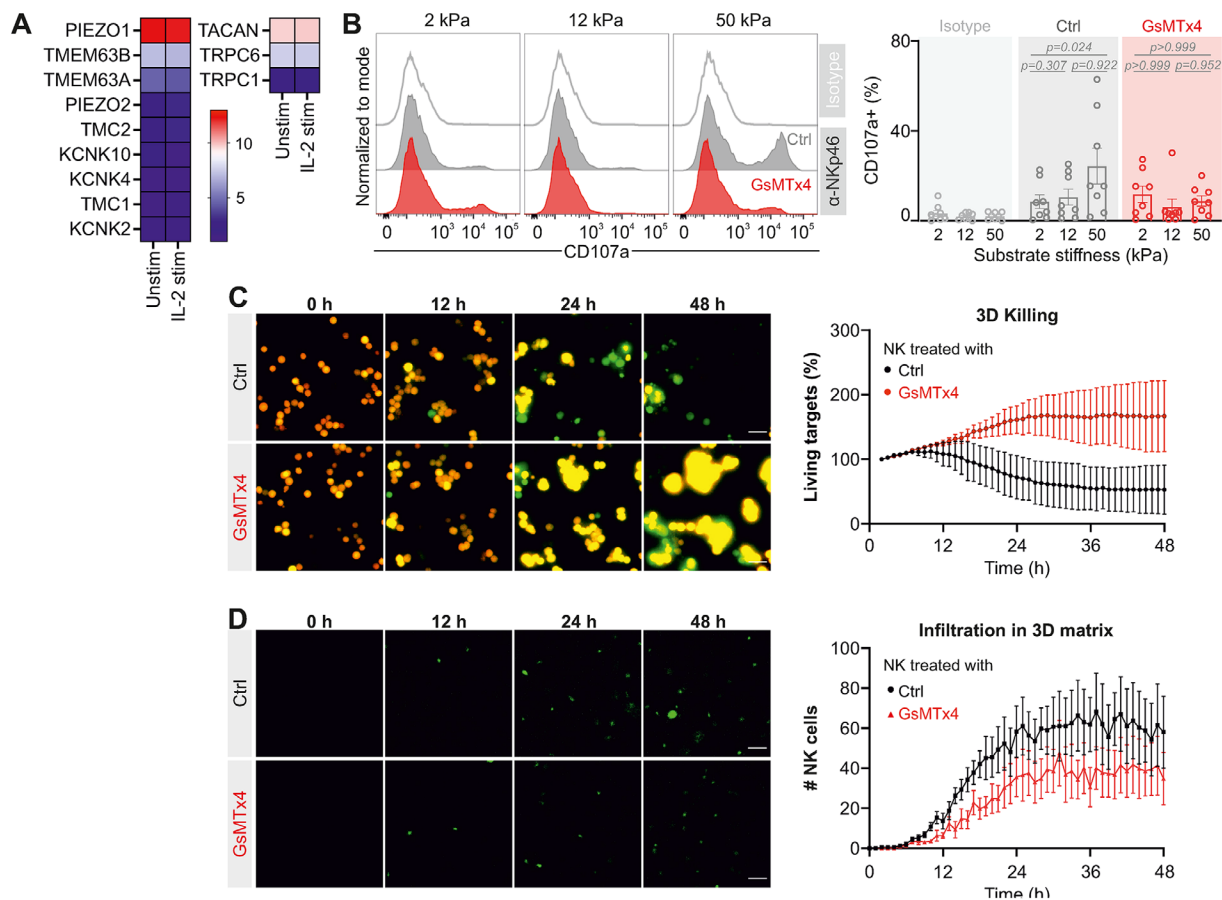
Figure 3. Inhibition of PIEZO1 reduces natural killer (NK)-cell killing efficiency in three-dimensional (3D). Primary human NK cells from healthy donors were stimulated with IL-2 for 3 days. (A) Heatmap for the expression of mechanosensitive ion channels in unstimulated and IL-2-stimulated NK cells. The analysis is based on previously published microarray data [45]. (B) GsMTx4 (50 μM) treatment abolishes substrate stiffness-dependent NK cell responsiveness. The activation of NK cells was evaluated using the CD107a degranulation assay. One representative donor is shown in the left panel, and the quantification of all donors ($n = 8$) is shown in the right panel. The Friedman test with Dunn's multiple comparisons test was used for statistical analysis. (C) The killing efficiency of GsMTx4-treated NK cells in 3D is impaired. K562-pCasper target cells were embedded in collagen matrices (2 mg/mL), and the NK cells were added from the top. Live target cells are in orange–yellow and apoptotic target cells in green. Time lapse of one representative donor is shown in the left panel, and the quantification of all donors ($n = 3$) is shown in the right panel. (D) GsMTx4-treated NK cells exhibit enhanced capability of infiltration into collagen matrices. The NK cells were stained with carboxyfluorescein succinimidyl ester (CFSE) and added on the top of solidified collagen matrices (2 mg/mL). The NK cells approaching the bottom were visualized (left panel) and quantified (right panel, $n = 4$). A 20× magnification was used to obtain the images. The data are presented as mean ± SEM. Scale bars are 40 μm.

treatment with DMSO or blebbistatin exhibited no impact on the proliferation kinetics of the K562-pCasper cells (Supporting Information Fig. 1), and the altered stiffness could persist (Supporting Information Fig. 2), reinforcing our conclusion that the observed changes in killing efficiency against DMSO- or blebbistatin-treated target cells are not a result of alterations in proliferation kinetics per se, but rather attributable to changes in target cell stiffness. Furthermore, analysis of live cell imaging showed a significant reduction in the time required for NK killing (i.e. duration from contact to apoptosis) and the total contact time between NK and target cells (i.e. duration from contact till detachment) in the case of stiffened tumor cells compared to the control group (Fig. 2E and F). Together, these results suggest that the stiffness of target cells has a significant impact on the outcome of NK killing efficiency.

PIEZO1 mediates NK-cell responsiveness to target cell stiffness

Mechanosensing is crucial for cells to detect the stiffness of surrounding environment and the cells they encounter. Among the mechanosensitive channels, PIEZO1 is the most predominantly expressed in primary human NK cells (Fig. 3A). Both unstimulated and stimulated NK cells expressed high levels of PIEZO1 protein, with the majority (>95%) of NK cells expressing PIEZO1 (Supporting Information Fig. 3A). PIEZO1 is present on the plasma membrane, exhibiting a distribution pattern similar to F-actin (Supporting Information Fig. 3B). To examine the functional role of PIEZO1 in stiffness-regulated NK activation, we used GsMTx4, a peptide isolated from spider venom that inhibits the mechanosensitivity of PIEZO1 [23]. Our results show that the
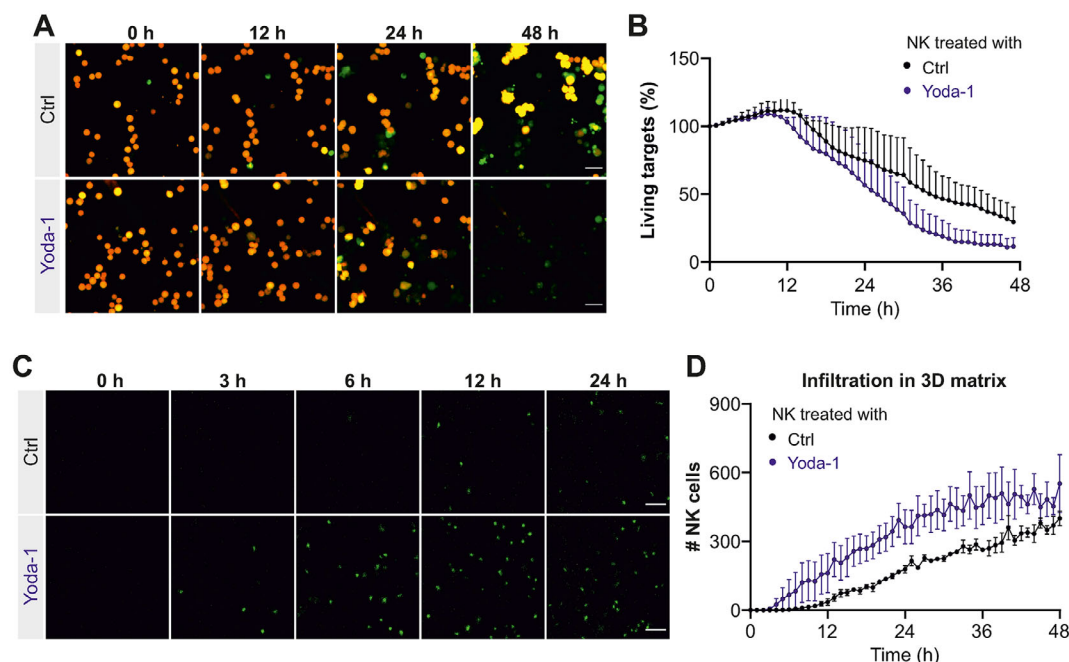
Figure 4. PIEZO1 activation enhances natural killer (NK)-cell killing efficiency in three-dimensional (3D). Primary human NK cells from healthy donors were stimulated with IL-2 for 3 days. Yoda-1 (1 μM) was present in the medium during the experiments. (A and B) Yoda-1 treatment enhances the killing efficiency of NK cells in 3D. K562-pCasper target cells were embedded in collagen matrices (2 mg/mL), and the NK cells were added from the top. Live target cells are in orange–yellow, and apoptotic target cells in green. Time lapse of one representative donor is shown in (A), and the quantification of all donors ($n = 3$) is shown in (B). (C and D) NK infiltration into 3D collagen matrices is enhanced by Yoda-1 treatment. The NK cells were stained with carboxyfluorescein succinimidyl ester (CFSE) and added on the top of solidified collagen matrices (2 mg/mL). The NK cells approaching the bottom were visualized (C) and quantified (D, $n = 3$). A 20× magnification was used to obtain the images. The data are presented as mean ± SEM. Scale bars are 40 μm.

surface stiffness-dependent degranulation of NK cells was completely abolished by GsMTx4 treatment (Fig. 3B), indicating that PIEZO1 plays a pivotal role in mediating mechanosensing in NK cells.

To investigate the effects of PIEZO1 perturbation on NK-cell killing function, we further evaluated NK-cell killing efficiency in a 3D scenario. Results from the 3D killing assay showed that GsMTx4-treated NK cells exhibited a substantially reduced killing efficiency compared to the control group (Fig. 3C, Supporting Information Movie 3). Stiffness of the target cells was not affected by the presence of GsMTx4 (Supporting Information Fig. 4A). To explore the underlying mechanisms, we examined the lytic granule pathway and NK-cell migration. We found that GsMTx4 treatment did not alter the expression of cytotoxic proteins such as perforin and granzyme B (Supporting Information Fig. 4B). Furthermore, degranulation induced by target cell recognition was even slightly enhanced (Supporting Information Fig. 4C). Notably, the numbers of NK cells that infiltrated the 3D collagen matrix were greatly reduced after GsMTx4 treatment (Fig. 3D, Supporting Information Movie 4). Aside from PIEZO1, GsMTx4 also targets a few other mechanically activated ion channels, such as TRPC1, TRPC6, and TACAN. Although the expression levels of TRPC1, TRPC6, and TACAN are very low, if not negligible, compared to PIEZO1 (Fig. 3A). These observations suggest that PIEZO1-mediated mechanosensing is crucial for NK cells to execute their

killing function in 3D mainly by regulating NK infiltration into the 3D matrix.

To further validate the effect of PIEZO1, we used a PIEZO1-specific agonist, Yoda-1 [24] (Supporting Information Fig. 5). Indeed, Yoda-1-treatment of NK cells accelerated killing kinetics in 3D collagen matrices with a significant reduction in the initiation time of killing events (Fig. 4A and B, Supporting Information Movie 5). No difference was observed in degranulation induced by target cell recognition (Supporting Information Fig. 6A), or in the conjugation between NK cells and target cells (Supporting Information Fig. 6B) for Yoda-1-treated NK cells. Interestingly, infiltration of NK cells into 3D collagen matrix was substantially accelerated by Yoda-1 treatment (Fig. 4C and D, Supporting Information Movie 6). Vehicle-treated NK cells first appeared in the focal plane at 6.6 ± 1.6 h, whereas first Yoda-1-treated NK cells approached the focal plane at around 4.8 ± 1.7 h (Fig. 4D). In addition, in a matrix-free environment, Yoda-1 treatment enhanced NK killing efficiency against both nontreated and softened tumor cells (Supporting Information Fig. 7A and B), whereas the inhibition of PIEZO1 using GsMTx4 hindered NK killing against stiffened target cells (Supporting Information Fig. 7C), indicating that PIEZO1 can directly regulate the killing capacity of NK cells. Our results collectively suggest that PIEZO1 regulates both the NK killing processes and infiltration capability into 3D matrix,

thereby fine-tuning the ultimate outcomes of tumor cell elimination.

Discussion

In our study, we have demonstrated that the killing efficiency of NK cells can be modulated by manipulating the stiffness of target cells. Cell softening is a recently discovered characteristic of malignant tumor cells, which is associated with tumorigenicity and malignancy. A rich body of evidence proves that cancer cells are softer than their nonmalignant normal counterparts [25]. For example, cancerous breast epithelial cells are more deformable than their normal counterparts as determined by optical stretching [26]. Ovarian cancer cells have Young's modulus in the range of 0.5–1 kPa, whereas their nonmalignant counterparts have a stiffness of around 2 kPa, as determined by atomic force microscopy [9]. Similarly, cervical cancer cells have an elastic modulus of ∼2 kPa, which is lower than that of normal human cervix epithelial cells (elastic modulus E ∼4–5 kPa) [10]. Notably, even among malignant cells, the stiffness can vary, and softer cancer cells exhibit enhanced tumorigenicity, metastasis, and stemness. For example, between two ovarian cancer cell lines from the same specimen, the soft cells (HEY A8, ∼0.5 kPa) are more invasive than their stiffer counterparts (HEY, ∼0.9 kPa) [9]. Soft cancer cells (breast cancer and melanoma cells, ∼0.2–0.3 kPa) require only ten cells to generate metastatic tumors in the lungs, whereas even 100 stiff cancer cells (∼0.8–1 kPa) are unable to produce any detectable lung metastasis [12]. Softer cancer cells not only form more colonies with bigger sizes in vitro but also have a substantially higher frequency of forming tumors in vivo [12]. Stemness-associated genes are also upregulated in soft tumor cells [12]. Additionally, a study using cancer organoids embedded in 3D collagen has shown that cancer cells at the peripheral region are softer than the cells in the core region, and softer cancer cells are more invasive and metastatic [13]. Tumor cells can be further softened by migration through confined spaces [13]. In our study, the stiffness of nontreated tumor cells (∼1 kPa), softened tumor cells (∼0.6–0.7 kPa), or stiffened tumor cells (∼1.2–1.4 kPa) falls within the range of physiological stiffness as reported in the aforementioned studies. Our results demonstrate that softening (or stiffening) tumor cells substantially reduces (or enhances) elimination by NK cells, providing direct evidence supporting the hypothesis that cell softening is a mechanism by which malignant cells evade immune surveillance.

How does the softening or stiffening of tumor cells affect the cytotoxicity of NK cells? In the process of cell killing, several key steps are critical, such as the initiation of IS formation, lytic granule enrichment and release, cytotoxic protein uptake by target cells, and the detachment of NK cells after killing. Our study shows that softening or stiffening of tumor cells does not significantly alter lytic granule release, indicating that the events upstream of lytic granule release, such as IS formation and lytic granule enrichment, are unlikely to be significantly affected. However, we observed that the duration required to induce apopto-

sis or necrosis of tumor cells is prolonged for softened tumor cells compared to their stiff counterparts. Perforin-mediated pore formation on the plasma membrane of target cells is a critical step for directly lysing target cells or facilitating granzyme entry into target cells to induce apoptosis. Reduced tension of target cells impairs perforin-mediated pore formation and perforin-dependent killing [27]. Therefore, to kill softened tumor cells, NK cells likely need to release more perforin or require more time to form the pores. Both scenarios require a longer duration for the killing process.

Following a successful killing, NK cells must detach from the dying or dead target cells in a timely manner to search for other targets and carry out more killing. Intriguingly, our observations show that the duration from the initiation of target cell apoptosis to the detachment of NK cells from stiffened target cells is substantially shorter than that from their softer counterparts. This finding suggests that alteration in tumor cell stiffness may influence the process of NK-cell detachment. It is reported that conjugation with newly identified target cells can accelerate NK-cell detachment from old target cells [28] and failed NK-cell killing is linked to extended contact times [29, 30]. Thus, the shortened contact times we observed for stiffened tumor cells possibly owe to more efficient NK-cell killing. Studies on cytotoxic T lymphocytes suggest that recovery of cortical actin at the IS is essential to terminate lytic granule secretion, suggestively enabling or promoting T cells to detach from their target cells [31]. PKCθ is required to break the symmetry of the IS, allowing naive T cells to disengage from their target cells [32]. Additionally, calcium influx in T cells and apoptotic contraction also contribute to T-cell disengagement from a target cell [33, 34]. Therefore, it is possible that NK cells employ similar mechanisms to terminate killing processes and disassemble the IS, which is necessary for detachment from target cells. Interestingly, cell stiffness changes or increases after cell death [35, 36], which can serve as a direct cue to initiate NK-cell detachment.

Recent studies have revealed that mechanical cues, particularly stiffness, can regulate the functions of NK cells. When primary human NK cells are stimulated with IL-2 on MICA-functionalized substrate with varying stiffness (30, 150, and 3000 kPa), they exhibit a bell-shaped response, with the maximum degranulation and clustering of DAP10 (an adaptor molecule downstream of NKG2D) occurring at 150 kPa [37]. The application of mechanical forces to NK cells via MICA-functionalized nanowires (diameter ∼ 50 nm) enhances lytic granule degranulation upon NKG2D activation [38]. Similarly, stiffer sodium alginate beads (34 and 254 kPa) functionalized with NKp30 antibody can induce full NK-cell activation characterized by MTOC translocation and lytic granule polarization, whereas softer beads (9 kPa) failed to do so [7]. Our data also suggest that NK cells exhibit greater degranulation triggered by activating receptors on stiffer hydrogels (12 and 50 kPa) compared to soft hydrogels (2 kPa) for most donors. However, for some donors, the levels of degranulation were comparable across all three stiffness levels. This variability is not associated with different expression levels of PIEZO1, as PIEZO1 expression levels

are in a comparable range for various donors. Our findings suggest that NK-cell responsiveness to stiffness is donor-dependent and may be attributed to variations in the expression of additional effector molecules involved in mechanosensing or transduction.

Mechanical cues are detected by various professional mechanosensors, primarily mechanosensitive ion channel families, among which are the PIEZO family, TREK/TRAAK K2P (two-pore potassium) channels, TMEM63 (hyperosmolality-gated calcium-permeable) channels, and TMC (transmembrane channel-like) 1/2 [14, 39]. In our study, we report that PIEZO1 is the predominant mechanosensitive channel expressed in NK cells, indicating its indispensable role in mechanotransduction in NK cells. We observed that inhibiting PIEZO1 using GsMTx4 nearly abolished NK-cell responsiveness to different substrate stiffness, greatly impaired NK-cell-mediated cytotoxicity, and substantially reduced NK-cell infiltration into 3D collagen matrices. Conversely, activating PIEZO1 with Yoda-1 enhanced the killing efficiency and infiltration capacity of NK cells. These findings demonstrate that PIEZO1-mediated mechanosensing is crucial for NK killing functions, highlighting PIEZO1 as a promising target to modulate NK functions, particularly in the context of solid tumors.

Materials and methods

Antibodies and reagents

The following antibodies were purchased from BioLegend: PerCP anti-human CD3, BV421 anti-human CD3, APC anti-human CD56, BV421 anti-human CD107a, Biotin anti-human NKp46 (CD335), Biotin Mouse IgG1-κ Isotype, BV421 anti-human perforin, PE anti-human perforin, and PE anti-human granzyme B. Calcein-AM and carboxyfluorescein succinimidyl ester (CFSE) were purchased from Thermo Fischer Scientific, GsMTx4 from Smartox Biotechnology, blebbistatin from Cayman Chemical, Yoda-1 from Tocris, and Fibricol Collagen solution (10 mg/mL bovine type I) from Advanced Biomatrix.

Cell culture

Human peripheral blood mononuclear cells (PBMCs) of healthy donors were isolated from the Leukocyte Reduction System Chamber using a gradient centrifugation method with Lymphocyte Separation Medium 1077 (PromoCell). Primary NK cells were isolated from the PBMCs using a human NK-cell isolation kit (Miltenyi) and then cultured in AIM V media with 10% FCS in the presence of recombinant human IL-2 (100 U/mL, Miltenyi) for 3 days, unless mentioned otherwise. The purity is higher than 96%. As for K562 and K562-pCasper cells, they were cultured in RPMI medium supplemented with 10% FCS and 1% penicillin and streptomycin (Thermo Fischer Scientific). For K562-pCasper cells, which stably express a FRET-based apoptosis reporter [21], the

culture medium was additionally supplemented with puromycin (0.2 μg/mL) (VWR).

Preparation and biofunctionalization of hydrogels

Poly(acrylamide-*co*-acrylic acid) (PAAm-*co*-AA) hydrogels of varying stiffness were prepared and functionalized as previously described [19]. Briefly, AAm monomer and bis-AAm crosslinker were mixed in different ratios, maintaining a constant ratio of AA. Hydrogel discs were prepared between two coverslips. PAAm-*co*-AA hydrogels were first functionalized with biotin-PEG8-NH2 by an EDC/NHS activation step as follows. The PAAm-*co*-AA film was covered with 100 μL EDC/NHS solution (39/12 mg in 0.1 M, pH 4.5 MES buffer) for 15 min, washed thoroughly with PBS, and directly incubated with 100 μL of biotin-PEG8-NH2 (1 mg/mL) solution in a Petri dish for 2 h at RT. The functionalized hydrogels were washed with PBS three times and kept in PBS at 4°C until use. Functionalized hydrogels of varying stiffness were then incubated with streptavidin solution (100 μL, 100 μg/mL) for 1–1.5 h (2 kPa) or 2.5–3 h (12 and 50 kPa) according to a previously reported protocol [19]. Streptavidin-functionalized hydrogels were then incubated with biotinylated anti-NKp46 (100 μg/mL, 30 μL) or IgG isotype (100 μg/mL, 30 μL) overnight at 4°C.

CD107a degranulation assay

To assess stimulation-induced NK degranulation, NK cells were either settled on substrates functionalized with NKp46 antibody or incubated with K562 cells in the presence of BV421 anti-CD107a antibody and protein transport inhibitor Golgi stop (BD Biosciences) at 37°C with 5% CO_2 for 4 h. Then the cell suspension was stained with PerCP anti-human CD3, APC anti-human CD56 antibodies at 4°C in dark for 30 min. The samples were analyzed using FACSVerse (BD Biosciences). The $CD3^-CD56^+$ population was gated for NK cells. FlowJo v10 (FLOWOJO, LLC) was used for data analysis.

Determination of NK-cell killing kinetics

To determine NK killing efficiency in 3D environments, the assay was conducted as described previously [40]. Briefly, K562-pCasper target cells were resuspended in neutralized bovine collagen I (2 mg/mL) and plated in a black 96-well plate with flat clear bottom (Corning/Merck) at a density of 25 000 cells/40 μL per well. The plate was centrifuged to spin down the target cells on the bottom and then polymerized at 37°C with 5% CO_2 for 1 h. NK cells were added on the top of the collagen matrix with an E:T ratio of 1:1 if not otherwise specified. A high-content imaging system ImageXpress (Molecular Devices) was used to acquire images at 37°C with 5% CO_2 every 20 min for 48 h. K562-pCasper target cells with a FRET signal above the threshold (maximal FRET

signals in GFP-positive target cells) were taken as live target cells. The number of live target cells at each time point was normalized to that at time 0. AIMV medium supplemented with 10% FCS was used in this assay. The images were processed and analyzed using ImageJ.

To determine NK killing capacity in a matrix-free 2D scenario, K562-pCasper target cells were settled in a 96-well half-area microplate with clear flat bottom (Corning/Merck) at a density of 25 000 cells per well at RT for 20 min. Subsequently, NK cells were added from above with an E:T ratio of 0.5:1. Killing events were visualized using ImageXpress at 37°C with 5% CO_2 every 20 min for 8 h.

NK-cell migration in 3D collagen matrices

NK cells were stained with CFSE (5 μM in PBS/4.5% FCS) at room temperature for 15 min, washed once with PBS, then resuspended in AIMV/10% FCS, and kept at 37°C with 5% CO_2 overnight for recovery. Sample preparation for light-sheet microscopy was described previously [41]. Briefly, CFSE-stained NK cells were resuspended in neutralized bovine collagen I (2 mg/mL), and this cell suspension was polymerized in a capillary at 37°C with 5% CO_2 for 1 h. Subsequently, the sample was mounted in the sample chamber filled with RPMI medium. *Z*-stacks (step size ~2 μm for ~100 slices) were acquired using a Z.1 light-sheet microscope (Zeiss) at 37°C every 30 s for 30 min. Imaris 8.1.2 (Bitplane) was used to automatically track fluorescently labeled NK cells to quantify cell velocity and persistence.

Analysis of NK-cell infiltration into 3D collagen matrices

NK cells were stained with CFSE (5 μM in PBS/4.5% FCS) at room temperature for 15 min, washed once with PBS, then resuspended in AIMV/10% FCS, and kept at 37°C with 5% CO_2 overnight for recovery. Neutralized bovine collagen I (2 mg/mL) was plated 40 μL per well in a black 96-well plate with flat clear bottom (Corning/Merck). The plate was kept at 37°C with 5% CO_2 for 1 h. After solidification, CFSE-stained NK cells (25 000 cells/well) were added on the top of the matrix. To identify the position of the bottom, one well plated with NK cells without collagen was used as reference. Images focused on the bottom were acquired using ImageXpress at 37°C with 5% CO_2 every 20 min for 48 h. ImageJ was used to identify fluorescently labeled NK cells and quantify the number of infiltrated NK cells for each time point.

Determination of cytotoxic protein expression

NK cells were washed twice with PBS containing 0.5% BSA, then stained with PerCP anti-human CD3, APC anti-human CD56 antibodies at 4°C in dark for 30 min. To assess the expression of perforin and granzyme B, these prestained NK cells were fixed

with prechilled 4% paraformaldehyde (PFA) for 20 min, permeabilized with PBS containing 0.1% saponin, 0.5% BSA, and 5% FCS at room temperature for 10 min, then stained with BV421 anti-human perforin and PE anti-human granzyme B antibodies at room temperature in dark for 40 min. The samples were analyzed using FACSVerse (BD Biosciences). The $CD3^-CD56^+$ population was gated for NK cells. FlowJo v10 (FlowJo, LLC) was used for data analysis.

Real-time deformability cytometry (RT-DC)

To assess the stiffness of K562-pCasper cells, RT-DC (Zellmechanik Dresden) was used [42]. K562-pCasper were either treated with DMSO or Blebbistatin for 12 h, after which they were resuspended in 100 μL of cell carrier B solution (PBS with the addition of long-chain methylcellulose polymers of 0.6 w/v%). A microfluidic PDMS chip with a 300 μm long central constriction of 30 μm × 30 μm cross-section was assembled on the stage of an inverted microscope (Zeiss). The cell suspension was loaded on the chip using a syringe pump. The cells flowing through the microfluidic channel deform due to the shear stresses and pressure gradient caused by the flow profile [43]. Each event is imaged live using a CMOS camera and analyzed in real-time. At least 3000 events were acquired per condition at a flowrate of 0.16 μL/s. The mechanical properties of the cells were analyzed using Shape Out 2 (Zellmechanik Dresden), which employs linear mixed models to calculate statistical significances.

Immunostaining

NK cells stimulated with 100 U/mL IL-2 for 3 days were seeded on the poly-L-ornithine-coated coverslip for 15 min at RT, then were fixed with 4% PFA, and permeabilized with 0.1% Triton-100 in PBS at RT for 15 min, followed by a blocking step with 2% BSA in PBS at RT for 1 h. Samples were incubated with anti-PIEZO1 antibody at 4°C overnight and then with Alex488 goat anti-rabbit secondary antibody. F-actin and nucleus are labeled with phalloidin and Hoechst 33342, respectively. The images were acquired by Cell Observer wide-field microscopy with 40× oil objective (1.3 NA) with a step size of 0.3 μm for *Z*-stacks. The acquired images were deconvolved using the Huygens Essential Software.

Ca^{2+} imaging

Ca^{2+} imaging was carried out as described previously [44]. Briefly, Jurkat T cells were loaded with Fura-2-AM (1 μM) at RT for 25 min, resuspended in 1 mM Ca^{2+} Ringer's solution, and then seeded on a poly-L-ornithine-coated coverslip. Live-cell imaging was acquired excitation of 340 nm, 380 nm, and infrared every 5 s at RT. After the first 30 cycles, measurements were paused, and Yoda (1 μM in 1 mM Ca^{2+} Ringer's solution) was perfused into the chamber, and then the measurements were resumed. This time point was defined as Time 0. The images were analyzed using T.I.L.L. Vision software.

Ethical considerations

Research carried out for this study with material from healthy donors (Leukocyte Reduction System Chambers from human blood donors) has been authorized by the local ethics committee of the "Ärztekammer des Saarlandes" (Identification Nr. 84/15, Prof. Dr. Rettig-Stürmer).

Statistical analysis

GraphPad Prism 8.3 Software (GraphPad) was used for statistical analysis. For RT-DC, linear mixed models were used. For other statistical analyses, D'Agostino and Pearson tests were used to test the normality. Between two paired groups, paired *t*-test was used for normal distribution, and a Wilcoxon matched-pairs signed rank test was used for nonnormal distribution. Between two unpaired groups, unpaired *t*-test was used for normal distribution and Mann–Whitney–*U*-test was used for nonnormal distribution. To compare three or more groups, one-way ANOVA test was used, and multiple comparisons were done with Dunn's multiple comparisons test.

Conflict of interest: Oliver Otto is shareholder of Zellmechanik Dresden distributing technology for real-time deformability cytometry.

Author contributions: AKY performed most of the experiments and the corresponding analysis, if not mentioned otherwise; Jingnan Zhang prepared hydrogels; Xiangda Zhou performed real-time killing assay and the analysis and helped with image processing, figures, and movies; Galia Montalvo, Franziska Lautenschläger, Doreen Biedenweg, and Oliver Otto helped with RT-DC; Renping Zhao performed immunostaining and Ca^{2+} imaging; Shulagna Sharma examined the purity of NK cells and PIEZO1 expression; Markus Hoth and Aránzazu del Campo helped with data interpretation and provided critical feedback on all aspects

of the project; Bin Qu generated concepts and designed experiments; All authors contributed to the writing, editing, and cross-checking of the manuscript.

Data availability statement: The data that support the findings of this study are available from the corresponding author upon reasonable request.

References

1 Sivori, S., Vacca, P., Del Zotto, G., Munari, E., Mingari, M. C. and Moretta, L., Human NK cells: surface receptors, inhibitory checkpoints, and translational applications. *Cell. Mol. Immunol.* 2019. **16**: 430–441.

2 Orange, J. S., Formation and function of the lytic NK-cell immunological synapse. *Nat. Rev. Immunol.* 2008. **8**: 713–725.

3 Krzewski, K. and Coligan, J. E., Human NK cell lytic granules and regulation of their exocytosis. *Front. Immunol.* 2012. **3**: 335.

4 Pickup, M. W., Mouw, J. K. and Weaver, V. M., The extracellular matrix modulates the hallmarks of cancer. *EMBO Rep.* 2014. **15**: 1243–1253.

5 Rianna, C., Radmacher, M. and Kumar, S., Direct evidence that tumor cells soften when navigating confined spaces. *Mol. Biol. Cell* 2020. **31**: 1726–1734.

6 Roberts, A. B., Zhang, J., Raj Singh, V., Nikolić, M., Moeendarbary, E., Kamm, R. D., So, P. T. C., et al., Tumor cell nuclei soften during transendothelial migration. *J. Biomech.* 2021. **121**: 110400.

7 Friedman, D., Simmonds, P., Hale, A., Bere, L., Hodson, N. W., White, M. R. H. and Davis, D. M., Natural killer cell immune synapse formation and cytotoxicity are controlled by tension of the target interface. *J. Cell. Sci.* 2021. **134**: jcs258570.

8 Matalon, O., Ben-Shmuel, A., Kivelevitz, J., Sabag, B., Fried, S., Joseph, N., Noy, E., et al., Actin retrograde flow controls natural killer cell response by regulating the conformation state of SHP-1. *EMBO J.* 2018. **37**: e96264.

9 Xu, W., Mezencev, R., Kim, B., Wang, L., Mcdonald, J. and Sulchek, T., Cell stiffness is a biomarker of the metastatic potential of ovarian cancer cells. *PLoS One* 2012. **7**: e46609.

10 Hayashi, K. and Iwata, M., Stiffness of cancer cells measured with an AFM indentation method. *J. Mech. Behav. Biomed. Mater.* 2015. **49**: 105–111.

11 Han, Y. L., Pegoraro, A. F., Li, H., Li, K., Yuan, Y., Xu, G., Gu, Z., et al., Cell swelling, softening and invasion in a three-dimensional breast cancer model. *Nat. Phys.* 2020. **16**: 101–108.

12 Lv, J., Liu, Y., Cheng, F., Li, J., Zhou, Y., Zhang, T., Zhou, N., et al., Cell softness regulates tumorigenicity and stemness of cancer cells. *EMBO J.* 2021. **40**: e106123.

13 Rianna, C., Radmacher, M. and Kumar, S., Direct evidence that tumor cells soften when navigating confined spaces. *Mol. Biol. Cell* 2020. **31**: 1726–1734.

14 Kefauver, J. M., Ward, A. B. and Patapoutian, A., Discoveries in structure and physiology of mechanically activated ion channels. *Nature* 2020. **587**: 567–576.

15 Hope, J. M., Dombroski, J. A., Pereles, R. S., Lopez-Cavestany, M., Greenlee, J. D., Schwager, S. C., Reinhart-King, C. A., et al., Fluid shear stress enhances T cell activation through Piezo1. *BMC Biol.* 2022. **20**: 61.

16 Liu, C. S. C., Raychaudhuri, D., Paul, B., Chakrabarty, Y., Ghosh, A. R., Rahaman, O., Talukdar, A., et al., Cutting edge: Piezo1 mechanosensors optimize human T cell activation. *J. Immunol.* 2018. **200**: 1255–1260.

17 Jairaman, A., Othy, S., Dynes, J. L., Yeromin, A. V., Zavala, A., Greenberg, M. L., Nourse, J. L., et al., Piezo1 channels restrain regulatory T cells but

are dispensable for effector CD4($^+$) T cell responses. *Sci. Adv.* 2021. **7**: eabg5859.

18 **Solis, A. G., Bielecki, P., Steach, H. R., Sharma, L., Harman, C. C. D., Yun, S., De Zoete, M. R., et al.**, Mechanosensation of cyclical force by PIEZO1 is essential for innate immunity. *Nature* 2019. **573**: 69–74.

19 **Zhang, J., Zhao, R., Li, B., Farrukh, A., Hoth, M., Qu, B. and Del Campo, A.**, Micropatterned soft hydrogels to study the interplay of receptors and forces in T cell activation. *Acta. Biomater.* 2021. **119**: 234–246.

20 **Alter, G., Malenfant, J. M. and Altfeld, M.**, CD107a as a functional marker for the identification of natural killer cell activity. *J. Immunol. Methods* 2004. **294**: 15–22.

21 **Backes, C. S., Friedmann, K. S., Mang, S., Knörck, A., Hoth, M. and Kummerow, C.**, Natural killer cells induce distinct modes of cancer cell death: discrimination, quantification, and modulation of apoptosis, necrosis, and mixed forms. *J. Biol. Chem.* 2018. **293**: 16348–16363.

22 **Chan, C. J., Ekpenyong, A. E., Golfier, S., Li, W., Chalut, K. J., Otto, O., Elgeti, J., et al.**, Myosin II activity softens cells in suspension. *Biophys. J.* 2015. **108**: 1856–1869.

23 **Bae, C., Sachs, F. and Gottlieb, P. A.**, The mechanosensitive ion channel Piezo1 is inhibited by the peptide GsMTx4. *Biochemistry* 2011. **50**: 6295–6300.

24 **Syeda, R., Xu, J., Dubin, A. E., Coste, B., Mathur, J., Huynh, T., Matzen, J., et al.**, Chemical activation of the mechanotransduction channel Piezo1. *Elife* 2015. **4**: e07369.

25 **Alibert, C., Goud, B. and Manneville, J. B.**, Are cancer cells really softer than normal cells? *Biol. Cell* 2017. **109**: 167–189.

26 **Guck, J., Schinkinger, S., Lincoln, B., Wottawah, F., Ebert, S., Romeyke, M., Lenz, D., et al.**, Optical deformability as an inherent cell marker for testing malignant transformation and metastatic competence. *Biophys. J.* 2005. **88**: 3689–3698.

27 **Basu, R., Whitlock, B. M., Husson, J., Le Floc'h, A., Jin, W., Oyler-Yaniv, A., Dotiwala, F., et al.**, Cytotoxic T cells use mechanical force to potentiate target cell killing. *Cell* 2016. **165**: 100–110.

28 **Netter, P., Anft, M. and Watzl, C.**, Termination of the activating NK cell immunological synapse is an active and regulated process. *J. Immunol.* 2017. **199**: 2528–2535.

29 **Jenkins, M. R., Rudd-Schmidt, J. A., Lopez, J. A., Ramsbottom, K. M., Mannering, S. I., Andrews, D. M., Voskoboinik, I., et al.**, Failed CTL/NK cell killing and cytokine hypersecretion are directly linked through prolonged synapse time. *J. Exp. Med.* 2015. **212**: 307–317.

30 **Anft, M., Netter, P., Urlaub, D., Prager, I., Schaffner, S. and Watzl, C.**, NK cell detachment from target cells is regulated by successful cytotoxicity and influences cytokine production. *Cell. Mol. Immunol.* 2020. **17**: 347–355.

31 **Ritter, A. T., Kapnick, S. M., Murugesan, S., Schwartzberg, P. L., Griffiths, G. M. and Lippincott-Schwartz, J.**, Cortical actin recovery at the immunological synapse leads to termination of lytic granule secretion in cytotoxic T lymphocytes. *Proc. Natl. Acad. Sci. USA* 2017. **114**: E6585–E6594.

32 **Sims, T. N., Soos, T. J., Xenias, H. S., Dubin-Thaler, B., Hofman, J. M., Waite, J. C., Cameron, T. O., et al.**, Opposing effects of PKCtheta and WASp on symmetry breaking and relocation of the immunological synapse. *Cell* 2007. **129**: 773–785.

33 **Bohineust, A., Garcia, Z., Beuneu, H., Lemaître, F. and Bousso, P.**, Termination of T cell priming relies on a phase of unresponsiveness promoting disengagement from APCs and T cell division. *J. Exp. Med.* 2018. **215**: 1481–1492.

34 **Sanchez, E. E., Tello-Lafoz, M., Guo, A. J., De Jesus, M., Elbanna, Y. A., Winer, B. Y., Budhu, S., et al.**, Apoptotic contraction drives target cell release by cytotoxic T cells. *Nat. Immunol.* 2023. **24**: 1434–1442.

35 **Nikolaev, N. I., Müller, T., Williams, D. J. and Liu, Y.**, Changes in the stiffness of human mesenchymal stem cells with the progress of cell death as measured by atomic force microscopy. *J. Biomech.* 2014. **47**: 625–630.

36 **Islam, M., Brink, H., Blanche, S., Diprete, C., Bongiorno, T., Stone, N., Liu, A., et al.**, Microfluidic sorting of cells by viability based on differences in cell stiffness. *Sci. Rep.* 2017. **7**: 1997.

37 **Mordechay, L., Le Saux, G., Edri, A., Hadad, U., Porgador, A. and Schvartzman, M.**, Mechanical regulation of the cytotoxic activity of natural killer cells. *ACS Biomater. Sci. Eng.* 2021. **7**: 122–132.

38 **Le Saux, G., Bar-Hanin, N., Edri, A., Hadad, U., Porgador, A. and Schvartzman, M.**, Nanoscale mechanosensing of natural killer cells is revealed by antigen-functionalized nanowires. *Adv. Mater.* 2019. **31**: e1805954.

39 **Douguet, D. and Honoré, E.**, Mammalian mechanoelectrical transduction: structure and function of force-gated ion channels. *Cell* 2019. **179**: 340–354.

40 **Zhao, R., Yanamandra, A. K. and Qu, B.**, A high-throughput 3D kinetic killing assay. *Eur. J. Immunol.* 2023. **53**: 2350505.

41 **Schoppmeyer, R., Zhao, R., Hoth, M. and Qu, B.**, Light-sheet microscopy for three-dimensional visualization of human immune cells. *J. Vis. Exp.* 2018. **13**: 57651. https://doi.org/10.3791/57651

42 **Otto, O., Rosendahl, P., Mietke, A., Golfier, S., Herold, C., Klaue, D., Girardo, S., et al.**, Real-time deformability cytometry: on-the-fly cell mechanical phenotyping. *Nat. Methods* 2015. **12**: 199–202.

43 **Mietke, A., Otto, O., Girardo, S., Rosendahl, P., Taubenberger, A., Golfier, S., Ulbricht, E., et al.**, Extracting cell stiffness from real-time deformability cytometry: theory and experiment. *Biophys. J.* 2015. **109**: 2023–2036.

44 **Qu, B., Pattu, V., Junker, C., Schwarz, E. C., Bhat, S. S., Kummerow, C., Marshall, M., et al.**, Docking of lytic granules at the immunological synapse in human CTL requires Vti1b-dependent pairing with CD3 endosomes. *J. Immunol.* 2011. **186**, 6894–6904.

45 **Zöphel, S., Schäfer, G., Nazarieh, M., Konetzki, V., Hoxha, C., Meese, E., Hoth, M., et al.**, Identification of molecular candidates which regulate calcium-dependent CD8($^+$) T-cell cytotoxicity. *Mol. Immunol.* 2023. **157**: 202–213.

Abbreviations: **IS**: immunological synapse · **RT-DC**: real-time deformability cytometry · **PFA**: paraformaldehyde

*Full correspondence:*Dr. Bin Qu, Biophysics, Center for Integrative Physiology and Molecular Medicine (CIPMM), School of Medicine, Saarland University, 66421, Homburg, Germany
e-mail: bin.qu@uks.eu

REVIEW

Characterization of immune cell migration using microfabrication

Doriane Vesperini[1,2] · Galia Montalvo[1,2,3] · Bin Qu[3,4] · Franziska Lautenschläger[1,2]

Abstract

The immune system provides our defense against pathogens and aberrant cells, including tumorigenic and infected cells. Motility is one of the fundamental characteristics that enable immune cells to find invading pathogens, control tissue damage, and eliminate primary developing tumors, even in the absence of external treatments. These processes are termed "immune surveillance." Migration disorders of immune cells are related to autoimmune diseases, chronic inflammation, and tumor evasion. It is therefore essential to characterize immune cell motility in different physiologically and pathologically relevant scenarios to understand the regulatory mechanisms of functionality of immune responses. This review is focused on immune cell migration, to define the underlying mechanisms and the corresponding investigative approaches. We highlight the challenges that immune cells encounter in vivo, and the microfabrication methods to mimic particular aspects of their microenvironment. We discuss the advantages and disadvantages of the proposed tools, and provide information on how to access them. Furthermore, we summarize the directional cues that regulate individual immune cell migration, and discuss the behavior of immune cells in a complex environment composed of multiple directional cues.

Keywords Immune cells · Amoeboid migration · Microfabrication · Target search

Migration of immune cells is central for immune surveillance

From the early stages in the development of the immune system, precursors of immune cells migrate from bone marrow to the thymus and to secondary lymphoid organs to continue their differentiation, or to specific tissues to become resident sentinel cells (Germain et al. 2012). When an infectious agent enters the body, two lines of defense can be activated: innate immunity and adaptive immunity. Innate immunity is a rapid immune response that is initiated within minutes after intrusion of a pathogen, without any specific pre-activation. Adaptive immunity, on the other hand, is antigen-dependent and generates immunological memory (Marshall et al. 2018). In general, immune surveillance is dependent on the constant traffic of immune cells, in terms of their migration through the blood and lymphatic systems. From there, they can be recruited to sites of tissue damage or infection, and fine-tune their effector properties in specific secondary lymphoid organs (Fig. 1a).

Innate immune cells arrive first at inflammation sites, and while killing pathogens to resolve any infection, they release cytokines (including chemokines) that recruit other innate and adaptive immune cells. Some specialized innate immune cells, such as dendritic cells (DCs), collect the antigens at inflammation sites and then migrate back to the secondary lymphoid organs to trigger activation of adaptive immune cells (de Winde et al. 2020). Neutrophils activate a rapid migratory response, which means that they are among the first innate immune cells to arrive at a site of inflammation when a pathogen enters the body. Neutrophils can also then re-enter the vasculature, in a process termed "reverse transendothelial migration" (de Oliveira et al. 2016).

All authors contributed equally to this study.

✉ Bin Qu
bin.qu@uks.eu

✉ Franziska Lautenschläger
f.lautenschlaeger@physik.uni-saarland.de

1 Department of Experimental Physics, Saarland University, 66123 Saarbrücken, Germany
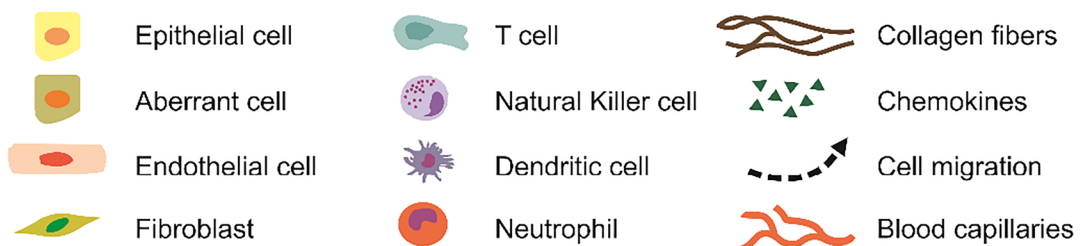
2 Center for Biophysics, Saarland University, 66123 Saarbrücken, Germany

3 Biophysics, Center for Integrative Physiology and Molecular Medicine (CIPMM), School of Medicine, Saarland University, 66421 Homburg, Germany

4 Leibniz Institute for New Materials, 66123 Saarbrücken, Germany
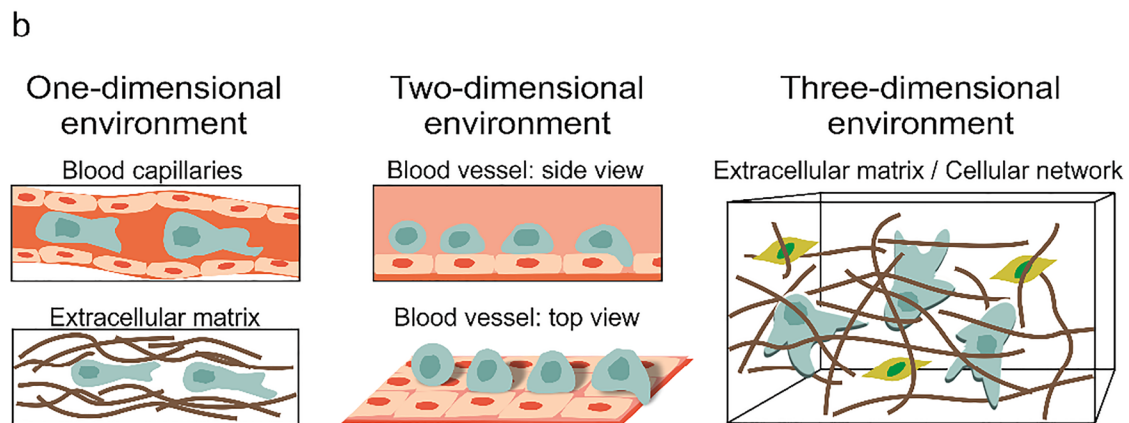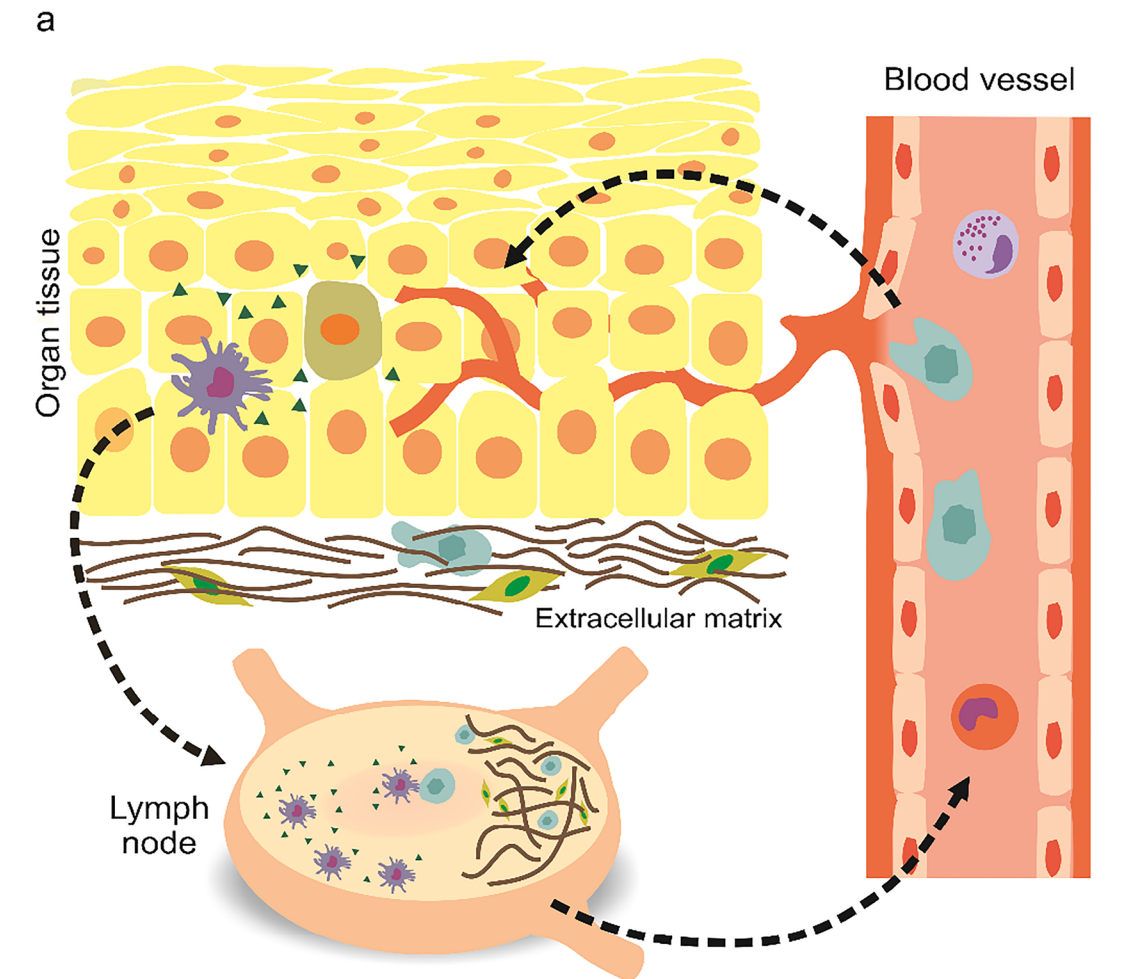
◀ **Fig. 1** Immune cell migration in vivo and the diverse scenarios encountered. a) Overview of immune cell migration in vivo. From blood vessels, immune cells transmigrate into and then patrol peripheral tissues/organs to clear invaders and/or collect antigens. Then, immune cells enter lymph vessels and migrate toward the lymph nodes. Peripheral dendritic cells (DCs) are responsible to collect antigens from aberrant (infected or malignant) cells in peripheral tissues (skin is shown here). Upon recognition of an invader or aberrant cells, an immediate immune response is initiated locally. Then, professional antigen-presenting cells (APCs) go to the lymph nodes, where the adaptive immune cells (B and T cells) are activated. Activation is then followed by proliferation. Effector cells enter the blood circulation and transmigrate into the respective inflammation sites. b) Schematic of 1D, 2D and 3D scenarios encountered by immune cells during migration. T cells are drawn here in the illustration as an example of immune cells. 1D is found in blood/lymph capillaries and in the cavities/channels in ECM. The blood vessel walls, which immune cells are rolling on, correspond to a 2D scenario. In general, while patrolling the tissues, immune cells face a 3D environment with ECM as a main component

Natural killer (NK) cells are essential players for the elimination of pathogen-infected or tumorigenic cells in an antigen-independent manner. Although the recirculation and movement of NK cells among human organs are not yet fully understood (Di Vito et al. 2019), it is well accepted that NK cells not only populate the peripheral blood, but also reside in almost every tissue and organ. This suggests that these NK cells can either migrate and reside in tissues, or they can constantly recirculate through the organs (Di Vito et al. 2019).

Dendritic cells are professional antigen-presenting cells that link the innate and adaptive immune systems. DCs migrate through different tissues and across many barriers; they leave the bone marrow and travel through the blood to seed all organs and tissues (de Winde et al. 2020). When a pathogen enters, the tissue-resident immature DCs at the site of inflammation collect and process the antigenic material. Similarly, DCs can detect tumor antigens and take them to the secondary lymph nodes to activate the adaptive immune responses against cancers (Nourshargh and Alon 2014). As a result of their stimulation, DCs further differentiate to a mature phenotype with up-regulated chemokine receptors. These mature DCs leave the inflammatory site and return to the draining lymph nodes to activate T cells and B cells (de Winde et al. 2020).

Together with B cells, T lymphocytes represent the adaptive immune system (Garcia 2019). The life cycle of T cells starts in the bone marrow, continues in the thymus, and then throughout the body, until they encounter their specific target cells (Krummel et al. 2016). This encounter can occur in lymph nodes, where T cells are activated by the professional antigen-presenting cells. Before activation, naïve T cells show random migration and speed fluctuations, as they alternate between periods of fast and slow movements (Krummel et al. 2016). This mode of migration allows individual T cells to examine a large area of a lymph node (Moreau and Bousso

2014). Suboptimal stimulation is considered to be the physiological trigger for T cells to change the direction of their migration more frequently and hence to keep searching. When T cells encounter matching antigen-presenting cells, they halt and establish an immunological synapse with the target cells (Moreau and Bousso 2014; Moreau et al. 2015). Upon activation, T cells change their migration program and start to move from the lymph nodes to the corresponding "battle field" in the peripheral tissues (Lämmermann and Germain 2014). To carry out their killing functions, cytotoxic T lymphocytes (mainly as activated T cells) use cytotoxic granules or the Fas/FasL pathways to destroy infected cells or tumor cells (Barry and Bleackley 2002). Promotion of migration of these cytotoxic T lymphocytes results in their higher killing efficiency (Schoppmeyer et al. 2017).

Immune cell migration modes

The different geometries that immune cells encounter in vivo, together with their intrinsic properties, determine their migration modes. In general, cell migration can be classified into two modes: mesenchymal and amoeboid migration (Liu et al. 2015; Moreau et al. 2018). Mesenchymal migration is characterized by strong adhesion sites, proteolytic degradation of the extracellular matrix (ECM), elongated cell shape with long membrane protrusions, and slow cell movement. This type of movement mostly describes the behavior of epithelial-derived and cancer cells, rather than immune cells. For amoeboid migration, although this classification is still under constant review and varies across studies, several common aspects are widely accepted: low cell adhesion, independence from proteolytic degradation of the ECM, and rounded cell morphology with a highly contractile rear part, known as the uropod (Renkawitz et al. 2009). In vivo, immune cells mostly use the amoeboid mode of motility. The migration speed of immune cells is not constant, but varies between fast (~20 μm/min) and slow (<1 μm/min) migration phases (Chabaud et al. 2015). Such a migration pattern has been described in theoretical studies of intermittent search behavior, and it thus helps immune cells to optimize their broad space exploration and direct their migration to inflammatory sites (Bénichou et al. 2006; Bénichou et al. 2011; Petrie et al. 2009). Interestingly, the different cell types are not absolutely committed to either mesenchymal or amoeboid migration, as they can transition between these states. The mechanism behind this transition appears to be dependent on the activation status of the cells, their physiological context, their interactions with the ECM, and their adaptation to the cellular environment (Huse 2017; Liu et al. 2015). A generic model to explain migration transitions indicates the relevance of these two parameters: the intrinsic properties of the cells, and the environmental characteristics (Liu et al. 2015).

Regulation of immune cell migration

Cell migration can be broken down into various steps, which include polarization, protrusion in the direction of motion, adhesion, translocation of the cell body, and retraction of the uropod (Mayor and Etienne-Manneville 2016). The proportion and relevance of each step depends on the migration mode, the experimental conditions, and the cell type. More specifically, polarization as the first step refers to the formation of a stable front and rear for migrating cells. For immune cells, the polarity might be an intrinsic property, like the ability of neutrophils to self-polarize (de Oliveira et al. 2016). However, polarization can also be induced by stimuli, such as chemotactic or mechanotactic signals, which will be elaborated upon further in the following sections. Protrusions describe membrane extensions in the direction of migration, and two main protrusive structures have been described: filopodia (long, unbranched, parallel actin bundles) and lamellipodia (branched networks of thin, short actin filaments) (Blanchoin et al. 2014). In ameboid migration, actomyosin-based contractility creates pressure and the flow of the cytoplasm towards the uropod. This flow forms spherical membrane expansions, often called "**blebs**" which facilitate the forward movement (Huse 2017). To move, the forces need to be transmitted from the cell membrane to the substratum. In adhesion-dependent migration, such as mesenchymal migration, this process is predominantly mediated by adhesion molecules (integrins) (Ridley et al. 2003). However, immune cells can migrate independent of the integrins (Lämmermann et al. 2008), and instead via unspecific friction forces with the environment (Hawkins et al. 2009). Following the development of protrusions, the cell body translocates, a process that is coordinated by and dependent on myosin II, which together with microtubules, controls the translocation of the nucleus. Finally, for the retraction of the uropod, several mechanisms converge (Capuana et al. 2020; Mayor and Etienne-Manneville 2016); e.g., interplay between microtubule depolymerization, and actomyosin-mediated retraction during DCs migration (Kopf et al. 2020).

All of these migration steps are supported by the three main components of the cytoskeleton: actin filaments, microtubules, and intermediate filaments. In immune cells, the actin cytoskeleton provides protrusive and contractile forces in cooperation with myosin IIA. The microtubule network not only provides tracks for organelles and vesicles to be transported within the cell, but also contributes to maintenance of nuclear morphology. Signaling pathways coordinate the dynamic interactions between the cytoskeletal elements (Devreotes and Horwitz 2015). These elements include, for example, the Rho-family of GTPases (involved in indirect regulation of actin dynamics), actin regulators such as the formins (involved in polymerization of actin), the Arp2/3 complex (involved in

nucleation and branching of actin), and members of the WASP/WAVE family (Arp2/3 activators). As the cytoskeletal components can dynamically adapt to the environment, this allows the cells to "squeeze through" small spaces, where the size of the relatively stiff nucleus becomes a decisive limiting factor. Squeezing of the nucleus might induce DNA damage (Denais et al. 2016; Lammerding and Wolf 2016; Raab et al. 2016) if the DNA repair mechanisms are insufficient or defective, therefore limiting cell survival and triggering apoptosis (Denais et al. 2016; Raab et al. 2016). Interestingly, immune cells have multilobed nuclei, which effectively reduces the absolute size of the stiffest object that needs to be squeezed through any constrictions. This property certainly reduces the risk of nuclear rupture and DNA damage during this squeezing of the cell contents (Yamada and Sixt 2019).

The intermediate filaments are responsible for the maintenance of the overall cell shape, and also for the integrity of the nucleus (Danielsson et al. 2018; Hohmann and Dehghani 2019; Huse 2017). The intermediate filament vimentin has a fundamental role in maintenance of nuclear integrity during cell migration (Patteson et al. 2019b), as well as in regulation of cell speed and cell persistence (see Box 1 for definitions) during migration (Patteson et al. 2019). Indeed, epithelial cells treated to switch from keratin to vimentin expression undergo a transition from slow mesenchymal migration to fast amoeboid migration (Lavenus et al. 2020), which supports of the role of vimentin in amoeboid migration. Thus, while vimentin is broadly described as a regulator of mesenchymal migration, recent evidence supports its role equally in immune cell migration.

Box 1 Parameters and properties of cell migration

Cell speed
The mean cell speed is defined as the total distance of the cell migration divided by the total acquisition time. The instantaneous speed of migrating cells is calculated for two successive images.

Cell persistence
Cell persistence defines the "straightness" of the cell movement, which has different definitions depending on the device geometry used. In one dimension, there is a unique direction, so the persistence length corresponds to the mean length a cell travels before it stops or turns back, which is usually normalized to the channel length. In two dimensions and three dimensions, the cell persistence can be defined as the diameter of the smallest disk containing the whole cell trajectory divided by the total distance of the trajectory. Another common definition is the angular persistence, which also considers the turning angles all along the migration path. In all cases, the persistence scale lies between 0 (non-persistent) and $\lceil \pm 1 \rceil$ (highly persistent).

Mean first passage time
The mean first passage time is defined as the average time a searching cell takes to find a target, such as another cell (e.g., for procreation, immune synapse formation), a pathogen, or nutrients. This parameter depends on the number and motility of searchers and targets.

Challenges and scenarios immune cells encounter in vivo

While migrating through the body, immune cells face various scenarios, which range from one-dimensional (1D) to three-dimensional (3D) environments, and these cells often need to adapt and switch from one environment to another (Fig. 1b). 3D conditions are their most common environment in vivo, such as in peripheral tissues and organs, including the lymph nodes. Migration through 3D environments requires the cells to squeeze through complex extracellular structures with specific cellular adaptation to the mechanical features of the ECM (Yamada and Sixt 2019). Two-dimensional (2D) migration is the best-studied and best-understood form of cell migration in vitro (Ridley et al. 2003). In vivo, 2D immune cell migration can be seen during extravasation when cells roll on, attach to, and crawl along the walls of blood vessels, before they penetrate into the tissue (Filippi 2016; Nourshargh and Alon 2014). The first barrier immune cells encounter is the vessel wall composed of cells (endothelial and pericytes) and a basement membrane. During inflammation, immune cells squeeze in between endothelial cells or through them before transmigrating through the basement membrane. The penetration of cells into the tissues, called diapedesis, might be modified by a reorganization of the basement membrane that can lead to diseases (Friedl and Weigelin 2008; Korpos et al. 2013; Leclech et al. 2020). 1D scenarios are less common physiologically but still present in vivo. The capillaries of the lymphatic or vascular systems have a mean diameter of ~ 5 μm (Henderson et al. 2020). In those capillaries, whether leukocytes actively migrate and how is still not fully understood. Nevertheless, evidence from in vitro microchannel experiments shows that without external sheer force, murine CD8$^+$ T cells do crawl in the microchannels with a width of 4 μm or 8 μm (Jacobelli et al. 2010), suggesting that immune cells could migrate actively in these capillaries in vivo. In addition, hydrodynamic forces can further promote leukocyte movement in blood capillaries (Kameritsch and Renkawitz 2020). However, cells proceed along a line or a linear structure that can be considered as 1D migration (Jackson 2019; Nortley et al. 2019). Another example of 1D migration in vivo is during cell movement along ECM fibers, which depends on the local density and alignment of the collagen around the tissue or tumor boundaries (Yamada and Sixt 2019). A recent in vitro study shows that primary human CD8$^+$ T cells preferably migrate through the channels formed in collagen matrix (Sadjadi et al. 2020), suggesting another possible 1D scenario for immune cell migration in vivo. Thus, 3D, 2D, and 1D environments are all physiologically relevant conditions, whereby each requires the use of a different migratory mechanism by the immune cells.

The complexity of the environment shapes the migration of immune cells

As indicated, the environments that immune cells encounter in vivo are diverse, and can have different physical and chemical properties, such as the composition of the ECM, the stiffness and geometry of the tissue, and the presence of chemokines. All of these features collectively define the behavior of immune cells during their migration.

The ECM is defined as all of the noncellular components of tissues and organs. It consists mostly of proteoglycans and fibrous proteins, such as collagen (Lämmermann and Germain 2014). Those noncellular components can vary in composition, and therefore expose the embedded cells to varying surrounding properties, which in turn influences cell migration (Lange and Fabry 2013). Along with stiffness, porosity (the size of pores/channels in the ECM) and geometry are also key physical features of the ECM, and these can also influence immune cell migration. Spatially varying stiffness can be established, e.g., by different concentrations of structural proteins like collagen, and this can result in cell migration up a stiffness gradient, which is referred to as durotaxis. In a physiological context, stiffness gradients have been observed in a number of diseases, such as with lung fibrosis, breast cancer, and atherosclerosis (Hartman et al. 2017). These stiffness gradients have been shown to be a consequence of changes on ECM composition. Such increase in tissue stiffness from the tumor core to the periphery in cancers is believed to favor metastasis and tumor spreading (Hartman et al. 2017).

Another relevant feature that influences cell migration is the geometry of the ECM. The ECM often has a filamentous structure with enough space between fibers for cells to pass through, the size or width of which is largely dependent on fiber density. However, as migrating cells move along, the space occupied by the cells also moves, and the surrounding tissue deforms. The structural properties of the ECM are known to impact upon cell migration, such as, fiber density and organization (i.e., ECM porosity), and ECM protein composition. The path of least resistance with appropriate sizes of pores can thus provide a route for rapid cell passage during in vivo migration. This is especially relevant for immune cell migration, where there is no enzymatic modification of the surrounding ECM (Yamada and Sixt 2019). In addition to the ECM, cell networks can influence immune cell migration, such as the fibroblastic reticular cell network, which can form a structural backbone that actively guides T cell movements inside the lymph nodes.

Chemoattraction describes directed migration patterns towards higher concentrations of chemokines. Chemokines are

small proteins that are released by immune, epithelial, and endothelial cells in response to various stimuli, such as tissue injury or infection. These chemokines attract immune cells along the concentration gradient. Chemoattractant-driven migration is termed chemotaxis (or haptotaxis, if the gradient is bound to a substrate), and this has a key role in the regulation of immune cell behavior. For example, expression of the CCR7 chemokine receptor is required for activated DCs to migrate through the lymphatic system (Lämmermann and Germain 2014). The CCL19 and CCL21 chemokines are both ligands for CCR7, but CCL21 is considered to be the critical chemokine for the migration of activated DCs (Worbs et al. 2017). T cell migration is also guided by chemoattractants, such as CCL19, CCL21, and CXCL12, which are required for optimal naïve T cell motility in vivo (Lämmermann and Germain 2014). Chemokines in the lymph node increase basal T cell motility, although they do not appear to contribute to the search strategies undertaken by T cells at the initiation of a response. Although CCR7 is required for T cells to maintain their average speed, it does not control the other features of the random walk, including the directionality (Cotta-de-Almeida et al. 2017).

Fibroblasts are the major cellular component in the ECM, and lymphocytes are in contact with fibroblasts most of the time while they move through the lymph nodes. Therefore, the influence of fibroblasts on T cell migration is also of particular interest for studies of immune cell migration. Nevertheless, the signals that control those interactions remain poorly characterized. One mechanism whereby fibroblasts can guide T cell migration directly is through the creation of channels: e.g., by producing collagen and modifying the ECM, or by releasing cytokines and chemokines that guide T cell movements directly (Bajénoff et al. 2008).

Migration of immune cells in diverse microfabricated geometries

Understanding the relative roles of free migration versus mechanically or chemically guided cell movements is thus essential for the development of a better picture of how these events are regulated in vivo (Castellino et al. 2006). We summarize now the methods to investigate the effects of such environmental cues on immune cell migration.

Visualization of immune cell migration in vivo is feasible using, e.g., intravital microscopy; however, the interpretation of the results obtained remains difficult. Comparing direct in vivo observations with well-defined in vitro environments (i.e., in terms of geometry, mechanics, chemical and physical cues, see Fig. 2) is essential to go further in our understanding of immune cell migration and immune responses. In this section, we describe how immune cell migration is studied in terms of in vivo to in vitro experiments. We illustrate how

and why microfabrication can mimic physiological environments, at least partially, with a focus on different techniques and their implementation, as well as their applications. We analyze the pros and cons of each of these systems, and describe the specific questions they address in terms of immune cell migration (as summarized in Table 1). For general reviews about cell migration, please refer to (Ghibaudo et al. 2011; Lautenschläger and Piel 2013).

Characterization of immune cell migration using in vivo models to build in vitro systems

Intravital microscopy consists of imaging cells of a living animal through a transparent tissue or a transparent window placed in the body by surgery (Murooka and Mempel 2012). This can allow direct observations of immune cell migration in their physiological context, and in various tissues (Weigert et al. 2010). Depending on the experiment and the invasiveness of the surgery, the animal is sacrificed at the end of the experiment. This technique requires specific labeling of the cells, which is usually performed using transgenic animals. However, some parts of the body are not trivial to access in vivo and require ex vivo experiments that externalize a tissue or organ to study it. In vivo/ex vivo migration experiments are often performed on mice (Abdul Hamid et al. 2020; Raab et al. 2016) or zebrafish (Barros-Becker et al. 2017; Cougoule et al. 2012; Rosowski 2020), because they are small enough to be positioned under a microscope (e.g., confocal, multiphoton). The observation of the native environment of the cells has inspired the conception and design of in vitro experiments that are closer to the true physiological conditions, and where the effects of single mechanisms can be studied without the influence of other parameters. The advantages of in vitro experiments are that they can be well controlled, and limit the number of animals used for research.

Over the last two decades, the "microfabrication" technique has been used widely to provide reliable, versatile, and reproducible systems with well-defined geometries (Whitesides et al. 2001). To mimic the extracellular environment encountered during in vivo migration, a bottom-up approach has usually been used, where the levels of complexity can be tuned. The simplicity of each device enables exploration of the fundamental mechanisms related to single or collective cell migration that would not have been understood in the complexity of in vivo environments (Garcia-Arcos et al. 2019).

Microfabrication usually follows two steps. The first step consists of producing the silicon wafer that is the mold for the final device. The main techniques here are photolithography and two-photon lithography. The second step consists of producing the final device that is to be used directly for the experiments. Soft lithography and hydrogel-based systems are

Table 1 Characteristics, advantages, and drawbacks of various geometries used for in vitro studies

Aspect	One-dimensional microchannels			Two-dimensional surfaces			Three-dimensional
	Straight microchannel	Bifurcation	Constriction	Flat surface	Confined	Pillar forest	Hydrogel
In vitro geometry							
External stimulation	Chemotaxis	Barotaxis; chemotaxis	Topotaxis	Durotaxis; chemotaxis	Durotaxis; chemotaxis	Topotaxis; chemotaxis	Durotaxis; topotaxis; chemotaxis
In-vivo relevance	Capillaries; vessels; pore-like channels in tissues; migration along extracellular matrix fibers	Capillary bifurcations	Passage through tight pores in tissues; transmigration	Rolling along vessel walls	Migration: on epithelium surface, fiber surfaces in the extracellular matrix	Migration: through pores in extracellular matrix, in densely packed organs or lymph nodes; between obstacles (other cells)	Mimicking extracellular matrix stiffness and complexity
Materials	PDMS	PDMS	PDMS	Glass; hydrogels	Glass and PDMS	PDMS	Collagen; polyacrylamide; matrigel; gelatin; PLGA
What parameters can be tuned?	Cross-section shape (rectangular or cylindrical); channel size	Symmetry (asymmetric, symmetric); number of paths	Constriction size	Stiffness; coatings (Fibronectin, PEG, BSA, ICAM)	Height of the confinement (e.g. 1-20 μm for confining cells)	Pillar diameter, density, shape, organization	Stiffness; density; pore size; chemistry
Advantages	Ease of fabrication; compatible with high resolution microscopy; highly reproducible	Ease of fabrication; compatible with high resolution microscopy	Ease of fabrication; compatible with high resolution microscopy	Ease of fabrication; compatible with high resolution microscopy	Ease of fabrication; compatible with high resolution microscopy	Ease of fabrication; compatible with high resolution microscopy	Closer to physiological structures
Drawbacks	Reductionist geometry; nontunable stiffness	Reductionist geometry; nontunable stiffness	Reductionist geometry; nontunable stiffness	Does not predict migration in confined environments	Reductionist geometry; nontunable stiffness	Non-tunable stiffness	Complexity of the geometry; low reproducibility; difficulty to keep the focus during time lapse acquisitions
Applications	Cytoskeletal organization; polarization; chemotaxis; quantitative migration assay (speed and persistence measurements)	Which mechanisms are involved in cell decision making (barotaxis, chemotaxis, cell reorganization)?	Nucleus deformation and mechanics	How integrin-dependent cells migrate on flat surfaces; quantitative migration assays; search efficiency	How integrin-independent cells migrate on flat surfaces; quantitative migration assay; search efficiency	Topography; migration: facing obstacles (space between pillars larger than cell diameter), in a porous material (space between pillars smaller than cell diameter)	Three-dimensional invasiveness assay; mechanosensing; durotaxis; chemotaxis
References	[23, 64-68]	[69-73]	[36, 39, 74-76]	[77-80]	[20, 77, 81, 82]	[83-86]	[31, 41, 87]

PDMS, polydimethylsiloxane; PLGA, poly(d,l-lactic-co-glycolic acid); PEG, polyethylene glycol; BSA, bovine serum albumin; ICAM, intercellular adhesion molecule

Fig. 2 Migratory challenges and guidance cues encountered by immune cells during circulation. The extracellular regulation of cell migration includes: chemokines and stiffness gradients; the extracellular matrix (ECM) mechanics (including loose or highly cross-linked zones) and its topology (pores, or obstacles); the molecular composition of the matrix surrounding the cells (collagen, fibroblasts, chemokines) as well as pressure gradients. Center: Schematic representation of a polarized immune cell migrating directionally in an amoeboid migration mode. Amoeboid migration is characterized by a round cell morphology, low adhesive contacts and cell body deformation driven by actin protrusions. The microtubule organizing center is generally located at the back of the nucleus. The integrity of the nucleus is protected by a nuclear cage formed by intermediate filament proteins, such as vimentin
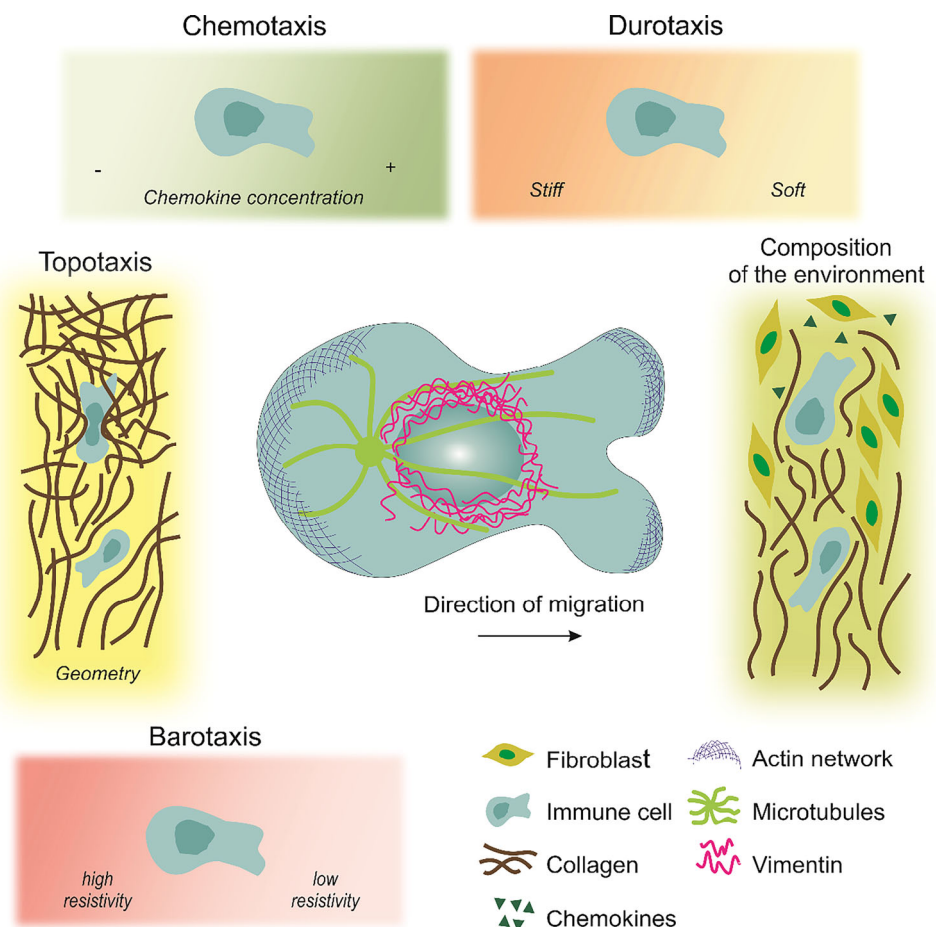
Table 2 Main characteristics of lithography techniques

Characteristic	Photolithography	Electron lithography and two-photons lithography	Three-dimensional bioprinting
Flatness	Homogeneous height given by the spin-coating speed	Structure can be tilted	Lines can appear due to needle shape
Resolution in xy	Down to ~1μm	Down to ~100nm	Size of nozzle (100 μm)or droplet (20 μm)
Resolution in z	1–100 μm	~100nm	<10 μm
Printing	Mask required	Direct printing, mask-less	Direct printing; mask-less
Equipment	UV lamp (e.g.,UV Kub); spin coater, two hot plates	Nanoscribe	Bioprinter
Costs	Low	High	Low
Comments	Two masks needed for a two-layer devices	Different height can be printed at the same time	Used with different kinds of materials; better for large structures (>500 μm); aims to print scaffold for organs
Example Suppliers	Selba, Rose photomask (for mask); Microfactory, Si-Mat (for wafer); Blackhole (from microfabrication kits to devices)	Nanoscribe' Semiconductor Production Systems; Heildelberg Instruments	All3DP; Biolife4D; Cellink

usually used for this purpose. More recently, 3D printing has allowed the direct fabrication of these devices with no need for the wafer production. Here, we present an overview of the most commonly applied techniques (Fig. 3) and their respective advantages and drawbacks (Table 2).

Photolithography

Photolithography emerged as a technique to respond to the needs for accuracy in the electronics field. It was first described for biological purposes at the beginning of the twenty-first century, by the group of Whitesides (Whitesides et al. 2001). The protocol has been described in detail before (Heuzé et al. 2011; Qin et al. 2010). Briefly, photolithography consists of spin coating a photoresist on the top of a silicon wafer. This photoresist is a light-sensitive material that is used to form a patterned coating on the silicon wafer. A commonly used negative photoresist is the epoxy-based structure known as SU8. The resist is soft baked and then exposed to UV light through a mask (Fig. 3a). The mask can be plastic or chromium-coated glass, which depends on the resolution required and the design features, and can be made using any of the specific computer-aided design software, such as CleWin, AutoCad, and LayoutEditor. Chromium-coated glass masks have the highest resolution (down to ~1 μm), but they are relatively costly. Plastic masks are much cheaper (around €100 for A4 format), and have an XY resolution of about 5 μm. Photoresists are either positive resists, when the UV light exposure makes the resist soluble in the developer, or negative resists, when the UV light exposure initiates the resist cross-linking to make it insoluble in the developer. Therefore, the features of the mask need to be the inverse of the final structure designed for a device when a negative photoresist is used, such as with SU8 or ma-N. The reticulation of the resist

is then set by post baking. The last step consists of removing the unreticulated resist using the developer.

Photolithography is the most commonly used technique for microfabrication, and it was built on the expertise developed for the microelectronics field. No specific or expensive equipment is required for photolithography, which is based on only a spin-coater, a UV-lamp, and two hot-plates. This equipment is also not demanding of space. Although photolithography is usually carried out in a clean room, it can be used under a chemical hood in a dark room for structures >5 μm. Ready-to-start sets are commercially available and relatively affordable (<€10,000). Moreover, the homogeneous height of the samples is guaranteed due to the spin-coating step. However, there are also several major limitations in this method. The resolution on the X/Y axes is limited by diffraction, which means that investigation of features below 1 μm is not feasible. Furthermore, the height of the final device is not accurately reproducible in the micrometer range, as it is very sensitive to various external conditions, such as resist viscosity, spinning speed, stability of backing temperature, room temperature (optimal, 20–22 °C), and humidity (usually ~45%). In addition, photolithography is a long process that progresses from the computer-aided design conception to the wafer production over at least several days, and more often, several weeks. For a multi-layer structure, a so-called mask aligner is needed, along with as many masks as the number of layers that are required. Other techniques overcome those limitations by using direct printing, which does not require any mask, saves time, and makes multi-layer fabrication easier.

Electron-beam lithography and two-photon lithography

Unlike an indirect method like photolithography, there are numerous direct printing techniques that are available, such
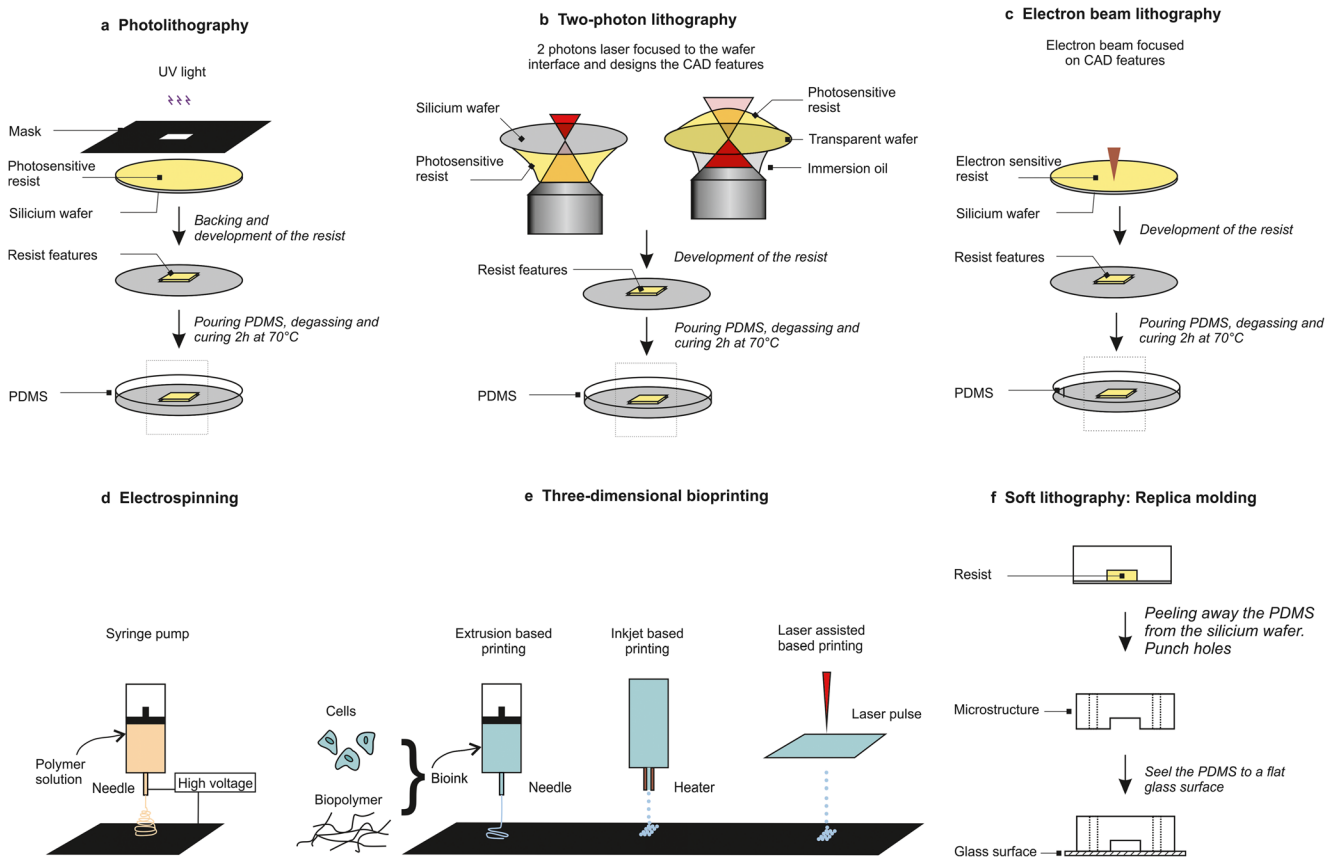
Fig. 3 Techniques used to study in vitro cell migration. (a) Photolithography: the photosensitive resist is exposed to UV light through a mask where the features are designed. (b) Two-photon lithography: mask-free technique where the features are directly printed in the resist from the resist–wafer interface with a piezo motion in the three space dimensions (X, Y, Z). The resist is up or down depending on the wafer transparency (image inspired by (Bückmann et al. 2012)). (c) Electron beam lithography: mask-free technique where the features are directly printed by reticulation of the resist in contact with the electron beam. (d) Electrospinning: mask free technique where a polymer solution is extruded from a needle around which a high voltage electric field is formed, and deposited on a surface that can be rotating. The 2D membrane fabricated using this technique can then have random to aligned nanofibrous structures depending on the needle translation. (e) Three-dimensional bioprinting: mask-free technique where a bio-ink consisting of cells and biopolymers is directly deposited on a surface by extrusion-, inkjet- or laser-assisted-based printing. (f) Soft lithography: this step follows the production of the wafer with one of the techniques presented in (a, b, and c); polydimethylsiloxane (PDMS) is peeled away from the wafer, punched, cut, cleaned and bound to a glass surface. CAD, computer-aided design

as electron-beam lithography (Altissimo 2010) and two-photon lithography (Farsari and Chichkov 2009) (characteristics summarized in Table 2). These mask-free lithography techniques have the advantage that they can reach spatial resolution of about 100 nm, and simple 3D structures of different heights can be printed in one step. Both techniques are adapted to 3D nanofabrication and are very versatile (Niesler and Hermatschweiler 2015). For each scan in the Z direction, the resist/wafer interface has to be precisely determined. To avoid floating structures, the first two to three layers are contained in the wafer; however, this step can induce tilt, in terms of the height (e.g., left side 1 μm higher than right side). For thin structures, a tilt of 1 μm in height can be unacceptable, which will depend on the application. As mask fabrication is not needed, the overall process is considerably shorter compared to photolithography. For example,

production of a system with micrometer resolution for an area of several square centimeters normally only takes several hours, except for some complex geometries and/or for very high resolution. The time of printing depends on the balance between the size and the precision for the three space dimensions required.

Two-photon lithography has benefited from the development of femtosecond lasers. In contrast to the standard UV-initiated and mask-based photolithography method, the reticulation for two-photon lithography is initiated locally by two-photon absorption on the area of focus, which is reached with an ultrafast laser (Fig. 3b). Then, as for standard photolithography, the uncured resist (i.e., not exposed to the laser) is removed with the developer.

Electron-beam lithography can achieve a resolution even below 10 nm in all three dimensions (Fig. 3c). However, as the

electron beam goes through the material, high aspect ratios in 2D structures are not easy to obtain. Instead of using photosensitive resists, electron-beam lithography uses resists that are sensitive to electron beam radiation (Vieu et al. 2000). The most commonly used electro-sensitive resists are made from polymethyl-methacrylate, as this has the highest spatial resolution (<10 μm) compared to other resists, such as EBR-9 (copolymer of trifluoroethyl-a-chloroacrylate and tetrafluoropropyl-a-chloroacrylate; resolution, ~100 μm), and its fabrication is easier than for polybutene-1-sulfone positive resists (Tseng et al. 2003). Electron-beam lithography is highly reproducible for heights in the range of 10 nm and features from 10 to 1 mm, which makes it useful for patterning (Kolodziej and Maynard 2012). These techniques allow the production of devices for confined migration or migration on 2D surfaces studies but do not allow transmigration studies. For this purpose, other techniques permit in vitro membrane production.

Electrospun membranes

Transmigration is a crucial challenge for immune cells as they continuously cross the ECM barrier of the basement membrane. In vivo studies revealed that neutrophils and macrophages migrate across the basement membrane but that neutrophils transmigration is more invasive (Voisin et al. 2009). The basement membrane is a thin densely packed membrane mainly composed of laminin and collagen type VI. It is located around muscles, fat, and in between pericyte cells and endothelial cells in blood vessels (Jayadev and Sherwood 2017). The complex structure of the basement membrane makes it difficult to be studied in vivo, therefore in vitro models have been developed (Sobreiro-Almeida et al. 2019). In the early twenty-first century, polymer membranes or Matrigel were used in Boyden chambers to study the invasion ability of cells (Kleinman and Jacob 2001). Even though Boyden chambers were a first step to investigate transmigration, their structure was far from the one of basement membranes. Therefore, new methods emerged to mimic more physiological structure of the basement membrane, such as the electrospinning technique.

The electrospinning technique consists of producing fibrous scaffolds (Kumbar et al. 2008). Thin fibers (in the range of some nanometer to some micrometer in diameter) are produced by applying a high-voltage electric field to a polymer solution. The polymer fibers are extruded through a needle with a diameter that depends on the tip size of the needle, the polymer viscosity, the voltage applied, and the distance between the surface and the needle. The fibers are deposited on the charged rotating or flat surface in a random or parallel organization (Fig. 3d). This technique has the advantages to produce homogeneous fiber sizes. Polymers such as polycaprolactone have been used in order to study immune cells migration through a fibrous membrane of various density (Jin et al. 2015). The 2D structures are then used as a scaffold, and can be coated with collagen for more physiological properties of basement membrane. More recently, electrospinning has been used to directly embed cells into the biopolymers fibers (Hong et al. 2019) and provides promising applications in the field of tissue engineering when coupled with hydrogels solutions and 3D printing.

Hydrogel fabrication

To study the influence of the mechanical properties of a substrate during cell migration, 2D and 3D structures have been developed using hydrogels. Hydrogels consist of hydrophilic polymer chains that are mixed in an aqueous phase. The formulations range from synthetic (e.g., poly(d,l-lactic-*co*-glycolic acid), polyethylene glycol, poly-methyl-methacrylate) to natural (e.g., collagen, agarose, alginate, gelatin, chitosan, fibrinogen, hyaluronic acid) origins. The gels are crosslinked by UV light, temperature or chemicals. Hydrogels have the advantage that they can be transparent and biocompatible, like polydimethylsiloxane (PDMS), and they have better free diffusion coefficient for small molecules. Hydrogels can be sensitive to temperature or pH, and their stiffness can be globally tuned, even though their local stiffnesses can vary (i.e., hydrogels can have heterogeneous stiffness). Nevertheless, one major technical issue for hydrogel fabrication is the swelling of the gel after the addition of the medium or other aqueous solutions. For immune cell migration, the reproducibility of accurate shapes for confinement (e.g., pore size) can be challenging.

Hydrogels have been combined with microfluidics for more than 10 years now. To mimic the physiological ECM in terms of stiffness, pore size, and elasticity, more optimization is required for hydrogels (for more detail on hydrogels, see reviews (Goy et al. 2019; Zhang et al. 2016)). Nevertheless, the integration of gels into microdevices has created new opportunities for research that would not have been possible with microfluidics or hydrogels alone, such as long-term chemotaxis using agarose or collagen channels (Cheng et al. 2007; Shin et al. 2011), rapid bacteria responses to antibiotics (Choi et al. 2014), and cancer cell migration (Huang et al. 2018).

Three-dimensional printing

The previous methods here are mainly for 1D to 2D structure fabrication. However, reconstruction of a 3D environment is essential to provide a scenario that is close to physiological conditions. Three-dimensional printing is a direct method used to fabricate a desired 3D structure, which offers a reliable approach for the reconstruction of complex 3D geometries using a computer-aided design model, with high

reproducibility. This process is termed 3D "bioprinting" when the "ink" used is biocompatible. The initial aim of bioprinting was to produce artificial tissues and organs in vitro (Murphy and Atala 2014), or to regenerate organs in situ (Cui et al. 2017). Three-dimensional bioprinting has also been used for microfluidic applications (Ho et al. 2015): either to build microfluidic chips using bioprinting methods, or to combine 3D bioprinting and microfluidics for fabrication of transplanted organs with better resolution and more complex structures (Ma et al. 2018; Miri et al. 2018). Three-dimensional bioprinting is based mainly on an extrusion process of a bio-ink from a nozzle, which is generally composed of biopolymer gels and cells. This can provide direct fast and simple fabrication, even for complex microfluidic chips (e.g., containing multilayers, valves, mixers). However, it is not yet compatible with devices in the micrometer range, because the spatial resolution depends on the diameter of the printer nozzle and/or the size of the droplets, in terms of using extrusion-based lithography or inkjet lithography, respectively (see Fig. 3e). Currently, the spatial resolution attainable is about 100 μm for the nozzle and 20 μm for droplets (Bishop et al. 2017) (Table 2). Another challenge of bioprinting is that the bio-ink needs to meet many requirements, such as printability (He et al. 2016), optimal viscosity, and optimal gelling time (Colosi et al. 2016), characteristics that vary among the different bio-inks.

In summary, bioprinting is a promising technique to improve our knowledge in the fields of tissue engineering, drug screening, and toxicology testing in organs on chips (Ng and Yeong 2019). It opens new perspectives to investigate cell migration in three dimensions in downscaled artificial organs, or to create new devices of diverse stiffnesses; however, it cannot yet replace standard soft lithography.

Replica molding for microfabrication

Replica molding is one of the soft lithography techniques, and it is based on duplication of structures from a mold. It is a versatile technique that follows the production of the wafer (using one of the techniques presented above). In brief, it consists of pouring the PDMS elastomer over the silicon wafer, degassing this in a vacuum chamber, and curing it at 70 °C for 2 h. Then, the PDMS is peeled away from the master, cut, punched, and plasma bound to a glass surface (i.e., slide, dish) (Fig. 3f).

Polydimethylsiloxane has many advantages for the study of cell migration. First, it is biocompatible and nontoxic, which allows experiments on living cells over several hours. Secondly, it is porous, which allows gas exchange with the outer atmosphere and the corresponding CO_2 proportion necessary to maintain pH 7.4. Furthermore, its transparency makes it compatible with optical microscopy. PDMS is cheap, easy to fabricate, and can be adapted to all geometries. The

one major limit of PDMS is that its stiffness is not easily tunable.

Characterization of immune cell migration when facing external cues

As described in the previous sections, migrating cells face different types of environments in vivo, in their physiological context. Immune cells migrate through confined 3D complex ECMs of different stiffnesses and fibrillar densities, and they can face densely packed environments, like in lymph nodes, transmigrating through basement membrane, and within tissues. During their movement around the body, cells can also encounter 2D surfaces (e.g., blood vessel walls, lymphatic vessel walls) and can need to migrate in one dimension (i.e., in capillaries, following a fiber, passing through pores and channels in the ECM) (Fig. 1). As in vivo migration is the result of the combination of the mechanical parameters (e.g., stiffness, porosity gradients), physical parameters (e.g., pressure gradients), and chemical stimulation, it is challenging to dissect out and understand fully the role of individual properties from this complexity, especially for mechanical and physical properties. To study particular aspects of 1D, 2D, and 3D cell migration, many microfabricated structures have been produced to address a number of scientific questions, such as: (1) What is the effect of substrate stiffness on cell migration? (2) What is the minimal constriction (pore diameter) a cell can pass through? (3) What influences cell sensitivity to chemoattractants, pressure, and physical gradients? and (4) What are the key factors that remodel the cell cytoskeleton during migration? In this section, we summarize how external stimulation has been studied in diverse geometries and dimensions, and with the introduction of obstacles to cell searching areas, as examples of more complex environments, where different guidance cues can overlap.

Durotaxis

Durotaxis was defined for the first time in 2000 by the group of Wang (Lo et al. 2000), as the mechanical guidance of cell migration from a stiff to a soft substrate. They demonstrated that fibroblasts are more elongated and have a greater spreading area and stronger force generation on stiff compared to soft surfaces. Since then, most studies on durotaxis have been performed using mesenchymal cell migration (Plotnikov et al. 2012; Tse and Engler 2011; Vincent et al. 2013), cancer cell migration (DuChez et al. 2019; Kirmse et al. 2011), and collective cell migration (Spatarelu et al. 2019; Trepat and Fredberg 2011). Many of these studies were performed in two dimensions using different techniques, such as homogeneous stiffness gradients, as alternations of soft and stiff bands (Kuboki et al. 2014) or patterns (Ladoux and Mège 2017). Recently, 3D devices with mechanical gradients have been

developed to study cell migration and differentiation, and tissue engineering (Orsi et al. 2017). Several models have been defined to predict cell migration, although these are better suited to 2D migration via focal adhesions rather than to 3D migration (Feng et al. 2019; Harland et al. 2011). Moreover, although mesenchymal cell migration has been shown to follow contact guidance and stiffness gradients, it is still unclear how sensitive amoeboid cells are to durotaxis (Nuhn et al. 2018). As immune cells do not adhere, but instead migrate via pushing forces and rapid deformation, the effects of durotaxis on immune cells have not been as intensively studied.

To confine cells in a controlled manner, PDMS spacers produced using soft lithography are placed between the glass bottom of a dish and its "roof" (Le Berre et al. 2014; Liu et al. 2015) (Table 1). The stiffness of PDMS is much higher than the stiffness encountered by immune cells in their physiological environments. Therefore, a soft confiner made using agarose gel was proposed more recently (Prunet et al. 2020). This has the advantage that it has a stiffness close to the physiological context. Also, tuning the stiffness is a key parameter in the investigation of 3D migration in hydrogels, to better mimic the ECM structure (Nemir et al. 2010; Stowers et al. 2015). It has been shown that activated microglia cells are more sensitive to durotaxis than immature ones (Bollmann et al. 2015), which opens the hypothesis that immune cells might respond to ECM rigidity differently depending on their stage of maturation. To investigate durotaxis in immune cell migration, different hydrogel compositions can be used (see previous section for hydrogel fabrication) to tune stiffness and/or elasticity.

Topotaxis

Topotaxis is a term that has been used in scientific publications since the 1940s (Fraenkel and Gunn 1940), but it then referred to stimulus guidance in general (Nossal 1980). It is only since 2016 that topotaxis has been used to exclusively refer to topographical gradients (Park et al. 2016). Here, Park et al. used cancer cell lines where they migrated on top of nanoposts positioned within diverse density gradients. This 2D experiment suggested that the topography of the cell environment has a physical role in directing cell migration. In earlier studies, it had already been shown that cells follow nanoscale microfabricated grooves in vitro (Clark et al. 1991; Wójciak-Stothard et al. 1996), but this was not called topotaxis at the time. Later, topotaxis has also referred to pore-size gradients in one dimension (i.e., channels; Table 1) and to 3D structures (e.g., pillar forests; Table 1). In the literature, the movement from both sparse obstacles to dense obstacles and vice versa has been shown to depend on the ratio between the cell diameter and the space between the pillars. Cells usually tend to migrate through areas where the pore size is comparable to their diameter (Park et al. 2018; Wondergem et al.

2020). As soon as cells encounter obstacles (e.g., other cells, matrix fibers; in vitro: pillar forests), they modify their migration patterns, which initiates topotaxis effects (Schakenraad et al. 2020). In vitro, several constricting geometries have been designed to mimic cell migration through small ECM pores, generally either as a reduction in a channel section (Thiam et al. 2016) or the movement between pillars (Davidson et al. 2014).

In in vitro 1D channels, hydrodynamic forces can be avoided in order to only study spontaneous cell migration comparable with 3D migration. Studies with 1D channels highlight the position and deformability of the nucleus as a limiting factor for cell migration. When DCs are faced with constrictions of ≤3 μm, nuclear deformation can induce the rupture of the lamina envelope (Thiam et al. 2016). Compared to DCs, the nuclei of neutrophils are more deformable (Rowat et al. 2013), which allows these cells to squeeze through pores of <1 μm. Also, for a long time, the effects of external physical cues on cell migration were not studied independently, but mainly in combination with chemotaxis. Recently, it was shown for NK cells that their behavior is modified by topographic effects when following either parallel or perpendicular grooves (Xu and Pang 2019).

Two-dimensional topography has been shown to guide epithelial cells during wound healing (Marmaras et al. 2012). In the context of immune cells, the impact of the 2D topography on their migration still remains elusive. Apart from 2D conditions, immune cells also often face confined environments, which can be mimicked by either adding a roof or a pillar forest to the glass slide on which the cells are plated (Liu et al. 2015). Pillar forests have been developed to study porosity effects on cell migration. These consist of PDMS-based micropillars organized in an array. The pillars touch both the bottom surface and the roof of the set-up (Renkawitz et al. 2018). Depending on the density of the pillars, such a set-up can be used to investigate cell migration through a porous matrix, and to determine the effects of pore size and the presence of obstacles on cell migration (Wondergem et al. 2020). Pillars might represent topographic stimuli that help the directed migration of immune cells, or might act as obstacles that modify the random migration of the cells (Gorelashvili et al. 2014).

Barotaxis

Barotaxis refers to migration directions according to pressure gradients. Under physiological conditions, cells often have to choose between different paths (e.g., neutrophils circulation in capillaries (Wang et al. 2020)). The mechanisms that lead cells to take a particular path are not yet fully understood, and barotaxis is being explored as one of these. As hydraulic resistance generates small forces, only amoeboid cells are sensitive to barotaxis, while mesenchymal cells generate high

adhesion forces and use proteolysis to migrate. For immature DCs, macropinocytosis limits their sensitivity to barotaxis while exploring any space (Chabaud et al. 2015). During macropinocytosis, the cells take up medium at their front end, which is enough to inhibit the pressure forces. After maturation, DCs lose their ability for macropinocytosis, and instead they polarize and follow hydraulic forces toward the lymph nodes (Moreau et al. 2019). Recently, neutrophils migrating in asymmetric channels were shown to choose the path of least resistance (Prentice-Mott et al. 2013).

Several parameters are suggested to have a role in barotaxis, including cell organization and polarization. In particular, evidence shows that a nucleus-first position (Renkawitz et al. 2019) and microtubules (Ambravaneswaran et al. 2010) act as sensors to facilitate fast migration along the path of least resistance. Moreover, the TRPM7 cation channel has also been demonstrated to be a critical mechanosensor in cell decision-making (Zhao et al. 2019).

Chemotaxis

From all external guidance, chemotaxis has been the most intensively studied migration mode of immune cells, since around 1960. Chemotaxis is a general principle that defines a gradient of chemical signals (chemokines, growth factors, substrates or pheromones) and it can be observed in vitro and in vivo (Weber and Sixt 2013). These act as chemoattractants to guide cell migration toward the region with a higher concentration. When the chemical molecules are immobilized on the top of the substrate, the process is called haptotaxis.

Different cell types have specific sensitivities to different chemokines, which depend on their functions and their membrane receptors. This is essential for an efficient search, and to be able to attract the right cells at the right time to the right target. The formation of pseudopodia and the polarization of the cells are the two main responses of cells to chemokines (Van Haastert and Devreotes 2004). Immune cells use both haptotaxis and chemotaxis while patrolling the body, in order to collect information (Schwarz et al. 2017).

Microfluidics is a convenient tool to study chemotaxis in 1D (Prentice-Mott et al. 2016), 2D, or 3D structures. In narrow channels, cells touch all of the walls and block the fluid flow, which allows investigations into the specific impact of drugs or chemicals on one particular side of a cell. Asymmetrical chemical stimulation mimics the chemotaxis in tissues. When the cells sense a chemotactic gradient, they polarize in order to follow it.

The chemosensitivity of cells can be modified by other chemical compounds. It has been shown, for example, that neutrophils lose their sensitivity to N-formyl-L-methionyl-L-leucyl-L-phenylalanine when PI3 kinase is inhibited (which is known to inhibit chemosensitivity in cells). However, it has been demonstrated that this is only true in channels if the PI3K inhibitor is perfused at the front side of the cell, and not at the rear side (Irimia et al. 2007). That suggests that the polarity of the cell and the way it is exposed to different molecules can regulate its chemosensitivity, and thus its migration. Recently, 3D chemotaxis has been studied using microfluidic devices that provide liquid areas with different chemokine concentrations around a solid collagen area. Cells embedded in the collagen can then be exposed to stable chemical gradients in three dimensions (Aizel et al. 2017).

In pillar forests, chemotaxis and topotaxis can be studied together, to understand their respective influences on cell guidance. Cells usually migrate toward a chemoattractant and sparse organizations (Wondergem et al. 2020). It has been shown that if chemical and density gradients are opposing (i.e., higher chemical concentration on the same side as denser pillar organization), then they compete. For example, _D. discoideum_ will still migrate toward the chemoattractant, but with a probability to transit toward dense pillars much lower than for the use of aligned gradients (Wondergem et al. 2020). Overall, the cell organization and the response to physical and chemical external stimulation are likely to be the main parameters for all cells to explore their environment in an efficient manner, depending on their functions.

Complexity of the ECM: search strategies in a multi-factor environment

In vivo, cells migrate in complex structures such as the ECM, where all biomechanical, biophysical, and biochemical cues compete and enable cells to carry out their functions; e.g., for immune cells to find a target in an optimal time. Although correct immune cell migration is a prerequisite for an efficient immune response, different search strategies guided by all of the different cues indicated above are used to enable the cells to be in the right place at the right time. Many factors are involved in search strategies, including velocity, persistence, turning angle, and mean first passage time (see Box 1 for definitions). Microfabrication is a powerful process for the creation of new geometries and shapes to investigate obstructive systems during cell searching (i.e., "search problematics"). Pillar forests represent one example of structures that are well adapted to this purpose. Different questions can be asked depending on the size of the pillars, their geometrical organization, the height of the device, and the interpillar space. Pillar forests combine the advantages of 2D and 3D structures. First, the visualization of cell trajectories over several hours is easier compared to 3D migration. Secondly, the cell environment is dense and porous, as the cells can encounter many obstacles, which allow immune cells to migrate in an integrin-independent manner. Nevertheless, to date, there have been few studies that have described immune cell migration for diverse pillar organizations. The efficiency of cells

during search problematics was initially based on in vivo observations, and then characterized via simulations. We present here an overview of the different search strategies used by immune cells that have been investigated with the help of microfabricated tools.

Emerging evidence shows that cells use different search strategies according to their environment and their functions. It has been reported that immune cells use different types of random and intermittent search patterns (Bénichou et al. 2011). For example, T cells show a random walk (Preston et al. 2006) in vitro but follow a (nonBrownian) Lévy walk in vivo (Krummel et al. 2016), neutrophils are more prone to persistent motion (Jones et al. 2015), while DCs migrate in vitro in an intermittent random walk (Chabaud et al. 2015; de Winde et al. 2020; Worbs et al. 2017). A random walk (i.e., Brownian walk) results in an unpredictable path followed by the cells (Cahalan and Parker 2008; Miller et al. 2002). It has been shown in vivo that DCs adopt a slow random walk in the lymph node with extensive shape change. The fast modification of DCs shape combined with the fast and persistent migration of T cells enables a high number of DC/T cell interactions. It has been estimated that one DC encounters at least 500 different T cells in 1 h (Bousso and Robey 2003). The Lévy and intermittent walks are combinations of an alternation of fast persistent runs and slow, erratic pauses. The main difference between a Lévy walk and an intermittent random walk is the increased possibility of the cell finding a target during the fast motion of the Lévy walk (Moreau et al. 2018). Simulations have demonstrated that cell migration is much more complex and cannot be defined by any single one of these definitions, as it is a combination of all of them (Fricke et al. 2016; Wu et al. 2014). Notably, number of pathogens, number of immune cells, migration speeds, persistence, area to be examined, and time required to find a target all have roles in the efficiency of searching for targets. However, open questions still remain; for example: What is the optimal number of searching immune cells to find a defined number of targets (e.g., pathogens, cancer cells) for the most efficient immune response?

Conclusions and perspectives

Immune cells are patrolling tissues and vessels to defend our body against pathogens. Failing this task might lead to disease or illness. Therefore, immune cells have to fulfill many roles: (1) they have to find the pathogens, (2) treat the information, (3) transport and convey the information to other cells, (4) these cells then react to this information. In order to fully understand immune cell behavior, in particular immune cell migration, we need to have excellent possibilities to observe and to test parameters of immune cell migration. In this review, we provide a comprehensive summary of

microfabrication methods available to investigate immune cell migration. As migration is one of the decisive factors for proper execution of immune cell functions, which is significantly shaped by the environment, here we put a special focus on the context of the challenges (1D, 2D and 3D) imposed to cells migrating in vivo and the respective external regulatory factors (e.g., topography, stiffness, pressure, and chemoattractant). To investigate cell migration in a defined and tuneable way, recently emerging microfabrication has been proven to be powerful tools. Here we summarized the relevant techniques used to investigate cell migration (e.g., photolithography, electron-beam/two-photon lithography, hydrogel fabrication, electrospinning, 3D printing, and replica molding for microfabrication). In addition, we elaborated how the methods can be used to mimic particular aspects of those challenges. So far, we described techniques to test single challenge in static conditions. In living organisms, however, the environment is dynamic and constantly changing. It will be the future of in vitro investigation of immune cell migration to add this dynamic component into artificial environments, e.g., being able to alter the stiffness or geometry of the substrate as well as the chemical available cues while carrying out experiments. Also, several parameters can be combined to study the prevalence of one challenge, e.g., are the cells more sensitive to chemotaxis or topotaxis? In order to understand more complex immune cell behavior, e.g., the search efficiency, that is crucial in the future to develop dynamic experiments in devices that are combining several chemical, mechanical and physical challenges. Optogenetic tools are promising candidates to achieve such goals.

Code availability Not applicable.

Author contribution D.V. and G.M. wrote the manuscript. B.Q. and F.L. generated the ideas and revised the manuscript.

Data availability Not applicable.

Declarations

Conflict of interest The authors declare that they have no conflict of interest.

References

Abdul Hamid AI, Nakusi L, Givskov M, Chang YT, Marques C, Gueirard P (2020) A mouse ear skin model to study the dynamics of innate immune responses against *Staphylococcus aureus* biofilms. BMC Microbiol 20:22

Aizel K, Clark AG, Simon A, Geraldo S, Funfak A, Vargas P, Bibette J, Vignjevic DM, Bremond N (2017) A tuneable microfluidic system for long duration chemotaxis experiments in a 3D collagen matrix. Lab Chip. 17:3851–3861

Altissimo M (2010) E-beam lithography for micro−/nanofabrication. Biomicrofluidics 4:026503

Ambravaneswaran V, Wong IY, Aranyosi AJ, Toner M, Irimia D (2010) Directional decisions during neutrophil chemotaxis inside bifurcating channels. Integ Biol 2:639–647

Bajénoff M, Glaichenhaus N, Germain RN (2008) Fibroblastic reticular cells guide T lymphocyte entry into and migration within the splenic T cell zone. J Immunol 181:3947–3954

Barros-Becker F, Lam PY, Fisher R, Huttenlocher A (2017) Live imaging reveals distinct modes of neutrophil and macrophage migration within interstitial tissues. J Cell Sci 130:3801–3808

Barry M, Bleackley RC (2002) Cytotoxic T lymphocytes: all roads lead to death. Nat Rev. Immunol 2:401–409

Bénichou O, Loverdo C, Moreau M, Voituriez R (2006) Two-dimensional intermittent search processes: an alternative to Levy flight strategies. Phys Rev E 74:020102

Bénichou O, Loverdo C, Moreau M, Voituriez R (2011) Intermittent search strategies. Rev Mod Phys 83:81–129

Bishop ES, Mostafa S, Pakvasa M, Luu HH, Lee MJ, Wolf JM, Ameer GA, He T-C, Reid RR (2017) 3D bioprinting technologies in tissue engineering and regenerative medicine: current and future trends. Genes Dis. 4:185–195

Blanchoin L, Boujemaa-Paterski R, Sykes C, Plastino J (2014) Actin dynamics, architecture, and mechanics in cell motility. Physiol Rev 94:235–263

Bollmann, L., D. Koser, R. Shahapure, H. Gautier, G. Holzapfel, G. Scarcelli, M. Gather, E. Ulbricht, and K. Franze. 2015. Microglia mechanics: immune activation alters traction forces and durotaxis. Front Cell Neurosci 9

Bousso P, Robey E (2003) Dynamics of CD8+ T cell priming by dendritic cells in intact lymph nodes. Nat Immunol 4:579–585

Bückmann T, Stenger N, Kadic M, Kaschke J, Frölich A, Kennerknecht T, Eberl C, Thiel M, Wegener M (2012) Tailored 3D Mechanical Metamaterials Made by Dip-in Direct-Laser-Writing Optical Lithography. Adv Mater 24:2710–2714

Cahalan MD, Parker I (2008) Choreography of cell motility and interaction dynamics imaged by two-photon microscopy in lymphoid organs. Annu Rev Immunol 26:585–626

Capuana L, Bostrom A, Etienne-Manneville S (2020) Multicellular scale front-to-rear polarity in collective migration. *Curr Opin Cell Biol*. 62:114–122

Castellino F, Huang AY, Altan-Bonnet G, Stoll S, Scheinecker C, Germain RN (2006) Chemokines enhance immunity by guiding naive CD8+ T cells to sites of CD4+ T cell-dendritic cell interaction. Nat 440:890–895

Chabaud M, Heuze ML, Bretou M, Vargas P, Maiuri P, Solanes P, Maurin M, Terriac E, Le Berre M, Lankar D, Piolot T, Adelstein RS, Zhang Y, Sixt M, Jacobelli J, Benichou O, Voituriez R, Piel M, Lennon-Dumenil AM (2015) Cell migration and antigen capture are antagonistic processes coupled by myosin II in dendritic cells. Nat Commun 6:7526

Cheng SY, Heilman S, Wasserman M, Archer S, Shuler ML, Wu M (2007) A hydrogel-based microfluidic device for the studies of directed cell migration. Lab Chip. 7:763–769

Choi J, Yoo J, Lee M, Kim E-G, Lee JS, Lee S, Joo S, Song SH, Kim E-C, Lee JC, Kim HC, Jung Y-G, Kwon S (2014) A rapid antimicrobial susceptibility test based on single-cell morphological analysis. Sci Translat Med 6:267ra174–267ra174

Clark P, Connolly P, Curtis AS, Dow JA, Wilkinson CD (1991) Cell guidance by ultrafine topography in vitro. J Cell Sci 99:73–77

Colosi C, Shin SR, Manoharan V, Massa S, Costantini M, Barbetta A, Dokmeci MR, Dentini M, Khademhosseini A (2016) Microfluidic bioprinting of heterogeneous 3D tissue constructs using low-viscosity bioink. Adv Mater 28:677–684

Cotta-de-Almeida V, Dupre L, Savino W (2017) Editorial: T cell migration in health and disease. Front Immunol 8:132

Cougoule C, Van Goethem E, Le Cabec V, Lafouresse F, Dupré L, Mehraj V, Mège JL, Lastrucci C, Maridonneau-Parini I (2012) Blood leukocytes and macrophages of various phenotypes have distinct abilities to form podosomes and to migrate in 3D environments. Eur J Cell Biol 91:938–949

Cui H, Nowicki M, Fisher JP, Zhang LG (2017) 3D bioprinting for organ regeneration. Adv Healthc Mater 6:1601118

Danielsson F, Peterson MK, Caldeira Araujo H, Lautenschläger F, Gad AKB (2018) Vimentin diversity in health and disease. Cells 7:147

Davidson PM, Denais C, Bakshi MC, Lammerding J (2014) Nuclear deformability constitutes a rate-limiting step during cell migration in 3D environments. Cell Mol Bioengineer 7:293–306

de Oliveira S, Rosowski EE, Huttenlocher A (2016) Neutrophil migration in infection and wound repair: going forward in reverse. Nat Rev. Immunol 16:378–391

de Winde CM, Munday C, Acton SE (2020) Molecular mechanisms of dendritic cell migration in immunity and cancer. Med Microbiol Immunol 209:515–529

Denais CM, Gilbert RM, Isermann P, McGregor AL, te Lindert M, Weigelin B, Davidson PM, Friedl P, Wolf K, Lammerding J (2016) Nuclear envelope rupture and repair during cancer cell migration. Sci 352:353–358

Devreotes P, Horwitz AR (2015) Signaling networks that regulate cell migration. Cold Spring Harb Perspect Biol 7:a005959

Di Vito C, Mikulak J, Mavilio D (2019) On the way to become a natural killer cell. Front Immunol 10:1812

DuChez BJ, Doyle AD, Dimitriadis EK, Yamada KM (2019) Durotaxis by human cancer cells. Biophys J 116:670–683

Farsari M, Chichkov BN (2009) Two-photon fabrication. Nat Phot 3:450–452

Feng J, Levine H, Mao X, Sander LM (2019) Cell motility, contact guidance, and durotaxis. Soft Matter 15:4856–4864

Filippi M-D (2016) Mechanism of Diapedesis: Importance of the Transcellular Route. Adv Immunol 129:25–53

Fraenkel GS, Gunn DL (1940) The orientation of animals. Kineses, taxes and compass reactions. Clarendon Press, Oxford viii+352 pp. pp

Fricke GM, Letendre KA, Moses ME, Cannon JL (2016) Persistence and adaptation in immunity: T cells balance the extent and thoroughness of search. PLoS Comput Biol 12:e1004818

Friedl P, Weigelin B (2008) Interstitial leukocyte migration and immune function. Nat Immunol 9:960–969

Garcia KC (2019) Dual arms of adaptive immunity: division of labor and collaboration between B and T cells. Cell 179:3–7

Garcia-Arcos, J.M., R. Chabrier, M. Deygas, G. Nader, L. Barbier, P.J. Saez, A. Mathur, P. Vargas, and M. Piel. 2019. Reconstitution of cell migration at a glance. J Cell Sci 132

Germain RN, Robey EA, Cahalan MD (2012) A decade of imaging cellular motility and interaction dynamics in the immune system. Sci 336:1676–1681

Ghibaudo M, Di Meglio JM, Hersen P, Ladoux B (2011) Mechanics of cell spreading within 3D-micropatterned environments. Lab Chip 11:805–812

Gorelashvili M, Emmert M, Hodeck KF, Heinrich D (2014) Amoeboid migration mode adaption in quasi-3D spatial density gradients of varying lattice geometry. New J Phys 16:075012

Goy CB, Chaile RE, Madrid RE (2019) Microfluidics and hydrogel: a powerful combination. React Funct Polym 145:104314

Harland B, Walcott S, Sun SX (2011) Adhesion dynamics and durotaxis in migrating cells. Phys Biol 8:015011

Hartman CD, Isenberg BC, Chua SG, Wong JY (2017) Extracellular matrix type modulates cell migration on mechanical gradients. Exp Cell Res 359:361–366

Hawkins RJ, Piel M, Faure-Andre G, Lennon-Dumenil AM, Joanny JF, Prost J, Voituriez R (2009) Pushing off the walls: a mechanism of cell motility in confinement. Phys Rev Lett 102:058103

He Y, Yang F, Zhao H, Gao Q, Xia B, Fu J (2016) Research on the printability of hydrogels in 3D bioprinting. Sci Rep 6:29977

Henderson AR, Choi H, Lee E (2020) Blood and lymphatic vasculatures on-chip platforms and their applications for organ-specific in vitro modeling. Micromach (Basel) 11:147

Heuzé ML, Collin O, Terriac E, Lennon-Dumenil AM, Piel M (2011) Cell migration in confinement: a micro-channel-based assay. Methods Mol Biol 769:415–434

Ho CMB, Ng SH, Li KHH, Yoon Y-J (2015) 3D printed microfluidics for biological applications. Lab Chip 15:3627–3637

Hohmann T, Dehghani F (2019) The cytoskeleton, a complex interacting meshwork. Cells 8:362

Hong, J., M. Yeo, G.H. Yang, and G. Kim. 2019. Cell-Electrospinning and Its Application for Tissue Engineering. Int J Mol Sci 20

Huang Y, Tong L, Yi L, Zhang C, Hai L, Li T, Yu S, Wang W, Tao Z, Ma H, Liu P, Xie Y, Yang X (2018) Three-dimensional hydrogel is suitable for targeted investigation of amoeboid migration of glioma cells. Mol Med Rep 17:250–256

Huse M (2017) Mechanical forces in the immune system. Nat Rev. Immunol 17:679–690

Irimia D, Charras G, Agrawal N, Mitchison T, Toner M (2007) Polar stimulation and constrained cell migration in microfluidic channels. Lab Chip 7:1783–1790

Jackson, D.G. 2019. Leucocyte trafficking via the lymphatic vasculature— mechanisms and consequences. Front Immunol 10

Jacobelli J, Friedman RS, Conti MA, Lennon-Dumenil A-M, Piel M, Sorensen CM, Adelstein RS, Krummel MF (2010) Confinement-optimized three-dimensional T cell amoeboid motility is modulated via myosin IIA-regulated adhesions. Nat Immunol 11:953–961

Jayadev R, Sherwood DR (2017) Basement membranes. Curr Biol 27: R207–R211

Jin S, Park T-M, Kim C-H, Kim J-S, Le BD, HunJeong Y, Kwak J-Y, Yoon S (2015) Three-dimensional migration of neutrophils through an electrospun nanofibrous membrane. BioTech 58:285–292

Jones PJ, Sim A, Taylor HB, Bugeon L, Dallman MJ, Pereira B, Stumpf MP, Liepe J (2015) Inference of random walk models to describe leukocyte migration. Phys Biol 12:066001

Kameritsch P, Renkawitz J (2020) Principles of Leukocyte Migration Strategies. Trends Cell Biol 30:818–832

Kirmse R, Otto H, Ludwig T (2011) Interdependency of cell adhesion, force generation and extracellular proteolysis in matrix remodeling. J Cell Sci 124:1857–1866

Kleinman, H.K., and K. Jacob. 2001. Invasion assays. Curr Protoc Cell Biol. Chapter 12:Unit 12.12

Kolodziej CM, Maynard HD (2012) Electron-beam lithography for patterning biomolecules at the micron and nanometer scale. Chem Mater 24:774–780

Kopf A, Renkawitz J, Hauschild R, Girkontaite I, Tedford K, Merrin J, Thorn-Seshold O, Trauner D, Häcker H, Fischer K-D, Kiermaier E, Sixt M (2020) Microtubules control cellular shape and coherence in amoeboid migrating cells. J Cell Biol 219:e201907154

Korpos É, Kadri N, Kappelhoff R, Wegner J, Overall CM, Weber E, Holmberg D, Cardell S, Sorokin L (2013) The peri-islet basement membrane, a barrier to infiltrating leukocytes in type 1 diabetes in mouse and human. Diabetes 62:531–542

Krummel MF, Bartumeus F, Gerard A (2016) T cell migration, search strategies and mechanisms. Nat Rev. Immunol 16:193–201

Kuboki T, Chen W, Kidoaki S (2014) Time-dependent migratory behaviors in the long-term studies of fibroblast durotaxis on a hydrogel substrate fabricated with a soft band. Langmuir 30:6187–6196

Kumbar SG, James R, Nukavarapu SP, Laurencin CT (2008) Electrospun nanofiber scaffolds: engineering soft tissues. Biomed Mater 3: 034002

Ladoux B, Mège RM (2017) Mechanobiology of collective cell behaviours. Nat Rev Mol Cell Biol 18:743–757

Lammerding J, Wolf K (2016) Nuclear envelope rupture: actin fibers are putting the squeeze on the nucleus. J Cell Biol 215:5–8

Lämmermann T, Bader BL, Monkley SJ, Worbs T, Wedlich-Soldner R, Hirsch K, Keller M, Forster R, Critchley DR, Fassler R, Sixt M (2008) Rapid leukocyte migration by integrin-independent flowing and squeezing. Nat 453:51–55

Lämmermann T, Germain RN (2014) The multiple faces of leukocyte interstitial migration. Semin Immunopathol 36:227–251

Lange JR, Fabry B (2013) Cell and tissue mechanics in cell migration. Exp Cell Res 319:2418–2423

Lautenschläger F, Piel M (2013) Microfabricated devices for cell biology: all for one and one for all. Curr Opin Cell Biol 25:116–124

Lavenus SB, Tudor SM, Ullo MF, Vosatka KW, Logue JS (2020) A flexible network of vimentin intermediate filaments promotes migration of amoeboid cancer cells through confined environments. J Biol Chem 295:6700–6709

Le Berre M, Zlotek-Zlotkiewicz E, Bonazzi D, Lautenschläger F, Piel M (2014) Methods for two-dimensional cell confinement. Methods Cell Biol 121:213–229

Leclech, C., C.F. Natale, and A.I. Barakat. 2020. The basement membrane as a structured surface - role in vascular health and disease. J Cell Sci 133

Liu YJ, Le Berre M, Lautenschläger F, Maiuri P, Callan-Jones A, Heuze M, Takaki T, Voituriez R, Piel M (2015) Confinement and low adhesion induce fast amoeboid migration of slow mesenchymal cells. Cell 160:659–672

Lo C-M, Wang H-B, Dembo M, Wang Y-l (2000) Cell movement is guided by the rigidity of the substrate. Biophys J 79:144–152

Ma J, Wang Y, Liu J (2018) Bioprinting of 3D tissues/organs combined with microfluidics. RSC Adv. 8:21712–21727

Marmaras A, Lendenmann T, Civenni G, Franco D, Poulikakos D, Kurtcuoglu V, Ferrari A (2012) Topography-mediated apical guidance in epidermal wound healing. Soft Matter 8:6922–6930

Marshall JS, Warrington R, Watson W, Kim HL (2018) An introduction to immunology and immunopathology. Allergy Asthma Clin Immunol 14:49

Mayor R, Etienne-Manneville S (2016) The front and rear of collective cell migration. Nat Rev Mol Cell Biol 17:97–109

Miller MJ, Wei SH, Parker I, Cahalan MD (2002) Two-photon imaging of lymphocyte motility and antigen response in intact lymph node. Sci 296:1869–1873

Miri AK, Nieto D, Iglesias L, Goodarzi Hosseinabadi H, Maharjan S, Ruiz-Esparza GU, Khoshakhlagh P, Manbachi A, Dokmeci MR, Chen S, Shin SR, Zhang YS, Khademhosseini A (2018)

Microfluidics-enabled multimaterial maskless stereolithographic bioprinting. Adv Mater 30:1800242

Moreau HD, Blanch-Mercader C, Attia R, Maurin M, Alraies Z, Sanséau D, Malbec O, Delgado M-G, Bousso P, Joanny J-F, Voituriez R, Piel M, Lennon-Duménil A-M (2019) Macropinocytosis overcomes directional bias in dendritic cells due to hydraulic resistance and facilitates space exploration. Dev Cell 49:171–188.e175

Moreau HD, Bousso P (2014) Visualizing how T cells collect activation signals *in vivo*. Curr Opin Immunol 26:56–62

Moreau HD, Lemaitre F, Garrod KR, Garcia Z, Lennon-Dumenil AM, Bousso P (2015) Signal strength regulates antigen-mediated T-cell deceleration by distinct mechanisms to promote local exploration or arrest. Proc Natl Acad Sci U S A 112:12151–12156

Moreau HD, Piel M, Voituriez R, Lennon-Duménil A-M (2018) Integrating physical and molecular insights on immune cell migration. Trend Immunol 39:632–643

Murooka, T.T., and T.R. Mempel. 2012. Multiphoton intravital microscopy to study lymphocyte motility in lymph nodes. *In* Integrin and Cell Adhesion Molecules: Methods and Protocols. M. Shimaoka, editor. Humana Press, Totowa, NJ. 247–257

Murphy SV, Atala A (2014) 3D bioprinting of tissues and organs. Nat Biotechnol 32:773–785

Nemir S, Hayenga HN, West JL (2010) PEGDA hydrogels with patterned elasticity: novel tools for the study of cell response to substrate rigidity. Biotechnol Bioeng 105:636–644

Ng, W.L., and W.Y. Yeong. 2019. The future of skin toxicology testing – 3D bioprinting meets microfluidics. Int J Bioprint 5

Niesler F, Hermatschweiler M (2015) Two-photon polymerization — a versatile microfabrication tool. Laser Technik J 12:44–47

Nortley, R., N. Korte, P. Izquierdo, C. Hirunpattarasilp, A. Mishra, Z. Jaunmuktane, V. Kyrargyri, T. Pfeiffer, L. Khennouf, C. Madry, H. Gong, A. Richard-Loendt, W. Huang, T. Saito, T.C. Saido, S. Brandner, H. Sethi, and D. Attwell. 2019. Amyloid ß oligomers constrict human capillaries in Alzheimer's disease via signaling to pericytes. Sci 365

Nossal R (1980) Mathematical theories of topotaxis. In: Jäger W, Rost H, Tautu P (eds) Biological Growth and Spread. Springer, Berlin, pp 410–439

Nourshargh S, Alon R (2014) Leukocyte migration into inflamed tissues. Immun 41:694–707

Nuhn JAM, Perez AM, Schneider IC (2018) Contact guidance diversity in rotationally aligned collagen matrices. Acta Biomater 66:248–257

Orsi G, Fagnano M, De Maria C, Montemurro F, Vozzi G (2017) A new 3D concentration gradient maker and its application in building hydrogels with a 3D stiffness gradient. J Tissue Eng Regen Med 11:256–264

Park J, Kim D-H, Kim H-N, Wang CJ, Kwak MK, Hur E, Suh K-Y, An SS, Levchenko A (2016) Directed migration of cancer cells guided by the graded texture of the underlying matrix. Nat Mater 15:792–801

Park J, Kim DH, Levchenko A (2018) Topotaxis: a new mechanism of directed cell migration in topographic ECM gradients. Biophys J 114:1257–1263

Patteson AE, Pogoda K, Byfield FJ, Mandal K, Ostrowska-Podhorodecka Z, Charrier EE, Galie PA, Deptuła P, Bucki R, McCulloch CA, Janmey PA (2019) Loss of vimentin enhances cell motility through small confining spaces. Small 15:1903180

Patteson AE, Vahabikashi A, Pogoda K, Adam SA, Mandal K, Kittisopikul M, Sivagurunathan S, Goldman A, Goldman RD, Janmey PA (2019) Vimentin protects cells against nuclear rupture and DNA damage during migration. J Cell Biol 218:4079–4092

Petrie RJ, Doyle AD, Yamada KM (2009) Random versus directionally persistent cell migration. Nat Rev Mol Cell Biol 10:538–549

Plotnikov SV, Pasapera AM, Sabass B, Waterman CM (2012) Force fluctuations within focal adhesions mediate ECM-rigidity sensing to guide directed cell migration. Cell 151:1513–1527

Prentice-Mott HV, Chang C-H, Mahadevan L, Mitchison TJ, Irimia D, Shah JV (2013) Biased migration of confined neutrophil-like cells in asymmetric hydraulic environments. Proc Natl Acad Sci U S A 110:21006–21011

Prentice-Mott HV, Meroz Y, Carlson A, Levine MA, Davidson MW, Irimia D, Charras GT, Mahadevan L, Shah JV (2016) Directional memory arises from long-lived cytoskeletal asymmetries in polarized chemotactic cells. Proc Natl Acad Sci U S A 113:1267–1272

Preston SP, Waters SL, Jensen OE, Heaton PR, Pritchard DI (2006) T-cell motility in the early stages of the immune response modeled as a random walk amongst targets. Phys Rev E Stat Nonlin Soft Matter Phys 74:011910

Prunet, A., S. Lefort, H. Delanoë-Ayari, B. Laperrousaz, G. Simon, C. Barentin, *S. Saci*, F. Argoul, B. Guyot, J.P. Rieu, S. Gobert, V. Maguer-Satta, and C. Rivière. 2020. A new agarose-based microsystem to investigate cell response to prolonged confinement. Lab Chip

Qin D, Xia Y, Whitesides GM (2010) Soft lithography for micro- and nanoscale patterning. Nat Protoc 5:491–502

Raab M, Gentili M, de Belly H, Thiam H-R, Vargas P, Jimenez AJ, Lautenschläger F, Voituriez R, Lennon-Duménil A-M, Manel N, Piel M (2016) ESCRT III repairs nuclear envelope ruptures during cell migration to limit DNA damage and cell death. Sci 352:359–362

Renkawitz J, Kopf A, Stopp J, de Vries I, Driscoll MK, Merrin J, Hauschild R, Welf ES, Danuser G, Fiolka R, Sixt M (2019) Nuclear positioning facilitates amoeboid migration along the path of least resistance. Nat 568:546–550

Renkawitz, J., A. Reversat, A. Leithner, J. Merrin, and M. Sixt. 2018. Chapter 5 - Micro-engineered "pillar forests" to study cell migration in complex but controlled 3D environments. *In* Methods in cell biology. Vol. 147. M. Piel, D. Fletcher, and J. Doh, editors. Academic Press. 79–91

Renkawitz J, Schumann K, Weber M, Lammermann T, Pflicke H, Piel M, Polleux J, Spatz JP, Sixt M (2009) Adaptive force transmission in amoeboid cell migration. Nat Cell Biol 11:1438–1443

Ridley AJ, Schwartz MA, Burridge K, Firtel RA, Ginsberg MH, Borisy G, Parsons JT, Horwitz AR (2003) Cell migration: integrating signals from front to back. Sci 302:1704–1709

Rosowski EE (2020) Determining macrophage versus neutrophil contributions to innate immunity using larval zebrafish. Dis Models Mechan 13:dmm041889

Rowat AC, Jaalouk DE, Zwerger M, Ung WL, Eydelnant IA, Olins DE, Olins AL, Herrmann H, Weitz DA, Lammerding J (2013) Nuclear envelope composition determines the ability of neutrophil-type cells to passage through micron-scale constrictions. J Biol Chem 288:8610–8618

Sadjadi Z, Zhao R, Hoth M, Qu B, Rieger H (2020) Migration of Cytotoxic T Lymphocytes in 3D Collagen Matrices. Biophys J 119:2141–2152

Schakenraad K, Ravazzano L, Sarkar N, Wondergem JAJ, Merks RMH, Giomi L (2020) Topotaxis of active Brownian particles. Phys Rev E 101:032602

Schoppmeyer R, Zhao R, Cheng H, Hamed M, Liu C, Zhou X, Schwarz EC, Zhou Y, Knorck A, Schwar G, Ji S, Liu L, Long J, Helms V, Hoth M, Yu X, Qu B (2017) Human profilin 1 is a negative regulator of CTL mediated cell-killing and migration. Eur J Immunol 47:1562–1572

Schwarz J, Bierbaum V, Vaahtomeri K, Hauschild R, Brown M, de Vries I, Leithner A, Reversat A, Merrin J, Tarrant T, Bollenbach T, Sixt M (2017) Dendritic cells interpret haptotactic chemokine gradients in a manner governed by signal-to-noise ratio and dependent on GRK6. Curr Biol : CB 27:1314–1325

Shin Y, Jeon JS, Han S, Jung G-S, Shin S, Lee S-H, Sudo R, Kamm RD, Chung S (2011) In vitro 3D collective sprouting angiogenesis under orchestrated ANG-1 and VEGF gradients. Lab Chip 11:2175–2181

Sobreiro-Almeida R, Fonseca DR, Neves NM (2019) Extracellular matrix electrospun membranes for mimicking natural renal filtration barriers. Mat Sci Eng : C. 103:109866

Spatarelu C-P, Zhang H, Nguyen DT, Han X, Liu R, Guo Q, Notbohm J, Fan J, Liu L, Chen Z (2019) Biomechanics of collective cell migration in cancer progression: experimental and computational methods. ACS Biomater Sci Eng 5:3766–3787

Stowers RS, Allen SC, Suggs LJ (2015) Dynamic phototuning of 3D hydrogel stiffness. Proc Natl Acad Sci U S A 112:1953–1958

Thiam HR, Vargas P, Carpi N, Crespo CL, Raab M, Terriac E, King MC, Jacobelli J, Alberts AS, Stradal T, Lennon-Dumenil AM, Piel M (2016) Perinuclear Arp2/3-driven actin polymerization enables nuclear deformation to facilitate cell migration through complex environments. Nat Commun 7:10997

Trepat X, Fredberg JJ (2011) Plithotaxis and emergent dynamics in collective cellular migration. Trends Cell Biol 21:638–646

Tse JR, Engler AJ (2011) Stiffness gradients mimicking in vivo tissue variation regulate mesenchymal stem cell fate. PLoS One 6:e15978

Tseng AA, Kuan C, Chen CD, Ma KJ (2003) Electron beam lithography in nanoscale fabrication: recent development. IEEE Trans Electr Packag Manufact 26:141–149

Van Haastert PJM, Devreotes PN (2004) Chemotaxis: signalling the way forward. Nat Rev Mol Cell Biol 5:626–634

Vieu C, Carcenac F, Pépin A, Chen Y, Mejias M, Lebib A, Manin-Ferlazzo L, Couraud L, Launois H (2000) Electron beam lithography: resolution limits and applications. Appl Surf Sci 164:111–117

Vincent LG, Choi YS, Alonso-Latorre B, del Álamo JC, Engler AJ (2013) Mesenchymal stem cell durotaxis depends on substrate stiffness gradient strength. Biotechnol J 8:472–484

Voisin MB, Woodfin A, Nourshargh S (2009) Monocytes and neutrophils exhibit both distinct and common mechanisms in penetrating the vascular basement membrane in vivo. Arterioscler Thromb Vasc Biol 29:1193–1199

Wang X, Hossain M, Bogoslowski A, Kubes P, Irimia D (2020) Chemotaxing neutrophils enter alternate branches at capillary bifurcations. Nat Commun 11:2385

Weber M, Sixt M (2013) Live cell imaging of chemotactic dendritic cell migration in explanted mouse ear preparations. In: Cardona AE, Ubogu EE (eds) Chemokines: Methods and Protocols. Humana Press, Totowa, NJ, pp 215–226

Weigert R, Sramkova M, Parente L, Amornphimoltham P, Masedunskas A (2010) Intravital microscopy: a novel tool to study cell biology in living animals. Histochem Cell Biol 133:481–491

Whitesides GM, Ostuni E, Takayama S, Jiang X, Ingber DE (2001) Soft lithography in biology and biochemistry. Ann Rev Biomed Eng 3: 335–373

Wójciak-Stothard B, Curtis A, Monaghan W, MacDonald K, Wilkinson C (1996) Guidance and activation of murine macrophages by nanometric scale topography. Exp Cell Res 223:426–435

Wondergem JA, Witzel P, Mytiliniou M, Holcman D, Heinrich D (2020) Topographical guidance of highly motile amoeboid cell migration. Biophys J 118:606a

Worbs T, Hammerschmidt SI, Förster R (2017) Dendritic cell migration in health and disease. Nat Rev. Immunol 17:30–48

Wu PH, Giri A, Sun SX, Wirtz D (2014) Three-dimensional cell migration does not follow a random walk. Proc Natl Acad Sci U S A 111: 3949–3954

Xu Y, Pang SW (2019) Natural killer cell migration control in microchannels by perturbations and topography. Lab Chip 19: 2466–2475

Yamada KM, Sixt M (2019) Mechanisms of 3D cell migration. Nat Rev Mol Cell Biol 20:738–752

Zhang X, Li L, Luo C (2016) Gel integration for microfluidic applications. Lab Chip 16:1757–1776

Zhao R, Afthinos A, Zhu T, Mistriotis P, Li Y, Serra SA, Zhang Y, Yankaskas CL, He S, Valverde MA, Sun SX, Konstantopoulos K (2019) Cell sensing and decision-making in confinement: the role of TRPM7 in a tug of war between hydraulic pressure and cross-sectional area. Sci Adv 5:eaaw7243